ULTRATHIN CARBON-BASED OVERCOATS FOR EXTREMELY HIGH DENSITY MAGNETIC RECORDING

YEO JUEYUAN REUBEN
(B.Eng. (Hons.), Nanyang Technological University, Singapore)

A THESIS SUBMITTED FOR THE DEGREE OF DOCTOR OF PHILOSOPHY

DEPARTMENT OF ELECTRICAL AND COMPUTER ENGINEERING

NATIONAL UNIVERSITY OF SINGAPORE

2015

DECLARATION

I hereby declare that this thesis is my original work and it has been written by me in its entirety. I have duly acknowledged all the sources of information which have been used in this thesis.

This thesis has also not been submitted for any degree in any university previously.

Yeo Jueyuan Reuben
12 August 2015

Acknowledgments

I have so many people to thank who have helped or impacted me during my PhD journey of research and learning at NUS. It has been a very enriching experience. This thesis, which represents the culmination of my research work here at the Spin and Energy Lab (SEL), NUS, would not have been possible without these amazing, friendly people.

First and foremost, I would like to express my utmost gratitude to my main supervisor and advisor Professor C. S. Bhatia, for his unwavering support throughout my PhD over the last four years. Prof Bhatia has a vast expertise and network in the area of tribology of ultrathin overcoats for magnetic storage systems, and I consider myself fortunate to have learnt so much from him. I am grateful for his time and dedication spent in meeting with me frequently to discuss my progress, and for providing me with invaluable advice and insight with regards to my work.

I greatly appreciate my current co-supervisors Dr. Sudhiranjan Tripathy and Associate Professor Christina Lim, as well as my previous co-supervisor Associate Professor Sujeet K. Sinha for their support at various stages of my PhD. I am very grateful for them for generously providing the equipment and resources at the A*STAR Institute of Materials Research and Engineering (IMRE) and the NUS Mechanical Engineering Department, which constituted a major part of my work. I am also grateful to Associate Professor Daniel J. Blackwood for his help and advice on the electrochemical corrosion setup, corrosion measurements and analyses. I appreciate his

patience and helpfulness in the many meetings I had with him during the initial stages of calibrating the setup.

I am extremely grateful to my mentors/seniors Dr. Ehsan Rismani and Dr. Neeraj Dwivedi for their careful guidance and patience in imparting to me their knowledge and research skills in the areas of tribology, thin film fabrication, characterization and analysis, which have become so essential to my work. I cannot thank them enough for all the time they had spent with me to ensure that I got all the necessary training. They have become my close friends. I am also thankful for the other post-docs in our tribology team in SEL, namely Dr. Mohammad Abdul Samad, Dr. Nalam Satyanarayana and Dr. Partho S. Goohpattader, for their support and contributions in our projects.

A significant portion of time was spent at IMRE and at A*STAR's Institute of Microelectronics (IME) for sample characterization, and I am very grateful to the scientists and engineers there for their expert help in performing the characterizations and occasionally in data analysis. Special mention goes out to Dr. Zhang Zheng, Ms. Hui Ru Tan and Dr. Debbie Seng from IMRE and Mr. Kwek Wee Ming and Ms. Zhang Lu from IME.

For the work on tape heads, I would like to especially thank my mentors from the Information Storage Industry Consortium (INSIC) TAPE program, namely Dr. Geoff Spratt from Hewlett Packard for his consistent guidance on our progress in tape head overcoat development and his contribution in performing the long-term wear tests on the coated functional tape heads, as well as Dr. April Alstrin from Oracle Corporation for supplying us with tape heads and substrates.

The members of SEL, past and present, have also contributed immensely to my professional and personal growth through the ups and downs of my PhD journey. They have been and still are good friends, whom I will continue to treasure in the years to come. Some of the members that I had the pleasure of working with include: fellow SEL grad students and colleagues Miss. Li Ming Loong, Dr. Shreya Kundu, Mr. Karan Banerjee, Mr. Shawn Siew Yohannes, Dr. Deng Jun, Dr. Siddharth Rao, Dr. Son Jaesung, Dr. Qiu Xuepeng and Dr. Kalon Gopinadhan; SEL lab managers Mr. Jung Yoon Yong Robert and Dr. Liao Baochen; research engineer Mr. Sandeep Singh; and administration executive Ms. Habeebunisa.

Lastly, and definitely the most important people of all, I would like to thank my family (my dad, my mum, and my sister Vanessa) for their love, patience, encouragement and support throughout my PhD, and for being there for me at all times. With them, my time at NUS was made substantially more enjoyable and restful. Thank you so much.

Reuben Yeo
National University of Singapore
August 2015

Funding Sources:

This research was supported by the National Research Foundation, Prime Minister's Office, Singapore under its Competitive Research Programme (CRP Award No. NRF-CRP-4-2008-6). The work on tape heads was partially funded by the INSIC TAPE Program.

Table of Contents

Page

Thesis Summary

For future magnetic recording systems possessing extremely high storage densities, a lower magnetic spacing at the head-media interface is necessary to maintain strong readback signal integrity and writability. However, this occurs at the expense of drive reliability due to the lack of protection at the head-media interface. In this thesis, several novel ultrathin protective carbon-based overcoats for hard disk drive (HDD) media and magnetic tape drive heads were developed and investigated in terms of their functional and interfacial chemistry, chemical bonding environment and carbon microstructure.

In HDDs, ultrathin media overcoats are crucial to protect the recording media from wear and corrosion. Unfortunately, carbon overcoats (COCs) fabricated by conventional techniques are not able to effectively protect the media at thicknesses of $\leq$ 2 nm, and are not thermally stable for future heat-assisted magnetic recording (HAMR) technology at areal densities of > 1 Terabit/in^2. Here, media overcoat thicknesses of 1.6–1.8 nm were fabricated to achieve an areal density of 4 Terabits/in^2. By tailoring the energetics of the carbon species during deposition, a high sp^3-bonded carbon (sp^3C) overcoat of ~ 1.8 nm was grown by a filtered cathodic vacuum arc (FCVA) bi-level energy process that demonstrated superior tribological and corrosion protection with high thermal stability under HAMR conditions. Furthermore, by introducing an atomically-thin amorphous silicon nitride (SiN_x) interlayer, a 1.6 nm SiN_x/C bi-layer overcoat with excellent wear and corrosion protection was developed at low energies without affecting the macromagnetic

properties of the media. The role of SiN_x was critical in forming strong interfacial bonding between the media and COC, as well as enhancing sp^3C bonding due to the suppression of media-induced catalytic $sp^3C \rightarrow sp^2C$ transformation. These overcoats showed comparable corrosion and better wear/friction performance than thicker commercial COCs (~ 2.7 nm).

In magnetic tape drives, a magnetic spacing of 22 nm is desired by 2018 to achieve an areal density of ~ 20 Gigabits/in^2. The application of an ultrathin wear-durable head overcoat could extend the operational lifetime of the tape head by delaying the onset of pole-tip recession, which could produce an undesirable magnetic spacing of up to 40 nm. The improvement in wear durability was addressed by enhancing the adhesion and interfacial bonding at the head substrate-overcoat interface, which is counterintuitive to conventional approaches of overcoat fabrication. By introducing a 3 nm SiN_x interlayer for 7 to 20 nm bi-layer SiN_x/C overcoats, this resulted in the creation of two enhanced carbon-SiN_x and SiN_x-Al_2O_3/TiC substrate interfaces with extensive interfacial bonding. Remarkably, the ~ 20 nm SiN_x/C overcoats deposited on electrically-functional tape heads demonstrated an exceptional wear life of up to 40–50 million meters after being subjected to long-term testing in a simulated tape drive environment. This is the best performance reported in literature to date.

Finally, a monolayer graphene overcoat was explored for commercial hard disk media, which could drastically reduce the magnetic spacing. Despite being atomically thin (~ 3.5 Å), it was shown to improve the tribological

properties and corrosion resistance of uncoated commercial media based on preliminary results.

List of Tables

List of Figures

List of Symbols

°	Degrees (angle)
°C	Degrees Celsius
Ω	Ohms (electrical resistance)
<	Less than
≤	Less than or equal to
>	Greater than
~	Approximately
µm	Micrometer
@	At
0D	Zero-dimensional
1D	One-dimensional
2D	Two-dimensional
Å	Angstrom
A	Amperes
a.u.	Arbitrary units
a-C	Amorphous carbon
a-C:H	Hydrogenated amorphous carbon
a-C:N	Nitrogenated amorphous carbon
AES	Auger Electron Spectroscopy
AFM	Atomic Force Microscopy *or* Antiferromagnetic
Ag	Silver
AgCl	Silver chloride
Al	Aluminum
Al_2O_3	Aluminum oxide
AlTiC	Aluminum oxide/Titanium carbide composite
Ar	Argon
ASTC	Advanced Storage Technology Consortium
BaFe	Barium ferrite
BBSNR	Broad band signal-to-noise ratio
BE	Binding energy
Bi	Bismuth
BPM	Bit-patterned media
C	Carbon
CCD	Charge coupled device
cm	Centimeter
Co	Cobalt
COC	Carbon overcoat
CoCrPt	Cobalt chromium platinum
COF	Coefficient of friction
CoZrTa	Cobalt zirconium tantalum
Cr	Chromium

Cs	Caesium
CVD	Chemical vapor deposition
dB	Decibels
DC	Direct current
DLC	Diamond-like carbon
e.g.	For example
E_{oc}	Open circuit potential
eV	Electron-volts
FCVA	Filtered cathodic vacuum arc
Fe	Iron
FePt	Iron platinum
g	Grams
Gb	Gigabits
GMR	Giant magnetoresistance
GPa	Gigapascals
H	Hardness *or* Hydrogen
HAMR	Heat-assisted magnetic recording
HCA	Head cleaning agent
HDD	Hard disk drive
HDI	Head-disk interface
HiPIMS	High-power impulse magnetron sputtering
HMS	Head-media spacing
HRTEM	High resolution transmission electron microscopy
I	Current
I-V	Current-voltage
i.e.	That is to say
I_D/I_G	D peak-to-G peak intensity ratio
in	Inches
IME	Institute of Microelectronics, Singapore
IMRE	Institute of Materials Research and Engineering, Singapore
INSIC	Information Storage Industry Consortium
j_{corr}	Corrosion current density
k or **k_B**	Boltzmann's constant
keV	Kiloelectron-volts
kHz	Kilohertz
K_u	Magnetic anisotropy constant
LTO	Linear Tape Open
m	Meters
M	Molar (concentration) = mol/dm^3
MgO	Magnesium oxide
min	Minutes

mN	Millinewtons
MOKE	Magneto-optical Kerr effect
MPa	Megapascals
MR	Magnetoresistance
MTJ	Magnetic tunnel junction
mTorr	Millitorr
mV	Millivolts
N	Newtons (force) *or* Nitrogen
N_2	Nitrogen gas
nA	Nanoamperes
NiFe	Nickel iron *or* Permalloy
nm	Nanometers
O	Oxygen
PE	Protective efficiency
PECVD	Plasma enhanced chemical vapor deposition
PFPE	Perfluoropolyether
PMR	Perpendicular magnetic recording
Pt	Platinum
PTR	Pole tip recession
PVD	Physical vapor deposition
R_a	Average roughness
RF	Radio frequency
RH	Relative humidity
RMS	Root-mean-square
R_q	Root-mean-square roughness
s	Seconds
sccm	Standard cubic centimeters per minute
SEM	Scanning electron microscopy
Si	Silicon
Si_3N_4	Silicon nitride
SiN_x	Amorphous silicon nitride
SNR	Signal-to-noise ratio
sp^2C	sp^2-hybridized carbon
sp^3C	sp^3-hybridized carbon
SRIM	Stopping and range of ions in matter
SUL	Soft underlayer
T	Temperature
Ta	Tantalum
ta-C	Tetrahedral amorphous carbon
ta-C:H	Tetrahedral hydrogenated amorphous carbon
ta-C:N	Tetrahedral Nitrogenated amorphous carbon

Tb	Terabits
TB	Terabytes
TFC	Thermal fly-height control
Ti	Titanium
TiC	Titanium carbide
TiN	Titanium nitride
TMR	Tunneling magnetoresistance
TOF-SIMS	Time-of-flight secondary ion mass spectrometry
UV	Ultraviolet
V	Volume *or* voltage
XPS	X-ray photoelectron spectroscopy

Chapter 1: Introduction

The history of magnetic recording dates back more than a hundred years, since the invention of a magnetic wire recording system by Valdemar Poulsen [1]. Through numerous developments and breakthroughs in magnetic recording technology over the past century, two main formats of magnetic recording have endured and still exist today for digital data storage purposes, in the form of magnetic tape drives and magnetic disk drives.

When comparing between magnetic recording systems then and now, it is difficult not to marvel at the tremendous progress that has been made to achieve the data storage densities that we see in commercial tape and disk drives today. Data storage densities can be calculated in terms of areal density, which is the amount of magnetic bits that can be stored in a unit area of the magnetic medium of the recording system. For example, the first hard disk drive (HDD) developed by IBM in 1956, the RAMAC 350, had an areal density of just 2000 bits/in^2 and occupied a total space of roughly 2 m^3 [2]. In comparison, recent advancements in HDD technology have brought about the introduction of ~ 8 terabyte (TB) drives, occupying a volume of just 0.004 m^3 and having an areal density of close to 1 terabit/in^2 (Tb/in^2). This brings the improvement in the areal density of HDDs to almost 500 million times in the last 60 years. With the increase in areal density, the reduction of cost per bit also followed, making magnetic storage systems the cheapest forms of high density data storage around.

Today, huge amounts of digital content are being consumed and produced with the help of the Internet, with the total amount of digital data

estimated at ~ 4.4 zettabytes (4.4×10^{21} bytes) in 2013 – and this is anticipated to continue growing at an accelerated rate in the coming years [3]. Hence, continual improvements in areal densities to maintain the low cost of data storage systems are vital to accommodate this ever-increasing demand.

1.1 Basics of magnetic recording

While the technologies in HDDs and tape drives have seen major improvements throughout their history, the basic concept of magnetic recording is applied in both systems and has remained the same. A simple magnetic recording system comprises a granular ferromagnetic thin film media layer on which data can be recorded, and a magnetic write and read head to record and read back data from the media respectively. The write head contains a coil of wire wrapped around a soft ferromagnetic core material (such as a cobalt or nickel-iron alloy) with an "open ring" shape, as shown in Figure 1.1. During the write process, a current applied through the wire induces a magnetic field inside the ferromagnetic core, causing it to become magnetized. Hence, the write head is commonly known as an inductive write pole. This induced magnetic field is emanated from the head into the media, causing a cluster of magnetic grains in the recording layer to be magnetized in a certain direction. Each cluster of grains that is magnetized in the same direction makes up one magnetic bit of information, as shown schematically in Figure 1.1. By changing the direction of the current, the grains can be magnetized in the opposite direction to form another bit as the head moves along the media. In perpendicular magnetic recording (PMR), which is the current technology used in modern disk and tape media, the information is

recorded onto the media by magnetizing the grains in either in the "up" or "down" direction, as illustrated in Figure 1.1. The bits are stored along discrete tracks in the media. For hard disk media, the tracks are arranged in concentric rings spanning from the inner diameter to the outer diameter of the disk; whereas for tape media, the tracks are arranged parallel to the length of the tape.

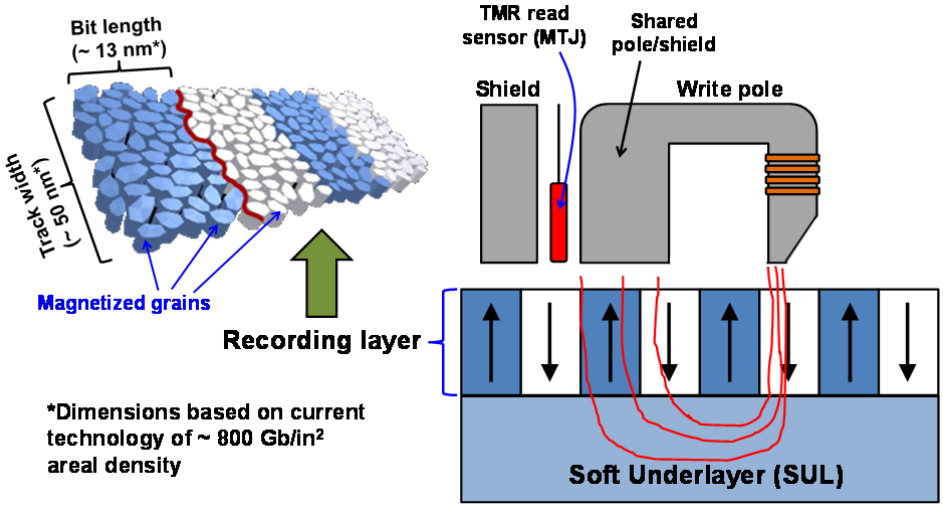

Figure 1.1 The perpendicular magnetic recording scheme, showing an integrated read/write head consisting of a write pole and TMR read sensor. The red lines at the write pole represent the field lines emanating from the write pole into the media during the recording process. The top view of the recording layer is presented, showing the arrangement of the magnetized grains and bits along a track. The dimensions of bit length and track width are based on current HDD technology of ~ 800 gigabits/in^2 (Gb/in^2) areal density.

To read back the data, modern read heads are essentially magnetic sensors which employ either the giant magnetoresistance (GMR) effect (which is currently used in tape heads) or the tunneling magnetoresistance (TMR) effect (which is currently used in HDD heads) [4–7].

Modern read sensors in tape heads are "spin valve" structures consisting of an antiferromagnetic "pinning" layer, an adjacent ferromagnetic "pinned" layer, a ferromagnetic "free" layer, and an ultrathin non-magnetic

metallic "spacer" separating the "pinned" and "free" layers as illustrated in Figure 1.2(a). The magnetization of the pinned layer is magnetically coupled or "pinned" to the antiferromagnetic pinning layer in one direction. On the other hand, the magnetization direction of the free layer can be switched depending on the magnetic field generated from the recording layer of the media. Fundamentally, the GMR effect can be understood based on electron conduction through the spin valve. The electrons can have two different spin orientations – either parallel or antiparallel to the magnetization direction. Electrons having a spin parallel to the magnetization direction experience less scattering during conduction, as compared to electrons which have an antiparallel spin, as shown in Figure 1.2(b). This is known as spin-dependent scattering. With large amount of scattering, the electrical resistance increases due to the lower mean free path of the electrons, and vice versa. Thus, intuitively, the overall resistance encountered in the parallel configuration of the pinned and free layers would be significantly lower than that in the antiparallel configuration. The change in the resistance between the parallel and antiparallel configuration gives rise to the GMR effect. The magnetoresistance (MR) value for GMR spin valves can be calculated by $\Delta R/R$, where ΔR is the difference in the resistance measured in the parallel and antiparallel configurations, and R is the resistance measured at zero applied field. GMR spin valves can exhibit MR values of up to 20% [8].

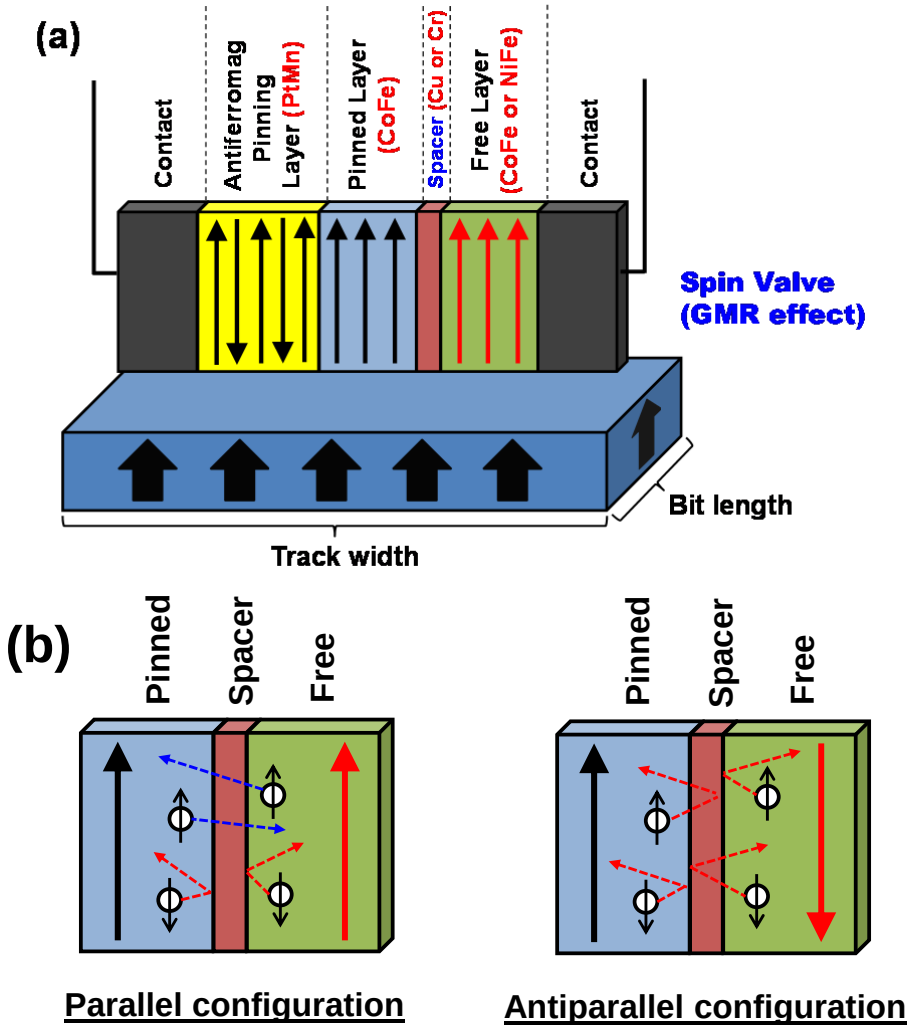

Figure 1.2 (a) Schematic showing the layers in the spin valve in a GMR read sensor such as one for the tape head. The free layer is magnetized in the "up" direction due to the magnetic field from the media bit, giving a parallel configuration in the spin valve. (b) Schematic showing the interfacial spin-dependent scattering of conduction electrons between the pinned and free layers for the parallel and antiparallel configurations. Stronger overall scattering occurs in the antiparallel configuration, resulting in a higher resistance.

The structure of a HDD read sensor is similar to the spin valve, except that the spacer is replaced with an ultrathin (~ 1–2 nm) electrically insulating layer such as MgO, as shown in Figure 1.3. This structure is known as a magnetic tunnel junction (MTJ). The working principle of the MTJ derives from two important quantum phenomena: 1) The conduction electrons are able

to pass through the ultrathin insulating barrier between the free and pinned magnetic layers by means of quantum tunneling, and 2) the spin of the electron is conserved when it tunnels through the insulating barrier. Based on quantum mechanics principles, the tunneling probability of the conduction electrons through the insulating barrier is higher when both free and pinned layers are aligned in the parallel configuration, but lower when the layers are aligned in the antiparallel configuration. Hence, a low tunneling probability leads to a higher electrical resistance, and vice versa. This gives rise to the TMR effect. One of the main benefits of the TMR effect in MTJ structures is that large MR values of up to 350% can be achieved [9]. At higher areal densities, larger MR values (i.e. higher sensitivity read sensors) are desired because of the reduced magnetic flux arising from smaller bit sizes. While present-day tape heads still use GMR spin valve read sensors, it is projected that future tape heads may also implement MTJ read sensors in the future with increasing areal density.

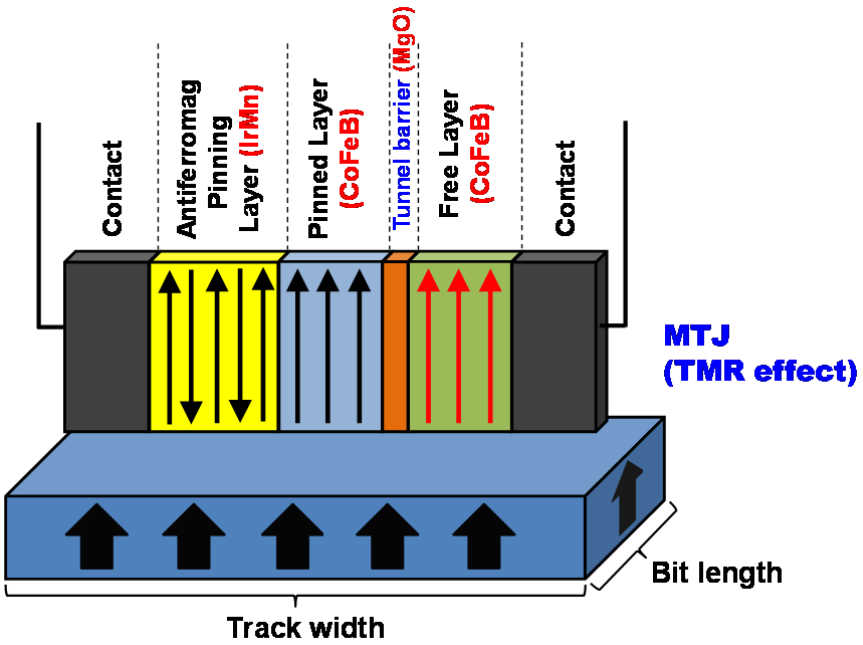

Figure 1.3 Schematic showing the layers in an MTJ read sensor such as one for the HDD read head.

1.2 Magnetic hard disk drives

Figure 1.4 shows a photograph of an opened modern HDD showing its internal components. The media is deposited on an ultra-smooth, rigid disk substrate of glass or aluminum alloy. The magnetic read/write head is attached at the end of an actuator arm and suspension assembly connected to a voice coil motor. This makes up the servo mechanism which is responsible for positioning the head above the desired track on the disk for data reading and writing. During operation, the disk spins at a high speed of 5400–15000 revolutions per minute, while the head flies just several nanometers above the disk surface.

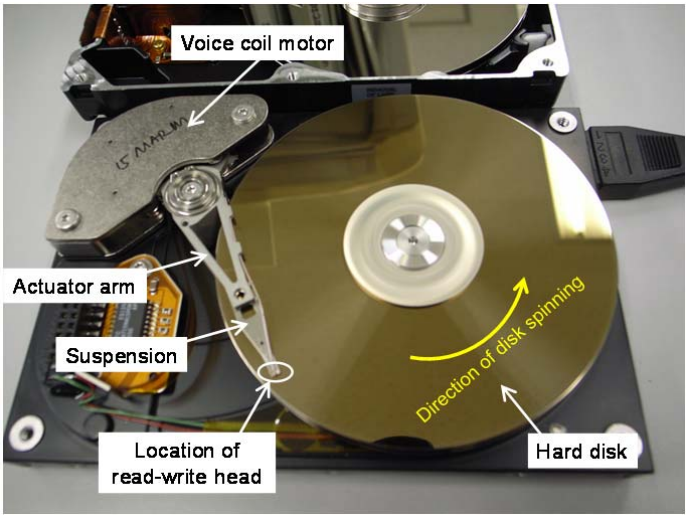

Figure 1.4 Components of the HDD. Data is stored in the disk, whereas the servo mechanism comprising the voice coil motor and actuator arm and suspension assembly positions the magnetic read/write head over a specific track on the disk for data recording and readback.

1.2.1 Magnetic read/write head

The magnetic read/write head is an integrated head which combines the inductive write pole together with the read sensor, as shown in the cartoon in Figure 1.1. In this integrated head, the write pole and read sensor are

positioned side by side, with the side of the write pole adjacent to the read sensor doubling as a soft ferromagnetic shield to prevent stray magnetic fields from neighboring bits of the media from affecting the sensor reading. The tiny read/write head is situated at the edge of a slider made of a hard Al_2O_3-TiC (AlTiC) composite ceramic substrate, which is a two-phase composite material comprising non-homogeneously sized TiC grains (~ 30%) distributed within an amorphous Al_2O_3 matrix (~ 70%). A hydrodynamic air-bearing surface design is etched into the underside of the AlTiC slider, which creates an air pressure profile between the slider and the disk so as to maintain a constant fly height as the disk spins [10, 11]. A photograph of the slider showing the read/write head and air-bearing surface is shown in Figure 1.5.

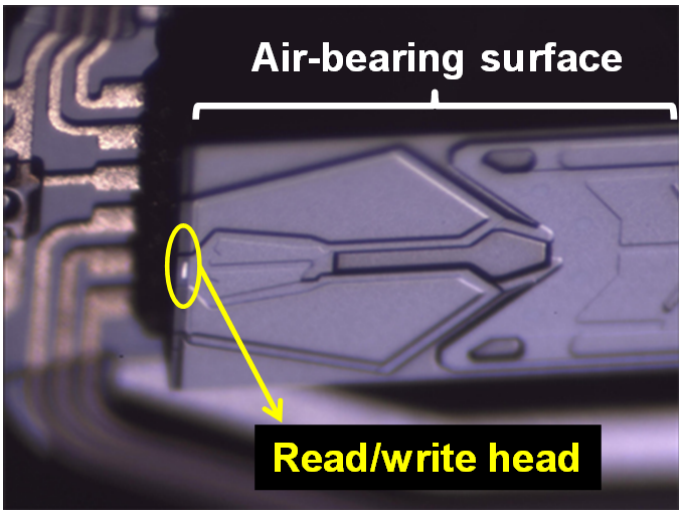

Figure 1.5 Photograph of an air-bearing surface on the underside of a slider. The location of the read/write head on the slider is indicated. [12].

1.2.2 Magnetic disk media

In HDDs utilizing PMR technology, media is commercially grown on the disk substrate by magnetron sputtering. A cross-sectional high resolution transmission electron microscope (HRTEM) image of a modern commercial

hard disk media stack consisting of several thin film layers is shown in Figure 1.6, with the individual layers labeled. While the function of each layer will not be discussed here, each layer contributes to achieve an optimized magnetic anisotropy in the magnetic recording layer situated at the top of the media stack. As shown in Figure 1.6, the recording layer is typically a CoCrPt:Oxide alloy, which is grown as columnar grains for PMR.

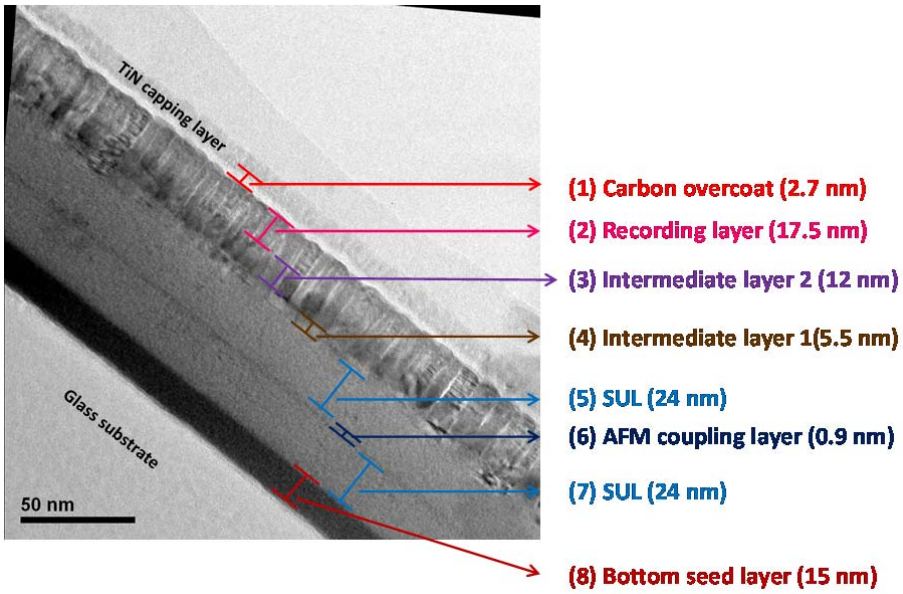

Figure 1.6 Cross-sectional HRTEM image of a commercial hard disk media stack, with the composition and approximate thickness of each layer labeled.

1.2.3 The head-disk interface

Due to the high velocities involved and the extremely low fly height of the head above the disk, frequent intermittent contacts having high impact forces can occur between the head and disk. As such, the head-disk interface (HDI) is one of the most important areas of the drive to be engineered so as to prevent damage to the head and media. The different components of the HDI are presented in a schematic as shown in Figure 1.7. As can be seen, the components of the HDI contribute to the head-media spacing (HMS), which is

~ 10 nm in present day HDDs for ~ 800 Gb/in^2 areal density [13]. The HMS is also known as the magnetic spacing, which is the distance between the bottom of the read/write head and the top of the recording layer. Such a low spacing is necessary to ensure both good writability of the data onto the media and a high SNR for data readback. In addition, sufficient corrosion protection is critical both for the read/write head as well as for the hard disk media to ensure data recording integrity. As described in Sections 1.1 and 1.2.2, a Co-based alloy (ferromagnetic material) is used for the read/write poles in the head and also for the magnetic recording layer in the disk. Co-based alloys are known to be very susceptible to corrosion and oxidation, and the oxidation of the Co-based poles or magnetic recording layer would lead to degradation in the performance/functionality of the read/write head and the media. This is achieved by the use of protective overcoats on the head and media. In view of this, the dimensions of each component at the HDI have been carefully controlled and optimized to obtain reliable write and read performance at current areal densities.

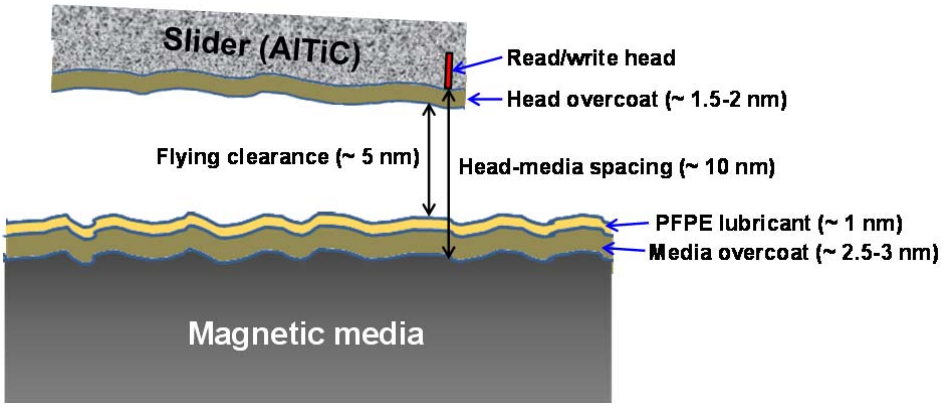

Figure 1.7 Schematic of the head-disk interface in current HDDs, with its components and their respective dimensions labeled.

1.2.3.1 Head overcoat

The primary purpose of the head or slider overcoat is to protect the slider and the read/write head materials from wear and corrosion. In the current technology, the total thickness of the head overcoat is ~ 1.5–2 nm. The overcoat, which is applied on the underside of the slider, typically consists of an ultrathin non-hydrogenated carbon overcoat (COC) and a silicon-based interlayer to promote the adhesion of the COC to the AlTiC substrate of the slider [14, 15]. For the head overcoat, the COC layer is fabricated by a technique known as filtered cathodic vacuum arc (FCVA) via a batch process, which has been found to provide a dense, hard and smooth film at low thicknesses with a high degree of coverage for corrosion resistance and wear durability [16–19]. Apart from providing wear and corrosion protection for the head, the head overcoat also acts as an inert barrier between the perfluoropolyether (PFPE) lubricant and the AlTiC material of the slider. It has been found that Al is prone to catalyze the decomposition of the lubricant, leading to the onset of lubricant degradation and end of life of the HDD [20–24].

1.2.3.2 Media overcoat

On top of the recording layer, a COC is required for protecting the underlying media from wear during intermittent contact between the head and the disk, as well as for corrosion/oxidation protection due to the ease of oxidation of the ferromagnetic media material. Without a protective overcoat, wear and corrosion of the media will lead to data loss and erasure through degradation of the recording layer. The use of an amorphous carbon thin film

as the COC layer was first proposed by Arnoldussen and Rossi [25]. Currently, media COCs possess a thickness of ~ 2.5–3 nm, and at such low thicknesses, wear and especially corrosion protection becomes more challenging because of the increasing difficulty to achieve sufficient coverage of the media. The overcoat is commonly fabricated using plasma-enhanced chemical vapor deposition (PECVD) processes to form a hydrogenated COC [13, 17]. PECVD of hydrogenated carbon films has the main advantage of avoiding the generation of particulates as observed in processes like FCVA, while being able to generate harder films with better coverage than the sputtering process [23, 26, 27]. In addition, the incorporation of a small amount of hydrogen was found to be beneficial for adsorption of the PFPE lubricant [28]. In some cases, a nitrogenated carbon layer can be incorporated to improve the mechanical toughness and wear resistance of the film, as well as its compatibility with the disk lubricant [21, 29–31].

1.2.3.3 Media lubricant

A monolayer of PFPE lubricant (~ 1 nm) is used as the media lubricant and is applied on top of the media COC via the dip-coating technique [32, 33]. PFPE is a class of fluoropolymers which contain a long chain fluorinated backbone. The most commonly used PFPEs for hard disk media are Fomblin Z-dol and Z-tetraol, which are fluoropolymers containing hydroxyl (–OH) end groups. Their structural formulae are represented as:

$$R–O–[–CF_2–CF_2–O–]_m–[–CF_2–O–]_n–R$$

where R = $–CF_2–CH_2–OH$ for Z-dol,

and R = $–CF_2–CH_2–O–CH_2–CH(OH)–CH_2–OH$ for Z-tetraol,

and m and n are integers which vary based on the molecular weights of the PFPE [34].

The purpose of the –OH end groups is for the PFPE molecule to chemically bond itself to the exposed dangling bonds at the COC surface, and in this way, the lubricant is able to saturate the surface dangling bonds [34]. The saturation of the dangling bonds and the presence of the fluorinated backbone both provide a low surface energy and low friction surface in order to reduce friction and stiction (static friction) upon head-disk contact. The use of different lubricant types and formulations is itself an area of ongoing research to improve the HDI. For example, PFPEs containing more functional groups and other multidentate forms of PFPEs can adhere better to the media COC surface, leading to less amount of lubricant transfer to the head slider, as well as a lower overall lubricant thickness because of the higher amount of bonding sites [35–37]. Lubricant additives such as phosphazene-based molecules can also be added into the lubricant formulation to further reduce the stiction during head-disk contact, prevent the catalytic decomposition of the PFPE and possibly contribute to the lubricant's higher thermal stability [21, 38].

1.2.3.4 Flying clearance

The flying clearance is another very critical aspect of the HDI. A lower HMS can be achieved by reducing the flying clearance. In HDDs today, the flying clearance can be actively reduced or controlled *in situ* via a method known as active thermal fly-height control (TFC) at the head [39, 40]. The concept of TFC is illustrated schematically in Figure 1.8. A heating element is

installed directly above the read/write head which can be activated during operation. By applying an appropriate amount of power to the heater, thermal expansion causes the read/write head to be protruded to a distance nearer the surface for the read/write operation while the rest of the slider remains at a higher clearance. This effectively reduces the magnetic spacing without the need to bring the whole slider nearer the disk surface.

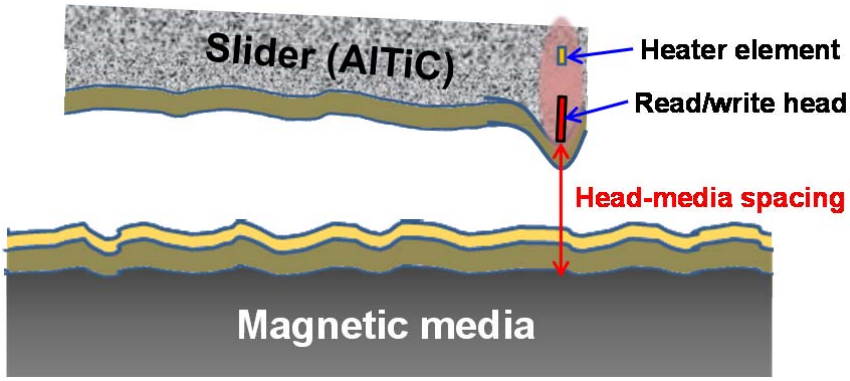

Figure 1.8 Schematic showing the concept of active thermal fly height control (TFC), lowering the head-media spacing through protrusion of the read-write head from the slider.

However, the low flying clearance of ~ 5 nm in modern HDDs inevitably leads to several other issues at the HDI [41], such as:

- An increased effect of attractive forces (van der Waals, electrostatic and meniscus forces) between the head and disk which can affect the fly height stability [42, 43].
- Increasing significance of the disk and slider roughness as well as the disk surface's micro-waviness in affecting the spacing variation and flying dynamics.
- Greater influence from the behavior of the lubricant at the HDI such as transfer/pickup of mobile lubricant by the slider from the disk,

lubricant redistribution across the disk, and the generation of "ripples" in the lubricant due to air shearing stresses resulting from the head flying dynamics [44].

1.2.4 The superparamagnetic effect

As the industry seeks to attain higher areal densities in HDDs, difficulties start to arise as the magnetic media grain size is scaled down to the nanometer scale. At this scale, a phenomenon known as the superparamagnetic effect starts to grow in significance. In a magnetic grain, the magnetization reversal energy is determined by the product of the magnetic anisotropy constant (K_u) and the volume of the grain (V). As the grain size reduces, K_uV decreases, thus reducing the energy required for magnetic switching. This continues until a point where the V is small enough for thermal fluctuations at room temperature to provide enough thermal energy (k_BT) to spontaneously switch the magnetization of the grain. This is the point where the grain exhibits superparamagnetic behavior.

For sufficient thermal stability for up to 10 years, magnetic recording systems should ideally possess a K_uV/k_BT ratio of at least 40 to 60 [45]. To increase the thermal stability with smaller V, the K_u of the media has to be increased by using magnetic materials with higher magnetocrystalline anisotropy such as FePt. However, doing so would make it difficult for data to be written onto the high K_u media with the current inductive write head fields, due to the high media coercivity. As such, going forward, there would have to be advancements in technologies that could delay or overcome the onset of the superparamagnetic effect.

1.2.5 Magnetic recording technologies for > 1 Tb/in^2 areal densities

Several magnetic recording technologies for future HDDs have been proposed by the industry in their roadmap to advance its areal density to > 1 Tb/in^2. These include heat-assisted magnetic recording (HAMR) [46, 47], bit-patterned media (BPM) [48, 49], microwave-assisted magnetic recording (MAMR) [50], shingled magnetic recording (SMR) [51] and two-dimensional magnetic recording (TDMR) [52]. Simultaneously, drive-level enhancements are being introduced to improve its reliability, such as the development of a helium-filled drive [53]. Out of these future magnetic recording technologies, the industry roadmap focuses on two major and promising technologies of HAMR, BPM, and a combination of both, which could potentially achieve an areal density of up to 10 Tb/in^2, as shown in Figure 1.9 [54]. A brief overview on HAMR and BPM technologies is provided as follows.

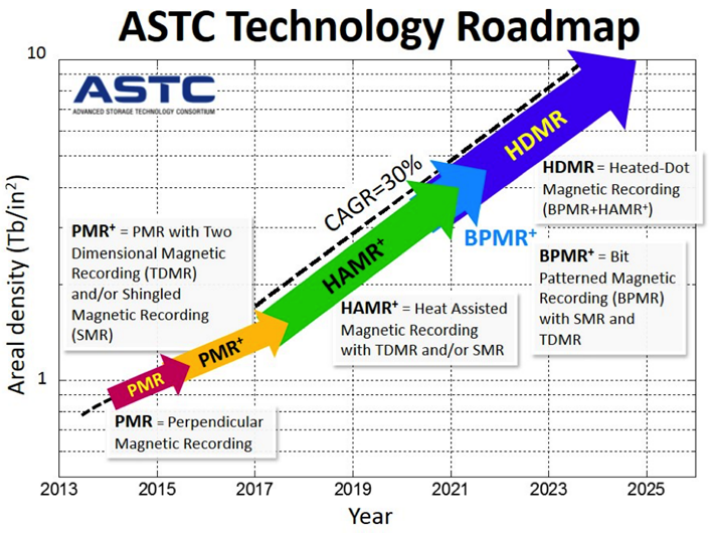

Figure 1.9 2014 Roadmap for HDDs drawn up by the Advanced Storage Industry Consortium (ASTC). [54].

1.2.5.1 Heat-assisted magnetic recording (HAMR)

In HAMR, high K_u media materials such as $L1_0$-oriented FePt media are utilized as the recording media to obtain higher thermal stability at low V. To solve the writability issue, HAMR employs a laser which temporarily heats up a localized spot on the FePt media layer. This enables its local magnetic coercivity to be reduced to a level below the available write field from the head so that the bit can be written into the media. After the writing process, the heat is removed and the coercivity returns to its original value at room temperature, thereby locking in the magnetization of the bit in the media. A simple schematic is shown in Figure 1.10 to illustrate the working principle of HAMR.

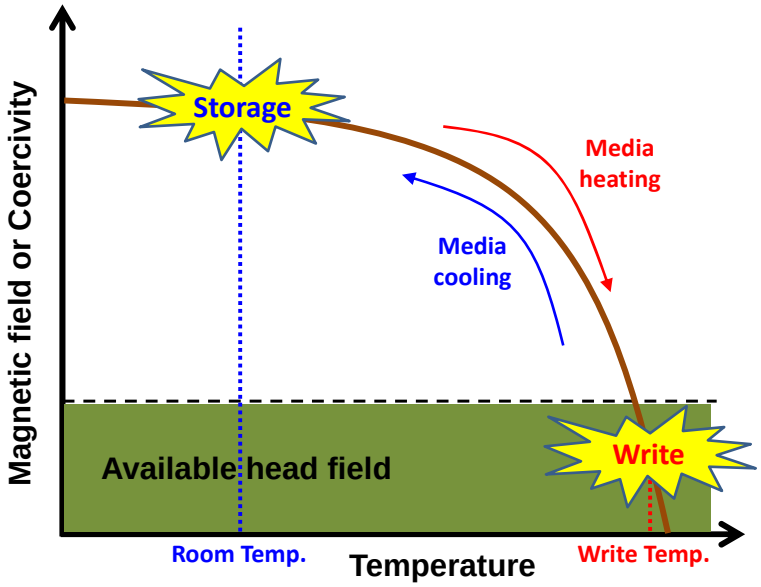

Figure 1.10 Schematic showing the heat assisted magnetic recording process (adapted from [46]).

1.2.5.2 Bit-patterned media (BPM)

BPM employs the concept of patterning the recording media into small dots/islands several nanometers in size arranged in an ordered array. These

islands can be patterned by advanced nanolithography or self-assembly techniques. The volume of each island in BPM is made to be larger than that of one magnetic grain in conventional PMR media so that the magnetic island has sufficient thermal stability. During recording, each island can be magnetized to form one magnetic bit, and since each island is physically separated from each other, they can be magnetically decoupled such that the magnetization of one bit does not influence its neighboring bit. This results in a bit size defined by the size of the magnetic island itself, which is much smaller in size than what is achieved in granular media. In this way, a higher areal density can be achieved [55].

1.2.6 Requirements at the head-disk interface for high density magnetic recording

To accommodate the increase in the areal density to > 1 Tb/in^2, further reduction of the HMS is required to maintain an adequate SNR. As a good estimate, the intensity of the readback signal can be scaled exponentially with the HMS according to the Wallace equation [56, 57], and for areal densities of > 1 Tb/in^2, the HMS should be reduced to less than 7 nm [41, 58]. Reducing the HMS would continue to demand the scaling down of the constituent HDI components as described in the previous sections. It is critical that while the thicknesses and dimensions at the HDI are reduced, the functional properties of each component and the recording performance are still maintained. As a guide, a roadmap of the HMS budget estimating the maximum thickness and dimension of each HDI component up to an areal density of 10 Tb/in^2 is presented in Figure 1.11. It should be noted that these estimates are based on

extrapolations from current technology, and for HAMR and BPM technologies, the media roughness could add to the HMS. Furthermore, the roughness of the head and disk overcoats, unevenness of the lubricant layer and micro-waviness of the disk substrate are not considered here in the HMS budget. Hence, these can be considered as generous estimates.

Areal Density (Tb/in^2)	HMS (nm)	Disk overcoat (nm)	Lubricant (nm)	Head overcoat (nm)	Flying clearance (nm)
1	6.5	2.5	1.0	1.7	1.3
4	4.5	1.8	0.9	1.2	0.6
10	3.0	1.0	0.7	1.0	0.3

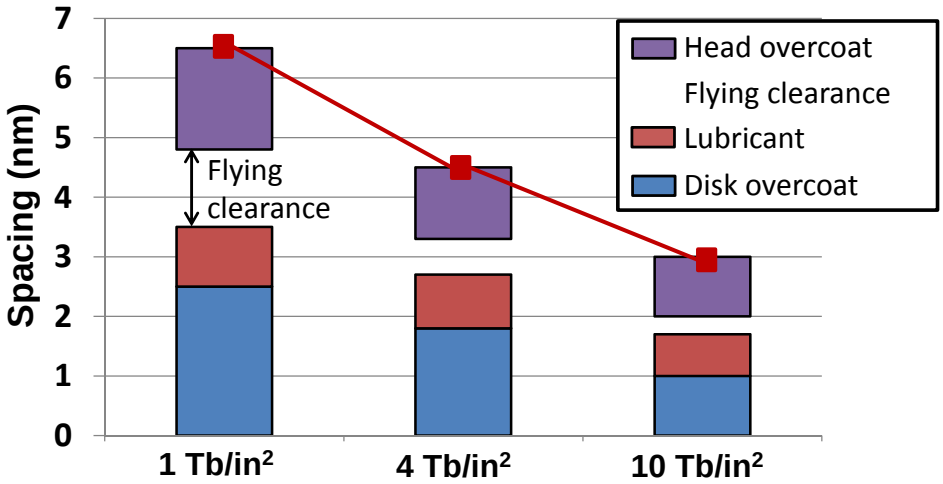

Figure 1.11 HMS budget estimate for areal densities of 1, 4 and 10 Tb/in^2. HMS values are estimated via a linear extrapolation of the HMS trend for previous years as shown in [13].

In this thesis, the various challenges of reducing the media COC thickness to ≤ 2 nm for > 1 Tb/in^2 areal densities [13, 30] are addressed. Despite the reduction in thickness, the media overcoat is still required to have high wear resistance, high corrosion resistance, low friction, low surface roughness and high thermal stability for HAMR application. In this regime, however, conventional PECVD deposition of COC does not provide sufficient coverage of the film onto the media [59, 60]. This leads to several issues such as:

- Formation of pinholes and defects in the COC, allowing moisture from the environment and metallic ions from the media to diffuse through the overcoat, leading to higher corrosion and oxidation of the media [61, 62].
- In terms of wear protection, a lower COC thickness would reduce the bulk volume of the overcoat, hence reducing the ability of the COC to provide sufficient mechanical protection.
- In addition, with lower coverage, the roughness of the overcoat would increase.

To address these issues at low overcoat thicknesses of ≤ 2 nm, as well as considering the feasibility of the overcoat in HAMR, novel overcoat fabrication techniques and/or novel overcoat structures/designs have to be developed, which will be discussed in subsequent chapters.

1.3 Magnetic tape drives

In contrast to magnetic disk drives, magnetic tape drives uses flexible tape media for storing data. Tape media is stored in a cartridge (~ 10 cm × 10 cm in size) containing a reel of tape ~ 800–1200 m in length, 0.5 inches (~ 1.3 cm) in width and ~ 5–6 μm in thickness [63, 64]. During operation, the tape is fed bi-directionally from the cartridge into a take-up reel and back. In the process, the tape passes over a tape head which is responsible for performing data recording and readback. Tape recording is a contact recording process, which means that the tape media has to be in continuous contact with the head. A photograph of a modern tape cartridge and drive and a drawing showing the

configuration of the tape and head during operation are shown in Figure 1.12. Based on the length and area of tape available per cartridge, the current areal density of tape is ~ 2–5 Gb/in^2, which is much lower than hard disk media [63]. Despite this, current tape cartridges have a storage capacity higher than that of modern disk drives and a lower cost per bit of storage. Furthermore, with the current thermal stability of the magnetic grains in the media, tape has the potential for long-term data storage for up to 30 years. In addition, tape drives require lower energy consumption during operation as compared to HDDs, with better reliability. However, one of the greatest disadvantages of tape recording is its long data access time, with an average data access time of 1–2 minutes as compared to only a few milliseconds for HDDs. Therefore, while HDDs are suitable for applications requiring faster data storage and retrieval such as for usage in personal computers and servers, tape drives are more desirable for long-term archival storage and data backup where the data does not need to be accessed frequently.

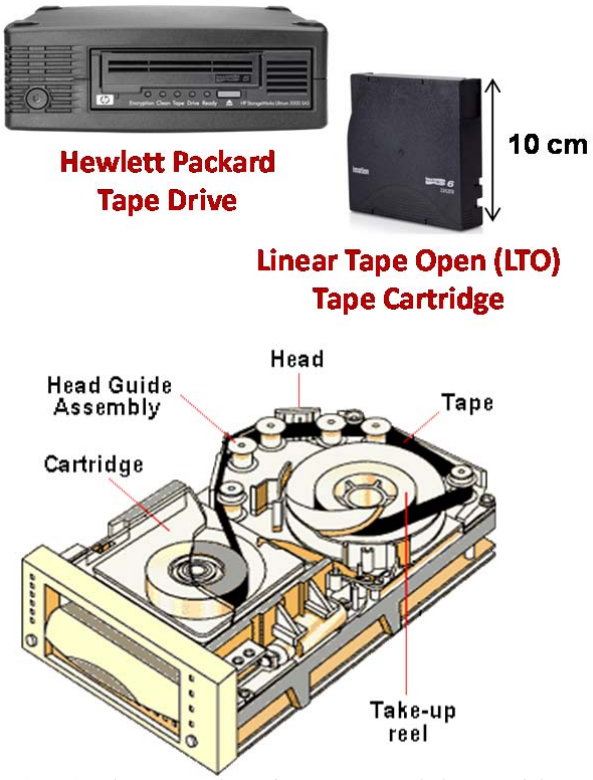

Figure 1.12 (Top) Photographs of a commercial tape drive and commercial Linear Tape Open (LTO) format tape cartridge. (Bottom) Drawing of an opened tape drive, showing its internal components and their configuration. [65].

1.3.1 Magnetic tape media

Current magnetic tape media is made of a flexible polymer tape substrate upon which the magnetic recording layer is deposited. Polymers of high elastic modulus such as polyethylene terephthalate (PET), polyethylene naphthalate (PEN) or aromatic polyamides (aramid) are commonly used as the substrate to maintain its mechanical integrity for it to be tough and elastic enough to prevent breakage/tearing arising from the high friction and tensional forces. The magnetic recording layer can be fabricated on the substrate by several methods. Evaporation and sputtering of the magnetic layer can be performed to obtain a continuous, granular media similar to that in hard disks. Another method is by using a slot die coating process to coat the top of the

tape substrate with a magnetic slurry containing a mixture of magnetic particles, lubricant (for low friction), a polymeric binder material (as a dispersant for the magnetic particles), and carbon black (to reduce static charges that can be generated in the tape during recording). The latter technique is used to fabricate particulate media such as hexagonal barium ferrite (BaFe) media. BaFe, being the most advanced tape media at present, has an average particle (grain) size of ~ 20 nm, which is smaller than previous generation metal particle media. This contributes to a higher areal density. In addition, the magnetic slurry also contains head-cleaning agents (HCA) which are essentially large abrasive particles such as alumina (Al_2O_3) and zirconia (ZrO_2), to clean up any contaminants from the tape which may adhere to the tape head surface during operation. Finally, a back coat of carbon is typically applied to the reverse side of the tape substrate to provide anti-static protection, prevent tape adhesion during unwinding from the reel, and provide mechanical support for the tape.

1.3.2 Magnetic tape head

Like in read/write heads for HDDs, the magnetic MR read sensor and inductive write pole for a tape head are both integrated into one read/write element. In contrast to the hard disk read/write head, a magnetic tape head contains 32 read/write elements arranged into two arrays known as modules (i.e. 16 elements corresponding to 16 data channels per module). In this way, as data is written onto the tape by an element on the first module, the element on the second module reads back the written data to confirm that it is error-free [66]. At the both ends of each array, there is a servo element for the

purpose of checking the position of the tape media on the head. The read/write element arrays are situated in an electrically insulating Al_2O_3 dielectric region, which provides electrical isolation between the element and the electrically-conducting AlTiC ceramic, as well as between the elements themselves. The hard AlTiC ceramic substrate makes up the major portion of the tape head, forming the tape-bearing surface for the purpose of bearing the load and friction of the tape during the contact recording process. A photograph of a commercial tape head (with its connecting cables removed) and a close-up optical micrograph of a servo element and a read/write element on one module of the tape head are shown in Figures 1.13(a) and (b). In addition, a labeled schematic of a read/write element and its surrounding area is presented in Figure 1.13(c).

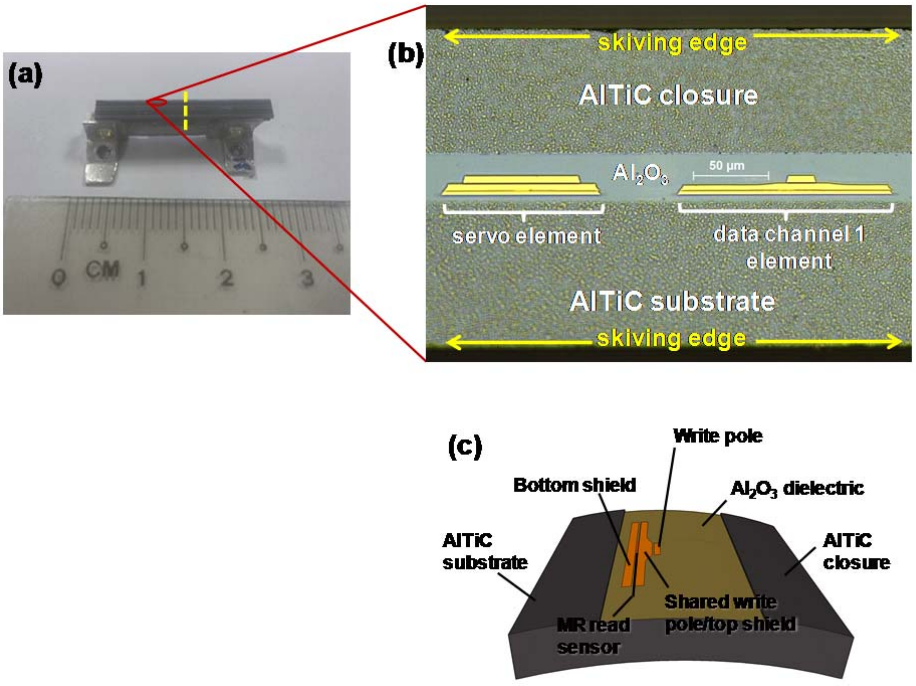

Figure 1.13 (a) Photograph of a commercial tape head with its connecting cables removed, (b) optical micrograph of a servo element and read/write element on the tape head module, and (c) labeled schematic showing a read/write element and its surrounding area. The yellow dashed line in (a) marks the place where the cross-section in Figure 1.14 is taken.

Many design features of the tape head have been developed over the years to obtain a recording process with high reliability, which will not be discussed at length in this thesis. However, two key features of the head design will be highlighted here. Figure 1.14 shows a drawing of the cross-section of the tape head along the yellow dashed line as indicated in Figure 1.13(a). The tape is labeled as 25 and the rows of read/write elements are located on the two modules labeled as 37 and 49. The first key feature is the presence of grooves along the length of the head, which are labeled as 33, 39, 43, 47 and 53 and the presence of skiving edges at the sides of the grooves. The skiving edges are also labeled in the optical micrograph of the head module in Figure 1.13(b). The function of the skiving edges is to prevent air and any debris on the tape from getting entrained between the tape and the head surface, which could otherwise increase the head-tape spacing [66, 67]. Consequently, this results in higher contact pressures and higher friction at the edges [67–69]. While the grooves act as collection areas for the debris, they also create a low pressure region in the cavity such that the tape is kept in contact with the head [70]. The second key feature is the slightly curved contour of the head. This is designed to control the degree of tape wrapping across the head, which in turn controls the head-tape spacing, contact pressures and friction of the tape on the head [67-69]. However, depending on the tape head model, tape heads may be fabricated to be curved or flat.

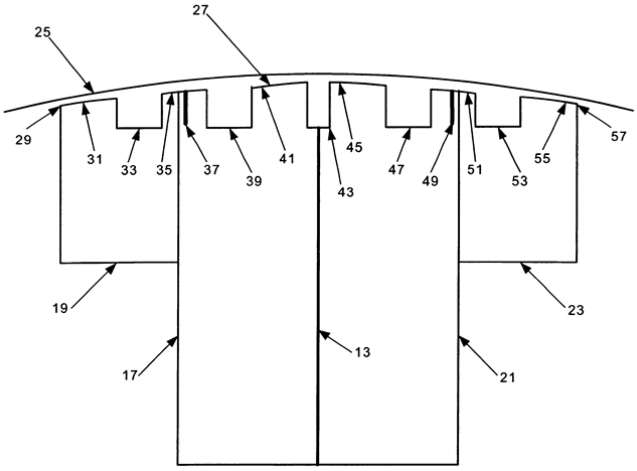

Figure 1.14 Drawing showing the cross-section of a commercial tape head cut along the yellow dashed line shown in Figure 1.13(a). Important parts of the tape head are referred to according to their numbers. [66].

1.3.3 Magnetic spacing at the head-tape interface

Similar to magnetic HDDs, an increase in the areal density in tape drives requires the reduction of the magnetic spacing, which is defined here as the distance between the read sensor in the head and the magnetic layer of the tape media. Figure 1.15 shows a cross-sectional schematic of one of the tape head modules across a read/write element.

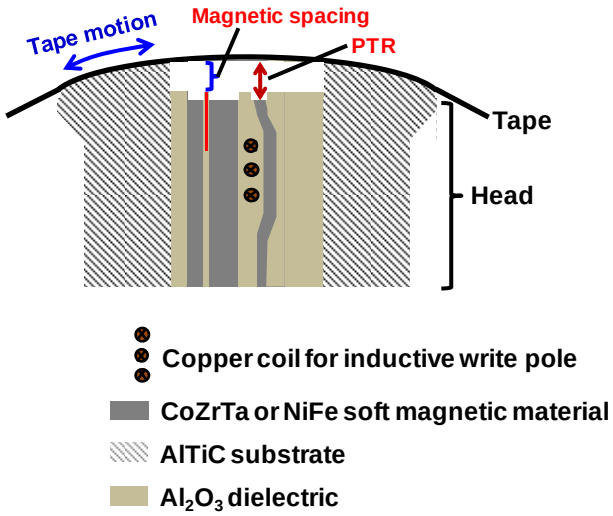

Figure 1.15 Cross-sectional schematic of a commercial tape head module cut across a read/write element to show the magnetic spacing and pole-tip recession (PTR).

As mentioned previously, the head design is one of the ways among many others which helps in maintaining low head-tape spacing and hence magnetic spacing. On the tape side, better media formulations in terms of lubricants and binder materials are being studied to obtain lower friction (for lower tape and head wear) as well as to reduce its surface roughness, which is also a factor in contributing to the magnetic spacing [63].

1.3.4 Issues arising from long-term head-tape interaction

It is not surprising that contact recording creates an aggressive environment at the head-tape interface, leading to high friction and abrasive wear in the long run. While various efforts have previously been made to reduce friction and wear at the tape head by applying an overcoat, the overcoats were either too thick or suffered from early wear or delamination [71–73]. As such, apart from one of the most recent models, tape heads do not possess a protective overcoat, thus directly exposing the AlTiC tape-bearing

surface, Al_2O_3 dielectric region and the read/write elements to the moving tape.

1.3.4.1 Pole-tip recession

With the absence of an overcoat, the onset of pole-tip recession (PTR) is one of the main tribological issues that needs to be addressed at the head-tape interface. PTR occurs due to the different wear rates of the hard AlTiC substrate material and the soft magnetic materials used in the MR read sensor, write pole and shields. PTR is a three-body abrasive wear mechanism initiated by the delamination of hard TiC grains from the AlTiC substrate [74, 75]. When the tape media runs across the head surface, the delaminated TiC particles act as the third body in abrasive wear. The softer read/write elements wear out much faster than the AlTiC substrate region, causing the poles and shields to recess with respect to the tape-bearing AlTiC surface. PTR, as labeled in Figure 1.15, therefore refers to the recession of the pole-tip (write pole) and the tape-bearing AlTiC surface (roughly the height of the tape above the pole-tip). At the end-of-life of the tape head, the PTR could produce an undesirable magnetic spacing of up to 40 nm [76]. This is detrimental for the recording process due to the lower SNR.

1.3.4.2 High running friction and stiction

Stiction occurs as a result of the temporary formation of adhesive junctions between two stationary contacting surfaces. As a consequence, a larger amount of force is required to separate them. This generally occurs in the case of two smooth surfaces with high surface contact areas (such as the

tape and head surface) at the beginning of tape motion or when the tape changes its direction. This is more obvious in high humidity and low tape velocity conditions [63]. This problem is expected to become more significant as the tape smoothness increases in future generation tapes. High stiction results in higher stresses and tension in the tape, which could lead to the delamination of the tape coating or even tearing of the tape in severe cases. To achieve higher data transfer rates in future drives, higher tape velocities would be required, so this could lead to a substantially large increase in the frictional forces [77]. Not only does high friction at the head-tape interface add to increased wear, but the combination of high running friction and stiction-induced stick-slip motion of the tape can also create longitudinal mechanical vibrations/oscillations in the moving tape, causing variations in its velocity [77–79]. This can lead to high bit error rates during the recording and reading processes.

1.3.4.3 Stain formation and debris accumulation

As the tape runs over the head, the large amount of heat generated and the high frictional forces can cause the magnetic coating components in the tape to get chemically bonded to the head surface and subsequently get transferred as debris which adhere onto the head. This phenomenon of material transfer onto the head is known as head staining and is undesirable as it increases the magnetic spacing. The abrasive HCAs in the tape can remove these debris or stains to a certain extent, but not completely.

1.3.4.4 Tribo-chemical effects of tape binder and lubricant

The tape lubricant aids largely in reducing the running friction and stiction between the head and tape to reduce wear, while the binder acts as a dispersant for the magnetic particles. Current binder formulations contain phosphorus and sulfur compounds bonded to the magnetic metallic ions of Fe or Co, while the lubricant contains ester groups. Such compounds, when catalyzed by transition metal species such as Ti in the TiC phase of AlTiC, can hydrolyze to form acids, forming metallic ions. These metallic ions can then be reduced by a charge transfer reaction at electrically conductive/grounded regions such as the AlTiC or read/write elements to form metallic deposits. Furthermore, the phosphorus compounds can erode the Al_2O_3 dielectric via a chemical reaction, forming insoluble deposits [63, 80]. The formation of such deposits increases the magnetic spacing and degrades the magnetic recording performance.

1.3.4.5 Electrical shorting of read sensors

The accumulation of electrically conductive deposits (such as carbon and metallic particles from the tape media) in the region of the read/write element can lead to what is known as conductive bridging across the gap between the read sensor and shield [63, 76]. This results in electrical shorting and failure of the read sensor.

1.3.5 Requirements at the head-tape interface for high density magnetic recording

Based on the issues mentioned above, it is therefore crucial for these problems to be addressed to reduce the magnetic spacing and improve the recording performance at the head-tape interface. For tape recording, the projected magnetic spacing up to year 2022 is presented in Figure 1.16 based on the projected areal density growth in the Information Storage Industry Consortium Tape Roadmap 2012 [63]. The allocated budget for head overcoat thickness is approximately half of the magnetic spacing.

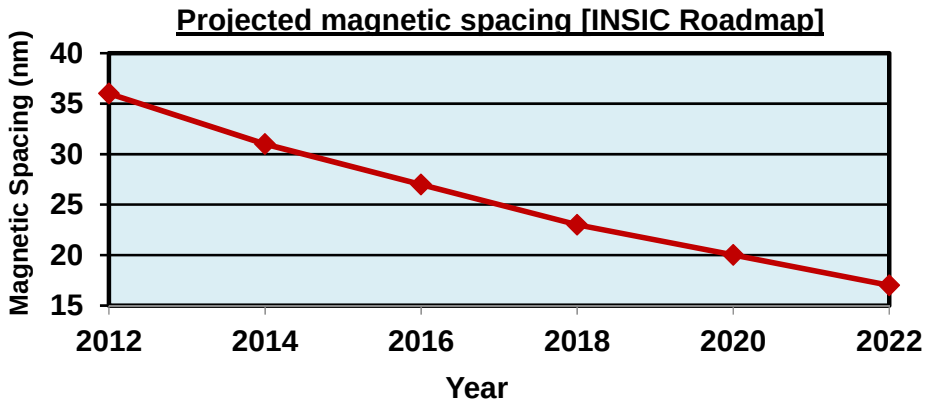

Figure 1.16 Projected magnetic spacing at the head-tape interface up to year 2022 [63]. The budget allocated for the head overcoat is approximately half of the magnetic spacing.

It is noteworthy that almost all of the above issues occur as a consequence of direct contact between the head and tape during operation. Hence, a straightforward solution would be to eliminate direct head-tape contact by applying an overcoat layer on the head surface. In this thesis, one of the aims is to develop such an overcoat layer for the head, which ideally possesses the following properties:

- High wear durability, in view of the aggressive wear environment. This requires the overcoat to possess good mechanical properties and excellent adhesion with the head AlTiC substrate.
- Ultra-low thickness and extremely low roughness to maintain low magnetic spacing and low friction.
- Chemically inert to avoid chemical reaction with the tape media.
- Electrically insulating to prevent electrical shorting of the read/write elements at the tape head surface.

1.4 Motivation of the thesis

The main goal of this thesis is to develop tribologically excellent and wear durable overcoats of ≤ 2 nm for hard disk media and ≤ 20 nm for tape heads, while maintaining or improving the functional properties of the media and head for their respective applications. Carbon, being one of the most versatile and abundant materials, is the material of choice for these overcoats because of its chemical stability (inertness) and ability to exhibit remarkable mechanical and tribological properties in the form of diamond-like amorphous carbon [81]. By modifying the deposition processes of carbon and adding an adhesion interlayer to the carbon overcoat, the microstructure of the carbon overcoat and its bonding with the substrate can be significantly enhanced to obtain the desired mechanical and tribological properties and even good thermal stability. This thesis seeks to investigate this relationship using various characterization techniques, and to evaluate the performance of the

coated media and heads in conditions that closely simulate those in real working drives.

1.5 Organization of the thesis

This thesis is divided into eight chapters. Chapter 1 provides an introduction to the current technologies being used in HDDs and tape drives, and gives an overview of the limitations and issues faced in the current technology at the head-media interface. The scope of this thesis is presented and several strategies are proposed to address these issues. Chapter 2 gives a current, state-of-the-art overview of carbon materials and its versatility in bonding and structure. An introductory review of amorphous carbon is covered in this chapter and subsequently provides readers a better understanding of the deposition processes used to acquire the desired bonding and microstructure of non-hydrogenated amorphous carbon thin films required for wear durable, tribologically superior, corrosion/oxidation resistant and thermally stable ultrathin overcoats for magnetic storage. Chapter 3 introduces readers to the range of techniques used in this thesis for the fabrication and characterization of ultrathin amorphous carbon films.

Following that, Chapters 4 and 5 explore the use of FCVA-processed ultrathin COCs on commercial media. Chapter 4 is split into three sections to investigate the effect of carbon ion energy by FCVA in developing an ultrathin COC for CoCrPt:Oxide media. The first section discusses the use of a high ion energy substrate pre-treatment step before deposition to attain good atomic mixing at the interface. The second section investigates the formation of an

overcoat with high thermal stability for HAMR. The third section describes a work carried out to optimize the carbon ion energy to obtain the best functional properties of the ultrathin COC for commercial media. Next, Chapter 5 probes the role of an atomically-thin silicon nitride interlayer in enhancing the bonding and microstructure of a FCVA-processed carbon overcoat with a total thickness of just 16 Å. The bonding and microstructure is discussed in relation to its functional properties on commercial media such as tribological, wear and corrosion/oxidation protection.

The whole of Chapter 6 is dedicated to the use of carbon-based overcoats for protection of magnetic tape heads. It is separated into three sections. The first section discusses the effectiveness of a bi-layer overcoat of silicon nitride and carbon developed by a facile magnetron sputtering technique. The second section reports the long-term wear durability achieved for a ~ 20 nm bi-layer overcoat comprising a silicon nitride interlayer and an FCVA carbon overlayer against running tape in a simulated tape drive environment. The third section investigates the mechanical, tribological and electrical properties of the head overcoats, which are then correlated to their bonding environments and structures.

In Chapter 7, graphene, which is essentially a monolayer of carbon but possesses unique properties, is proposed as a protective overcoat for hard disk media. Its protectiveness is discussed based on initial results which were recently obtained. Finally, Chapter 8 provides a summary and conclusion to the thesis, and discusses possible future works that can be performed in this area.

Chapter 2: Overview of amorphous carbon films

2.1 The versatility of carbon: structure and bonding

Carbon, one of the most versatile elements around, manifests itself in a wide variety of allotropic forms that exhibit a diverse range of properties. The reason for this extraordinary characteristic of carbon lies in its ability to exist in three types of hybridizations, namely sp^1, sp^2 and sp^3, as shown in Figure 2.1 [81]. Carbon as an atom has four valence electrons, out of which two electrons occupy the 2s orbital, and the other two electrons occupy one 2p orbital each. All four valence electrons of carbon actively take part in bonding. In sp^3 hybridization, the 2s orbital and three 2p orbitals of carbon are hybridized to form four equivalent sp^3 hybrid orbitals of equivalent energies, arranged in a tetrahedral structure as shown in Figure 2.1, with one electron occupying each hybridized orbital. These four orbitals can form strong C–C σ bonds when the sp^3 orbitals of adjacent carbon atoms overlap. In sp^2 hybridization, three electrons occupy three equivalent sp^2 hybridized orbitals arranged in a trigonal planar configuration, with the 2s orbital and two 2p orbitals taking part in hybridization. The third 2p orbital containing the last valence electron in this case remains unhybridized and at a higher energy level than the sp^2 hybridized orbitals. This orbital, known as a π orbital, is arranged perpendicular to the plane of the three sp^2 orbitals, as illustrated in Figure 2.1. During bonding, the sp^2 orbitals form strong σ bonds, whereas the π orbital forms a comparably weaker π bond via a side-to-side overlap with another π orbital on the adjacent atom, causing the π electrons to be delocalized between the two adjacent atoms. sp^2 bonding in carbon is typically depicted as a C=C

double bond, where the double bond consists of one σ bond and one π bond. sp^1 bonding in carbon follows a similar trend, forming two equivalent sp hybridized orbitals with higher σ bond energy and two π orbitals with lower π bond energy, resulting in a C≡C triple bond.

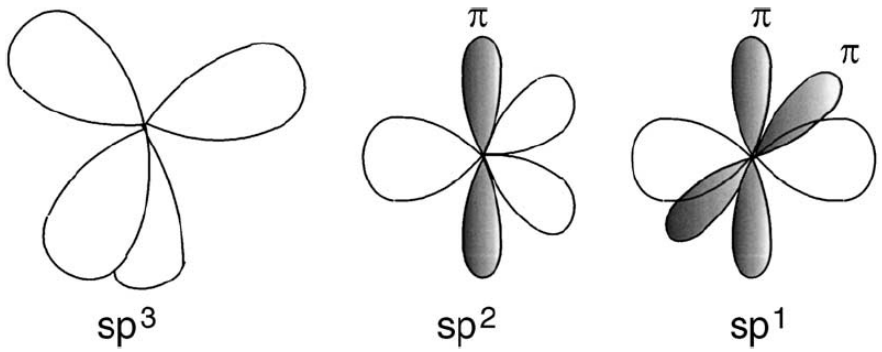

Figure 2.1 The three possible hybridizations of carbon during bonding. [81].

Consequently, carbon can be bonded to itself in any of the above configurations, resulting in different structures and ordering, as well as different mechanical, electrical and optical properties. Here two crystalline allotropes of carbon are compared – hexagonal crystalline graphite and diamond, and their crystal structures are shown in Figures 2.2(a) and 2.2(b) respectively. In diamond, all carbon atoms are fully sp^3 bonded (all σ bonds) with each atom bonded to four other atoms arranged in a dense, tetrahedral crystalline network. Because of its high bond density and strong σ bonding, it not only exists as one of the hardest materials known, but it is also an excellent electrical insulator as all its electrons are involved in σ bonding. Hexagonal crystalline graphite, on the other hand, consists of a highly ordered structure of carbon layers stacked above and below one another in an ABAB sequence as illustrated in Figure 2.2(a). Graphite contains pure sp^2 bonding, whereby within each layer, each carbon atom is bonded via σ bonds to three other

atoms in hexagonal rings. At the same time, delocalized π bonding takes place above and below the carbon layer which extends throughout the entire plane. This means that the π electrons can move freely between the sheets of graphite. However, only weak forces of attraction (widely regarded as dispersive van de Waals interactions) are present between the graphite sheets, making it easy to slide the sheets across one another. Therefore, while graphite exhibits strong covalent bonding within the layers, it possesses low bulk hardness due to the weak interlayer interactions, and the extensive delocalization of electrons in graphite makes it a good electrical conductor.

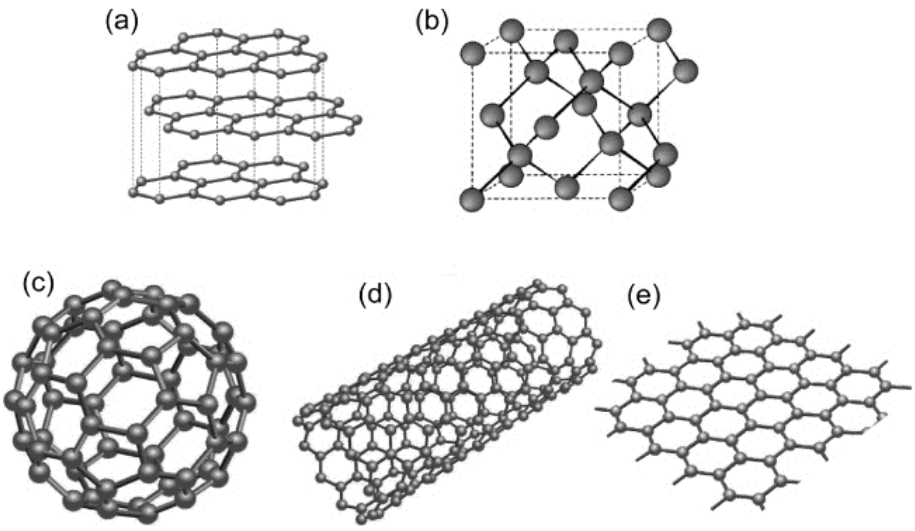

Figure 2.2 Various allotropes of carbon. (a) Hexagonal crystalline graphite, (b) cubic diamond, (c) C_{60} fullerene, (d) carbon nanotube, and (e) graphene. [82].

Hence, it can be seen that the bonding and structure in carbon play an important role in contributing to its properties. In addition to the above examples, fullerenes (0D), carbon nanotubes (1D) and graphene (2D) are some important low dimensional form of carbon materials and possess mainly sp^2-bonded carbon network, as shown in Figures 2.2(c)–(e) respectively.

2.2 Introduction to amorphous carbon films

Amorphous carbons form another big class of carbon allotropes. As the name suggests, amorphous carbons contain a certain degree of disorder (non-crystallinity) in contrast to the crystalline structures of diamond and graphite, as illustrated in Figure 2.3. Amorphous carbons are usually deposited as films on a substrate, containing a mixture of sp^2 and sp^3 bonding with little evidence of sp^1 bonding being present [83]. Hence, they can be regarded as intermediate structures between graphite (fully sp^2) and diamond (fully sp^3), and exhibit some character of both, depending on their sp^2/sp^3 fractions. In the presence of hydrogen during amorphous carbon film deposition, the inclusion of hydrogen atoms in the carbon network to form hydrogenated amorphous carbon is possible, depending on the deposition conditions.

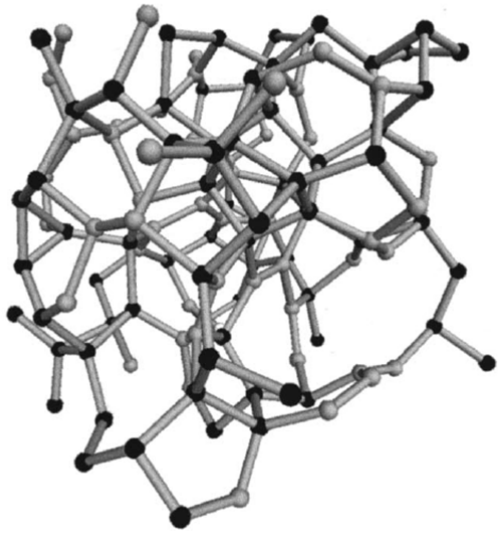

Figure 2.3 Typical structure of amorphous carbon. Black atoms represent sp^3-bonded carbon atoms whereas grey atoms represent sp^2-bonded carbon atoms in a disordered network. [84].

To illustrate the wide range of amorphous carbon film structures, Figure 2.4 presents a well-known ternary phase diagram of the amorphous

carbon-hydrogen system, with each side of the phase diagram representing the percentage of sp^2 carbon (sp^2C), sp^3 carbon (sp^3C) and hydrogen content, as depicted by the respective vertices [85]. The entire left side of the phase diagram shows the variation of sp^2C/sp^3C content for films with 0% hydrogen, also known as non-hydrogenated amorphous carbon films (hereon referred to as a-C films). At the bottom left vertex of the phase diagram with ~ 100% sp^2C bonding lie graphitic carbons such as char and soot, which exhibit similar properties to graphite, as well as glassy carbon. As the amount of sp^3C bonding increases, the a-C films start to exhibit more diamond-like character, i.e. an increase in hardness and density and a decrease in electrical conductivity. Hence, a-C films containing a significant amount of sp^3 bonding are usually termed as diamond-like carbon (DLC) [86]. As the sp^3 content in the film increases further to ~ 70–90%, a special name of tetrahedral amorphous carbon (ta-C) is given to these films as a large fraction of the carbon atoms becomes tetrahedrally bonded in an sp^3 network [87, 88].

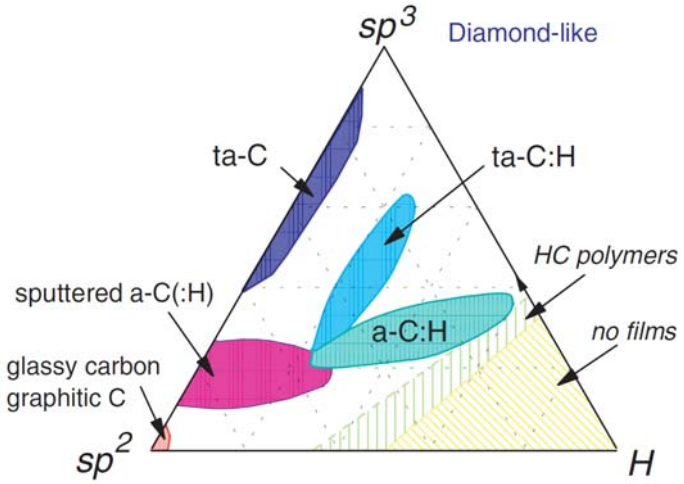

Figure 2.4 Ternary phase diagram of the amorphous carbon-hydrogen system. [85].

With the incorporation of hydrogen, hydrogenated amorphous carbon (a-C:H) films can be formed. This can be done for example by growing physical vapor deposition of carbon films in a hydrogen atmosphere, or by using hydrocarbon sources as a precursor for film growth in chemical vapor deposition processes [89, 90]. Softer a-C:H films can be obtained with ~ 40–60% H content, which are known as polymer-like a-C:H (PLCH) films. a-C:H films with intermediate hydrogen content (20–40%) possess relatively higher sp^3 C-C bonding than PLCH films and hence better mechanical properties. These films are usually termed as hydrogenated DLC films. Tetrahedral a-C:H (ta-C:H), which is considered to be a special class of hydrogenated DLC films, contains ~ 25–30% hydrogen content and significantly higher sp^3 C-C bonding (up to ~ 70%) [91]. a-C:H films with low hydrogen content of 10–20% deposited by magnetron sputtering or by PECVD at high bias possess high sp^2 bonding and sp^2 clustering. Such films can be called as graphite-like a-C:H (GLCH) films [92]. While the inclusion of hydrogen aids in saturating the sp^2C bonds in amorphous carbon to form sp^3 bonds with H, the sp^3 bonds of C–H are weaker than sp^3 C–C bonds, thus in general ta-C:H films have slightly lower hardness and lower density than ta-C films.

Similarly, other elements such as nitrogen and silicon can be incorporated to form alloyed amorphous carbon films with a range of properties, but they will not be discussed here. The primary interest of this work is on non-alloyed, non-hydrogenated a-C films.

2.3 Mechanism for sp^3C bond formation and its importance

The sp^3 content of a-C films is very important in achieving excellent properties such as high hardness and high density. For example the sp^3 content, bulk hardness and density of ta-C can reach up to 80–90%, ~ 65–80 GPa and ~ 3.3 g/cm^3 respectively, which are very close to the bulk hardness and density values of diamond (~ 100 GPa and 3.5 g/cm^3) with its mainly sp^3-bonded carbon network. With increased sp^3 bonding in the a-C film, lower surface roughness can also be achieved [87]. Furthermore, a-C films with high sp^3 content have also been found to possess high thermal stability and a low amount of graphitization upon thermal annealing at high temperatures of up to ~ 1270 K [93]. Thus, sp^3 C-C bonding is a very important parameter in order to obtain high wear and corrosion resistance and high thermal stability in amorphous carbon films.

The sp^3 content in a-C films is known to be largely dependent on the energetics of the a-C film deposition process [83]. In processes such as thermal evaporation, the carbon species (ions or atoms) being deposited possess very low kinetic energies (~ kT which is 0.025 eV at room temperature), resulting in the formation of carbon films with very high sp^2 and very low sp^3 content (~ 1–12% sp^3) [83, 88]. The reason for this observation is attributed to the insufficient energy required to promote the electron from the 2s to the 2p orbital for sp^3 hybridization [94]. DLC films can be deposited by more energetic processes such as sputtering, ion-assisted deposition, ion beam deposition and cathodic arc deposition, giving intrinsic kinetic energies of between 2.5–25 eV.

Lifshitz et al. [95] proposed that the main growth mechanism of carbon films by carbon hyperthermal species (possessing energies of 1 to 1000 eV) is based on a subplantation model that can be used to explain the variation of sp^2/sp^3 bonding with energy. When the incoming carbon species interact with the growing carbon film with sufficient energy, it is able to penetrate the subsurface of the film. This can result in either direct penetration trapping of the incoming carbon species into the film, or preferential displacement (knock-on) of the existing sp^2 bonded carbon as shown in Figure 2.5. This effectively increases the density at the subsurface of the film, causing the transformation of bonding hybridization from sp^2 to sp^3 [96]. After subsurface penetration, some of the carbon atoms undergo a relaxation process towards the surface, forming a surface sp^2-rich layer. This is illustrated in a schematic by Robertson in Figure 2.6 [81], which shows the fraction of energetic ions being able to penetrate the surface by the subplantation process ($f\phi$) and the fraction of trapped interstitials relaxing towards the surface ($n\beta$). Thus the fraction of ions that remains at the interstitial sites and contribute to densification is expressed as $n = f\phi - n\beta$.

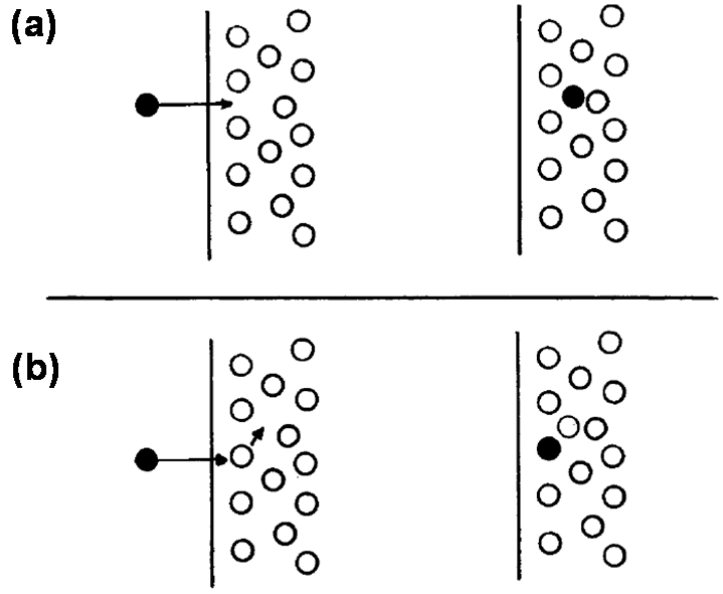

Figure 2.5 Mechanism of film growth by subplantation. (a) Penetration of energetic carbon species into the subsurface of the growing carbon film, and (b) preferential displacement of sp^2-bonded carbon atoms into the film. Both mechanisms contribute to increasing the density and sp^3 content of the film. [96].

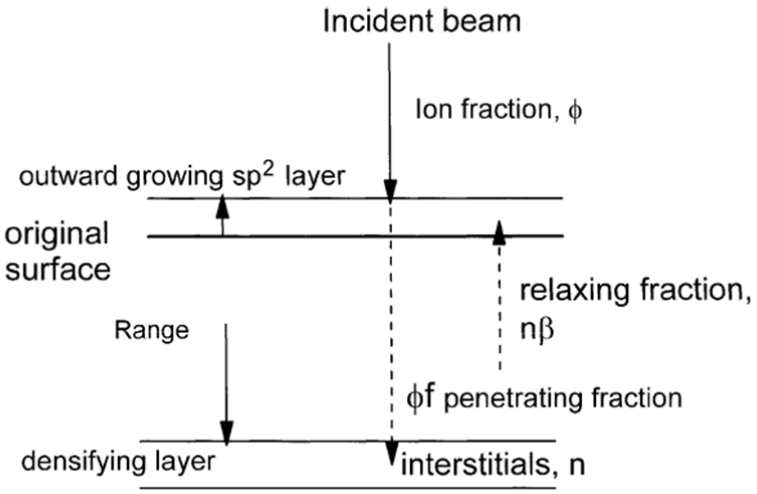

Figure 2.6 Diagram showing the fraction of incoming ions contributing to subsurface penetration, film densification as trapped interstitials, and relaxation towards the surface. [81].

The subplantation mechanism requires a certain energy threshold of the arriving carbon species to be effected. At low energies (< 10 eV), the carbon species do not have enough momentum to penetrate the growing

carbon film, thus the occurrence of subplantation is negligible. Furthermore, very low displacement or mobility of the carbon species is observed, and the incoming carbon species are trapped as interstitials within the growing film, forming a disordered network. This results in the formation of highly sp^2 bonded graphitic films. With medium energies (~ 30–500 eV), the preferential displacement mechanism is effected which favors the formation of sp^3 bonding and reduces the number of graphitic sp^2 sites, hence a high sp^3 fraction can be achieved. However, if the energies are too high (~ 500–1000 eV), the growing carbon film can be easily damaged and amorphized. As such there is an optimum deposition energy range in the medium energy regime for each deposition process and tool to obtain DLC films with the highest sp^3C content.

Many groups have successfully attempted to create DLC films using processes in which the carbon species possess intrinsic energies in this range, such as ion beam deposition, ion-assisted deposition, laser ablation, cathodic arc deposition and sputtering [87]. However, to create highly sp^3-bonded DLC films such as ta-C, C^+ ions are commonly used as the species for film growth, because of the potential to moderate the energy of the arriving ions at the substrate by applying a suitable substrate bias. For example, the first reported DLC films were grown via an ion beam deposition method by Aisenberg and Chabot in 1971 by applying a substrate bias of -40 V [97]. By varying the ion energy, ta-C films with ~ 70–90% sp^3 bonding have been reported using ion energies within the range of ~ 20–300 eV [87, 98]. Presently, it is regarded that maximum sp^3 bonding can be achieved within an optimum energy range of ~ 80–120 eV [99–101].

2.4 Thickness dependence of sp^3 content in ultrathin amorphous carbon films

One of the challenges that arises when thickness is reduced for a-C/ta-C films is that the sp^3 content has been observed to be reduced significantly (especially at ~ 2 nm thicknesses and below), despite being grown under the same conditions [102]. It has been shown that in ta-C films, a layered structure involving three layers of different densities can be formed [103, 104]. For thicker films, the bulk layer contains the highest density, hence it can be inferred that its contribution to the overall sp^3 content is the highest. The other two layers, one at the substrate-film interface and another at the surface, have a lower density, which result in higher sp^2 bonding (lower sp^3 bonding) in these regions. The thicknesses of these layers can vary depending on the deposition conditions [103–105]. While the mechanism of formation of the sp^2-rich interface layer is substrate dependent, the formation of the sp^2-rich surface layer is suggested to arise due to the mechanism of the deposition process involving ion bombardment and deposition temperature [104]. When the thickness of the film decreases, the bulk layer correspondingly decreases, resulting in an increased contribution from the surface and interface layers. Therefore, this contributes to the overall reduction in the sp^3 content of the film. Nevertheless, Beghi et al. and Ferrari et al. suggested that FCVA-processed carbon films deposited at optimum process conditions can have sp^3 bonding as high as ~ 50% at a thickness of 2 nm, which is still significantly higher than carbon films processed by magnetron sputtering and PECVD [103, 105].

Chapter 3: Overcoat fabrication and characterization

3.1 Overcoat fabrication techniques

Carbon films can be deposited by a range of deposition techniques including ion beam deposition, mass-selected ion beam deposition, pulsed laser deposition, magnetron sputtering, FCVA and PECVD-based techniques [23]. Presently, the magnetic data storage industry commonly uses the following techniques for the deposition of ultrathin COCs: 1) magnetron sputtering, 2) FCVA and 3) PECVD-based techniques (such as the plasma beam source method). For example in HDDs, as mentioned in Chapter 1, PECVD is currently being utilized to deposit an ultrathin a-C:H-based COC on hard disk media, whereas FCVA is being used to deposit the ultrathin COC on the slider and read/write head. In this section, the three COC fabrication techniques used in the industry as mentioned above are discussed.

3.1.1 Magnetron sputtering

Magnetron sputtering is one of the most common techniques used for deposition of thin films, due to its ease of use, good controllability of deposition conditions, as well as the ability to obtain smooth, continuous films with excellent quality. A schematic and a photograph of the magnetron sputtering chamber used in this work are presented in Figure 3.1. In a "bottom-up" sputter configuration, the substrate on which the film will be deposited is placed on a rotatable substrate holder, with the substrate facing

downwards. At the bottom, various targets are installed on magnetron guns connected to individual power sources.

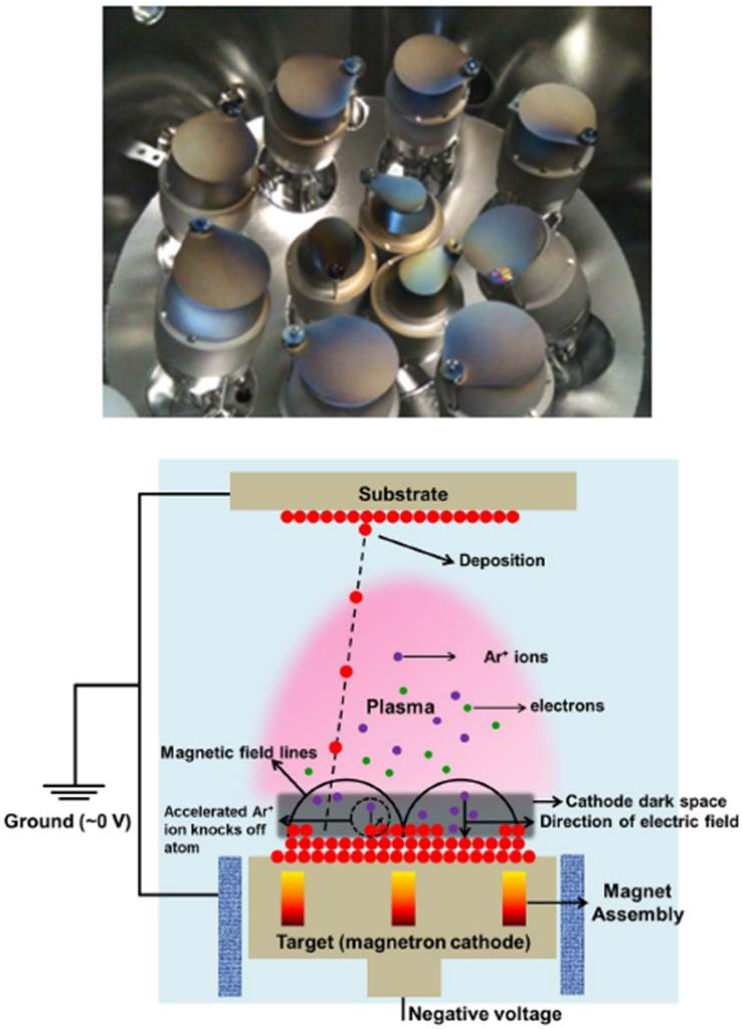

Figure 3.1 Schematic and photograph of the magnetron sputtering system with a "bottom-up" sputter configuration used in this work. [106, 107].

In magnetron sputtering, an inert process gas such as Ar is used. During deposition, a negative voltage is applied at the target (cathode), emitting secondary electrons in the process. These secondary electrons cause the Ar atoms to be ionized to Ar^+ ions, which then accelerate towards the negatively charged target (cathode). By means of momentum transfer, the Ar^+ ions cause neutral target atoms to be ejected (sputtered) out of the target

towards the substrate, where the film is deposited. Each magnetron gun contains a magnet assembly, which generates a magnetic field close to the target. This helps to concentrate the plasma of electrons and Ar^+ ions close to the target to obtain a higher degree of ionization, resulting in a higher sputter rate and yield.

By varying the process conditions for magnetron sputtering, different kinds of films, film quality and sputter rates can be achieved. For example, a reactive gas such as N_2 can be introduced together with Ar to deposit a nitrogenated carbon (a-C:N) film. This is known as reactive sputtering. Different modes of sputtering can also be used by connecting different power sources to the target. The radio frequency (RF) sputtering mode is more effective for sputtering insulating targets such as ceramics, because it prevents the buildup of charge on the target. The pulsed DC sputtering mode has several advantages over conventional DC sputtering due to increased plasma density and electron temperature, as well as suppression of arcing events at the target. These change the plasma chemistry and help in obtaining better quality films in a condensed state, such as in the case of carbon [108–111].

3.1.2 Filtered cathodic vacuum arc (FCVA)

The cathodic arc vacuum deposition technique is a physical vapor deposition (PVD) process widely used in industry and laboratories for the deposition of ultrathin films, due to its capability of controlling the deposition energy of the ionized carbon species. As the name suggests, cathodic arc deposition is an arc-driven deposition process performed in a high vacuum

environment, in which a high current is applied between the anode and the cathode (target) to generate an arc, resulting in the ejection of neutrals (target particles) and charged species (ions and electrons) at high velocities towards the substrate. The cathodic arc generates highly ionized plasma with an extremely high ions-to-neutrals ratio. By applying a substrate bias, the energy of the ions can be tuned, and in turn, the microstructure of the film can be controlled. For cathodic arc deposition of carbon, a graphite rod is used as the target, resulting in the ejection of carbon ions (mainly singly charged C^+) and carbon macroparticles. These macroparticles, with sizes ranging from several hundred nanometers up to tens of microns, are undesirable during deposition as they contribute to defects in the carbon film, reduction in sp^3 content, and increase in surface roughness. One of the methods to reduce the problem of macroparticles during film growth is by installing a curved magnetic filter coil, such as an S-bend coil as shown in Figure 3.2. This is known as FCVA deposition. In doing so, a magnetic field is generated through the center of the filter when a current flows through the coil, causing the ionized plasma of electrons and C^+ ions to follow the curved magnetic field through the bend. On the other hand, macroparticles which are of neutral charge do not follow the magnetic field and hence are filtered out of the plasma.

In the FCVA deposition of carbon, the C^+ ions which are ejected at the cathode have an intrinsic average energy of ~ 20–30 eV [87, 99, 112]. Subsequently, a negative bias can be applied at the substrate to tune the energy of the C^+ ions reaching the substrate. Thus, by tuning the C^+ ion energy, carbon films with desired qualities and properties can be deposited.

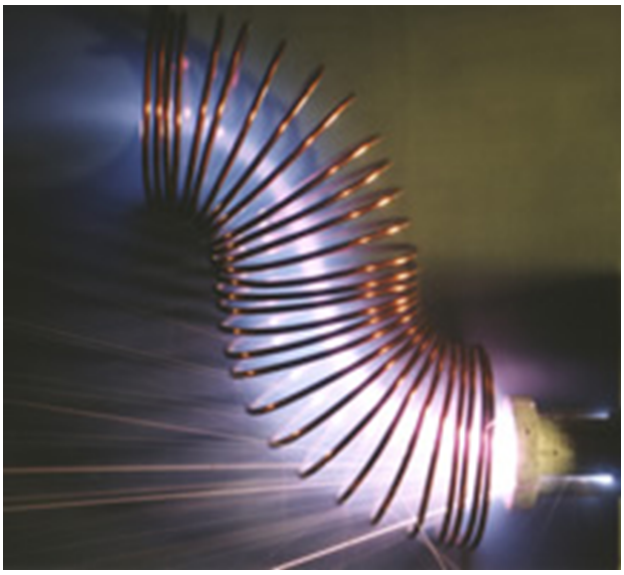

Figure 3.2 The S-bend macroparticle filter in an FCVA deposition system, containing two 90° bends. Bright streaks represent macroparticles being filtered out of the plasma. [113].

While the presence of the filter in FCVA helps to significantly reduce the number of macroparticles arriving at the substrate, it is still challenging to completely remove them. This is especially critical for hard disk media overcoats as the presence of macroparticles detrimentally affects the HDI reliability. Several research efforts are ongoing to ameliorate this issue, such as by using a real-time electrical filter [18]. Alternatively, other techniques such as high-power impulse magnetron sputtering (HiPIMS) can be considered to obtain an ion flux of C^+ with controllable energy in an Ar atmosphere without the generation of macroparticles [114]. However, as a HiPIMS system was not easily accessible for this work, the FCVA process was used to study the energetic carbon deposition process.

3.1.3 Plasma-enhanced chemical vapor deposition (PECVD)

PECVD is another technique used for the deposition of carbon films. PECVD is a type of CVD process where the use of a plasma serves to enhance the chemical reaction between the precursor gases and the substrate, hence the deposition of films can be carried out at ambient temperatures. In PECVD of a-C:H films, precursor hydrocarbon gases such as methane and acetylene are used to grow the film. The precursor gases are passed into a chamber containing a pair of electrodes. The substrates are placed on a powered electrode, which is much smaller than the opposite electrode (which is usually the whole chamber body itself connected to ground). This arrangement gives the maximum amount of power transfer to the powered electrode. A conventional PECVD process, however, has low ionization rates with the generation of a significant amount of neutrals and radicals. Hence, several variations of the PECVD process have been developed to achieve higher plasma densities and more highly ionized plasmas [23]. Some examples of such PECVD-based processes include plasma beam source (PBS) deposition [115] and electron cyclotron wave resonance (ECWR) deposition [116], where the plasma is first confined using a magnetic field and then extracted as a plasma beam with high energy. In doing so, high sp^3-bonded a-C:H films can be obtained. Currently, the HDD industry employs such modified PECVD-based processes for the deposition of media overcoats.

3.2 Overcoat characterization techniques

Characterization of the overcoats after deposition is essential for comparing and evaluating their performance as a suitable overcoat. In this

section, the different characterization techniques used in this thesis are introduced. As several of these characterization techniques are well-known, their working principles will not be discussed in detail here. More information on their working principles can be found in Appendix A and in various literature on thin film characterization techniques, such as [117, 118].

3.2.1 High resolution transmission electron microscopy (HRTEM)

One of the most important initial characterization techniques is to measure the thickness of the fabricated ultrathin overcoats. At low overcoat thicknesses such as those used in this work (≤ 20 nm), high resolution transmission electron microscopy (HRTEM) in the cross-sectional geometry is a useful technique to image the overcoats for the purpose of thickness measurement at atomic scale resolution. The basic working principle of HRTEM can be found in Appendix A.1. In this thesis, a Philips CM300 field emission gun transmission electron microscope (FEI Company, USA) at IMRE was used to perform cross-sectional HRTEM imaging of the fabricated overcoats for thickness measurement.

3.2.2 Tapping mode atomic force microscopy (AFM)

Atomic force microscopy (AFM) was used to map the topography of the sample surface, when it possesses features on the scale of a few hundred nanometers or less. In this thesis, topographical imaging and surface roughness measurements were conducted using tapping mode AFM in a Bruker Innova scanning probe microscope (Bruker, USA) to reduce both tip wear and mechanical damage to the surface. The working principle of tapping

mode AFM is described in Appendix A.2. A silicon probe with a tip radius of 8 nm was used for the tapping mode AFM measurements. At least three measurements were performed for each sample to get relatively consistent readings within the error bars.

3.2.3 Ball-on-disk tribological testing

The tribological properties such as the coefficient of friction (COF) and wear properties of the overcoats were evaluated using ball-on-disk configuration tribological testing. In the ball-on-disk configuration, the sample is made to come into contact with a counterface ball. A normal force is applied between the ball and sample, after which the sample is rotated with respect to the counterface ball, generating a circular wear track on the sample surface. During the test, the friction force (lateral force) can be measured with the aid of transducers or sensors within the setup and plotted with respect to the number of wear cycles. The COF, μ, can then be calculated by the equation $F = \mu N$, where F is the friction force and N is the normal force applied, and also plotted with respect to the number of cycles. The wear properties of the sample can also be evaluated by means of visual observation of the wear track and counterface ball surface before and after the tribological test, using an optical microscope. A sample with poorer wear properties would have a more severe wear track and large amount of debris transfer to the counterface ball.

In this thesis, a ball-on-disk nano-tribometer (CSM Instruments, Switzerland) was used to evaluate the tribological properties of flat samples. A photograph of the nano-tribometer used in this thesis is presented in Figure 3.3, with its key components labeled. A standardized testing procedure was

used as follows. A counterface ball of 2 mm diameter made of sapphire (Al_2O_3) was used for the sliding wear tests against the coated disk samples, whereby the sample was rotated under the counterface ball, forming a circular wear track. The sliding velocity and normal load applied were set at 2.1 cm/s and 20 mN respectively. This gives a contact pressure of ~ 260 MPa on Co-based media substrates [119] and ~ 350 MPa on AlTiC substrates [120]. All the tests were conducted for 10,000 cycles for at least two locations per sample to obtain consistent results. During each test, the friction force and COF data were recorded. All the tribological tests were conducted at RH of 55 ± 5% and temperature of 24 ± 1 °C.

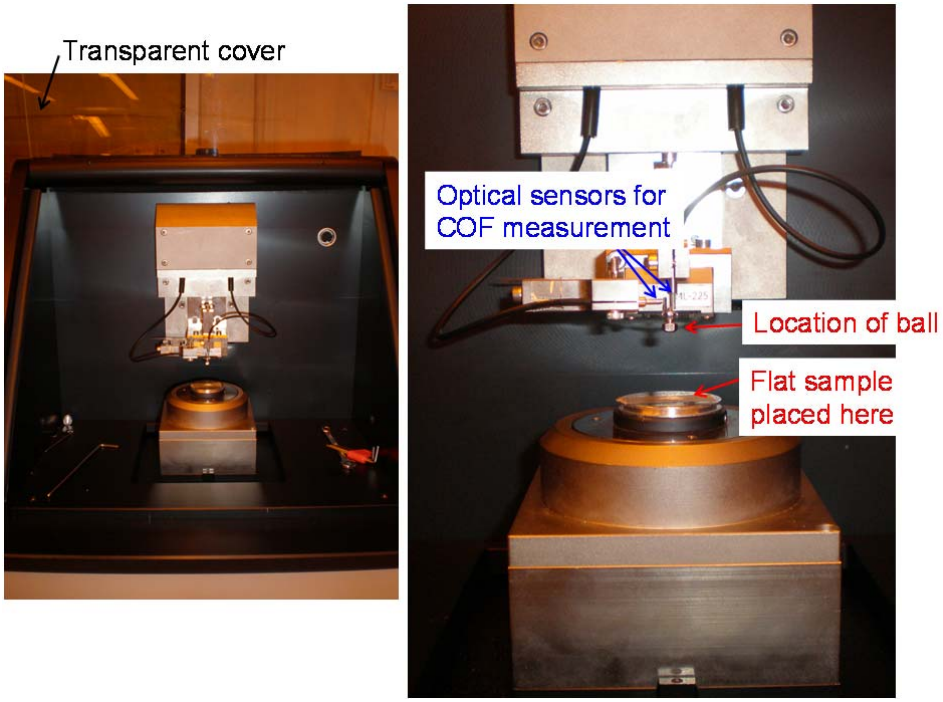

Figure 3.3 Photograph of the ball-on-disk nano-tribometer used in this work.

3.2.4 Electrochemical corrosion

The corrosion resistance of the overcoats deposited on hard disk media were evaluated using a custom built three-electrode electrochemical corrosion

setup as shown in Figure 3.4, modified based on a cell design by Balakrisnan et al. [121]. The setup consisted of a platinum wire counter electrode, silver/silver chloride reference electrode and the disk sample as the working electrode. All three electrodes were in contact with a piece of cotton wool soaked with the electrolyte of 0.1 M of sodium chloride solution. The sample area of contact with the electrolyte was confined using a rubber O-ring with a geometric area of ~ 0.24 cm^2.

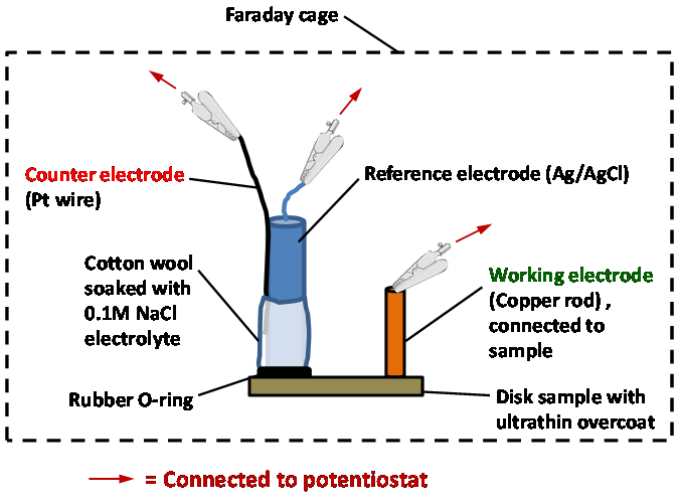

Figure 3.4 Schematic diagram of the custom built corrosion setup.

The corrosion resistance was measured by a conventional potentiodynamic polarization method, such as the one described in [122]. A Gamry Instruments PCI300 potentiostat connected to a computer interface was used for the corrosion measurements. The cables were first connected to the respective electrodes as shown in Figure 3.4. An open circuit delay was then performed for about 100 min for the open circuit potential (E_{oc}) to stabilize. Subsequently, the potential was swept 0.4 V above the E_{oc} at 0.1 mV/s and the corresponding current values were recorded to obtain an anodic curve. Similarly, a cathodic curve can also be obtained at another spot on the sample using the above procedure but by sweeping 0.4 V below the E_{oc}. In total, at

least three anodic and three cathodic curves were obtained for each sample to ensure consistency in the results.

The anodic and cathodic curves were plotted on a semi-logarithmic plot of potential versus log current, known as a Tafel plot. Using a Tafel extrapolation method [123], the linear portions of the anodic and cathodic curves were extrapolated towards the E_{oc}, and the intersection point gave the corrosion current. Finally, the corrosion current density (j_{corr}) was calculated by normalizing it to the geometric contact area. A higher j_{corr} implies that the corrosion rate of the underlying media is higher. Hence, the corrosion resistance of the overcoat can be seen as inversely proportional to j_{corr}.

3.2.5 Electrical properties

As mentioned in Section 1.3.4.5 of this thesis, the electrical resistance of tape head overcoats should be sufficiently high to avoid electrical shorting of the read sensors. For carbon-based overcoats, the sp^2-bonded phase is responsible for the COC's electrical conductivity, hence COCs with higher sp^2 (lower sp^3) content would usually show higher resistance [124]. In this work, to evaluate the electrical properties of the tape head overcoats, current-voltage (I-V) curves were measured on each overcoat using a probe station as shown in Figure 3.5(a), and the electrical resistance of the overcoat was extracted from the I-V curve. Electrical measurements were performed using a four-probe configuration as shown schematically in Figure 3.5(b). Two probes were used to supply the current using a Keithley 2400 sourcemeter while the other two probes were used to measure the voltage using a Keithley 2002 multimeter. The overcoat was deposited on either glass or silicon substrates.

Tantalum/copper (Ta/Cu) or tantalum/silver/tantalum (Ta/Ag/Ta) metal electrode contacts of ~ 100 nm thickness were deposited on the overcoat by sputtering for good electrical contact and to avoid damage of the ultrathin overcoat by the probe. The electrode geometry and distance between the electrodes were maintained within each set of samples such that a proper comparison of the electrical resistance values between each sample can be made.

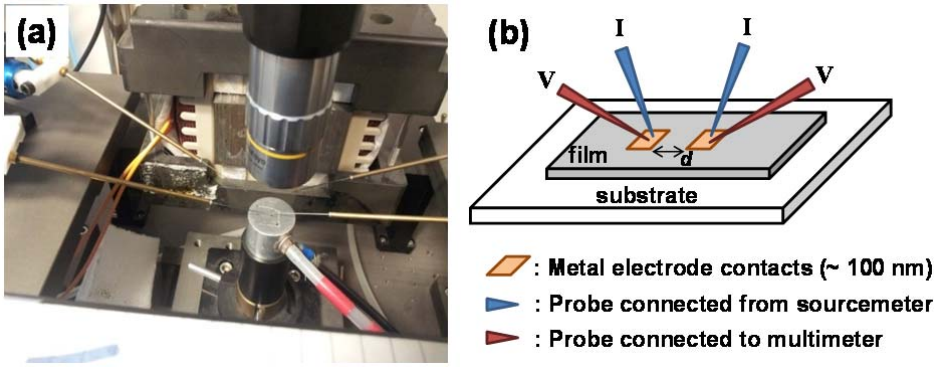

Figure 3.5 (a) Close-up photograph of the four-point probe station used for electrical measurements. (b) Schematic of the four-probe electrical test arrangement.

3.2.6 Mechanical properties

One of the widely used ways to evaluate the mechanical properties of thin films is by nano-indentation [125], from which important information such as the hardness and elastic modulus can be obtained. A description of the nano-indentation technique is provided in Appendix A.3. In this thesis, a MTS Dynamic Nanomechanical Probe nano-indenter system (MTS Systems Corporation, USA) at IMRE equipped with a diamond Berkovich geometry tip was used to perform the nano-indentations. At least 10 nano-indentations on 10 different locations on each sample (limited within an area of ~ 300 × 300 μm^2) were performed to obtain consistent results. For evaluating the hardness

of different overcoats, a graph of hardness versus penetration depth was obtained for each nano-indentation location.

3.2.7 Head-tape interface testing

Overcoats deposited on non-functional tape heads can be tested using a custom built head-tape interface tester setup to evaluate their performance against commercial tape media. Figure 3.6 shows a labeled photograph of the key components of the setup.

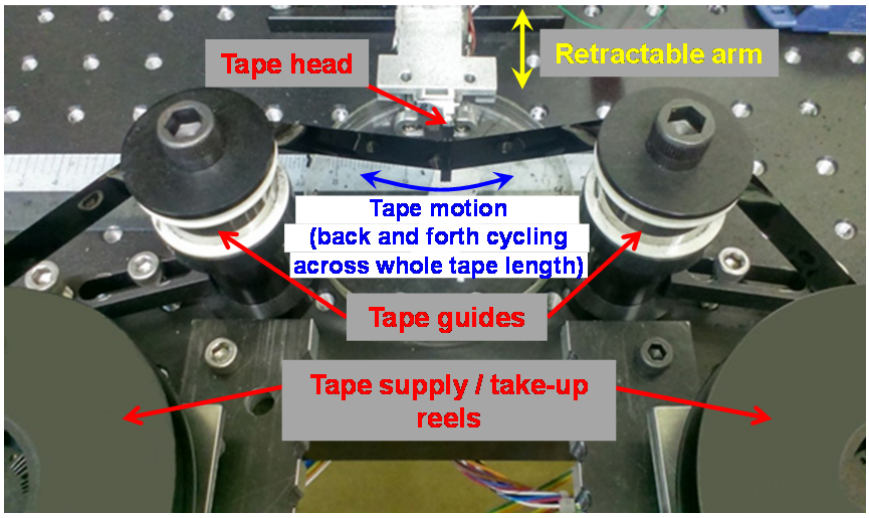

Figure 3.6 Photograph of the custom-built head-tape interface tester setup used in this work, with its key components labeled.

Once the head has been coated, it is loaded onto the retractable arm. Next, a commercial tape cartridge is loaded onto the supply reel, and an initial running length of tape from the supply reel is fed into the take-up reel. Two low-friction tape guides are used to transport the tape to and from the supply and take-up reels, with the purpose of avoiding lateral tape motion [126]. Just before starting the test, the head is brought into contact with the tape media as shown in Figure 3.6. The position of the head is calibrated to be positioned in the middle of the two tape guides, such that tape tension of 0.7 N is achieved.

During the tape test, the tape is cycled back and forth between the supply and take-up reels at a speed of 5.0 m s^{-1} across the entire tape length. The tape cycling is controlled by a SDS tape transport servo system with a computer interface. These parameters were set to simulate the tape transport conditions in an actual working tape drive. All tests on the head-tape interface tester were conducted at RH of 55 ± 5% and temperature of 24 ± 1 °C.

3.2.8 Time-of-flight secondary ion mass spectrometry (TOF-SIMS)

Time-of-flight secondary ion mass spectrometry (TOF-SIMS) is a surface sensitive technique (< 1 nm depth) used to detect the elemental composition of the surface. By combining TOF-SIMS with surface sputter etching, TOF-SIMS depth profiling can also be performed to analyze the elemental composition profile with respect to the depth into the sample surface. The working principles of TOF-SIMS and TOF-SIMS depth profiling are elaborated in Appendix A.4 and can also be found in Ref. [118].

In this thesis, TOF-SIMS measurements were performed at IMRE in a TOF-SIMS IV tool (IONTOF GmbH, Germany) using a pulsed 25 keV Bi^+ ion beam for analysis with a spot size of ~ 1 μm. For depth profiling, a 1 keV Ar^+ or Cs^+ ion beam was used to sputter a crater with an area of 300 × 300 μm^2, out of which a smaller area of 150 × 150 μm^2 from the crater middle was selected for analysis.

3.2.9 Auger electron spectroscopy (AES)

Auger electron spectroscopy (AES) is another surface-sensitive technique which can be used for elemental composition analysis. In contrast to TOF-SIMS, the surface is probed using high energy photons or electrons instead of ions. As such, AES can be seen as a generally non-destructive analysis technique for surface analysis. However, by combining sputter or ion beam etching, AES depth profiling into the surface can be performed. The working principle of AES is discussed in Appendix A.5 and can also be found in literature such as Ref. [118]. In this thesis, AES measurements were performed at IME using a JAMP Auger microprobe tool (JEOL, Japan) under ultra-high vacuum conditions in the range of ~ 10^{-9} Torr.

3.2.10 X-ray photoelectron spectroscopy (XPS)

X-ray photoelectron spectroscopy (XPS), or *electron spectroscopy for chemical analysis* (ESCA), is a useful non-destructive characterization technique which can be used to probe the surface chemical state/bonding with a sampling depth of 3–10 nm into the surface. In comparison with AES, XPS is also a non-destructive technique that uses a monochromatic X-ray source to probe the surface. Additionally, when combining the use of sputter or ion beam etching of the surface, XPS depth profiling can be performed. The working principle of XPS can be found in Appendix A.6, and also in good references such as Ref. [118].

In this thesis, XPS measurements were performed at IMRE under an ultra-high vacuum condition of ~ 3 × 10^{-9} Torr in a VG ESCALAB 220I-XL

system (Thermo Fisher Scientific, UK) using a monochromatic Al Kα X-ray source (energy ~ 1486.6 eV) with a spot size of 400 μm. Where not specified, XPS measurements were performed at take-off angles normal to the surface.

3.2.11 Raman spectroscopy

In this work, Raman spectroscopy is primarily used for understanding the carbon microstructure of the fabricated ultrathin carbon-based overcoats. Raman spectroscopy exploits the Raman effect, which is described in detail in Appendix A.7. Amorphous carbon film spectra, when well-fitted, show common features within the wavenumber range of 800–2000 cm^{-1}, namely the G and D peaks occurring between 1360–1560 cm^{-1}, and the T peak occurring at around 1060 cm^{-1}. While G and D peaks can be observed under visible wavelength excitation, the T peak can only be distinctly observed when higher energy UV excitation (~ 244 nm wavelength) is used. The dominant peaks in the carbon spectra are the G and D peaks which are due to the resonance vibrations of the π bonds at sp^2 sites. In particular, the G peak results from the bond stretching modes of sp^2 carbon in the ring and chain configurations, whereas the D peak results from the breathing modes of sp^2 carbon in the ring configurations only, as illustrated in Figure 3.7 [127]. The T peak, on the other hand, results from higher energy vibrations of sp^3 carbon bonds when a significant amount is present [86].

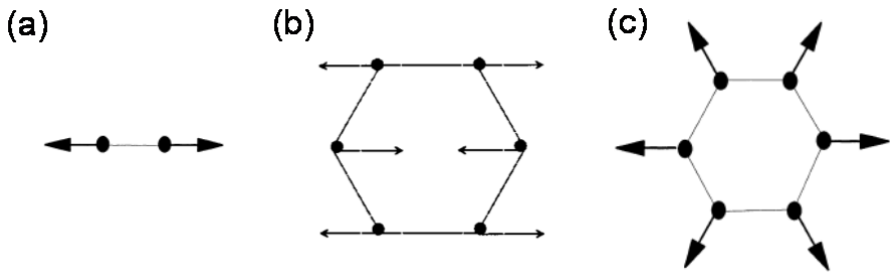

Figure 3.7 Eigenvectors showing the (a) stretching mode for carbon in a chain configuration, (b) stretching mode for carbon in a ring configuration, and (c) breathing mode for carbon in a ring configuration. (a) and (b) give rise to the G peak and (c) gives rise to the D peak in the Raman spectrum. [81, 127].

More information such as the G peak position and the ratio of the D peak-to-G peak intensity (commonly referred to as the I_D/I_G ratio) can be obtained from the fitted Raman spectra data. Ferrari and Robertson's three-stage model is commonly used to relate the above data to the amount of disorder (amorphization) within the material, degree of sp^2 clustering, as well as providing an estimate for the amount of sp^2/sp^3 bonding within the carbon film [127].

In this thesis, Raman measurements at different laser excitation wavelengths were carried out using a Jobin Yvon LABRAM-HR Raman setup in an ambient environment at IMRE. Due to the ultra-low thicknesses of the overcoats, the laser was maintained at a low power while other parameters such as CCD camera exposure and data acquisition time were calibrated to achieve suitable signal-to-noise ratios. In all cases, a laser spot size of ~ 1 μm was used.

Chapter 4: Optimization of ultrathin carbon overcoats on hard disk media

As described in Chapter 1, reduction of the protective COC thickness down to ≤ 2 nm on hard disk media is essential based on current PMR technology, in order to achieve areal densities of > 1 Tb/in^2. Because of its potential to achieve comparably higher sp^3C bonding and a denser carbon network, and hence better film coverage at lower overcoat thicknesses, FCVA is a promising option for COC fabrication on future media. In addition, the ability to tune the energy of the incoming C^+ ions by controlling the substrate bias is advantageous for optimizing the functional properties of the COC. This can be achieved by optimizing the FCVA process. Two of the most important factors affecting the overcoat protectiveness are the C^+ ion energy and the overcoat thickness. Recent studies on pure Co and FePt media have shown that at sufficiently high C^+ ion energies of 90 eV and above, the formation of a mixed carbon-media layer at the media surface can be beneficial in improving the tribological properties and thermal stability at the surface [119, 128]. In addition, by applying more than one energy during the FCVA process, greater atomic mixing at the interface may be achieved with enhanced tribological properties [129]. Therefore, in this chapter, the effects of C^+ ion energy, thickness and the extent of atomic mixing on the microstructural and functional properties of ultrathin COCs are discussed, and how the FCVA process can be optimized to achieve the most desirable functional properties for the media.

4.1 Determination of ion energies for FCVA carbon embedment and deposition

Stopping and range of ions in matter (SRIM) simulations were carried out to model the embedment depth distribution of the C^+ ions with the media when the C^+ ion energies were varied. For example, three energies of 50 eV, 90 eV and 345 eV were selected in this case to model low energy, medium energy and high energy impingements respectively, at an angle normal to the surface. The media used in all the simulations was cobalt (Co), since it is the major element present in commercial CoCrPt:oxide alloy media (~ 70 at%) [130]. The ion range distributions are presented in Figure 4.1.

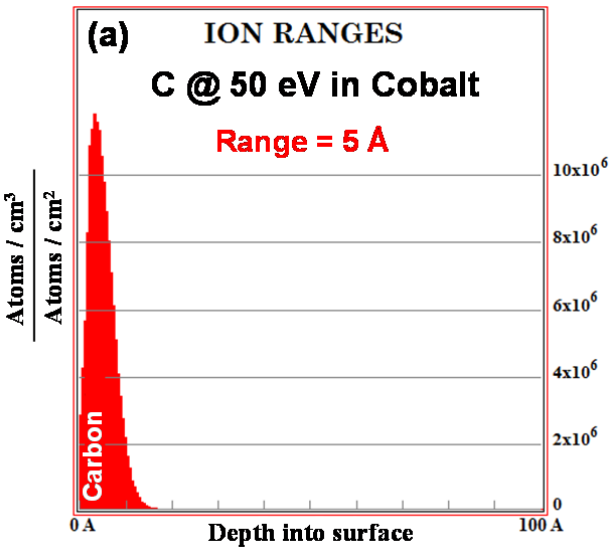

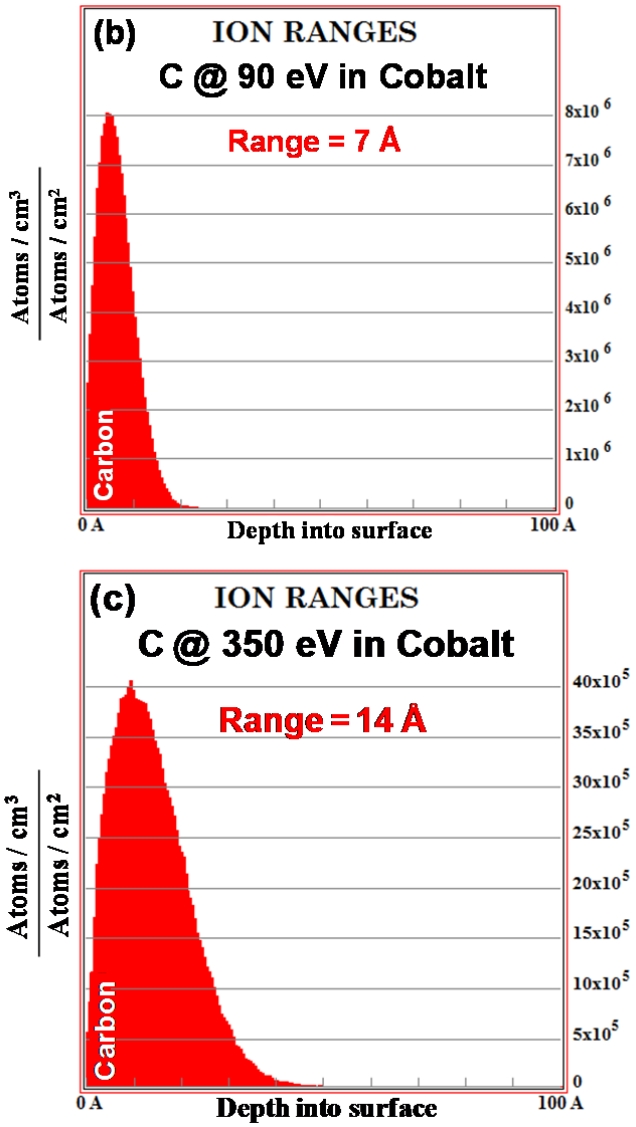

Figure 4.1 SRIM simulations showing the ion ranges of carbon in Co-based media when subjected to C^+ ion energies of (a) 50 eV, (b) 90 eV and (c) 345 eV. The horizontal axis represents the depth into the media with 0 Å target depth representing the media surface.

From the ion distribution profiles, it is clearly seen that the depth of carbon embedment increases with increasing ion energies. At 50 eV, the ion range (corresponding to the depth with maximum ion distribution) is predicted to be 5 Å into the Co media surface. In comparison, ion energies of 90 eV and 345 eV result in ion ranges of 7 Å and 14 Å respectively. Moreover, the ion distribution profile tends to have a larger straggle at higher energy (i.e. a larger

spread of the ion distribution profile into the media), whereas the distribution profile for lower energy is sharper and concentrated nearer the surface. The reason for these observations is that higher energy ions have greater momentum and requires a larger depth of the solid to stop it completely. Hence, high energy ions result in deeper embedment and greater atomic mixing within the media, whereas low energy ions result in shallower embedment and more deposition on the media surface. Therefore with the aid of SRIM simulations, the COC fabrication process can be optimized by tuning substrate bias to achieve different degrees of atomic mixing and deposition.

4.2 Overcoat formation on CoCrPt:Oxide media by an FCVA bi-level C350/90 eV energy process

With the knowledge that high energy ions contribute to greater atomic mixing, and that there is an optimum energy range of ~ 80–120 eV to achieve the highest fraction of sp^3C bonding (as mentioned in Chapter 2), one approach in this work is to employ a bi-level energy process scheme using the FCVA process for COC fabrication. This scheme comprises two steps: Firstly, a high energy C^+ ion surface embedment/pre-treatment step at ~ 350 eV for a very short time, followed by a medium energy C^+ ion shallow embedment and deposition step at ~ 90 eV. The motivation for this bi-level energy scheme is as follows. The first step of high energy substrate pre-treatment at 350 eV contributes to higher amounts of atomic mixing and the formation of a dense interfacial layer. This was observed by Rismani et al. when a similar scheme was applied to AlTiC substrates [120]. Subsequently, the second step of

medium energy bombardment at 90 eV contributes to less embedment but more overcoat formation with high sp^3C content. The employment of a bi-level energy scheme thus combines the synergistic effects of deposition at two different energies into one overcoat.

4.2.1 Overcoat fabrication

The schematic of the FCVA bi-level energy process of 350 eV followed by 90 eV (hereon termed as the C350/90 process) on CoCrPt:Oxide commercial media is presented in Figure 4.2. Full commercial media disks containing ~ 2.7 nm of commercial COC and ~ 1.3 nm of PFPE lubricant obtained from an industry collaborator were used as the starting substrates. The substrates were loaded into a commercial FCVA deposition system (Nanofilm Technology International, Singapore). By a calibrated Ar^+ ion beam etching process, the commercial lubricant and COC layers were first removed along with the top ~ 1–2 nm of the magnetic media. Following that, the media was exposed to C^+ ions of ~ 350 eV in the first surface pre-treatment step, after which C^+ ions at ~ 90 eV were used to form the COC layer in the second step. The total thickness of the C350/90 overcoat was intended to be < 2 nm, by varying the time in the surface pre-treatment and deposition steps.

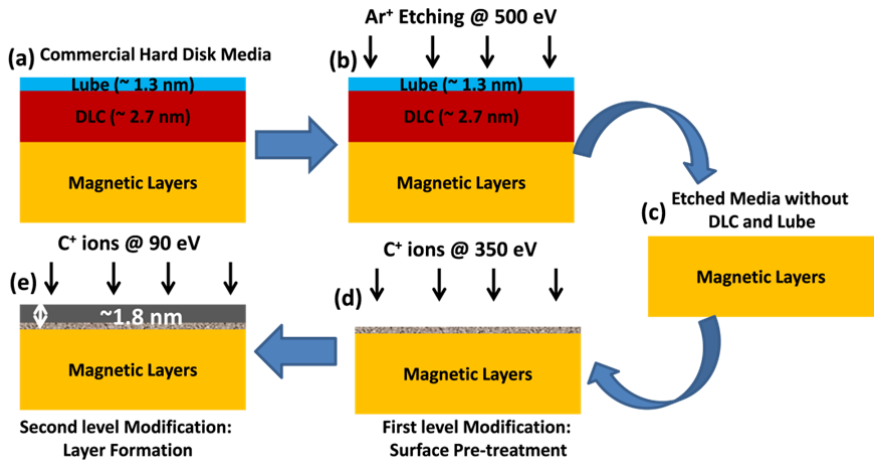

Figure 4.2 Schematic of the FCVA C350/90 eV bi-level energy process.

It was assumed that in this particular FCVA system, the C^+ ions generated had an intrinsic energy of ~ 20 eV without any applied substrate bias [23, 131]. Thus, to achieve C^+ ion energies of ~ 350 eV and ~ 90 eV, substrate biases of -330 V and -70 V were applied in each step respectively. A pulsed substrate bias scheme was employed in each of the two steps with a 20 kHz frequency and a duty cycle of 0.6 (i.e. each cycle consists of 30 µs of bias ON time followed by 20 µs of bias OFF time), following the biasing scheme used by Rismani et al. [120]. The surface potential of a non-conductive film, such as ta-C, can be controlled by a pulsed DC voltage. This is in contrast to a continuous DC voltage, which may produce surface charging, resulting in a significant difference in the surface potential and the applied voltage. This will therefore affect the quality of the films [132]. Pulsed substrate biasing has been found to allow for better substrate-film intermixing leading to densification and better interfacial adhesion [133].

Prior to deposition, SRIM simulations were carried out to model the depth profile of bi-level energy process at C350/90 and compared with single

energy process at 90 eV in Figure 4.3. It was observed that while the peak carbon distribution for both cases was around 3–5 Å beneath the media surface, the C350/90 process gave a tail extending up to 2 nm beneath the surface, which indicates a greater extent of atomic mixing of carbon at the media surface.

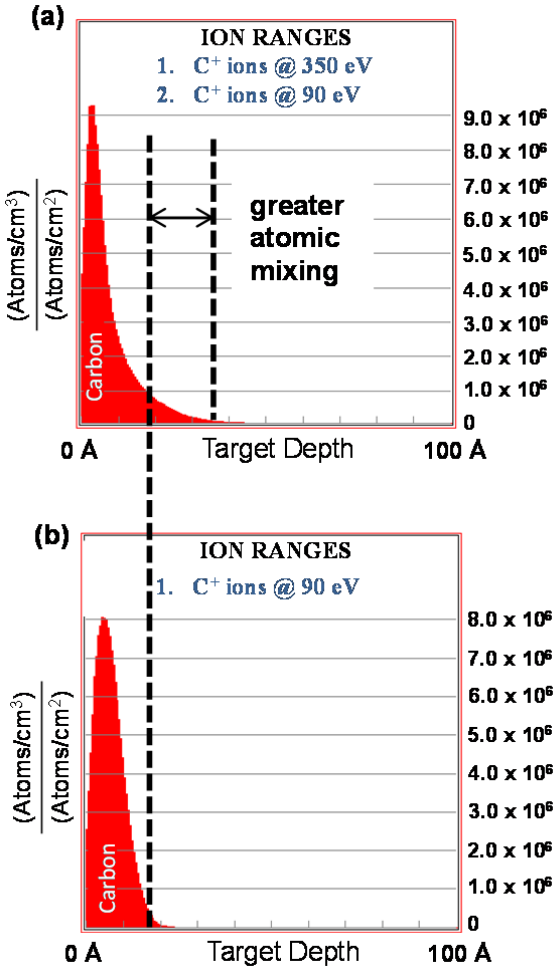

Figure 4.3 SRIM simulations showing the ion ranges of carbon in Co-based media when subjected to (a) the FCVA bi-level energy process of C350/90 eV, and (b) single ion energy of 90 eV. Dashed lines indicate a greater atomic mixing depth of 2 nm into the media surface for the C350/90 eV process.

4.2.2 Thickness characterization

Cross-sectional HRTEM imaging was performed on the C350/90 overcoated media sample for thickness measurement. At the same time, the full commercial media sample containing ~ 2.7 nm COC and ~ 1.3 nm PFPE lubricant (hereon termed as sample CML) was also imaged for comparison purpose. Both images are presented in Figures 4.4(a) and 4.4(b).

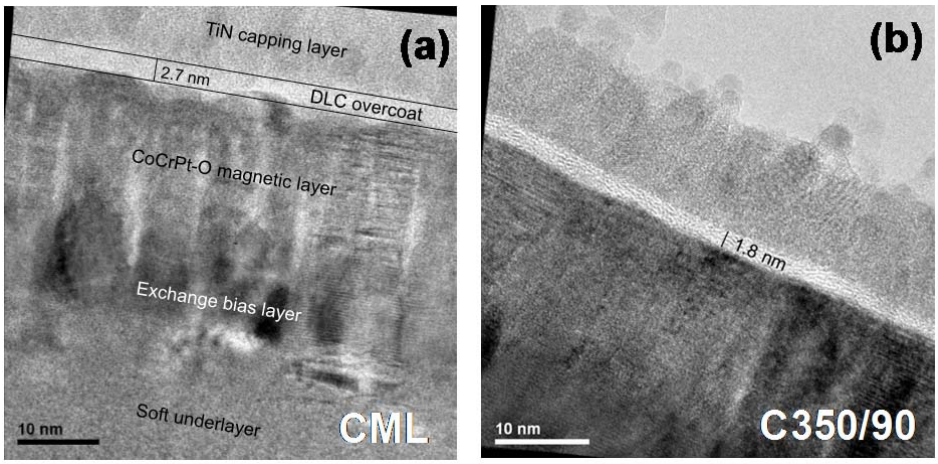

Figure 4.4 Cross-sectional HRTEM images showing the cross-sectional structure of the media and measured COC thicknesses for (a) full commercial media disk CML and (b) sample C350/90 after the FCVA bi-level energy process.

The first clear difference that can be observed is the lower overcoat thickness of ~ 1.7 nm in sample C350/90 as compared with ~ 2.7 nm in sample CML. Secondly, the roughness of the media-overcoat interface was clearly observed to be higher in sample CML than in sample C350/90. This can be attributed to a combination of the Ar^+ etching process of the media as well as the high energy C^+ ion embedment in the C350/90 process which smoothened the media surface. Lastly, the COC in sample C350/90 can be seen to possess a dense nano-layered microstructure in contrast to an amorphous structure in sample CML. It was subsequently investigated by

Dwivedi et al. that these nano-layers as observed in HRTEM were likely to be interspersed graphene/fullerene-like nanostructures formed within the amorphous carbon matrix during the FCVA process. The details are not discussed here but readers can refer to Ref. [134] for more information.

4.2.3 Surface roughness

As highlighted in Section 1.2.5, obtaining sub-nanometer smoothness at the head-disk interface is extremely important to achieve a lower magnetic spacing. In addition, a lower surface roughness helps in reducing the corrosion due to the better surface coverage and thickness uniformity of the overcoat [23, 30]. Surface roughness measurements were performed on sample C350/90 using tapping mode AFM over a scan area of $2 \times 2\ \mu m^2$. Its surface roughness was compared with two other samples, namely: 1) sample BM, which is a specially prepared bare commercial media disk without COC and without lubricant, and 2) sample CM, which is a specially prepared commercial disk sample with ~ 2.7 nm commercial COC but without lubricant. Figure 4.5 shows a bar chart plot of the root-mean-square (RMS) roughness (also known as R_q) and average roughness (R_a). As can be seen, all three samples exhibited sub-nanometer roughnesses. Comparatively, sample C350/90 had the lowest surface roughness of the three, which was even lower than the commercial media overcoat. This clearly demonstrated the effectiveness of the FCVA process in creating an ultra-smooth COC for hard disk media without increasing the roughness of the media.

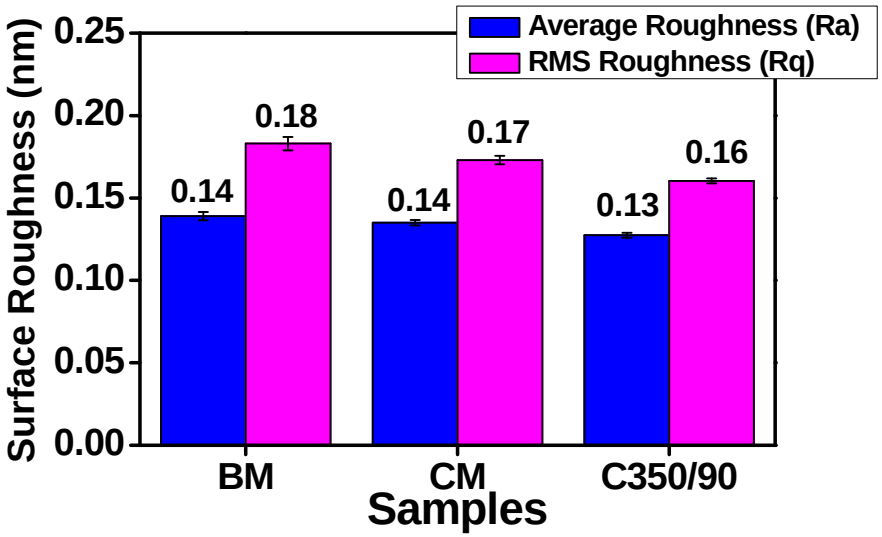

Figure 4.5 R_a and R_q values measured for samples BM, CM and C350/90.

4.2.4 Corrosion resistance

Samples BM, CM and C350/90 were subjected to three-electrode electrochemical corrosion testing to analyze their corrosion resistance properties. The extrapolated j_{corr} of the three samples are collated and shown in Table 4.1. Furthermore, for comparison of the overcoat effectiveness, the corrosion protective efficiency (PE) values of the overcoated samples were calculated based on the following equation [135]:

$$\%PE = \frac{j^0{}_{corr} - j_{corr}}{j^0{}_{corr}} \times 100\%$$

where $j^0{}_{corr}$ is the corrosion current density of sample BM without any overcoat. Not surprisingly, the average j_{corr} of sample BM was the highest at 17 ± 6 nA/cm^2, indicating that it had the least corrosion resistance. Conversely, sample CM demonstrated the lowest average j_{corr} at 2.9 ± 1.0 nA/cm^2. It is interesting to note that sample C350/90 exhibited a relatively low average j_{corr} as well at 3.1 ± 1.0 nA/cm^2, which is comparable to that of sample

CM. In terms of PE, sample CM and C350/90 had very similar PE values of 82.9% and 81.8% respectively. Hence, it can be concluded that samples CM and C350/90 had comparable corrosion resistance despite the lower overcoat thickness in sample C350/90.

Table 4.1 Protective efficiencies (PE) and j_{corr} values of samples BM, CM and C350/90.

Samples	j_{corr} (nA/cm^2)	Protective Efficiency (PE)
BM	17 ± 6	--
CM	2.9 ± 1.0	82.9%
C350/90	3.1 ± 1.0	81.8%

4.2.5 Tribological properties

Next, the tribological performance of sample C350/90 was compared with sample BM and sample CM. The combined plot of COF versus number of cycles for these three samples is shown in Figure 4.6(a). In addition, the optical micrographs of the counterface balls and wear tracks for the three samples after the tribological tests are presented in Figure 4.6(b).

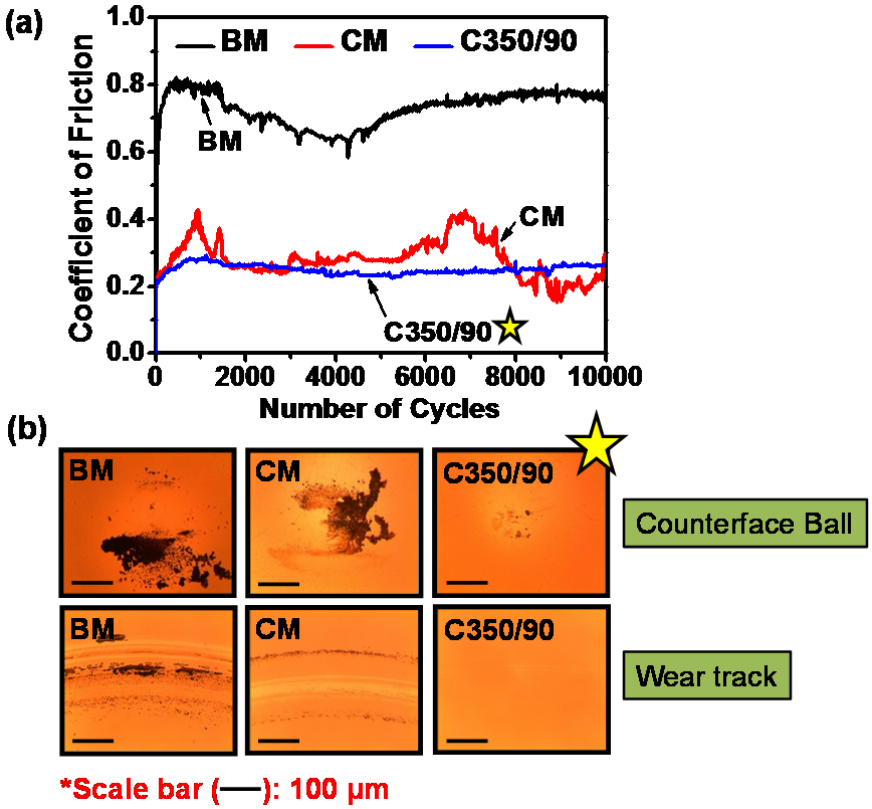

Figure 4.6 (a) Combined plot of COF versus number of cycles for samples BM, CM and C350/90. (b) Optical micrographs of the wear track locations and counterface balls after the ball-on-disk tribological tests.

It is remarkable that sample C350/90 with ~ 1.7 nm of COC showed a relatively steady COF value at ~ 0.2–0.25 all the way until test completion at 10,000 cycles. Sample CM, on the other hand, exhibited a fluctuating COF between 0.15–0.4 throughout the test. In contrast, sample BM exhibited the highest COF out of the three samples at 0.6–0.8, with an average COF of 0.75 during the last 4000 cycles. This suggests that an overcoat is essential for wear protection of the media. When comparing the optical micrographs of the counterface balls and wear tracks, it is also curious to note that sample C350/90 showed a barely visible wear track and almost no debris transfer onto the counterface ball. On the other hand, samples CM and BM show severe wear tracks and significant debris transfer to the balls. This highlights the

excellent tribological performance of the overcoat synthesized by the bi-level energy FCVA process in sample C350/90 despite its lower overcoat thickness compared to sample CM.

4.2.6 Experiments with a PFPE lubricant layer

So far, the above analyses were conducted on overcoated samples without any PFPE lubricant layer. To analyze how the samples will behave tribologically when a PFPE lubricant layer is applied on the surface, an extension of the above study was performed to coat samples BM and C350/90 with a layer of Fomblin Z-dol via a standard dip-coating process [136]. The dip-coating process parameters and lubricant concentration were calibrated by Fourier-transform infrared (FTIR) reflectance spectroscopy to obtain a uniform lubricant thickness of 1.1 ± 0.1 nm. Immediately after dip-coating, the PFPE-coated samples were heated at ~ 150 °C for 1.5 hours to improve the PFPE-substrate bonding and evaporate any excess solvent. The lubricated samples BM and C350/90 are hereon given the nomenclature of BML and C350/90L respectively.

Subsequently, samples BML and C350/90L were subjected to ball-on-disk tribological testing under the same conditions as the non-lubricated samples. Their tribological and wear properties were compared with the full commercial media sample CML. Figure 4.7(a) presents the comparison plot of COF versus number of cycles for the three lubricated samples and their non-lubricated counterparts, and their average COF values are plotted in a bar chart in Figure 4.7(b) for comparison purpose. The optical micrographs of the

counterface ball and wear track locations on all six lubricated and non-lubricated samples are shown in Figure 4.7(c).

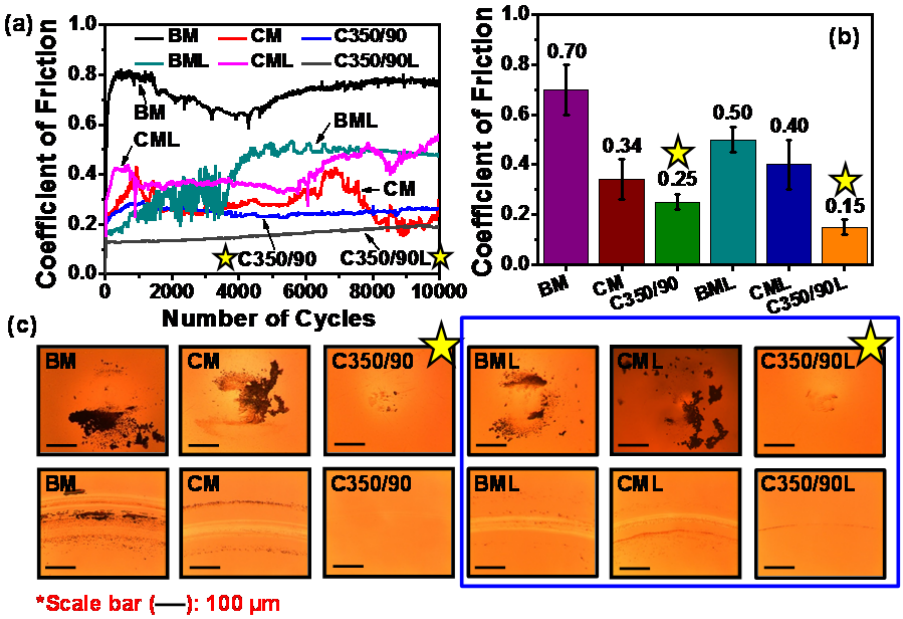

Figure 4.7 (a) Combined plot of COF versus number of cycles for lubricated samples CML, BML and C350/90L as well as non-lubricated samples CM, BM and C350/90. (b) Bar chart showing the average COF value of each sample. (c) Optical micrographs of the wear track locations and counterface balls after 10,000 cycles of ball-on-disk testing on all six samples. The images of the lubricated samples are highlighted with the blue box.

Based on the COF data, it can be seen that the PFPE layer had a beneficial effect in reducing the friction of both samples BM and C350/90. However, samples CM and CML both show COF values fluctuating roughly within the same range of ~ 0.25–0.5 throughout the test. From the optical micrographs, significant wear debris was still observed on the counterface balls for samples BML and CML, although their wear tracks were considerably less severe than their non-lubricated counterparts (samples BM and CM). Interestingly, sample C350/90L showed almost no wear debris transfer to the ball and a barely visible wear track. Thus comparing with sample C350/90, it can be said that although the PFPE lubricant contributed to

an improvement in the frictional properties of sample C350/90, it had a negligible effect on improving its wear performance, since sample C350/90 already exhibited superior tribological performance without lubricant. Therefore based on the tribological tests, samples C350/90 (without lubricant) and C350/90L (with lubricant) showed the best tribological and wear properties. Furthermore, it is interesting to note that, even without a PFPE layer, the FCVA-processed sample C350/90 exhibited a lower friction than sample CML which contains the commercial COC with PFPE.

4.2.7 Relation of functional properties to microstructure

In light of the stellar tribological and corrosion performance of sample C350/90, it is clear that the energetic FCVA bi-level energy process of C350/90 eV was beneficial in achieving these enhanced properties. To understand this further, the microstructure and chemical bonding within the COC and at the COC-media interface of sample C350/90 were analyzed using XPS and ultra-violet (UV) Raman spectroscopy.

XPS measurements were conducted on samples C350/90 and CM (samples having overcoat), and the spectra were taken at an electron take-off angle of 27° with respect to the surface normal. For both samples, wide XPS survey scans with BE range between 0–1300 eV were first captured to get an overview of the various photoemission peaks present within the range. Following that, individual high resolution core level spectra corresponding to the photoemission peaks of C 1s (arising mainly from the COC) and Co $2p_{3/2}$ and Cr $2p_{3/2}$ (arising mainly from the media) were captured in a smaller BE

range. All the core level spectra were background subtracted using Shirley background subtraction and Gaussian-Lorentzian fitting was performed to deconvolute the spectra and obtain their constituent bonding peaks. Finally, the bonding fractions were calculated by comparing the ratio of the areas under the peaks. The wide scan spectra and labeled deconvoluted C 1s, Co $2p_{3/2}$ and Cr $2p_{3/2}$ core level spectra for samples C350/90 and CM are presented in Figures 4.8(a)–(h), while the respective bonding fractions for each spectrum are tabulated in Tables 4.2 and 4.3.

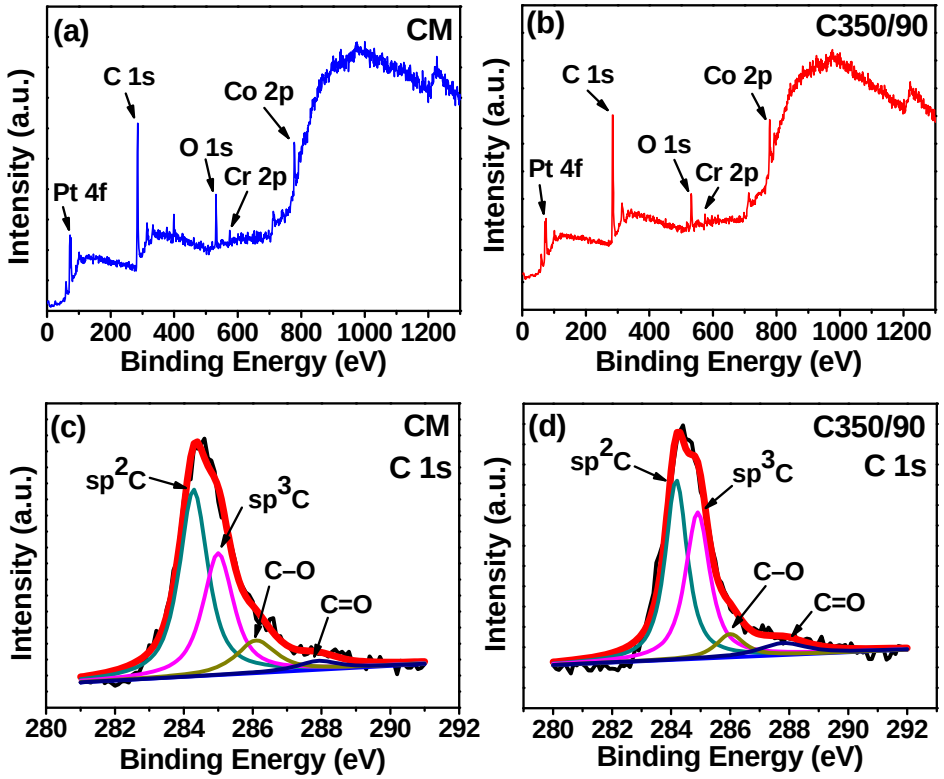

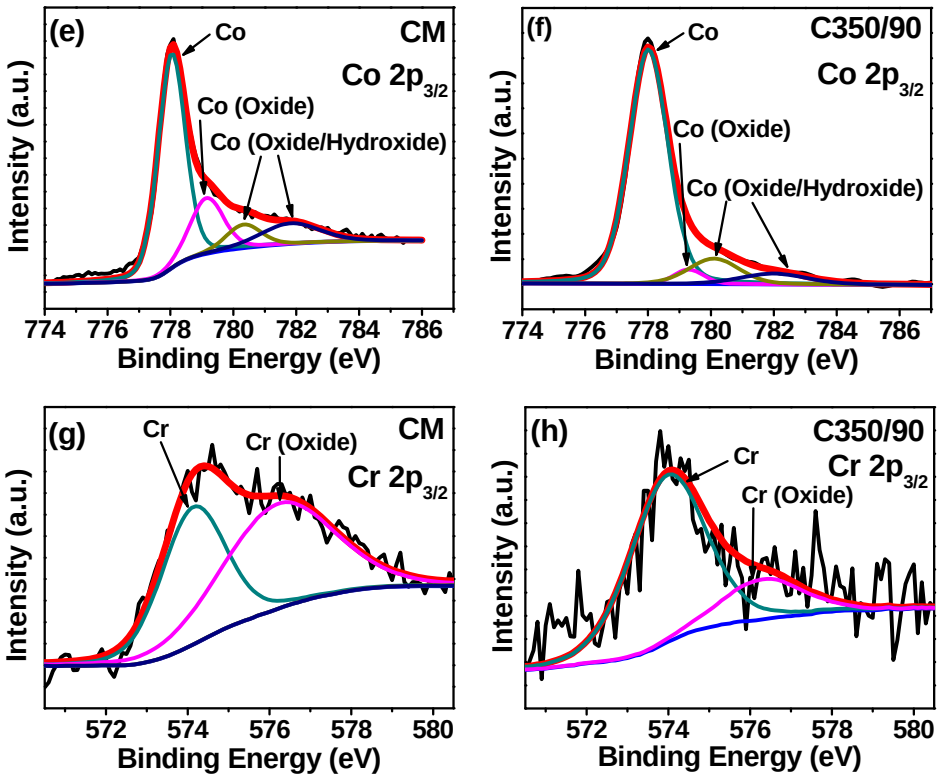

Figure 4.8 (a)–(b) XPS wide scan, (c)–(d) C 1s core level, (e)–(f) Co $2p_{3/2}$ core level and (g)–(h) Cr $2p_{3/2}$ core level spectra for samples CM and C350/90, respectively.

Table 4.2 Bonding fractions of the constituent peaks derived from the various XPS core level spectra of sample CM.

Samples	**Core Level Spectra**	**Binding energies (BE) and bonding fractions of constituent peaks**				
			Co	**Co (Oxide)**	**Co (Oxide/ Hydroxide)**	
	Co $2p_{3/2}$	BE (eV)	***778.0***	***779.2***	***780.3 & 781.8***	
		Bonding fraction (%)	59.7	19.2	21.1	
			Cr	**Cr (Oxide)**		
CM	**Cr $2p_{3/2}$**	BE (eV)	***574.1***	***576.2***		
		Bonding fraction (%)	43.2	56.8		
			sp^2C	**sp^3C**	**C–O**	**C=O**
	C 1s	BE (eV)	***284.28***	***285.0***	***286.1***	***287.9***
		Bonding fraction (%)	49.8	34.8	12.1	3.3

Table 4.3 Bonding fractions of the constituent peaks derived from the various XPS core level spectra of sample C350/90.

Samples	Core Level Spectra	Binding energies (BE) and bonding fractions of constituent peaks				
C350/90	Co $2p_{3/2}$		**Co**	**Co (Oxide)**	**Co (Oxide/ Hydroxide)**	
		BE (eV)	***778.0***	***779.3***	***780.1 & 782.0***	
		Bonding fraction (%)	78.8	3.7	17.5	
	Cr $2p_{3/2}$		**Cr**	**Cr (Oxide)**		
		BE (eV)	***574.0***	***575.9***		
		Bonding fraction (%)	80.6	19.4		
	C 1s		**sp^2C**	**sp^3C**	**C–O**	**C=O**
		BE (eV)	***284.17***	***284.9***	***286.0***	***287.8***
		Bonding fraction (%)	45.3	40.9	7.4	6.4

As can be seen in Figures 4.8(c) and 4.8(d), both the fitted C 1s core level spectra of samples CM and C350/90 contain contributions from sp^2C, sp^3C, C-O and C=O bonding [135, 137–139]. In the Co $2p_{3/2}$ spectra in Figures 4.8(e) and 4.8(f), contributions from metallic cobalt bonding, cobalt oxides and cobalt hydroxides could be observed as labeled [140–145]. Similarly, two constituent peaks in the Cr $2p_{3/2}$ spectra for both samples were observed in Figures 4.8(g) and 4.8(h) corresponding to metallic chromium bonding and chromium oxide bonding [146, 147]. From the various bonding fractions, not only can the sp^2C and sp^3C content within the two COCs be determined, but the extent of oxidation in the COC and media can also be compared by comparing the total amount of oxidized and un-oxidized fractions for each element in both samples. It was found that the sp^2C and sp^3C bonding fractions were 45.3% and 40.9% respectively for sample

C350/90. In comparison, sample CM contained sp^2C and sp^3C bonding fractions of 49.8% and 34.8% respectively. This clearly shows that sample C350/90 fabricated by the FCVA bi-level energy process possessed higher sp^3C bonding (and lower sp^2C bonding) despite having a lower COC thickness than sample CM.

In terms of oxidation within the COC, the total bonding fraction of carbon with oxygen (C-O and C=O) in each sample can be compared. Sample C350/90 exhibited slightly lower carbon-oxygen bonding at 13.8% and hence experienced less oxidation within the overcoat as compared to sample CM with 15.4% carbon-oxygen bonding. The amount of media oxidation was evaluated by comparing the total cobalt oxide/hydroxide and chromium oxide bonding fractions in both samples. Sample CM was revealed to have about twice as much cobalt oxidation and about three times as much chromium oxidation as compared to sample C350/90. Hence, this showed that less media oxidation took place in the case of sample C350/90.

UV Raman measurements (325 nm) were performed on samples CM and C350/90 to further analyze the microstructures of the COCs. Additionally, UV Raman was also performed on sample BM as a reference. The UV Raman spectra of the three samples are presented in Figure 4.9. A broad peak within this wavenumber range of 900-1800 cm^{-1} could be observed for both samples C350/90 and CM. After fitting the spectra (not shown here), the characteristic carbon D and G peaks could be observed for both samples. The D and G peaks for sample CM were found at wavenumbers of 1406 cm^{-1} and 1582 cm^{-1} respectively, whereas the D and G peaks for sample C350/90 were shifted to

higher wavenumber values of 1415 cm^{-1} and 1584 cm^{-1} respectively. On the other hand, the characteristic carbon peaks were not observed for the reference sample BM in this range due to the absence of COC. Based on three-stage model proposed by Ferrari and Robertson, the sp^3C bonding in sample C350/90 is estimated to be ~ 35–40%, which is in agreement with XPS results [86].

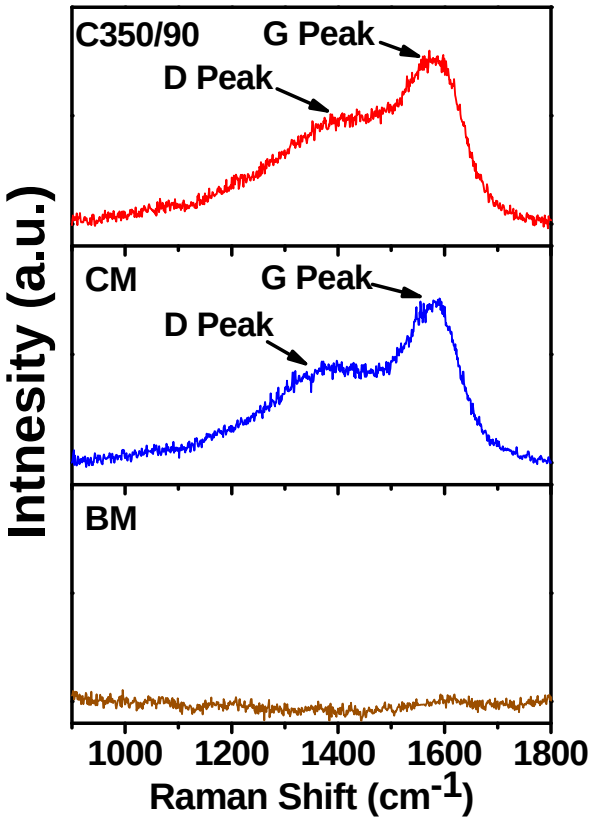

Figure 4.9 UV Raman spectra of samples C350/90 and CM indicating the approximate positions of the characteristic carbon D and G peaks.

Therefore, it is clear that in addition to the creation of greater atomic mixing at the media-COC interface by the 350 eV pre-treatment step, the high sp^3C bonding in sample C350/90 derived from the FCVA process is another important factor contributing to the improved tribological and wear performance over sample CM. While higher sp^3C bonding gives rise to higher

toughness (elasticity and hardness) of the COC, the greater extent of atomic mixing improved the adhesion of the COC with the media. Hence, the combination of these two factors led to the lower friction and improvement of the wear resistance of the COC. In relation to the corrosion/oxidation performance, a higher sp^3C fraction gives rise to a denser carbon network, which improves the film coverage (reduction of pinholes) such that diffusion of atmospheric oxygen through the COC and diffusion of Co and Cr metallic ion species towards the surface are inhibited. As a result the oxidation of the media and overcoat in sample C350/90 was observed to be lower than sample CM, while its corrosion resistance was maintained at lower COC thickness.

4.3 Thermal stability of the FCVA-processed carbon overcoat

One of the uncertainties faced by the media community in developing future HAMR media such as FePt is to develop a durable, ultrathin, yet thermally stable COC that is able to withstand high localized temperatures (~ 600–700 K) and rapid heating rates of ~ 10^{11} K/s [148]. Current a-C:H overcoats fabricated by PECVD have been shown to undergo degradation when subjected to such aggressive heating conditions [148, 149]. The effusion of hydrogen from the carbon-hydrogen network and the subsequent microstructural transformation of sp^3C to sp^2C bonding are found to be the main causes of poor thermal stability in a-C:H overcoats. Reports have shown that high sp^3C bonding is a key factor which contributes to the high thermal stability of COCs [23, 29]. For example, Ferrari et al. had demonstrated that

the thermal stability of non-hydrogenated carbon films was found to increase with increasing sp^3C content [29]. As the FCVA process is ideal for producing COCs with higher sp^3C bonding, FCVA-processed COCs are potentially suitable candidates for thermally stable HAMR media overcoats. In this context, some recent works have demonstrated the capability of FCVA-processed ultrathin overcoats to withstand higher temperatures than PECVD overcoats by thermal annealing [16, 150]. However, those works did not simulate HAMR-like recording conditions, which consist of intense localized heating by laser irradiation at high temperatures and heating rates on HAMR media for overcoat testing.

Recently, our group sought to evaluate the thermal stability of the COC on $L1_0$ FePt media fabricated by the FCVA bi-level energy process (C350/90 eV), when exposed to simulated HAMR-like conditions [151]. In addition, to probe the role of sp^3C bonding on thermal stability, an additional non-hydrogenated carbon overcoat deposited by DC sputtering and possessing significantly lower sp^3C bonding was also included in the study. After subjecting the samples to laser irradiation under HAMR-like conditions using an optical pump-probe setup, AFM and visible Raman spectroscopy measurements were performed to investigate any change in the topography and carbon microstructure. From AFM topography measurements, it was found that carbon removal occurred in the case of the sputtered COC, while almost no carbon removal was observed for the FCVA-processed COC after laser irradiation.

To probe the carbon microstructure change, visible Raman measurements were performed on the irradiated sputtered COC at the points within the irradiated spot, at the periphery of the spot and outside of the spot. Simultaneously, a visible Raman spectrum was also taken at the irradiated spot of the FCVA-processed overcoat for comparison. The Raman spectra and their respective locations are presented in Figure 4.10.

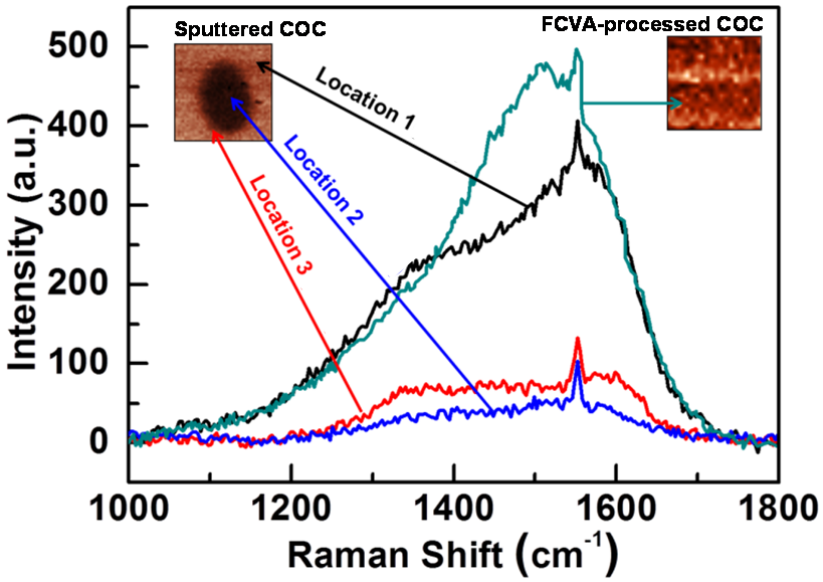

Figure 4.10 Visible Raman spectra taken at three locations in the irradiated region of the sputtered COC and at one location within the irradiated spot for the FCVA-processed COC. The spectra corresponding to the various locations are labeled according to the AFM 2D topography images (shown inset). [151].

For the sputtered COC, the intensities of the Raman peaks are clearly shown to decrease in the order of: outside the irradiated spot > at the periphery > in the middle of the irradiated spot. This suggested the decreasing carbon content in the same order. It was also found from the fitted Raman spectrum of the periphery location that there was significant amount of graphitization. Since both overcoats were non-hydrogenated, it was deduced that the enhanced thermal stability of the FCVA-processed COC was primarily due to its higher sp^3C bonding fraction, which agreed with other findings from

literature [128, 149, 150]. Hence, this experiment clearly demonstrated that especially in aggressive HAMR-like conditions, the presence of higher sp^3C bonding fraction is essential for COCs to attain higher thermal stability.

4.4 Ion energy optimization of the FCVA process without functional performance degradation

The FCVA bi-level energy process of C350/90 eV has so far shown remarkable tribological properties, excellent corrosion/oxidation protection and high thermal stability, demonstrating its outstanding potential for implementation on future media. However, the use of high energy C^+ ions, especially during the pre-treatment step of 350 eV for higher atomic mixing, may be detrimental to the magnetic performance of the media. Therefore, it was necessary for a systematic study to be carried out to investigate the effect of COC formation using low, moderate and high C^+ ion energies on the functional (macromagnetic) properties of the media, while still maintaining the excellent protective qualities of the FCVA-processed COC.

Our group recently performed such a study, selecting three energies of 50 eV, 90 eV and 345 eV for COC formation, each one corresponding to a different energy range of low, medium and high energy respectively [152]. In this work, samples were fabricated at single energies with different process times (corresponding also to different COC thicknesses). It was found that using high energy of 345 eV, the magnetic coercivity of the media was found to have increased significantly even at a short process time of 5 s, as compared to unmodified commercial media. On the other hand, when moderate and low

ion energies of 90 eV and 50 eV were applied, the coercivity was maintained or saw a negligible increase. This showed that the high energy process of 345 eV (~ 350 eV in the FCVA bi-level process pre-treatment step) resulted in the degradation in the macromagnetic performance in the media. The mechanism for the degradation of the media's magnetic properties was explained by the high energy C^+ ion embedment process creating disorder in the top surface of the media through displacement of the media atoms from their lattice positions.

It was thus necessary for the FCVA process to be optimized to avoid degradation of the media performance via the bi-level energy process of C350/90 eV. By performing tribological ball-on-disk experiments and three-electrode electrochemical corrosion testing, it was found that the COC processed using moderate ion energy 90 eV (sample C90, thickness ~ 1.8 nm) gave the best tribological performance whereas the COC processed using low ion energy of 50 eV (sample C50, thickness ~ 1.7 nm) gave the best corrosion performance. Taking advantage of both, an optimized bi-layer COC was proposed utilizing the energies of 90 eV and 50 eV which may possess the combined properties of good corrosion resistance and tribological performance, hereon labeled as sample C90/50. After performing ball-on-disk tribological tests and corrosion tests, the COF graphs and the optical micrographs of the wear track location and counterface balls for samples C50, C90 and C90/50 are presented in Figure 4.11, while the j_{corr} values of the three samples are presented in Table 4.4. Indeed, it was revealed that sample C90/50, with ~ 1.9 nm COC, showed a steady and low COF (~ 0.3–0.35) with

a very faint wear track and minimal debris transfer observed after the ball-on-disk tribological test of 10,000 cycles. Concurrently, in terms of corrosion performance, sample C90/50 gave an average j_{corr} value of 3.1 nA/cm^2, which is similar to that of the ~ 1.8 nm C350/90 overcoat (as reported in Section 4.2). Hence, it can be seen that the proposed optimized ~ 1.9 nm bi-layer COC fabricated by the FCVA C90/50 eV process not only showed both superior tribological and corrosion performance, but could also prevent significant degradation of the magnetic properties of the underlying media.

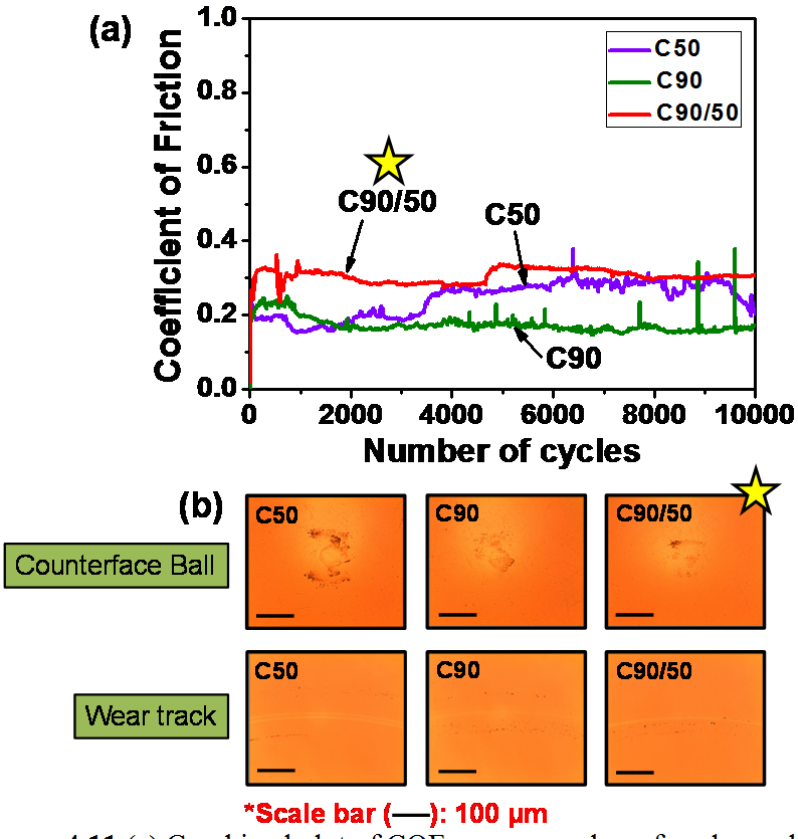

Figure 4.11 (a) Combined plot of COF versus *number of cycles and* (b) optical micrographs of the counterface balls and wear track regions for samples C50, C90 and C90/50. [152].

Table 4.4 COC thicknesses and j_{corr} values of samples C50, C90 and C90/50. [152].

Samples	COC thickness (nm)	j_{corr} (nA/cm^2)
C50	~ 1.7	4.5 ± 2.8
C90	~ 1.8	8.4 ± 2.5
C90/50	~ 1.9	3.1 ± 1.6

4.5 Conclusions

In this chapter, the efficacy of the FCVA bi-level process in creating thermally stable, ultrathin and ultra-smooth COCs with outstanding wear and corrosion protection is elucidated. Two important factors contribute to the above properties, which are 1) a suitable amount of atomic mixing at the media-COC interface to improve the adhesion between the overcoat and the media substrate, and 2) the high sp^3C content of ~ 40% as compared to sputtered and PECVD-processed COCs. The corrosion and ball-on-disk tribology results on non-lubricated samples revealed that the protective characteristics of the COC developed through the FCVA bi-level energy process were enhanced, in terms of lower friction, higher wear resistance and higher corrosion/oxidation protection. This can be attributed to a combination of the high sp^3C bonding fraction and the development of greater atomic mixing at the media-COC interface. With the introduction of a PFPE lubricant layer, the excellent wear resistance of the COC was maintained, whereas the friction was reduced by 20–40%. Hence, the beneficial effect of PFPE in providing a lower friction surface for the FCVA-processed COC can be observed.

However, it was found that the high process energy of 350 eV in the pre-treatment step was detrimental to the macromagnetic properties of the media. As such, through further optimization of the ion energies, a C90/50 eV FCVA process was proposed to obtain all the above qualities for the overcoat without degrading the magnetic performance of the underlying media. Based on the results, it was found that the C90/50 eV process was promising for the development of future ultrathin overcoats for commercial media.

Chapter 5: Development of a protective SiN_x/C bi-layer overcoat for hard disk media

5.1 Introduction

As discussed in the previous chapter, the COCs fabricated by the FCVA bi-level energy process have shown promising functional properties, in terms of lower friction, higher wear resistance and improved corrosion resistance. The high energy pre-treatment step at 350 eV helped to enhance the adhesion of the COC with the media due to atomic mixing, while COC deposition at 90 eV creates a carbon layer with high sp^3C bonding. However, it was revealed that this process resulted in the degradation of the magnetic properties of the media, which is not desirable. In addition, further enhancement of sp^3C bonding can be beneficial for improving the wear resistance, corrosion resistance, as well as the thermal stability of the overcoats. In this chapter, a new bi-layer overcoat structure is proposed by introducing an effective adhesion interlayer such that low ion energy C^+ deposition can be employed for the growth of the carbon layer while maintaining good adhesion and high sp^3C bonding. In this way, the enhanced functional properties of the ultrathin carbon-based overcoat can be achieved, whereas the low energy deposition of the carbon layer would not detrimentally affect the magnetic performance of the media.

5.2 Literature review

Silicon nitride (Si_3N_4) is widely known to be a tribologically superior ceramic refractory material, possessing qualities such as high hardness and wear resistance, which make it useful as a hard coating for mechanical tools. The hardness and rigidity of Si_3N_4 arise from the high bond density within the structure, whereby each N atom is bonded to three Si atoms and Si itself is bonded to four Si atoms. Silicon nitride can be deposited by CVD and sputtering techniques, and in such cases, non-stoichiometric, amorphous silicon nitride films (SiN_x) can be obtained. Despite its amorphous structure, short range order of trigonally-coordinated N bonded with tetrahedrally-coordinated Si still exists although long range ordering is lost, thus maintaining a dense network with the potential to form strong and extensive bonding. SiN_x has previously been explored for hard disk applications, owing to its good mechanical properties and its potential to minimize corrosion of the media because of its good coverage at low thicknesses even down to 10 Å [60, 153, 154]. However, due to its high propensity to oxidize, its high frictional characteristics and poor wear resistance (which will be discussed later), SiN_x as a monolithic overcoat is not suitable for media [153, 155–157].

Nevertheless, SiN_x has a strong affinity with carbon, and was found to provide strong adhesion between metal substrates (such as stainless steel) and DLC when it was used as an interlayer material [158]. When compared with other amorphous Si-based interlayers such as Si and SiC with thickness of ~ 350 nm, it was revealed that the SiN_x interlayer provided the best adhesion properties [158].

5.3 Motivation of this work

Hence, the development of a novel bi-layer overcoat, comprising a SiN_x interlayer between the media and COC, could be desirable for improving the corrosion protection (due to its good surface coverage at low thickness) as well as the wear resistance of the media (through improved adhesion of the COC with the media). Furthermore, the carbon overlayer could act as a capping layer to protect the SiN_x layer from being readily oxidized, which could lead to better frictional and wear properties of the overcoat. However, to achieve an ultra-low overcoat thickness of < 2 nm for future media overcoats, the individual layers of the bi-layer overcoat have to be extremely thin. Based on the work by Yen et al., it was reported that a minimum thickness of 5 Å of SiN_x had a visible effect in reducing the surface oxidation of the CoCrPt alloy-based media [154]. Therefore, in this work, an atomically-thin SiN_x interlayer of ~ 4 Å was used to investigate its effectiveness in providing corrosion protection.

For the a-C overlayer, a high sp^3C content was desired to achieve a dense carbon network for corrosion protection and good tribological properties. However at ultra-low thickness, the sp^3C content decreases drastically and coverage of the ultrathin carbon layer becomes an issue. Hence, to achieve the highest possible sp^3C bonding fraction at such low thickness, FCVA was the technique of choice to grow the ultrathin carbon layer. As discussed in Section 4.4, higher ion energies could lead to degradation of the magnetic media layer. Therefore, low energy FCVA

deposition was used here to form the carbon layer in order to minimize the amount of carbon embedment.

5.4 Experimental methodology

In this work, a bi-layer overcoat comprising a 4 Å SiN_x interlayer and a 12 Å carbon overlayer (hereon referred to as sample 4SiN12C) was proposed as a novel corrosion and wear protective overcoat for CoCrPt:Oxide commercial media. The process schematic for sample preparation is illustrated in Figure 5.1.

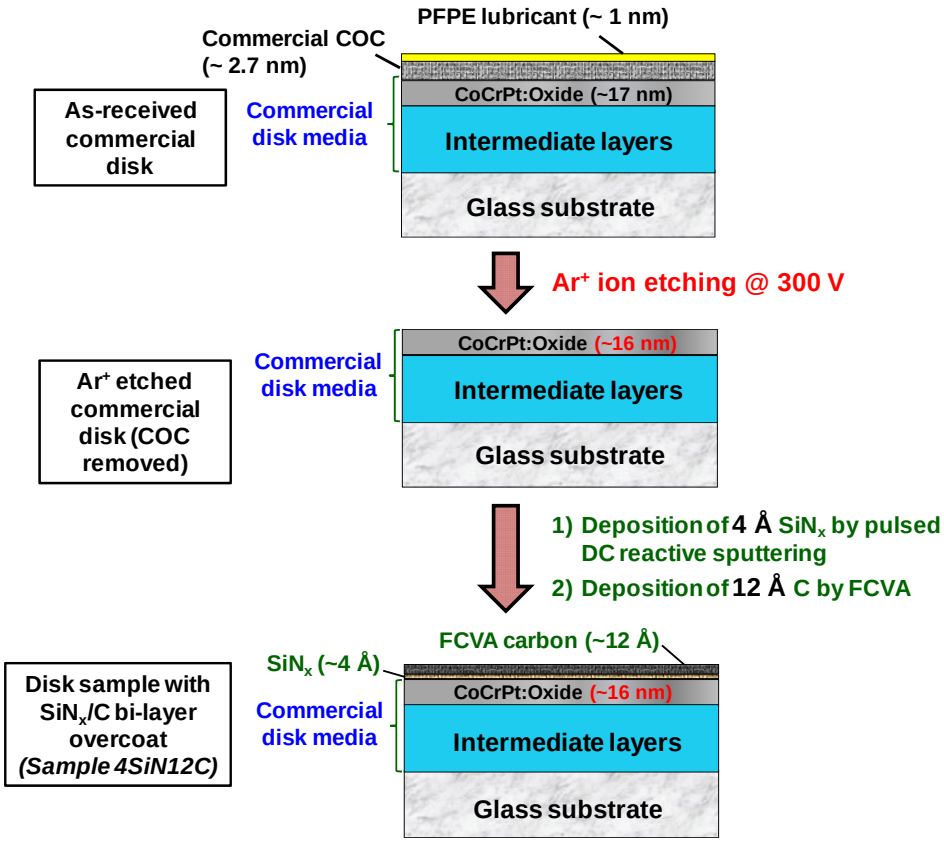

Figure 5.1 Schematic of the SiN_x/C bi-layer overcoat fabrication process.

All the sample preparation steps as described in Figure 5.1 were performed *in situ* in a Veeco NEXUS DLC-X deposition system, which is

equipped with an ion beam etch source, a sputtering source and a pulsed filtered cathodic arc source. This was to ensure that the entire etching and deposition process was carried out in the same chamber under high vacuum without exposure to the ambient, so as to prevent unintended oxidation of the samples. Starting substrates of full commercial CoCrPt:Oxide media disks were used for this work. To first remove the existing lubricant and commercial COC layers, Ar^+ ion beam etching at 300 eV energy was performed. The removal of the lubricant and COC layers was monitored using an attached SIMS detector and the etching process was stopped immediately once the top of the media layer was detected. The etching process was optimized so that the magnetic and microstructural properties of the commercial media were intact. The magnetic properties were checked using a vibrating sample magnetometer (VSM) and by MFM, whereas the crystallographic orientation of the media was checked by X-ray diffraction (XRD). Deposition of the 4 Å SiN_x interlayer was first carried out by pulsed DC reactive sputtering of a Si target in an Ar/N_2 process gas mixture. A 2:1 gas volume ratio of Ar to N_2 was used to obtain an approximately stoichiometric Si_3N_4 composition within the SiN_x film, as determined by Yen et al. [60]. Next, a pulsed FCVA deposition process was used to deposit 12 Å of the carbon overlayer by applying a high current pulsed power supply at the graphite target at a duty cycle of 0.001. The generated C^+ plasma was filtered through a 90° bend magnetic coil before passing through a plasma shaping coil while heading towards the substrate. No substrate bias was applied in this system such that the ion energy of the C^+ ions arriving at the substrate was ~ 25 eV. The deposition rates for SiN_x and carbon, as well as the thickness and etch rate uniformity, were individually

calibrated by X-ray reflectivity measurements. This process produced a total SiN_x/C bi-layer overcoat thickness of 16 Å. Two additional sample sets were similarly fabricated on commercial media, with one set containing a monolithic 16 Å carbon overcoat (referred to as sample 16C) and the other set containing a monolithic 16 Å SiN_x overcoat (referred to as sample 16SiN). This was done to maintain the same total overcoat thickness, with the aim of evaluating and comparing their protective qualities with the bi-layer overcoat. These three samples were further compared with two reference samples of CM and BM (structures as described in Section 4.2).

All the samples were characterized by HRTEM, AFM, ball-on-disk tribological tests, electrochemical corrosion measurements and MOKE measurements to investigate their overcoat thickness, surface roughness, tribological properties, corrosion performance and macromagnetic properties, respectively. In-depth microstructural and bonding environment analyses were subsequently performed on carbon-based overcoats by Raman spectroscopy and XPS respectively.

5.5 Results and discussion

5.5.1 Overcoat thickness and surface roughness

The cross-sectional HRTEM images of samples CM, 16C, 16SiN and 4SiN12C are shown in Figures 5.2(a)–(d) respectively.

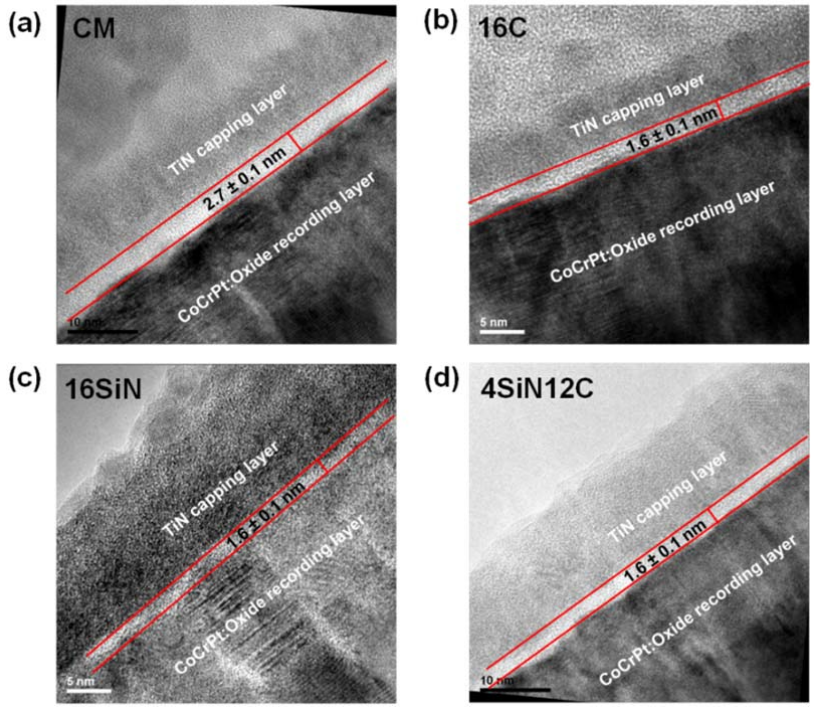

Figure 5.2 Cross-sectional HRTEM images of samples (a) CM, (b) 16C, (c) 16SiN and (d) 4SiN12C, showing the measured overcoat thicknesses as marked out with red solid lines.

From the images, the thicknesses of the fabricated overcoats were measured to be 1.6 ± 0.1 nm, which matched the intended thicknesses to be deposited, thereby confirming the accuracy of the deposition rate calibration. For comparison, the COC thickness of CM is also presented in Figure 5.2(a) and is shown to be 2.7 ± 0.1 nm. It should be noted that due to the thinness of the 4 Å SiN_x layer and its similar image contrast with a-C, the SiN_x layer in the SiN_x/C bi-layer overcoat of sample 4SiN12C could not be distinguished. Hence, only the total overcoat thickness was measured. Surface roughness measurements were conducted on the four overcoated samples and their R_a and R_q values were plotted in Figure 5.3. It was found that the roughnesses of samples 16C, 16SiN and 4SiN12C were almost the same (R_q ~ 0.20 nm) but slightly lower than that of CM (R_q ~ 0.25 nm). The decrease in roughness was

attributed mainly to the surface etching process during lubricant and COC removal, which could have smoothened the media surface before overcoat deposition, as was also previously observed for sample C350/90 in Section 4.2.

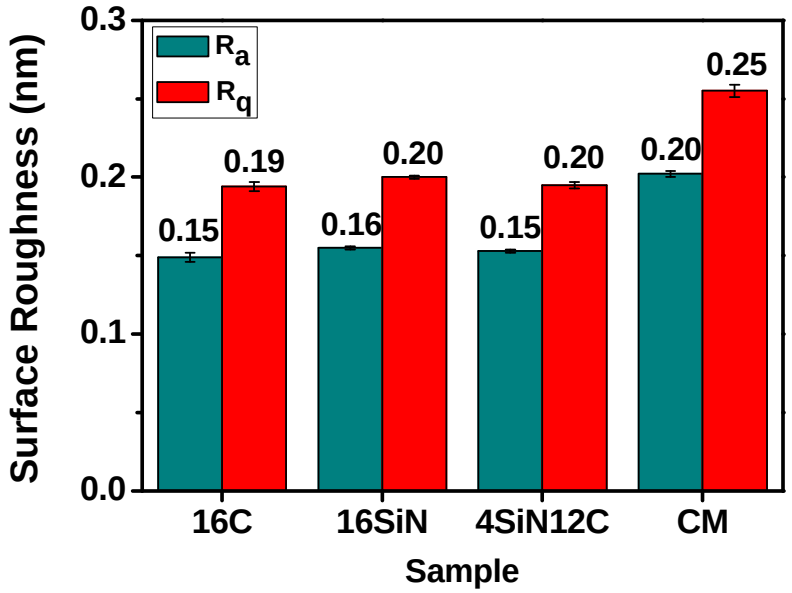

Figure 5.3 Surface roughness (R_a and R_q) values of the four overcoated samples 16C, 16SiN, 4SiN12C and CM.

5.5.2 Tribological properties and wear resistance

The COF values recorded during the ball-on-disk tribological tests for the 16 Å monolithic SiN_x and carbon overcoats were compared with the 16 Å bi-layer SiN_x/C overcoat. As reference samples, samples CM and BM were tested under the same conditions to compare their tribological behavior with the 16 Å overcoated samples. The tribological curves of COF versus number of cycles for all the above five samples are plotted in Figure 5.4(a), while the average COF value for each sample was extracted and plotted in a bar chart as shown in Figure 5.4(b).

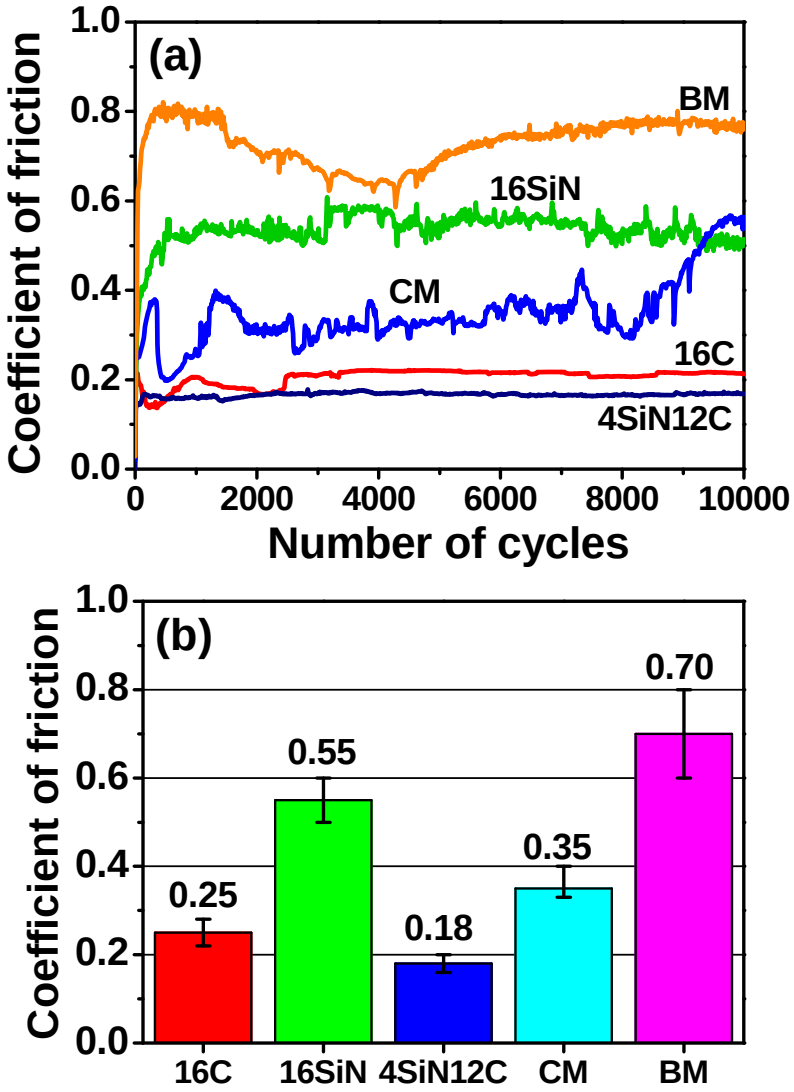

Figure 5.4 (a) COF graphs of samples 16C, 16SiN, 4SiN12C, CM and BM with respect to the number of cycles. (b) Average COF values extracted from the COF graphs for each sample.

Interestingly, the two overcoats with FCVA-processed carbon layers exhibited the lowest friction, which was very stable and lasted throughout the test. Average COF values of 0.25 and 0.18 were observed for samples 16C and 4SiN12C, respectively. In contrast, monolithic SiN_x in sample 16SiN gave rise to a COF ranging between 0.5–0.6 with an average value of 0.55. This COF value, though lower than that observed for sample BM (average COF of 0.70),

was higher than the COF observed for sample CM (average COF of 0.35). This implied that there was some degree of wear protection up to 10,000 cycles when 16 Å of SiN_x was applied onto the bare media; however, it was not as wear protective as the other overcoated media.

To evaluate the wear resistance of the different overcoats, optical micrographs of the counterface balls and wear track locations were acquired and are presented in Figure 5.5. On immediate visual observation, the most severe wear track and largest amount of wear debris generated onto the counterface ball were observed for uncoated bare media sample BM. Following that, samples 16SiN and CM showed severe wear tracks and a considerable amount of wear debris transfer as well, with sample 16SiN having a relatively more severe track than sample CM, but CM having slightly more debris transfer than 16SiN. Hence, samples 16SiN and CM could be seen to have similarly poor wear resistance after 10,000 cycles of ball-on-disk testing. However, for both samples 16C and 4SiN12C, there was an extremely faint wear track on the sample when observed through the optical microscope. With regard to wear debris transfer onto the counterface ball, a very small amount of wear debris was observed in sample 16C whereas the amount of wear debris could be considered as negligible in the case of sample 4SiN12C. Thus in terms of wear resistance, the bi-layer SiN_x/C overcoat exhibited the best performance, followed by monolithic carbon processed by FCVA. Monolithic SiN_x and commercial media COC both exhibited considerably poorer wear resistance under the same conditions.

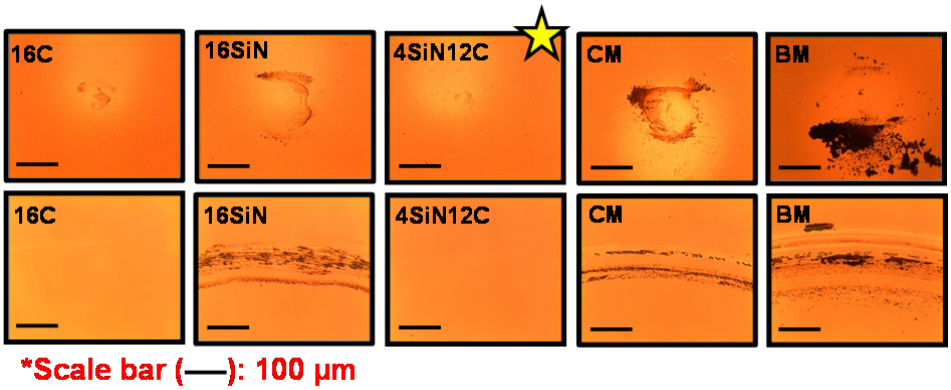

Figure 5.5 Optical micrographs of the counterface ball (top images) and wear track locations on the sample (bottom images) for samples 16C, 16SiN, 4SiN12C, CM and BM after the ball-on-disk tribological test.

5.5.3 Corrosion resistance

The corrosion performance of the various overcoated and non-overcoated media were evaluated by the potentiodynamic polarization method and the average j_{corr} values are summarized in a bar chart as shown in Figure 5.6. Between the four overcoated samples of 16C, 16SiN, 4SiN12C and CM, the average j_{corr} values were comparable on the whole, even though sample CM had a higher total overcoat thickness compared to the other three fabricated overcoats. This revealed the effectiveness of both FCVA-processed carbon and sputtered SiN_x for corrosion protection. Now comparing between the three 16 Å overcoats (while keeping in mind that all three exhibited good corrosion protection), sample 16SiN gave the lowest average j_{corr} of 1.9 nA/cm^2, while sample 16C had the highest average j_{corr} of 3.4 nA/cm^2. This proved that SiN_x was almost twice as effective in protecting the media from corrosion as compared to even FCVA-processed a-C. When compared to the SiN_x/C bi-layer overcoat in sample 4SiN12C, an average j_{corr} of 2.2 nA/cm^2 was observed, which was slightly higher than that of sample 16SiN. Thus it

can be seen that the application of the 4 Å SiN_x interlayer provided additional corrosion protection for the FCVA-processed a-C overlayer.

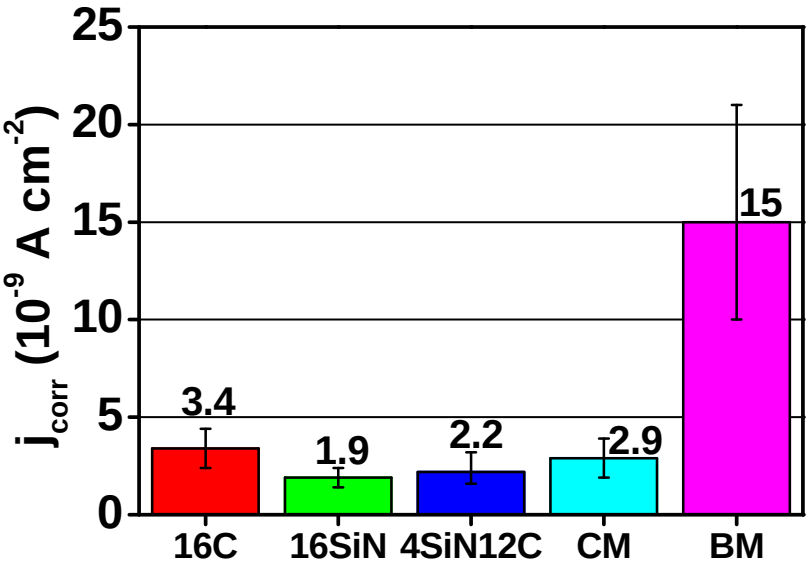

Figure 5.6 Average extrapolated j_{corr} values for samples 16C, 16SiN, 4SiN12C, CM and BM.

5.5.4 Macromagnetic properties

The macromagnetic properties of the overcoated media samples were measured by MOKE microscopy to investigate any change in the magnetic performance of the media after the Ar^+ ion beam etching and overcoat deposition process. Figure 5.7 presents the out-of-plane MOKE hysteresis loops for samples 16C, 16SiN and 4SiN12C, plotted together with the hysteresis loop of commercial media sample CM as a benchmark. The shapes and sizes of the loops were found to be similar for all four samples, revealing that both the etching and deposition processes did not alter the magnetic properties of the media, in contrast to when high energy C^+ ion bombardment was applied onto commercial media as observed in Section 4.2. Thus it can be

seen that the FCVA carbon deposition energy at 25 eV was low enough not to deteriorate the magnetic properties.

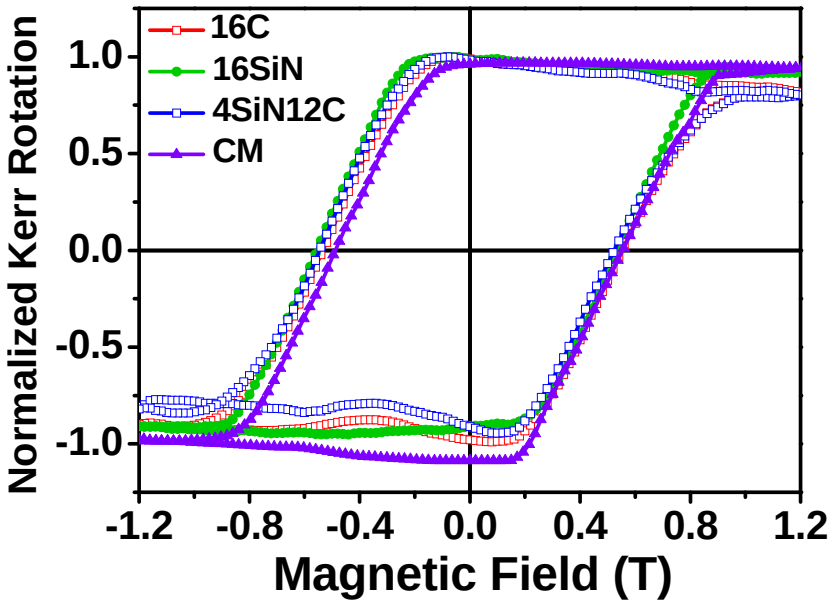

Figure 5.7 Out-of-plane MOKE hysteresis loops measured for samples 16C, 16SiN, 4SiN12C and CM.

5.5.5 Bonding environment, microstructure and structure-functional property relationship

The synergistic effect of the SiN_x and a-C layers in the 16 Å SiN_x/C bi-layer overcoat has so far been shown to effectively enhance the functional properties of corrosion resistance and wear resistance over monolithic a-C and SiN_x of the same thickness, without degrading the macromagnetic properties of the media. It is hence of importance to understand the reason for this enhancement by relating it to its chemical bonding and microstructure. First of all, the bonding environment of the bi-layer overcoat was studied by XPS to probe the chemical bonding within the ultrathin overcoat. A take-off angle of 65° with respect to the sample surface was used. XPS measurements were also

taken for the other two samples with carbon-containing overcoats (samples 16C and CM) as well as another sample containing only a monolithic 12 Å a-C overcoat fabricated by the same FCVA process (hereon referred to as sample 12C). The purpose of sample 12C was to serve as a reference to compare with sample 4SiN12C where both overcoats had the same carbon layer thickness. For all the four samples, the core level C 1s, Co $2p_{3/2}$ and Cr $2p_{3/2}$ spectra were recorded. In addition, Si 2p and N 1s core level spectra were recorded only for sample 4SiN12C. All the XPS spectra were deconvoluted to reveal their constituent bonding peaks and were analyzed to obtain their respective bonding fractions by calculating the ratio of the areas under the peaks. For easy comparison purpose, a summary graph of the various bonding fractions extracted from the C 1s, Co $2p_{3/2}$ and Cr $2p_{3/2}$ spectra for the above samples is displayed in Figure 5.8. Readers are referred to Refs. [159, 160] for further details on the analyses.

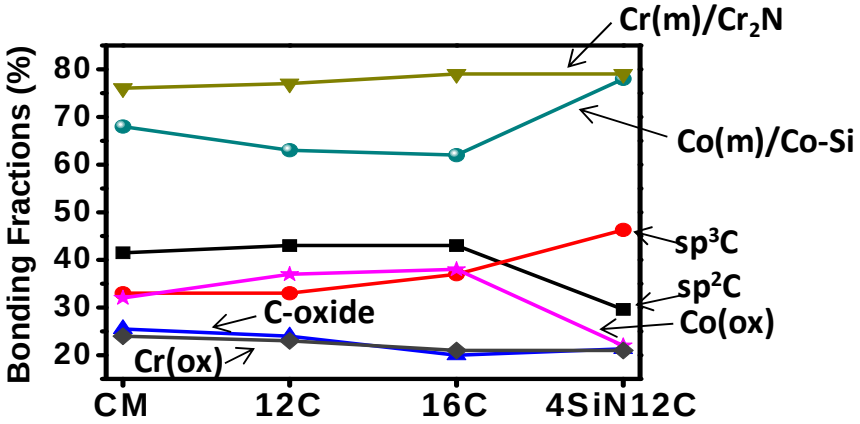

Figure 5.8 Summary of the bonding fractions of samples CM, 12C, 16C and 4SiN12C as extracted from the XPS C 1s, Co $2p_{3/2}$ and Cr $2p_{3/2}$ core level spectra.

From the bonding fraction information, it was found that in terms of carbon bonding, sample 4SiN12C possessed the highest sp^3C bonding fraction

of ~ 46% and the lowest sp^2C bonding fraction of ~ 29%. In comparison to the same thickness of a-C in sample 12C, where there was ~ 33% of sp^3C bonding and ~ 43% of sp^2C bonding, it is clear that the presence of the 4 Å SiN_x layer had enhanced the sp^3C bonding within the carbon layer. In terms of oxidation of cobalt and chromium (originating from the media), sample 4SiN12C was also found to possess the least amount of Co(oxide/hydroxide) and Cr(oxide/hydroxide) bonding fractions out of the four samples, at ~ 22% and ~ 21% respectively. This corroborated with the electrochemical corrosion results whereby sample 4SiN12C was found to have the best corrosion (oxidation) resistance among the carbon-based overcoats. To reveal the different types of bonding occurring within sample 4SiN12C, the deconvoluted C 1s, Si 2p, N 1s, Co $2p_{3/2}$ and Cr $2p_{3/2}$ spectra of sample 4SiN12C are presented in Figures 5.9(a)–(e) respectively.

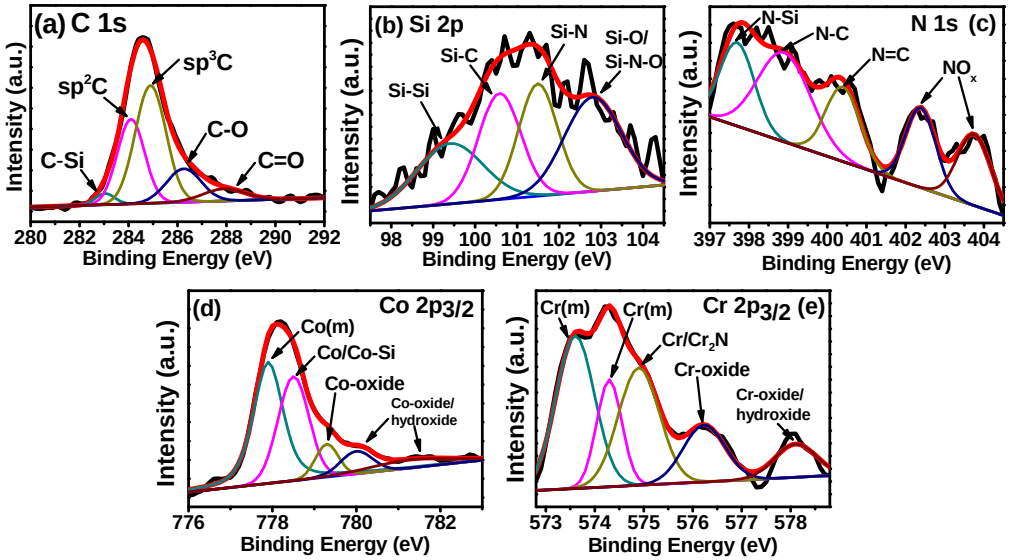

Figure 5.9 Deconvoluted XPS core level spectra of sample 4SiN12C showing the labeled constituent peaks. (a) C 1s, (b) Si 2p, (c) N 1s, (d) Co $2p_{3/2}$, and (e) Cr $2p_{3/2}$ core level spectra.

From Figure 5.9, inter-elemental bonding peaks can be clearly observed in each core level spectrum of sample 4SiN12C, such as C–Si, Si–C, N–C, N=C, Co–Si and Cr_2N bonding, which were not observed in the spectra of the other samples. The development of these additional bonds arise from the interfacial bonding between the SiN_x interlayer and the carbon overlayer, as well as between the SiN_x and media layer. These additional interfacial bonds are beneficial in increasing the adhesion between the carbon overlayer and the media, and in doing so, help to improve the wear resistance of the overcoat on media.

To probe deeper into the microstructure of the carbon-containing overcoats, visible and UV Raman measurements were performed using laser wavelengths of 488 nm and 325 nm respectively. The visible and UV Raman spectra for samples CM, 12C, 16C and 4SiN12C are presented in Figures 5.10(a)–(d) and Figures 5.10(e)–(h) respectively, with the D and G peak positions indicated on each spectrum.

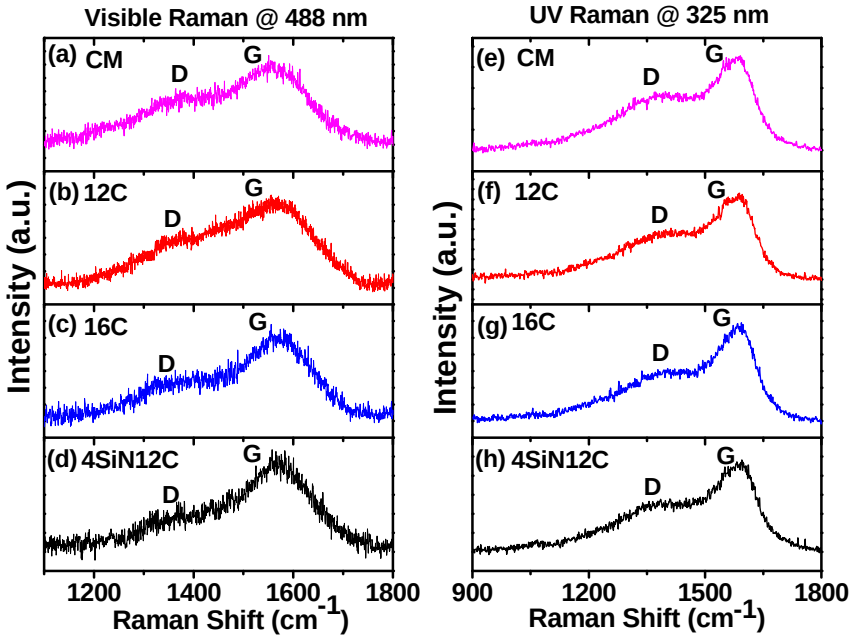

Figure 5.10 (a)–(d) Visible Raman spectra and (e)–(h) UV Raman spectra of samples CM, 12C, 16C and 4SiN12C.

After performing appropriate fitting of the D and G peaks, the G peak position and the I_D/I_G ratios were extracted. Under UV excitation, the G peak position can provide information about the sp^2C and sp^3C bonding. With reference to the three-stage model by Ferrari and Robertson, a shift in the G peak position towards higher wavenumbers in stage 3 suggests an increasing sp^3C bonding fraction within the carbon layer [86]. From the fitted spectra, the G peak positions for samples CM, 12C, 16C and 4SiN12C were found to be at wavenumbers of 1582 cm^{-1}, 1582 cm^{-1}, 1586 cm^{-1} and 1588 cm^{-1}, respectively. This suggested that the sp^3C content increased from samples CM ~ 12C < 16C < 4SiN12C, which agreed well with the results obtained by XPS. Under visible excitation, the nature of sp^2C clustering can be derived from the I_D/I_G ratios, whereby a higher I_D/I_G ratio would suggest an increase in sp^2C cluster size [161]. The I_D/I_G ratios of samples CM, 12C, 16C and 4SiN12C were

found to be 0.6, 0.7, 0.5 and 0.4, respectively, thus the degree of sp^2C clustering can be seen to be decreasing from 12C > CM > 16C > 4SiN12C.

As seen from the trend, the reduction of FCVA carbon layer thickness from 16C to 12C led to a decrease in the sp^3C content and an increase in the sp^2C clustering. Hence, it should be expected that for 12 Å of carbon layer thickness sample 4SiN12C, the sp^3C content and sp^2C clustering should be about the same as that of sample 12C. However, the introduction of the SiN_x interlayer instead helped to enhance the sp^3C bonding with the overcoat. The reason for this observation is because the media contained Co and Pt – metals which can act as catalysts in the transformation of $sp^3C \rightarrow sp^2C$, leading to an increase in the sp^2C bonding at the metal-carbon interface [162–166]. Hence, since the monolithic FCVA carbon overcoats in samples 12C and 16C were directly deposited onto the media surface, and due to the thinness of the overcoats, the sp^2C content at the media-carbon interface, which constituted a significant portion of the overcoat, was greatly increased. On the other hand, the SiN_x interlayer acted as a barrier layer preventing direct interaction of the carbon layer with the media, hence preventing/reducing this catalytic sp^2C transformation in sample 4SiN12C. Secondly, the introduction of the SiN_x interlayer promoted the formation of extensive interfacial bonding as observed by XPS, creating an atomically-thin composite interfacial layer at the media-overcoat interface. Due to the increased bonding taking place between the Co and Pt atoms in the media with the Si and N atoms in SiN_x, this reduces the catalytic activity of Co and Pt to some extent, which results in a lower sp^2C content. Thirdly, the presence of Si from the SiN_x interlayer could have

promoted the formation of higher sp^3 bonding with carbon, since Si is only able to bond in the sp^3 hybridization. This could have contributed to the reduction in the sp^2C cluster size as observed from the lower I_D/I_G ratio for sample 4SiN12C [86].

In summary, the higher sp^3C content and improved interfacial bonding obtained from the SiN_x/C bi-layer overcoat design contributed in providing a low and stable COF, better wear performance as well as improved corrosion/oxidation protection of the magnetic media. This was confirmed by ball-on-disk tribological tests and electrochemical corrosion measurements.

5.6 Conclusions

In this work, the efficacy of an atomically-thin 4 Å interlayer of SiN_x in a novel SiN_x/C bi-layer overcoat for commercial hard disk media was revealed and highlighted. The overcoat was found to exhibit desirable corrosion and tribological performance at a thickness of just 16 Å, without degrading the magnetic properties. The presence of this atomically-thin SiN_x layer was crucial in enhancing the bonding environment and microstructure of the overcoat. The SiN_x interlayer promoted the formation of extensive interfacial bonding at the SiN_x-carbon and SiN_x-media interfaces and contributed in reducing the direct interaction of carbon with media, hence improving the interfacial adhesion and at the same time reducing the undesirable catalytic $sp^3 \rightarrow sp^2$ transformation of carbon in the overlayer. As a consequence, the tribological properties, wear resistance and corrosion/oxidation resistance were much improved as compared to the

monolithic carbon overcoats. It was also shown that because of the ease of oxidation of SiN_x in the ambient atmosphere, monolithic SiN_x cannot perform well as a wear durable overcoat on its own. Hence, this work highlights the necessity and importance of the SiN_x/C bi-layer structure which enabled the combination of the desirable protective characteristics of both materials in one overcoat.

Chapter 6: Wear-durable protective overcoats for functional tape heads

6.1 Introduction

As highlighted in Section 1.3.4.1, PTR in the tape head is one of the major challenges faced in magnetic tape recording, which causes an increase in the magnetic spacing. In addition, tribo-electrochemical reactions can also occur through direct contact between the read/write elements and the tape material, resulting in the formation of metallic deposits [167]. Hence, the application of an ultrathin, wear durable, electrically insulating and chemically inert overcoat on the tape-bearing surface of the head is one possible way to alleviate the issues of PTR and tribo-chemical interactions.

Many researchers have experimented on a variety of overcoats for magnetic tape heads, such as zirconia, chromium oxide, chromium nitride, aluminium oxide and DLC [72, 73, 76, 168–170]. Unfortunately, most of these overcoats either had thicknesses which are too large for the current technology (~ 40–50 nm) [73, 170] or had suffered premature wear and delamination [72, 168, 170]. At such high areal densities, the thickness of the overcoat should be maintained as low as possible while maintaining its high wear durability and other protective characteristics. Recently, Rismani et al. had developed ultrathin (~ 10–11 nm) overcoats on commercial tape heads using the FCVA technique. They adopted the bi-level energy process similar to the one that was used in Section 4.2 for hard disk media, whereby a high energy surface pre-treatment step was performed at 350 eV before the deposition of ta-C layer

at medium energy of 90 eV [120]. Prior to the FCVA bi-level energy process, an interlayer of TiN [171] or Si [172] could be deposited to form an atomically-mixed composite interlayer to improve the wear durability of the overcoats. With these approaches, the improved durabilities of these overcoats were demonstrated on non-functional tape heads for up to 1 million meters of testing with commercial tape media in an ambient relative humidity and temperature environment.

Although these efforts were promising, they were not sufficient in completely evaluating the wear durability of the coated tape heads in a commercial tape drive environment, where the electrical functionality and long-term wear durability are essential for tape drive reliability. For example, while Rismani et al. were able to demonstrate the durability of their ~ 10–11 nm overcoats for up to 1 million meters, the overcoats' wear durabilities were not studied beyond this length, which is far less than its required lifetime [173]. Secondly, the use of electrically conducting interlayers such as TiN could lead to electrical shorting of the read sensors to the shield (conductive bridging) [76]. Previous researchers have shown that the maximum durability of ~ 20 nm thick overcoats were in the range of ~ 3–5 million meters [76, 169]. Therefore, based on these shortcomings, this chapter explores the following approaches in developing future wear-durable tape head overcoats:

1) Developing a facile overcoat fabrication process which can be easily integrated into the current tape head fabrication process;

2) Exploring novel overcoat designs which can potentially significantly enhance the overcoat's durability and at the same time avoid electrical shorting of the read sensors;

3) Demonstrating the high wear durability and electrical functionality of the overcoat in an actual tape drive environment.

SiN_x stands out as a promising candidate for an adhesion interlayer. The advantageous effects of an atomically-thin SiN_x as an adhesion interlayer for 16 Å SiN_x/C bi-layer overcoats had been demonstrated in Chapter 5 to provide effective wear and corrosion protection of commercial hard disk media. Apart from these excellent properties, SiN_x films are also commonly known to possess high electrical resistivity, making them a good candidate as an electrically insulating interlayer material for tape heads. In this chapter, the feasibility of two types of ultrathin bi-layer SiN_x/C overcoats for functional tape heads is investigated – one fabricated totally by a magnetron sputtering process (Section 6.2) and the other with the carbon layer fabricated by the FCVA bi-level energy surface modification process (Section 6.3). Finally, the mechanical and electrical properties of monolithic carbon overcoats and bi-layer SiN_x/C overcoats fabricated by both processes are compared and discussed in terms of their structural-property relationship (Section 6.4).

6.2 A facile approach to develop a SiN_x/C overcoat for functional tape heads

6.2.1 Motivation of this work

In this work, an approach to create a novel ultrathin yet wear-resistant tape head overcoat simply by a facile method of magnetron sputtering is described. This allows the overcoat fabrication step to be easily integrated into the existing head fabrication process and adopted by the tape drive manufacturing industry. The overcoat used in this work is a bi-layer structure comprising a ~ 3 nm interlayer of Si/SiN_x deposited by RF sputtering, followed by a ~ 4 nm overlayer of a-C deposited by pulsed DC sputtering. For the interlayer, an ultrathin layer of ~ 1 nm Si was applied before depositing ~ 2 nm SiN_x to further enhance the adhesion at the AlTiC substrate. Due to the high probability of mixing between the ultrathin Si and SiN_x layers, the Si/SiN_x interlayer will be considered here as a single SiN_x interlayer. Because of the very low amount of layer intermixing that can be obtained from the sputtering process as compared to FCVA, the objective of this work is to create suitable interfaces to achieve enhanced interfacial bonding. The role of these enhanced interfaces and interfacial bonding on the wear resistance properties of the ~ 7 nm bi-layer overcoat will be assessed in relation to its tribological properties and its wear durability on a non-functional tape head. Finally, the performance of this overcoat on a functional tape head in a simulated tape drive environment will be evaluated for the first time.

6.2.2 Experimental methodology

The depositions of all the overcoats used in this work were performed *in-situ* in an in-house sputter deposition tool (AJA International, USA) with a background pressure in the range of ~ 10^{-9} Torr. Figures 6.1(a)–(d) show the schematic of the deposition process for the SiN_x/C bi-layer overcoat on a tape head. In addition, for the purpose of other overcoat characterizations, flat Si substrates and flat AlTiC substrates were also included in the same batch. Prior to the overcoat deposition, the substrates were temporarily exposed to Ar plasma for substrate cleaning, as shown in Figure 6.1(b), by applying an RF substrate bias. Subsequently, the 1 nm Si adhesion layer and 2 nm SiN_x layer were deposited by RF sputtering of Si and Si_3N_4 targets respectively, as depicted in Figure 6.1(c). Finally, the 4 nm a-C layer was deposited by pulsed DC sputtering (Advanced Energy Industries Inc., USA) at a frequency of 150 kHz and duty cycle of 0.4, as illustrated in Figure 6.1(d). All the layers were deposited in an Ar atmosphere at a working pressure of 3 mTorr and a flow rate of 20 sccm.

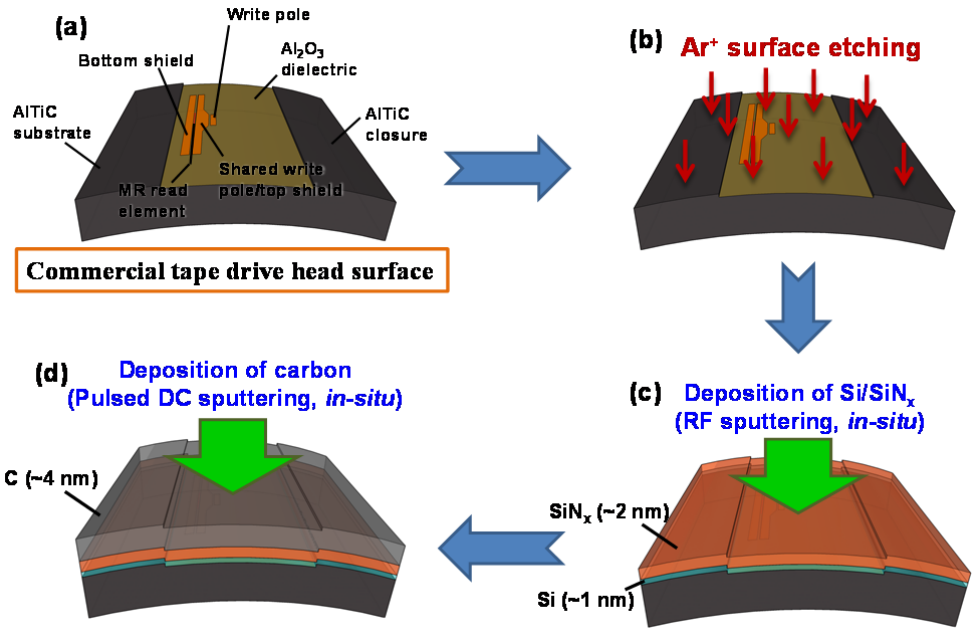

Figure 6.1 Schematic illustration of the bi-layer overcoat deposition process. (a) Overview of the commercial tape drive head surface before surface modification, (b) Ar^+ plasma surface cleaning of the head, (c) deposition of the Si and SiN_x adhesion interlayers, and (d) deposition of the a-C overlayer.

A monolithic overcoat of Si/SiN_x and a monolithic overcoat of a-C were also fabricated with intended similar overall thicknesses, in order to reveal the efficacy of the SiN_x/a-C bi-layer design. The monolithic Si/SiN_x overcoat was fabricated by RF sputtering on Ar^+ cleaned flat substrates to obtain the desired thicknesses of ~ 1 nm for Si and ~ 6 nm for the SiN_x overcoat. The monolithic a-C overcoat was grown by pulsed DC sputtering on the Ar^+ cleaned flat substrates to achieve a desired overall thickness of ~ 7 nm. In total, three types of overcoats will be compared. Table 6.1 summarizes the structures of the three overcoats used in this work, their desired and actual overcoat thicknesses as well as their respective sample nomenclatures which will be used hereon in this section.

Table 6.1 Structures, nomenclature and overcoat thickness of the three overcoats used in this work.

Sample Nomenclature	Sample Structure	Intended Overall Thickness	Actual Thickness Measured by HRTEM
SiN3/C4	Substrate/Si (1 nm)/SiN_x (2 nm)/a-C (4 nm)	7 nm	7.0 ± 0.3 nm
SiN7	Substrate/Si (1 nm)/SiN_x (6 nm)	7 nm	8.0 ± 0.3 nm
C7	Substrate/a-C (7 nm)	7 nm	6.5 ± 0.3 nm

All of the three overcoats were first characterized by HRTEM to measure their actual thicknesses. Figures 6.2(a)–(c) present the cross-sectional HRTEM images for samples SiN7, C7 and SiN3/C4 respectively. Although SiN7 had a slightly higher thickness of ~ 8.0 nm and C7 had a slightly lower thickness of ~ 6.5 nm, nevertheless the thicknesses measured were close and comparable to the desired values of ~ 7 nm. Next, ball-on-disk tribological tests were performed to evaluate their tribological properties and relative wear resistance by observing their variation of COF throughout the test duration, as well as the optical images of the wear track region and counterface ball after the test. Following that, the monolithic C7 and SiN3/C4 bi-layer overcoats deposited on the non-functional tape head were subjected to head-tape wear testing for up to 1 million meters with commercial Linear Tape Open Generation 6 (LTO-6) BaFe tape. The wear durabilities of the overcoats after the tests were compared with the performance of an uncoated tape head by means of AFM surface profiling and AES surface elemental mapping. Subsequently, UV Raman spectroscopy and XPS were performed for the carbon-containing overcoats of SiN3/C4 and C7 only to investigate their carbon overcoat microstructure and interfacial bonding, respectively. Last but

not least, the procedure for applying the SiN3/C4 overcoat on a functional tape head is described and the functional performance of the SiN3/C4 coated functional tape head in a simulated tape drive environment, conducted with the help of an industrial collaborator, is reported.

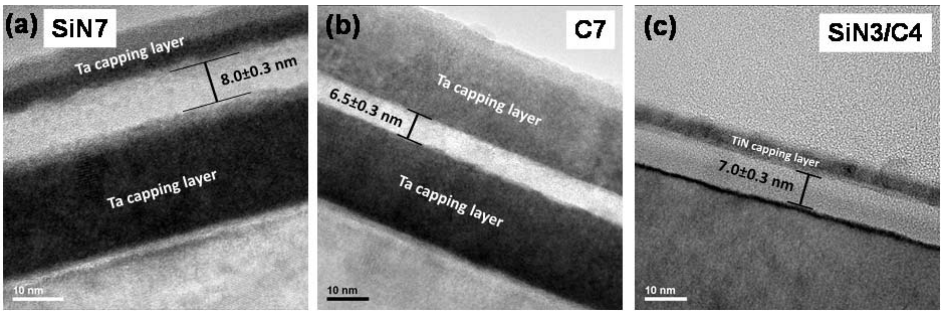

Figure 6.2 Cross-sectional HRTEM images showing the measured overcoat thicknesses of (a) SiN7, (b) C7, and (c) SiN3/C4.

6.2.3 Tribological properties

The SiN7, C7 and SiN3/C4 overcoats which were deposited on flat AlTiC substrates were subjected to ball-on-disk tribological tests for up to 10,000 cycles. The plots of COF versus number of cycles for the three overcoats are shown in Figure 6.3(a). As a reference, the COF plot of an uncoated AlTiC substrate subjected to the same Ar^+ plasma etching process was also recorded and presented on the same graph. Optical micrographs of the counterface ball and the wear track region on the sample were also captured after the tribological tests and are presented in Figure 6.3(b).

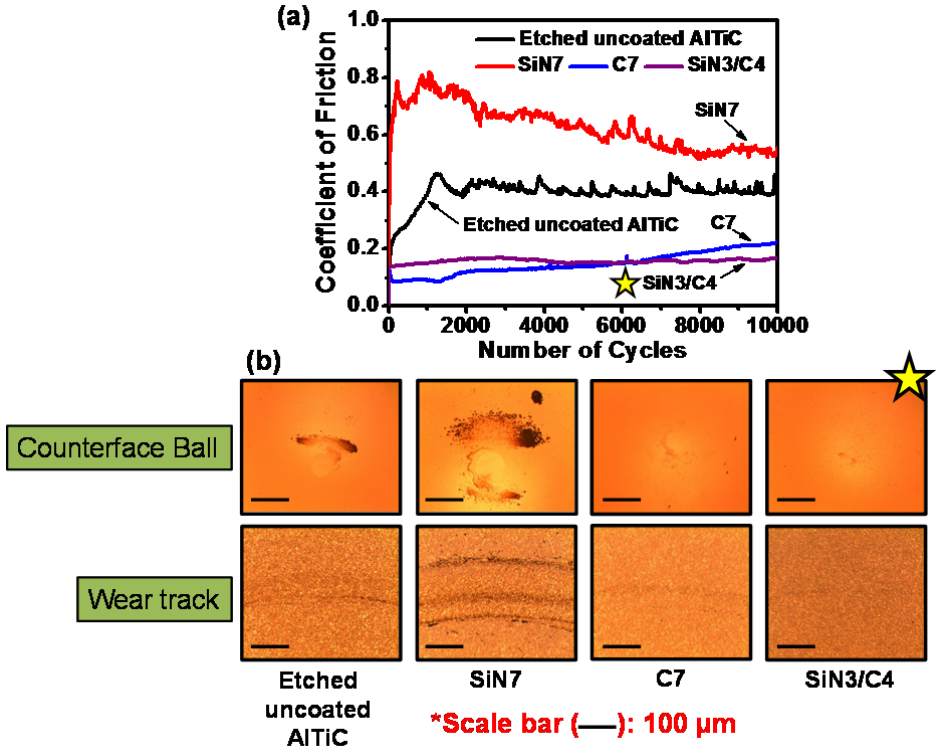

Figure 6.3 (a) Plots of COF versus number of cycles measured during the ball-on-disk tribological tests, and (b) optical micrographs of the sample wear track regions and counterface balls after the tribological tests for samples SiN7, C7, SiN3/C4 and an etched uncoated AlTiC substrate.

When studying the tribological performance of the etched uncoated AlTiC substrate, its COF saw fluctuations in the range of 0.4–0.45 until completion of the test. The optical micrographs showed some material transfer to the ball and a visible wear track could be seen on the substrate. In comparison, the tribological performance of the 8.0 nm SiN7 overcoat on AlTiC was found to be worse, exhibiting a higher fluctuating COF in the range of 0.6–0.8 until test completion. A severe wear track and considerably higher amount of material transfer to the ball were observed for SiN7 as compared to the uncoated AlTiC, revealing the poor wear resistance of the Si/SiN_x overcoat. A similar poor tribological performance was also observed for the monolithic 16 Å SiN_x overcoat on a commercial hard disk media substrate in Chapter 5. Rismani et al. had also observed a similar behavior for a ~ 10 nm

SiN_x overcoat on AlTiC [155]. Thus, it can be seen that monolithic Si/SiN_x showed poor wear resistance as an overcoat, which can be attributed to the oxidation of the SiN_x surface upon exposure to ambient air [174].

When considering the tribological performances of the carbon-containing overcoats, sample C7 displayed a COF of ~ 0.1 for the initial ~ 1250 cycles, beyond which the COF saw a gradual increase until a maximum of ~ 0.22 upon test completion. The optical micrographs of sample C7 after the test also showed significantly less material transfer to the ball with a minor wear track observed on the sample. Interestingly, sample SiN3/C4 containing the bi-layer overcoat showed a low and stable COF of ~ 0.14 until the end of the test, with negligible material transfer to the ball and a barely visible wear track. These results corroborate with the findings obtained in Chapter 5 for the 16 Å monolithic and bi-layer ultrathin overcoats on hard disk media, indicating that although Si/SiN_x on its own does not exhibit good wear resistance, it is able to improve the wear resistance of the carbon overlayer when it is used as an interlayer. These results highlight the efficacy of the bi-layer overcoat in providing high wear resistance with low friction.

It should be noted that although the C7 and SiN3/C4 overcoats on flat AlTiC substrates both showed excellent tribological performance in the ball-on-disk tests, the scenario would be totally different in an operational tape drive given its aggressive wear environment. Since the SiN7 overcoat on the flat AlTiC substrate exhibited poor tribological performance in the ball-on-disk test, the subsequent stages of overcoat testing focused on comparing only the carbon-containing monolithic C7 and bi-layer SiN3/C4 overcoats.

6.2.4 2D surface profiles before and after tape testing

Before conducting any head-tape wear tests, the 2D surface profiles of the SiN3/C4 and C7 coated tape heads were mapped by AFM to determine their surface topographies. In addition, the surface topography of a commercial unetched and uncoated tape head was also mapped by AFM as a reference sample. The 2D surface profiles of these three tape heads are shown in Figures 6.4(a), 6.4(c) and 6.4(e). Furthermore, 1D line scans were also taken across the read and write poles, extending from the AlTiC substrate to the closure, to plot the variation of surface height across the AlTiC surface, read/write element and Al_2O_3 dielectric. The locations of the line scans are indicated by the bold black lines on the 2D surface profiles and are shown below the respective 2D profile images. In each line scan, a dashed red line is drawn according the contour of the AlTiC tape-bearing surface to aid in visualizing the position of the tape media on the head, for the purpose of estimating the PTR. The line scans are also divided into numbered sections to demarcate the different parts of the head along the line scan, which are defined in the caption of Figure 6.4. Subsequently, the two coated tape heads and the commercial uncoated tape head were tested against commercial LTO-6 BaFe tape for 1 million meters in the tape/head interface tester. After the wear tests, the heads were removed and once again imaged by AFM. The 2D profiles and line scans for the three heads after 1 million meters tape wear were mapped again to investigate the changes in the head surface topography, and are presented in Figures 6.4(b), 6.4(d) and 6.4(f).

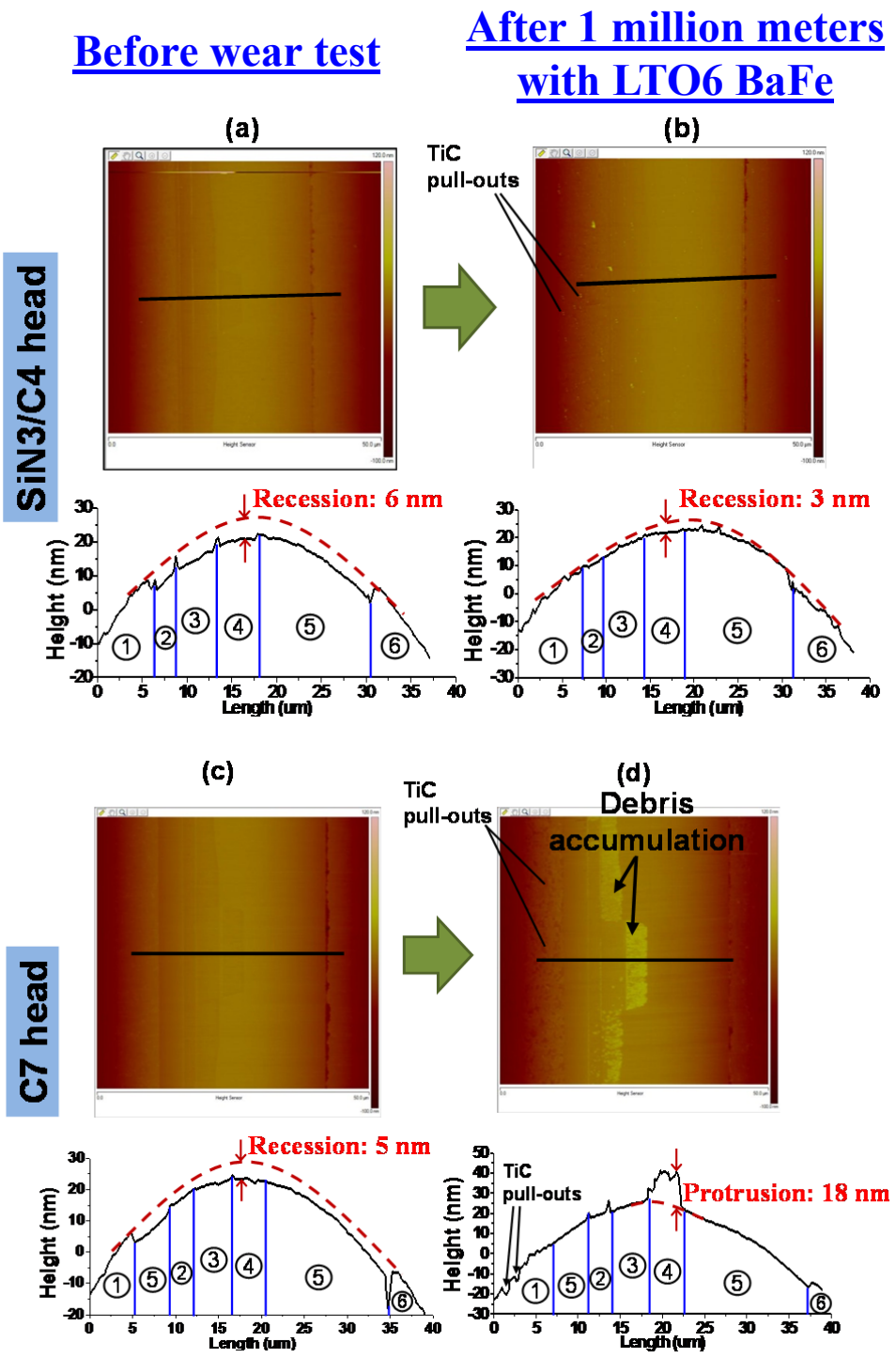
Before wear test
After 1 million meters with LTO6 BaFe
SiN3/C4 head
(a)
(b)
TiC pull-outs
Recession: 6 nm
Recession: 3 nm
Height (nm)
Length (um)
C7 head
(c)
(d)
TiC pull-outs
Debris accumulation
Recession: 5 nm
Protrusion: 18 nm

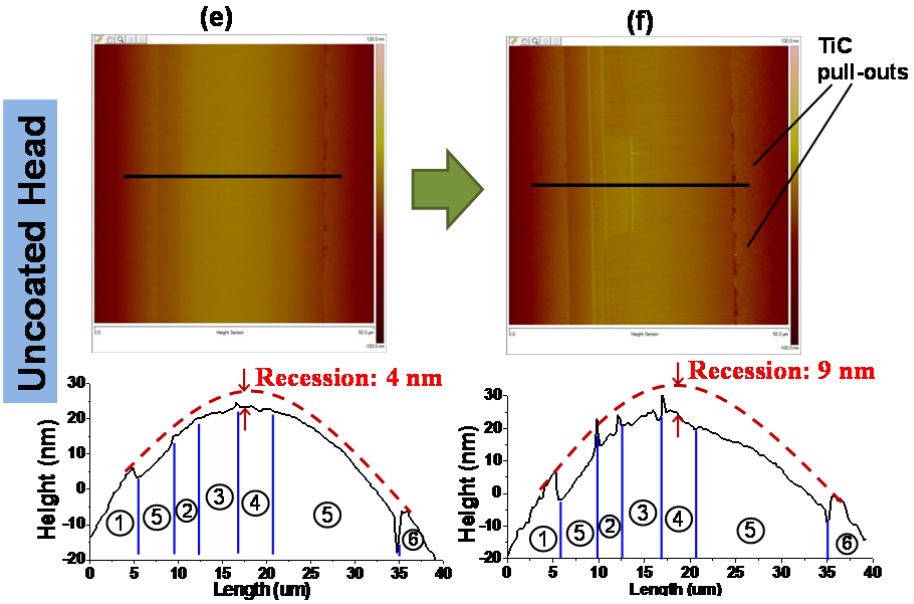

Figure 6.4 AFM 2D surface topography profiles and 1D line scans for the (a)–(b) SiN3/C4 tape head, (c)–(d) C7 tape head, and (e)–(f) commercial uncoated head, before and after 1 million meters of tape testing with LTO-6 BaFe tape. The bold black lines on the 2D profiles indicate the locations where the 1D line scans were taken. For easy reference, line scans are divided into numbered sections corresponding to: 1) AlTiC substrate, 2) bottom shield, 3) shared top shield/write pole, 4) write pole, 5) Al_2O_3 dielectric, and 6) AlTiC closure.

Based on the surface profiles and line scans of the three heads before the tape tests in Figures 6.4(a), 6.4(c) and 6.4(e), the surfaces can be seen to be smooth and particle-free. It should be noted that a slight recession (darker contrast) at the shields and write pole regions can be observed in the profiles of the SiN3/C4 and C7 coated tape heads. This is attributed to the Ar^+ cleaning process before sputter deposition of the overcoat, which caused slightly more etching of the softer magnetic shield and pole material as compared to the harder Al_2O_3 dielectric and AlTiC regions. From the line scans, the recessions in the SiN3/C4, C7 and uncoated tape heads were estimated to be 6, 5 and 4 nm respectively. After the 1 million meter tape tests, the surface topography of the SiN3/C4 coated tape head remained relatively smooth over the Al_2O_3 dielectric and read/write elements, with minimal sign of debris on the surface,

as seen in Figure 6.4(b). Furthermore, the recession had decreased from ~ 6 nm before the tape test to ~ 3 nm after the 1 million meter tape test. In contrast, as observed in Figure 6.4(d), the C7 coated tape head contained a significantly large amount of debris which was collected at the shield and pole regions of the read/write element. From the line scan, the accumulated height of the debris was estimated to be up to 18 nm. Debris accumulation in the read/write element region is detrimental as it would increase the magnetic spacing, resulting in a poor SNR. Additionally, very small recessed regions can be observed at the AlTiC substrate and closure regions near the Al_2O_3 dielectric for the C7 tape head. It is well understood that these recessions are the result of TiC grains being pulled out from the tape-bearing surface when it is exposed to the running tape [74, 175]. With the evidence of pull-outs from the AlTiC, this indicates that the overcoat at these regions had been completely removed after 1 million meters of tape test. For the uncoated commercial tape head, the recession was seen to have increased from ~ 4 nm to ~ 9 nm. Surprisingly, however, the surface of the uncoated commercial tape head was still free of debris even after 1 million meters of tape test. Additionally, though not as severe as the C7 coated tape head, some surface TiC pull-outs could be observed at the AlTiC regions just next to the Al_2O_3 dielectric for the uncoated commercial tape head and the SiN3/C4 coated tape head, leading to some roughening in these regions as observed in the line scans. This suggests that the AlTiC regions near the Al_2O_3 dielectric and read/write elements are highly susceptible to tape wear, which was confirmed by AES surface elemental mapping (to be discussed in the next section).

6.2.5 Surface elemental composition after tape testing

Further analyses on the SiN3/C4 and C7 coated tape heads after the tape tests were conducted by AES to understand and compare their surface elemental compositions. Particularly, the surface maps of carbon and oxygen for the two heads were obtained. In addition, a point scan was performed at a location above the element for both tape heads to obtain the AES spectrum at that point, presented in a first derivative plot with respect to KE. Figures 6.5(a) and 6.5(b) show the AES C and O surface maps for the SiN3/C4 and C7 tape heads respectively after the tape test. A scanning electron microscope (SEM) image of the scanned areas is also provided for both analyzed heads and presented in each figure.

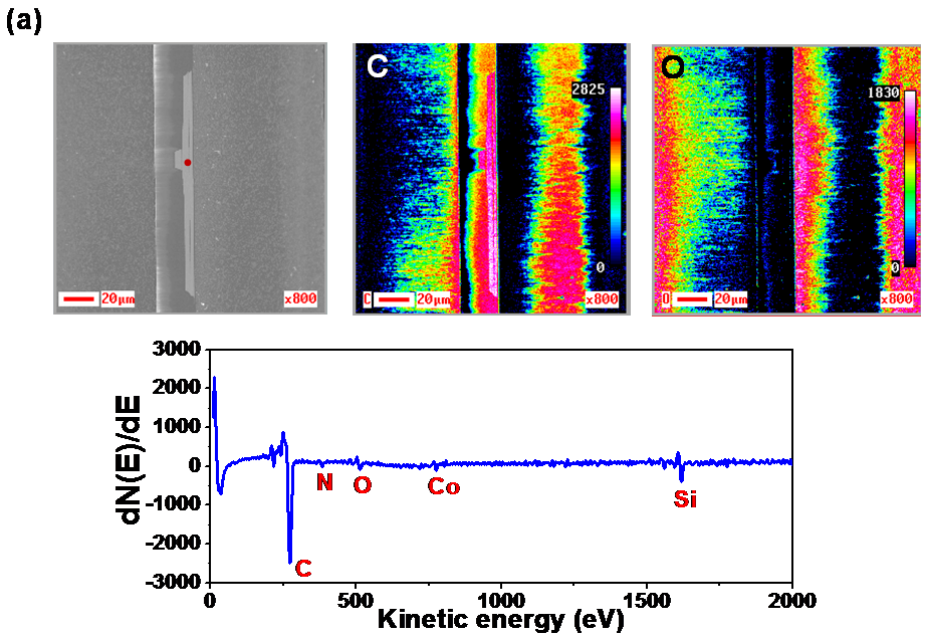

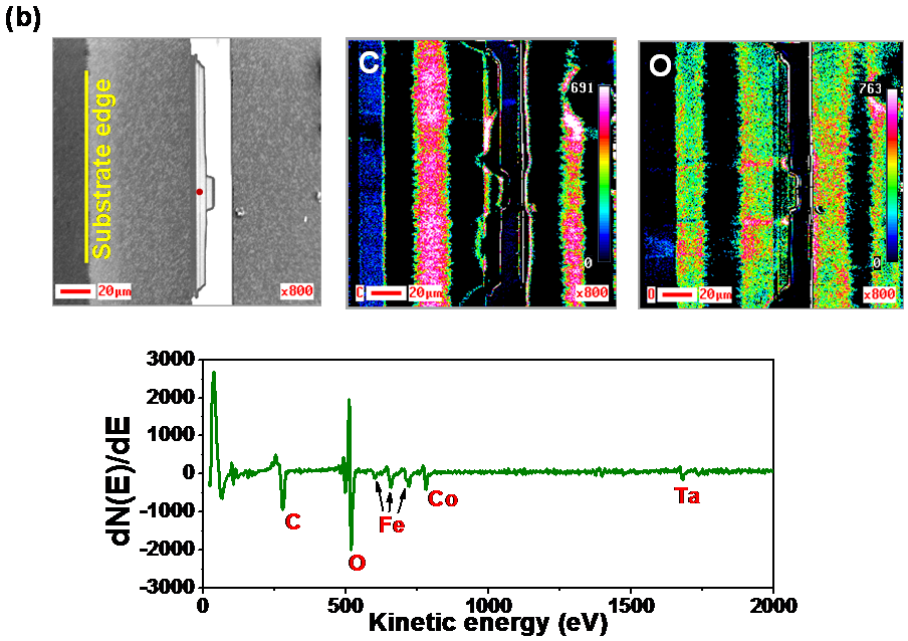

Figure 6.5 SEM image and AES surface elemental maps of C and O for the (a) SiN3/C4 tape head and (b) C7 tape head after 1 million meters of tape test with LTO-6 BaFe tape. The substrate edge of the C7 tape head is indicated with a yellow line in the SEM image. AES point scan spectra were taken at the point on the read/write element as indicated by the red dot in the respective SEM images. The spot size for the AES point scan was 5 µm.

For each elemental map, the hot colors (such as red and white) represent a higher intensity of the element in that region, whereas the cool colors (such as blue) represent a lower intensity of the element, as depicted by the color bar. It can be clearly seen in Figure 6.5(a) that for the SiN3/C4 tape head, there is a high intensity of C still covering the area of the element, parts of the surrounding Al_2O_3 dielectric, as well as on most parts of the AlTiC substrate and closure regions. It is interesting to find that a very high C intensity (and correspondingly low O intensity) was present over the element poles and shields. This shows that a relatively thick layer of carbon was still protecting the element and not much wear of the overcoat had occurred in this area. This finding was also supported by the AES point scan spectrum which showed the presence of a large C peak and presence of Si (from the SiN_x

interlayer). However, it is evident that some wear of the carbon in the SiN3/C4 bi-layer overcoat occurred at the substrate skiving edges as well as at the substrate edge nearest to the element. This result corroborated with the observation in its AFM 2D surface profile. The higher wear rate of the overcoat in these regions is likely due to the higher contact pressures experienced at these regions of the AlTiC tape-bearing surface, especially at the skiving edges [176]. Moreover, it should be pointed out that the O intensity gradually increases from the central regions of the AlTiC substrate and closure towards the edges. The gradual increase in O intensity (gradual decrease in C intensity) shows that the wear process for the bi-layer SiN3/C4 overcoat is a gradual wear process and not a delamination process where the intensity gradient would be abrupt. The presence of O can be attributed to the oxidation of SiN_x. Therefore, where the intensity of C decreased, the carbon in the bi-layer was removed, exposing the underlying SiN_x which became oxidized in the ambient. Hence, this resulted in a higher intensity of O. These results show that the SiN_x interlayer helps to enhance the adhesion of the bi-layer overcoat and prevent overcoat delamination.

On the other hand, the C elemental map of the C7 tape head in Figure 6.5(b) shows a low intensity over most of the area, except at the central portions of the AlTiC substrate and closure regions. Hence it can be seen that the COC had been mostly removed, especially over the read/write element region. Correspondingly, a high intensity of O was observed in this area. Nevertheless, there was some C content detected at the gaps between the shields of the element. With reference to its AFM 2D surface profile and the AES point scan on the read/write element, the presence of C here can be

attributed to the worn COC material or tape debris accumulated at the gaps. On further analysis of the AES point scan spectrum on the element region in Figure 6.5(b), the debris was found to consist of the elements O, Fe, C, Co and Ta. This reveals that the debris contained material mainly from the BaFe tape (Fe, C), COC (C), as well as from the element itself (Co, Ta). Finally, the SEM images also provide some information on the absence or presence of the carbon layer in the C7 and SiN3/C4 tape heads. The Al_2O_3 dielectric region of the C7 tape head showed a much brighter SEM image contrast as compared to the Al_2O_3 region of the SiN3/C4 tape head. The bright contrast in SEM appears due to electron charging of the surface when there is no conductive path for the electrons to be conducted away. Since carbon is relatively conductive, the presence of carbon would be able to reduce the charging effect on the head surface. However, with the absence of the COC on the Al_2O_3 region of the C7 tape head, electron charging occurred on the insulating Al_2O_3 material. In comparison, the electron charging effect was minor on the Al_2O_3 region of the SiN3/C4 head, only occurring in areas where the carbon layer had been worn off, which corresponded well with its AES elemental map.

In summary, based on the AFM and AES results, it can be concluded that out of the three tape heads tested, the SiN3/C4 overcoat demonstrated the best performance in terms of wear protection of the head, with the carbon layer still clearly present on the read/write element after 1 million meters of tape test. Conversely, the C7 overcoat showed the worst performance with the highest magnetic spacing, as a result of debris accumulation on the read/write element.

6.2.6 Microstructure of the carbon layer

UV Raman (325 nm) spectroscopy measurements were performed to probe the microstructure of the carbon overcoat in the monolithic carbon and bi-layer SiN_x/C overcoats on flat AlTiC substrates. The UV Raman spectra of samples C7 and SiN3/C4 are shown in Figures 6.6(a) and 6.6(b) respectively. The characteristic D and G peaks can be clearly identified in the UV Raman spectra of these a-C overcoats. Under UV excitation, the G peak positions in samples C7 and SiN3/C4 were found to be at wavenumbers of 1579 cm^{-1} and 1580 cm^{-1} respectively after performing appropriate fitting of the spectra. As such, the difference in the G peak position in both samples under UV excitation is not very significant, indicating that the carbon microstructure in these two samples should be similar in terms of sp^3C and sp^2C bonding. In addition, the I_D/I_G ratios in samples C7 and SiN3/C4 were calculated and found to be ~ 0.67 and ~ 0.7, respectively. Once again, the difference in the I_D/I_G ratios for both overcoats is insignificant, suggesting that the sp^2C ring-like clustering present in these two overcoats should also be similar.

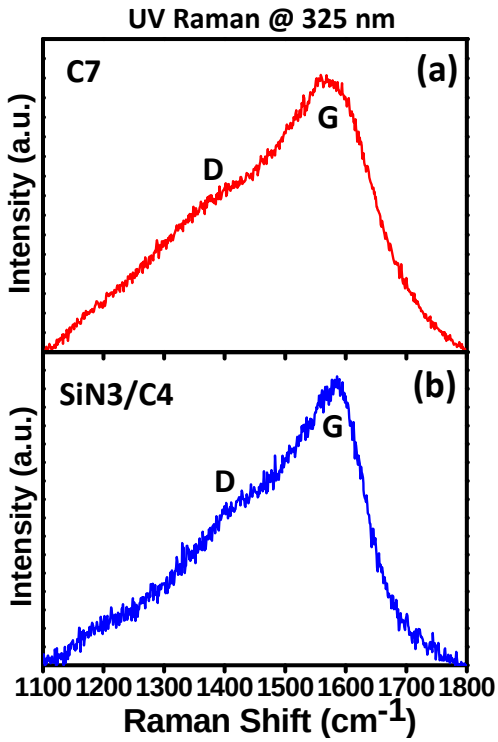

Figure 6.6 (a)–(b) UV Raman spectra of samples C7 and SiN3/C4 respectively, recorded at excitation wavelength of 325 nm.

6.2.7 Probing the interfacial bonding by depth profiling

Depth profiling can be performed on the overcoat to analyze the elemental composition and chemical bonding at different depths of the overcoat thickness. Probing the variation of elemental composition with respect to depth can be performed by the TOF-SIMS depth profiling technique, whereas probing the chemical bonding with respect to depth can be performed by XPS depth profiling. In this section, in order to understand the mechanisms responsible for the improved wear properties of the SiN3/C4 overcoat, the main interest is to use the TOF-SIMS and XPS depth profiling techniques to approach the depths where the carbon-SiN_x interface and the SiN_x-AlTiC interface could be analyzed in terms of their elemental composition (mixing) and interfacial bonding.

6.2.7.1 Depth profiling by TOF-SIMS

TOF-SIMS depth profiling measurements were performed on the C7 and SiN3/C4 overcoats deposited on flat AlTiC substrates to investigate the variation of composition of the two overcoats with respect to their thickness, as well as to explore the possibility of various types of interfacial bonding through atomic interactions and/or intermixing at the interfaces [163, 177]. Figures 6.7(a) and 6.7(b) show the TOF-SIMS depth profiles for samples C7 and SiN3/C4 respectively, where the detected secondary ion intensity is plotted as a function of etching time. As can be seen in the TOF-SIMS depth profile for the C7 overcoat, the overcoat contains mostly carbon, with the presence of some amount of oxygen due to contamination from the ambient environment. The intensities of Al and TiC, however, were negligible in the overcoat region. After approximately 400 s of sputter etching, the intensity of C started to decrease while the intensities of O, Al and TiC started to increase. This represented the depth where the carbon-AlTiC interface was approached. With longer sputtering time, the intensities of O, C, Al and TiC plateaued showing no variation with respect to sputtering time. The high intensities of Al and TiC indicated that the depth had reached the AlTiC substrate. On the other hand, the TOF-SIMS depth profile of the SiN3/C4 overcoat showed a high intensity of C during the initial seconds of etching. This was followed by an increase in the intensities of Si and N and a gradual reduction in the C intensity as the depth approached the carbon-SiN_x interface. As the etching time increased, the intensities of Si and N reached a maximum as the bulk Si/SiN_x interlayer region was approached. A further increase in the etching time led to a reduction in the intensities of Si and N and an increase in the

intensities of O, Al and TiC as the depth approached the SiN_x-AlTiC interface. As etching time increased beyond this interface, the main signals of O, Al and TiC were observed which were derived from the bulk AlTiC substrate. The thick vertical lines drawn in the depth profiles of samples C7 and SiN3/C4 indicate the locations of the interfacial regions for both samples. Thus it can be clearly seen that sample C7 contains only one interface while sample SiN3/C4 contains two interfaces.

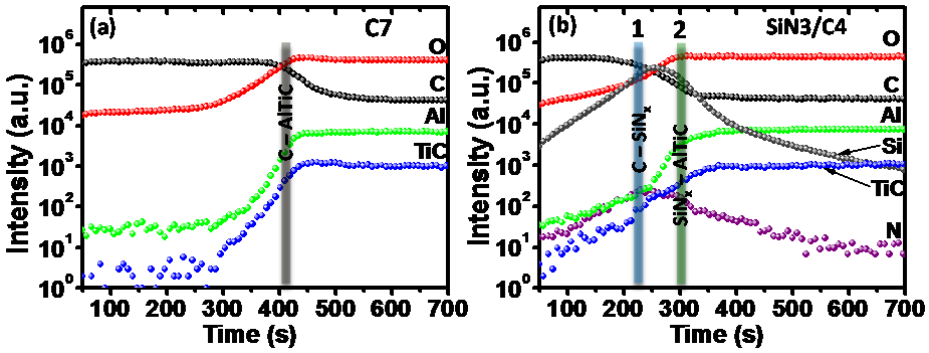

Figure 6.7 TOF-SIMS depth profiles of samples (a) C7 and (b) SiN3/C4. The depth profiles of each element are labeled accordingly. The locations of the interfaces in the two samples are also indicated and labeled by thick vertical lines.

Overall, the TOF-SIMS depth profile analysis for the C7 and SiN3/C4 overcoats revealed that the monolithic C7 overcoat on AlTiC possessed only one carbon-AlTiC interface, whereas the bi-layer SiN3/C4 overcoat on AlTiC resulted in the creation of two interfaces. The increased number of interfaces can lead to more atomic interactions and intermixing of the layers at the interface. This promotes higher interfacial bonding in the bi-layer overcoat than in the monolithic carbon overcoat, which is advantageous for improving the overcoat's wear durability.

6.2.7.2 Depth profiling by XPS

To probe the different types of interfacial bonding present in the SiN3/C4 bi-layer overcoat, its bonding environment was examined by XPS depth profiling. Where applicable, the XPS core level spectra of C 1s, O 1s, Si 2p, N 1s, Al 2p and Ti 2p were recorded based on the presence of the respective peaks at each depth level. The XPS general scan and core level spectra were first recorded for the as-deposited SiN3/C4 sample (0 min etching time). Following that, depth profiling was performed by sputter etching the surface for up to 5 min so as to approach the SiN_x interlayer and probe the interfacial bonding of Si and N with the AlTiC substrate and carbon overlayer. XPS general scans and core level spectra were recorded at 1.5, 3.0 and 5.0 mins etching time to reveal the variation of chemical bonding and composition with depth.

Figure 6.8 shows the general (wide-range) scans of sample SiN3/C4 at 0, 1.5, 3.0 and 5.0 mins of etching time. At 0 min, only the C 1s and O 1s peaks were obvious, but as etching was performed for up to 1.5 min and 3 min, the C 1s, O 1s, Si 2p, N 1s, Al 2p and Ti 2p peaks were all evident in the general scans. However, when the etching time was increased to 5.0 min, the Si 2p and N 1s peaks disappeared, leaving only the C 1s, Al 2p, Ti 2p and O 1s peaks present in the general scan. Thus from the general scans, the transition from the carbon overcoat layer to the SiN_x interlayer and finally to the AlTiC substrate at 5.0 min can be clearly observed.

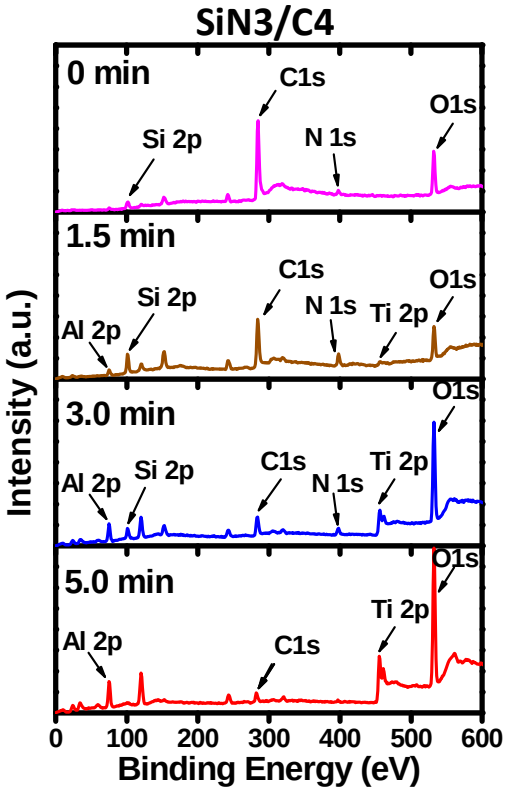

Figure 6.8 General (wide-range) XPS scans of sample SiN3/C4 recorded at etch times of 0, 1.5, 3.0 and 5.0 min. The relevant peaks in the scans are labeled.

Subsequently, careful examination of the various core level spectra at each etch time was performed. The core level spectra of each element obtained at different etch times are plotted together on a combined plot for easy comparison. Figure 6.9(a) shows the combined plot of the C 1s core level spectra of sample SiN3/C4 obtained from 0 to 5.0 min. It can be seen that the intensity of the C 1s peak decreased sharply as the etching time increased from 0 min to 3.0 min. However, the C 1s spectra at 3.0 min and 5.0 min etching times showed similar intensities of carbon, although the shapes of the two spectra are clearly different. The position of the C 1s peak was observed to shift towards lower binding energies as the etching time increased from 0 min to 5.0 min. Through deconvolution of the C 1s spectra to derive its constituent

bonding peaks, the reason for this shift was revealed to be due to the various types of interfacial bonding with carbon, which will be discussed later. For the Si 2p and N 1s core level spectra of sample SiN3/C4 presented in Figures 6.9(b) and 6.9(c) respectively, the intensities of the Si 2p and N 1s peaks increased as the etching time was increased from 0 min to 1.5 min, and then decreased when the etching time was further increased past 1.5 min until the lowest peak intensities were observed at 5.0 min etching times. The highest peak intensities for Si 2p and N 1s obtained at the etching time of 1.5 min can be attributed to the observation of its maximum signals from the SiN_x interlayer region or close to the SiN_x-C interface. The peaks in the Al 2p and Ti 2p spectra in Figures 6.9(d) and 6.9(e) follow a systematic trend as well. Since the depth approached closer to the AlTiC substrate with increasing etching time, the intensities of these peaks were also found to increase steadily with increasing etching time from 0 min to 5.0 min.

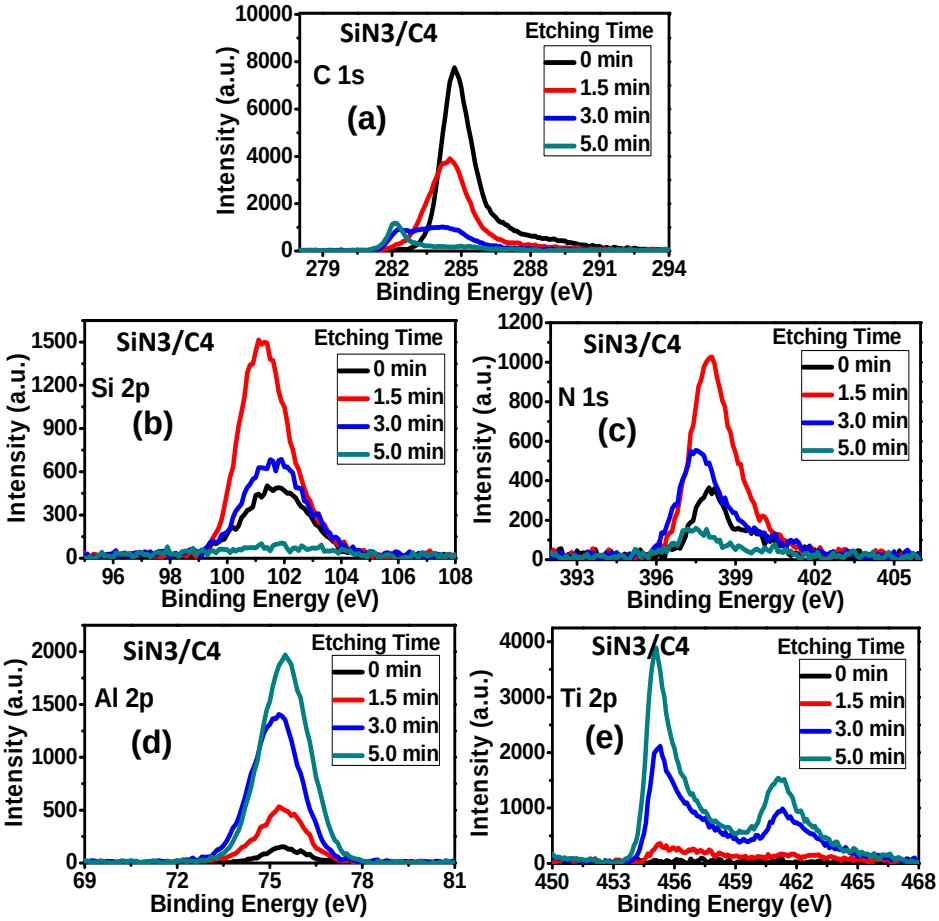

Figure 6.9 Combined plots of XPS core level spectra of sample SiN3/C4 recorded at etching times of 0, 1.5, 3.0 and 5.0 min. (a) C 1s, (b) Si 2p, (c) N 1s, (d) Al 2p, and (e) Ti 2p core level spectra plots.

In order to extensively analyze the bonding environment and the various types of interfacial bonding in sample SiN3/C4, the various core level spectra were deconvoluted with either Gaussian or Gaussian-Lorentzian components after performing Shirley background subtraction. First of all, the bonding environment in the as-deposited carbon layer was analyzed and compared with that of the monolithic COC in sample C7. Figures 6.10(a) and 6.10(b) show the deconvoluted C 1s core level spectra of the as-deposited overcoats of SiN3/C4 and C7 (0 min etch time) for the investigation of carbon bonding and hybridization. The C 1s core level spectra of both samples revealed four constituent peaks corresponding to sp^2C bonding, sp^3C bonding,

C–O bonding, and C=O bonding [138, 152, 178, 179]. By finding the ratio of the areas under the sp^2C and sp^3C peaks, the sp^2C and sp^3C bonding fractions for sample C7 were estimated to be 58.5% and 23.0% respectively, while the sp^2C and sp^3C bonding fractions for sample SiN3/C4 were estimated to be 59.8% and 22.0% respectively. As such, the sp^3C and sp^2C bonding fractions in both samples were almost similar, which corroborate well with the UV and visible Raman results.

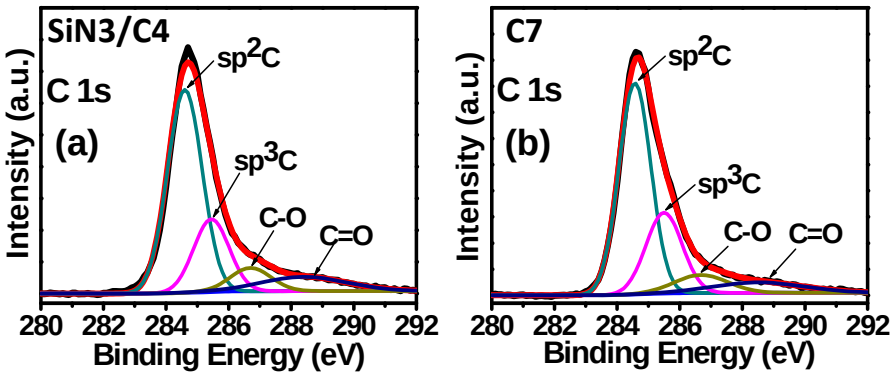

Figure 6.10 Deconvolution of XPS C 1s core level spectra at 0 min etching time for samples (a) SiN3/C4 and (b) C7.

Since it has been established that the microstructures of the carbon layers in samples SiN3/C4 and C7 are almost similar, it is important to understand the role of the interfaces and interfacial bonding in promoting the wear resistance of the bi-layer overcoat. The deconvoluted C 1s core level spectra of sample SiN3/C4 after etching for 1.5, 3.0 and 5.0 min, as presented in Figures 6.11(a)–(c), were analyzed so as to probe the carbon-related bonding at the C-SiN_x interface, SiN_x-AlTiC interface and the bulk AlTiC substrate respectively.

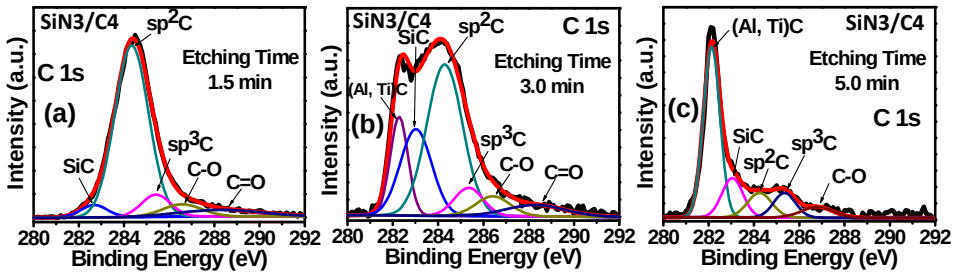

Figure 6.11 (a)–(c) Deconvoluted XPS C 1s core level spectra at 1.5, 3.0 and 5.0 min etching times respectively for sample SiN3/C4.

After an etching time of 1.5 min, where the depth reached the C-SiN_x interface, the C 1s spectrum showed an extra peak of Si–C, in addition to the other characteristic peaks observed in the C 1s spectrum at 0 min etching time (i.e. sp^2C, sp^3C, C–O and C=O peaks). The appearance of the additional Si–C peak was attributed to the interfacial bonding between carbon and silicon at the C-SiN_x interface [159, 179, 180]. When the etching time was increased to 3.0 min to reach the SiN_x-AlTiC interface, two additional peaks attributed to Si–C and (Al, Ti)C were observed, in addition to other characteristic peaks. The (Al, Ti)C peak arises due to the bonding present in the AlTiC substrate [181–183], whereas the generation of the Si–C peak could possibly be due to: 1) bonding of Si with C coming from the underlying AlTiC substrate, 2) bonding of Si with C from the self-diffusion of C from the carbon overlayer into the SiN_x interlayer, or 3) C from the carbon overlayer being embedded into the SiN_x interlayer as a result of knock-on effects from Ar^+ ion etching of the sample during XPS depth profiling. Finally, when the etching time was increased to 5.0 min at a depth within the bulk AlTiC substrate, the (Al, Ti)C peak became the most intense, with small Si–C, sp^2C, sp^3C and C–O peaks detected in the C 1s spectrum. The generation of Si–C here could be attributed to Ar^+ ion etching induced embedment of Si into the AlTiC substrate, such

that the Si atoms can interact with C in the AlTiC and give rise to Si-C bonding. The formation of all these different types of interfacial bonding at various depths, mainly occurring at the C-SiN_x and SiN_x-AlTiC interfaces at 1.5 min and 3.0 min etching times respectively, are advantageous for wear durability of the overcoat.

To further investigate the bonding at the two interfaces, the Si 2p and N 1s core level spectra after 1.5 and 3.0 min of etching time were also examined. Figure 6.12(a) shows the deconvoluted Si 2p core level spectrum after 1.5 min etching time, revealing five constituent peaks corresponding to Si–Si, Si–C, Si–N, Si–O/Si–N–O, and Si=O [159, 160, 172, 180, 184, 185]. Among these peaks, the maximum peak intensity or area under the peak was observed for Si–N bonding arising from the SiN_x layer. Interestingly, the second most intense peak was derived from Si–C bonding, formed as a consequence of interfacial bonding between Si and C which could occur at both the top and bottom interfaces of the SiN_x interlayer. This revealed the enhanced interfacial bonding taking place at the interfaces. The deconvoluted N 1s spectrum after 1.5 min etching time, as presented in Figure 6.12(b), also supports the result of high Si-N bonding as seen in the Si 2p spectrum. A very intense Si-N peak was observed [159, 185, 186], in addition to its less intense peaks of nitrile (C≡N) [187], sp^2C–N [188] and (Al, Ti)N [189, 190]. The nitrile and sp^2C–N peaks revealed the interfacial bonding of C with N, while the minor (Al, Ti)N peaks indicated the interfacial bonding of the substrate elements of Al and Ti with N.

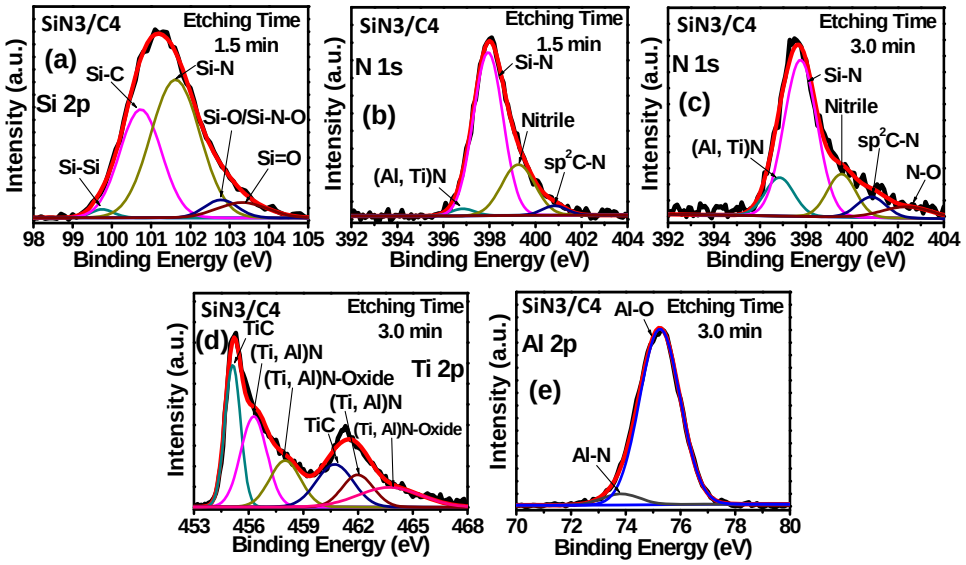

Figure 6.12 Deconvoluted XPS core level spectra of (a) Si 2p after 1.5 min etching time, (b) N 1s after 1.5 min etching time, (c) N 1s after 3.0 min etching time, (d) Ti 2p after 3.0 min etching time, and (e) Al 2p after 3.0 min etching time for sample SiN3/C4.

The deconvoluted spectra of Si 2p and N 1s after 3.0 min etching time showed similar constituent peaks to the spectra obtained after 1.5 min etching time. However, the N 1s core level spectrum showed an additional peak of N–O bonding [159, 187, 191] after 3.0 min etching time, giving a total of five constituent peaks in its spectrum, as shown in Figure 6.12(c). As compared to the N 1s spectrum after 1.5 min etching time, the N 1s spectrum after 3.0 min etching time showed two other changes: 1) an increase in the intensity of the (Al, Ti)N peak, and 2) a slight decrease in the intensity of the Si–N peak. These observations arose due to the depth approaching the bulk AlTiC substrate with increased etching time. Since AlTiC contains a significant amount of oxygen, it is likely that the interfacial bonding between nitrogen from the SiN_x interlayer with O in AlTiC contributed to the N–O bonding.

Last but not least, the deconvoluted Al 2p and Ti 2p core level spectra after 3.0 min of etching time were also extensively analyzed to probe the

interfacial bonding at the SiN_x-AlTiC interface. Figures 6.12(d) and 6.12(e) show the Ti 2p and Al 2p core level spectra respectively after deconvolution. The Ti 2p core level spectrum showed three peaks altogether in both Ti $2p_{3/2}$ and Ti $2p_{1/2}$ doublets, corresponding to Ti–C [192], (Ti, Al)N [193, 194], and (Ti, Al)N–oxide [171, 194]. The appearance of the Ti–C peak is due to the contribution from the AlTiC substrate, while the (Ti, Al)N and (Ti, Al)N–oxide peaks arise due to the interfacial interaction of the substrate elements of Ti, Al and O with nitrogen from the SiN_x interlayer. This is consistent with what was observed in the N 1s core level spectrum recorded after 3.0 min etching time as well. On the other hand, the Al 2p core level spectrum showed a major Al-O peak (such as in Al_2O_3) with a minor Al–N peak due to the interfacial bonding of nitrogen from the SiN_x interlayer with Al in the substrate [195, 196].

Overall, the detailed XPS analysis showed that in both types of overcoats (monolithic C7 and bi-layer SiN3/C4), the microstructures of the carbon layers were similar in terms of sp^3 and sp^2 carbon bonding. However, the advantage of the bi-layer overcoat was that it exhibited more extensive interfacial bonding between the carbon overlayer, Si/SiN_x interlayer and the AlTiC substrate. This is due to the interaction of the elements of the different layers at the interfaces to form strong interfacial bonds (such as Si–C, nitrile, sp^2C–N, (Al, Ti)N, Al–N bonding), in addition to the existence of Si–N bonding within the SiN_x layer. As a result, the wear durability of the SiN3/C4 bi-layer overcoat was significantly improved compared to the monolithic C7 overcoat. This highlights the critical role of enhanced interfaces and interfacial

bonding in improving the wear resistance of the overcoat at thicknesses as low as ~ 7 nm.

6.2.8 Functional performance above 1 million meters

To analyze the functional performance of the SiN_x/a-C overcoat for the first time, the overcoat was deposited onto a commercial working (electrically functional) tape head with its cables still attached. A special arrangement was made in order to deposit the bi-layer overcoat on the tape head, as illustrated in Figure 6.13. The functional tape head was handled carefully with proper electrical grounding ensured throughout the process so as to prevent any electrostatic discharge which may damage the electrical functionality of the head. To protect deposition on the cables, they were carefully arranged in a special substrate holder and then covered with vacuum-compatible aluminum foil, as shown in Figures 6.13(a) and 6.13(b), respectively. The substrate holder holding the functional tape head was placed in the magnetron sputtering chamber and subjected to the overcoat deposition process as described in Section 6.2.2.

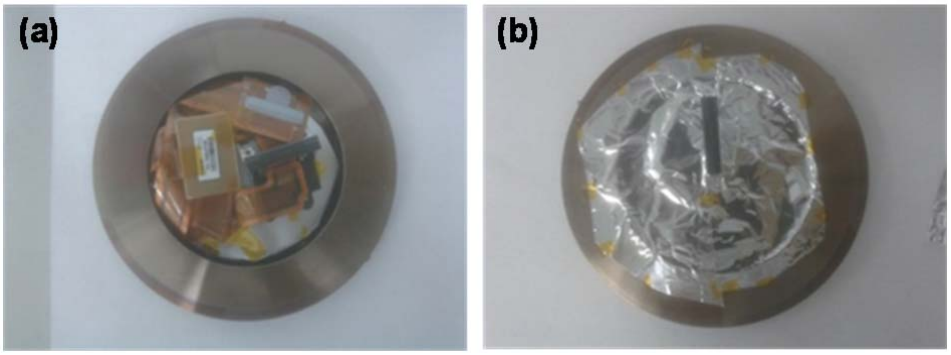

Figure 6.13 Arrangement of the functional tape head for the deposition of the SiN_x/C bi-layer overcoat by magnetron sputtering. (a) Placement of the functional tape head with its cables intact inside the substrate holder, and (b) covering of the cables of the tape head using vacuum-compatible aluminum foil, exposing only the tape-bearing surface of the tape head.

After the coating process was completed, the coated tape head was carefully transferred into a tray and shipped to an industrial collaborator for functional tape testing. A brief description of the functional tape testing procedure is as follows. Before performing the tape test, the coated tape head was first visually inspected under an optical microscope to observe the surface of the overcoat at one particular read/write element of the head and its neighboring AlTiC substrate and closure regions. The coated functional tape head was then first installed in a modified tape drive specially used for qualifying the electrical and mechanical performance of standard tape heads. Commercial tape media was run across the tape head surface while standard industrial testing procedures [197] were used to inspect and qualify the tape head condition at regular intervals by means of visual inspection (optical microscopy) and parametric tests to evaluate its electrical performance as the tape test progressed. Readers are referred to Appendix B for the details of the parametric data measurements used for qualification of electrical performance of the tape head. All the tests were performed in a cleanroom environment with temperature and relative humidity maintained at 22 °C and 50 % respectively. After every five million meters of tape test, the tape was replaced with a fresh cartridge.

The SiN_x/C bi-layer coated tape head was tested for a total length of 12.5 million meters with commercial tape. From the parametric tests, the parameters of broadband signal-to-noise ratio (BBSNR), 2T output and resolution were measured. A combined plot of the BBSNR, 2T output and resolution is presented in Figure 6.14(a) showing their variation with length of the tape test.

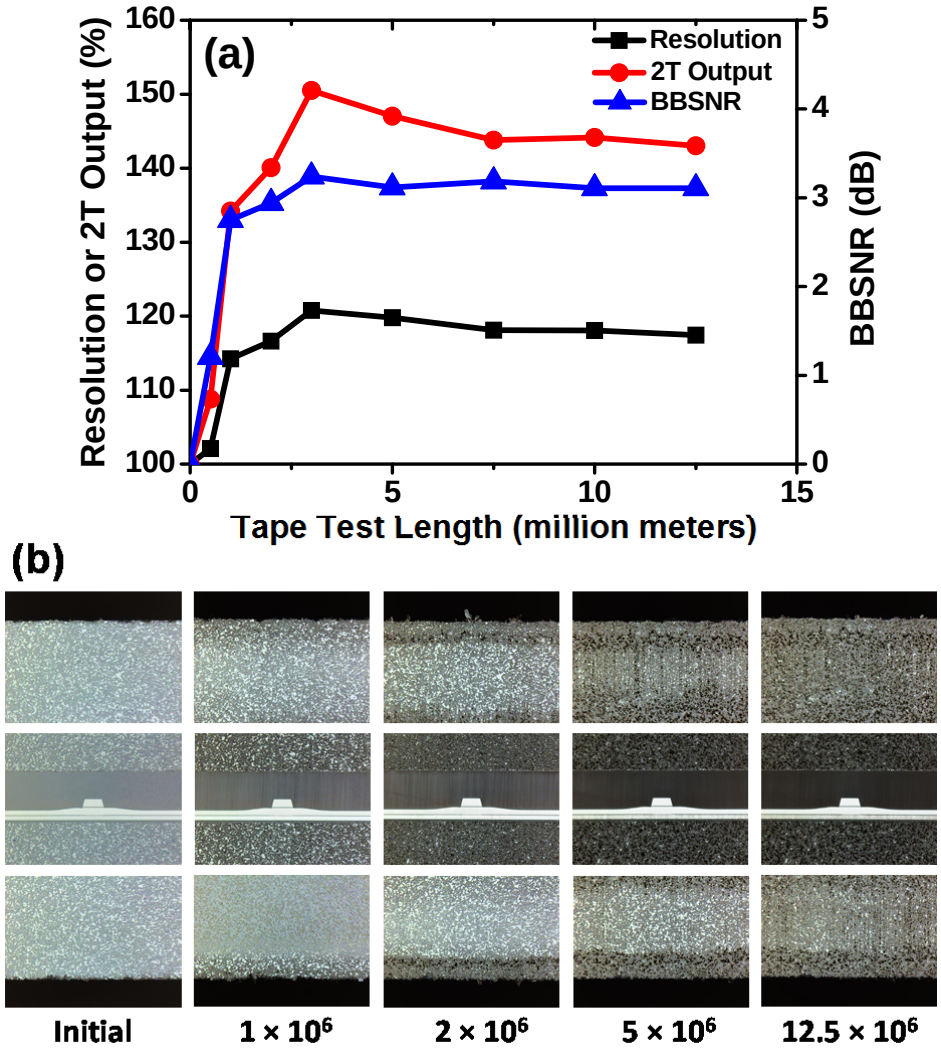

Figure 6.14 (a) Parametric data measurements showing the variation of resolution, 2T output and BBSNR with respect to tape test length. The variations in the signals are based on the change with respect to the signals obtained before the wear test (0 million meters). (b) Optical micrographs of the same read/write element and its adjacent AlTiC substrate and closure regions, captured before the tape test and after 1, 2, 5 and 12.5 million meters of tape testing.

Based on the parametric data, it can first of all be concluded that the bi-layer overcoat fabrication process did not damage the electrical functionality of the tape head, as the readback signals could be easily measured from the coated head. The variations in the signals are based on the change with respect to the signals obtained before the wear test (0 million

meters), i.e. the resolution and 2T output were normalized to 100% at 0 million meters while the BBSNR was normalized to 0 dB at 0 million meters. It was clearly observed that the first 1 million meters of tape testing resulted in the sharpest increase in the values of the three parameters, followed by a more gradual but still considerably large increase from 1 million meters to 3 million meters of tape testing where all the three signals reached their peaks. Subsequently, the signals started to see a small but continuous reduction from 3 million meters of tape testing all the way until 12.5 million meters. At the same time, the optical micrographs of the read/write element taken before the tape test and after 1, 2, 5 and 12.5 million meters of tape testing are presented in Figure 6.14(b). It can be clearly observed that the contrast of the tape head surface gradually became darker from the initial image captured before the start of the tape test. The regions on the tape head with lighter contrast represent the presence of the bi-layer SiN_x/a-C overcoat on the tape head surface, hence where the darker regions started to appear, those regions would signify the removal or absence of the overcoat, which would imply that the overcoat had suffered significant wear or had been worn out in those areas. As can be seen in the images, the onset of overcoat wear (darkening of image contrast) began at 1 million meters, occurring primarily at the skiving edges and the areas nearest to the Al_2O_3 dielectric. Due to the contour of the tape head, these regions experienced the highest contact pressures with tape [67, 198], contributing to their higher wear rates as compared to the other regions of the tape-bearing surface.

With the observation of overcoat wear in the optical images, the increase in the three signal parameters in the parametric measurements can

thus be explained by a reduction in the magnetic spacing due to the increased wear of the overcoat, leading to a reduction in the overcoat thickness. The reduced magnetic spacing in turn contributed to an improvement in the readback signal, according to the Wallace equation [57]. Therefore, a large increase up to 3 million meters of tape testing can be attributed to the continuous and large amount of overcoat wear and removal. After 3 million meters, the degradation of the signals indicated that the magnetic spacing started to increase. Without the presence of the protective overcoat over the magnetic elements, this implied that PTR had started to occur from 3 million meters onwards whereby the magnetic elements started to wear out. This observation was corroborated with the optical images at 5 and 12.5 million meters where the contrast over the Al_2O_3 dielectric region just adjacent to the read/write element was the darkest, indicating the absence of the overcoat in that region. Therefore, from these results, the wear life of the SiN3/C4 overcoat on a functional tape head before it was totally removed can be regarded to be ~ 3 million meters.

6.2.9 Conclusions

This work discussed the effectiveness of a novel ~ 7 nm SiN_x/a-C bi-layer overcoat as a wear durable protective overcoat for tape heads. One of the main advantages of this overcoat design is that it can be fabricated by the magnetron sputtering technique which allows it to be easily integrated into an existing tape head manufacturing process. Its tribological properties and wear performance with tape were compared with a monolithic sputtered a-C overcoat of similar thickness. It was found that while the bi-layer SiN_x/a-C

overcoat showed similar tribological properties to the monolithic a-C overcoat such as low friction and high wear resistance based on the ball-on-disk tribological test, its performance on the coated non-functional tape head with commercial tape after 1 million meters of tape test was improved over the monolithic overcoat in terms of better wear durability and much less debris accumulation on the tape head surface. The enhanced wear durability of the SiN_x/a-C overcoat was attributed to the formation of two enhanced interfaces with the introduction of the SiN_x interlayer, namely the carbon-SiN_x interface and the SiN_x-AlTiC interface, which promoted the formation of extensive interfacial bonding via atomic interactions between the layers at the two interfaces, as elucidated by XPS depth profiling. Finally, the overcoat was applied for the first time on electrically functional tape heads to test its feasibility on actual tape heads. Through functional tape testing in a simulated tape drive environment, it was revealed that not only did the SiN_x/a-C coating process not damage the electrical functionality of the read/write elements at the tape head surface, but the bi-layer overcoat design was also able to protect the tape head for up to 3 million meters of testing with commercial tape. As the wear durability of up to 3 million meters using a 7 nm thick overcoat has not yet been reported in literature, this approach could be used to develop tape drives with higher areal densities.

6.3 Remarkable wear life of a SiN_x/ta-C overcoat on a functional tape head

6.3.1 Motivation of this work

Recent efforts have seen the development of ~ 10 nm thick ta-C based ultrathin overcoats fabricated using the FCVA process for tape heads, through high energy pre-treatments and development of composite interlayers to enhance the adhesion and wear resistance, and hence wear life of the overcoats [120, 171, 172, 199]. However, the tape tests in those works were limited to a total length of only 1 million meters, which is insufficient to evaluate the actual wear life of the overcoat in an actual working tape drive. Furthermore, the overcoats were deposited on non-functional tape heads, inviting questions on the overcoats' applicability and compatibility on functional tape heads, especially when a highly energetic ion deposition process such as FCVA is used.

In this work, a ~ 20 nm thick bi-layer SiN_x/ta-C overcoat was developed, comprising a composite interlayer of amorphous silicon/silicon nitride (Si/SiN_x) pre-treated with high energy C^+ ions at 350 eV, followed by a ta-C layer deposited atop using C^+ ions at medium energy of 90 eV. The aim of this work is to compare the wear durability of this newly designed overcoat with overcoats used in existing literature, as well as to develop overcoats with wear durability suitable for the whole operational lifetime of tape drives. Once again, Si/SiN_x is considered as a single SiN_x interlayer here. The resultant 20 nm bi-layer SiN_x/ta-C overcoat deposited on flat substrates was first subjected to standard tribological tests and characterizations to evaluate its properties.

Subsequently, to address the issue of overcoat compatibility with functional tape heads, the SiN_x/ta-C overcoat was applied on an electrically functional commercial tape head, using a similar procedure as described in Section 6.2.9. The coated functional head was shipped to an industry collaborator for electrical parametric testing to evaluate its functional performance with the overcoat. This was followed by a long-term tape wear test to measure the overcoat durability and variation of its functional performance with continuous tape testing under a simulated tape drive environment.

6.3.2 Experimental methodology

An electrically functional commercial tape head, flat AlTiC substrate samples and flat Si wafer samples were used as starting substrates for deposition of the SiN_x/ta-C bi-layer overcoats in the same deposition run. The installation of the functional tape head was performed according to the procedure as described in Section 6.2.9, after which the flat AlTiC and Si substrates were affixed on top of the aluminum foil cover by Kapton® tape. For this overcoat, the deposition was performed in the following sequence of three stages. The substrates were first placed in the magnetron sputtering chamber and then subjected to Ar plasma cleaning for 3 min to remove any surface contaminants on the substrates before overcoat deposition. In the second stage, a ~ 5 nm thick Si/SiN_x layer was deposited *in situ* onto these substrates by RF magnetron sputtering of Si and Si_3N_4 targets at room temperature to get ~ 1 nm of Si and ~ 4 nm of SiN_x. In the third stage, the Si/SiN_x-coated samples were carefully transferred to an FCVA chamber (Nanofilm Technologies International, Singapore) for high energy C^+ ion pre-

treatment and ta-C layer deposition. Due to surface oxidation of SiN_x upon exposure to the ambient during sample transfer into the FCVA chamber, the top ~ 2 nm surface layer of SiN_x was etched using Ar^+ ions at 500 eV after being transferred into the FCVA tool. This was done before proceeding with *in situ* high energy pre-treatment and ta-C deposition on the etched SiN_x layer at 350 eV and 90 eV respectively. The FCVA process was calibrated to obtain the formation of a mixed layer of SiN_x and carbon of ~ 2–3 nm thickness at 350 eV before the deposition of a ta-C layer of ~ 16–17 nm thickness, to achieve an overall overcoat thickness of ~ 20 nm. The whole FCVA process was performed at room temperature without applying intentional heating. Pulsed substrate biases of -330 V and -70 V were applied to achieve the 350 eV and 90 eV ion energies, respectively. The duty cycle of the pulsed substrate biasing scheme was maintained at 0.6 (60% substrate bias ON and 40% substrate bias OFF), following the same process used by Rismani et al. [120].

After the samples had been fabricated, HRTEM cross-sectional imaging was first performed on the coated flat Si substrate to verify the thickness of the SiN_x/ta-C overcoat. Ball-on-disk tribological testing and AES depth profiling were performed on the flat AlTiC substrates to investigate the tribological performance of the overcoat and probe the variation of the elemental composition with overcoat thickness, respectively. The microstructure of the ta-C layer was examined by UV and visible Raman spectroscopy, and the interfacial bonding was probed using XPS depth profiling. The coated functional tape head was subjected to functional testing with tape according to the functional testing procedure as outlined in Section

6.2.9. Long-term functional tape tests were carried out on the SiN_x/ta-C coated tape heads up to a length of 50 million meters with commercial tape, with the tape being replaced with new tape cartridges every five million meters.

The cross-sectional HRTEM image of the SiN_x/ta-C overcoat on the flat Si substrate is shown in Figure 6.15. The measured thickness of the overcoat was 19.5 ± 0.5 nm, which is close to the expected thickness of 20 nm. However, due to the similar contrast and amorphous structures of Si/SiN_x and ta-C, it is difficult to distinguish between the two layers. Subsequent characterizations by XPS and AES depth profiling verified the presence of the Si/SiN_x layer.

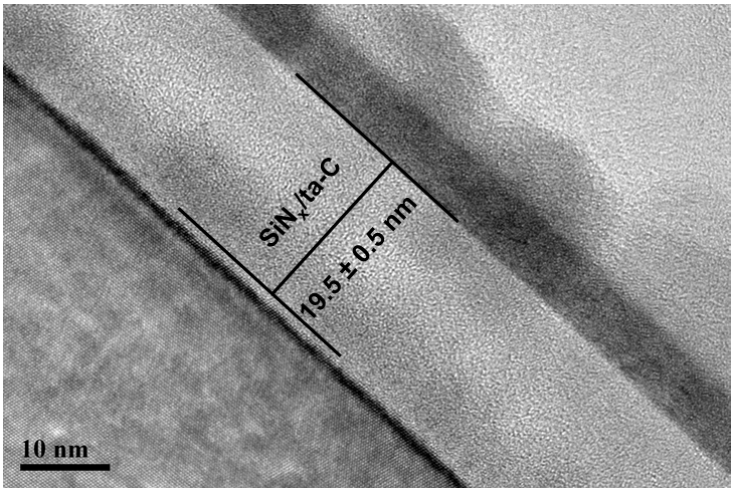

Figure 6.15 Cross-sectional HRTEM image of the SiN_x/ta-C overcoat deposited on Si with its thickness measured.

6.3.3 Tribological properties

In addition to the SiN_x/ta-C overcoat deposited on AlTiC pre-cleaned by substrate bias etching, tribological tests were also performed on flat as-received (unetched) bare AlTiC substrates as well as etched bare AlTiC substrates, in order to evaluate the effectiveness of the bi-layer overcoat in

improving the friction and wear resistance of the AlTiC substrate. The combined COF plot and optical micrographs of the three samples are presented in Figures 6.16(a) and 6.16(b) respectively. As compared to bare AlTiC and etched bare AlTiC, the SiN_x/ta-C bi-layer overcoat deposited on etched AlTiC showed a significantly lower and stable COF (0.1–0.13) and highest wear resistance in terms of negligible material transfer to the ball and a barely visible wear track. Thus, the ball-on-disk tribological test results revealed the excellent frictional and wear resistance characteristics of the bi-layer overcoat.

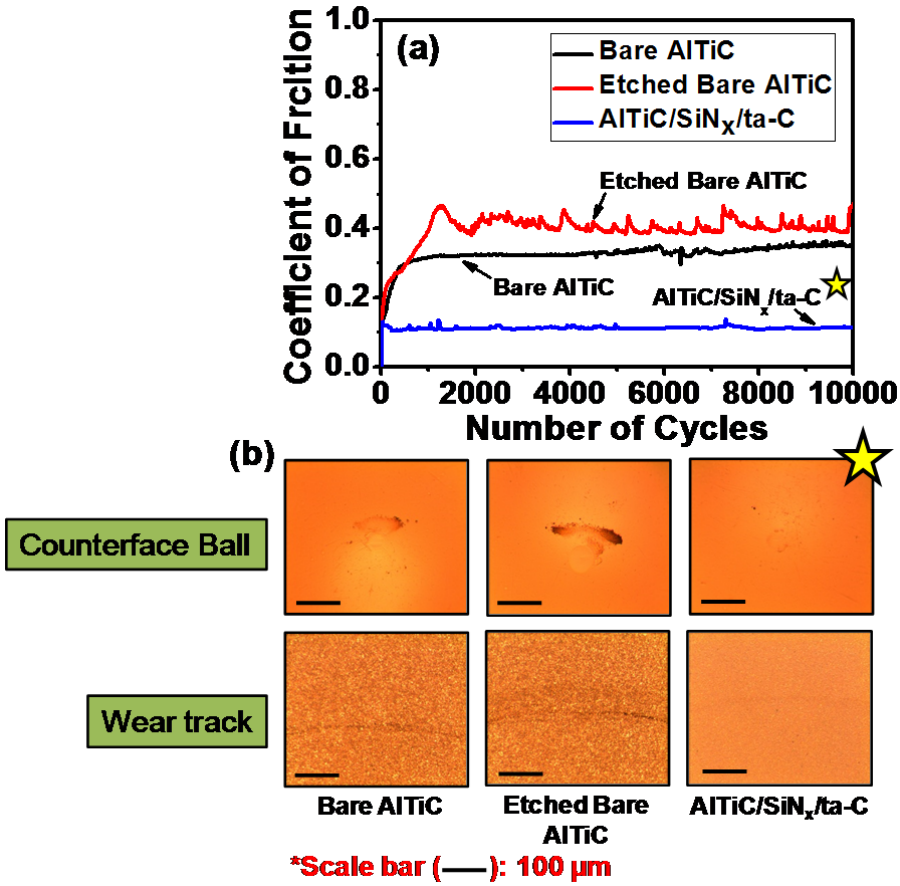

Figure 6.16 (a) Combined plot of COF versus number of cycles and (b) optical micrographs for the samples of bare AlTiC, etched bare AlTiC and AlTiC coated with the SiN_x/ta-C bi-layer overcoat.

6.3.4 Microstructure of the ta-C layer

The UV (325 nm) and visible (488 nm) Raman spectra for the SiN_x/ta-C bi-layer overcoat are presented in Figures 6.17(a) and 6.17(b). Both spectra revealed the presence of the G peak as a result of the bond stretching mode for a pair of sp^2-bonded carbon atoms. However, while the D peak was observed to be absent in the UV Raman spectrum, it appeared as a faint peak in the visible Raman spectrum. Since the D peak arises due to the presence of ring-like sp^2-bonded structures in the carbon network while the G peak arises due to the presence of both sp^2-bonded ring-like and chain-like structures, the results therefore indicated that the carbon network of the bi-layer overcoat consisted primarily of chain-like sp^2C bonding. What is interesting is that the UV Raman spectrum displayed a small T peak appearing at ~ 1000 cm^{-1}, and this is associated with sp^3 C–C bonding. Ferrari and Robertson have also previously observed the presence of a faint T peak under 325 nm UV Raman excitation for an ~ 88% sp^3-bonded ta-C film [161]. After appropriate fitting of the D and G peaks was performed for both spectra (not shown here), a significant dispersion of the G peak between both spectra was revealed, resulting from its shift from ~ 1594 cm^{-1} in the UV Raman spectrum to ~ 1555 cm^{-1} in the visible Raman spectrum. The G peak dispersion value suggested that the carbon network consisted of sp^2-bonded chain-like structures within the network but also possessed a high sp^3C bonding fraction [161].

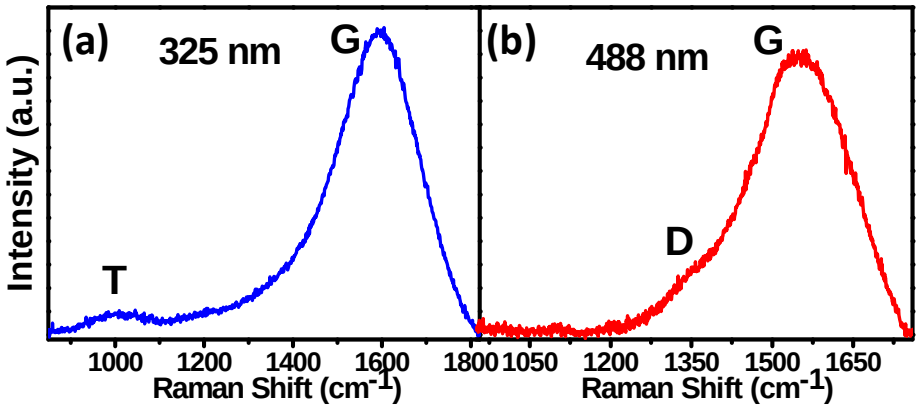

Figure 6.17 (a) UV Raman (325 nm) and (b) visible Raman (488 nm) spectra of the SiN_x/ta-C overcoat deposited on a flat AlTiC substrate. The positions of the G and T peaks in the UV Raman spectrum and the G and D peaks in the visible Raman spectrum are indicated.

6.3.5 Probing the variation of elemental composition with overcoat thickness

AES depth profiling of the SiN_x/ta-C overcoat was performed by measuring the AES spectra at a location on the coated flat AlTiC substrate after every 30 s of sputter etching of the surface by Ar^+ ions. The peak intensities of each element obtained from the first derivative spectra after each round of sputter etching were plotted in a depth profile of intensity versus etching time (corresponding to the depth into the surface). The AES depth profile was recorded to investigate the variation of overcoat composition with respect to the overcoat thickness/depth and to reveal any possibility of layer intermixing, especially within the SiN_x interlayer which was subjected to the high energy C^+ pre-treatment step by FCVA.

Figure 6.18 presents the AES depth profile of the SiN_x/ta-C bi-layer overcoat on flat AlTiC. The variation of the elements C, Si, N, O, Al, and Ti as detected in the depth profile is in good agreement with the expected

overcoat composition. At the surface of the SiN_x/ta-C overcoat, a high intensity of C arising from the ta-C layer was observed. As the depth approached the SiN_x interlayer, the C intensity decreased while the intensity of Si increased and peaked within the SiN_x interlayer region. This was followed by a decrease in the Si intensity and an increase in the intensities of Al, Ti and O as the AlTiC substrate was approached. There was also an increase in N intensity, but this was attributed not to the increase in the composition of N into the substrate, but due to a peak overlap of N and Ti in the AES spectrum, which could result in the detection of Ti as N. Upon examination of the SiN_x interlayer region and its interfaces, as highlighted by the blue rectangle in Figure 6.18, there is evidence of intermixing of elements such as C, Si, N/Ti, and O within the interlayer due to the presence of these elements in significant quantities in this region. This could contribute to enhancing the interfacial bonding at the interfaces and covalent bonding between these elements in the interlayer itself.

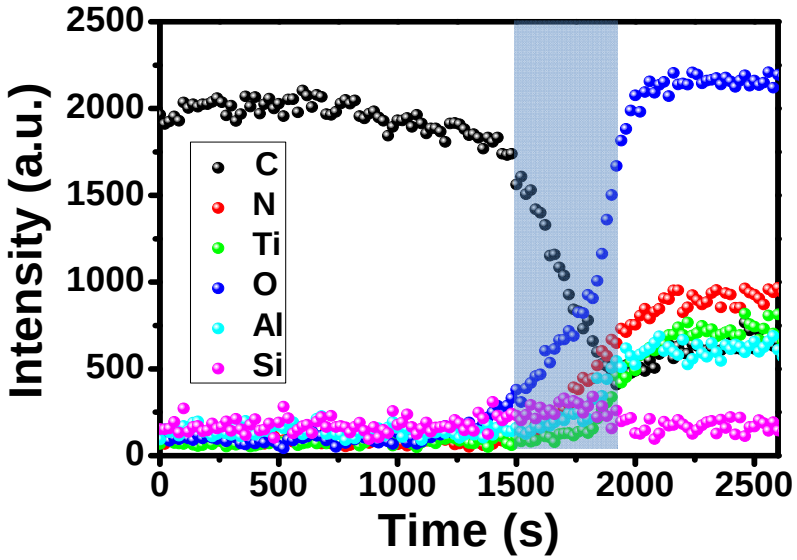

Figure 6.18 AES depth profile of the SiN_x/ta-C bi-layer overcoat deposited on a flat AlTiC substrate, showing the profiles of C, N, Ti, O, Al and Si with respect to etching time (depth into the surface). The blue rectangle represents the location of the SiN_x interlayer region where elemental intermixing can be observed.

6.3.6 Probing the bonding environment in the ta-C layer and at the interfaces

XPS depth profiling was performed on the SiN_x/ta-C bi-layer overcoat deposited on a flat AlTiC substrate for etching times of up to 10 min, so as to record the XPS spectra from the surface, interlayer and substrate regions. The C 1s core level spectrum at etching time of 0 min was chosen to estimate the sp^3C and sp^2C bonding fractions in the ta-C layer, since the carbon microstructure could be modified due to ion bombardment during etching. Figure 6.19(a) shows the deconvoluted C 1s core level spectrum of the as-deposited overcoat, with three constituent peaks corresponding to sp^2C bonding, sp^3C bonding and C–O bonding [109, 159, 160]. The relative amounts of these constituent peaks were calculated according to the ratio of

the areas under the peaks, and were found to be ~ 22%, ~ 72% and ~ 6% for sp^2C, sp^3C and C–O bonding, respectively.

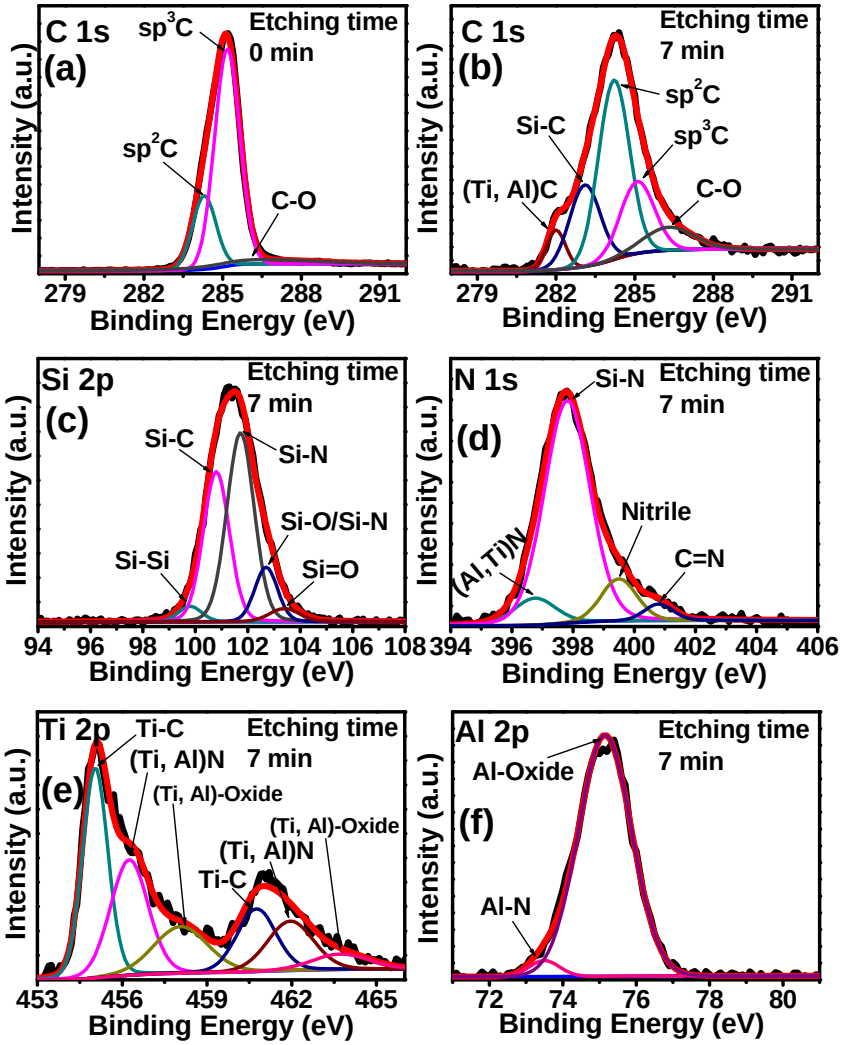

Figure 6.19 Deconvoluted XPS core level spectra of (a) C 1s at 0 min etching time, and (b)–(f) C 1s, Si 2p, N 1s, Ti 2p and Al 2p respectively at 7 min etching time performed on the SiN_x/ta-C bi-layer overcoat deposited on a flat AlTiC substrate. Constituent peaks are labeled showing the various bonds present.

The significantly high amount of sp^3C bonding was achieved as a consequence of the use of optimized FCVA process parameters for deposition, i.e. the use of 90 eV energy C^+ ions by implementing an appropriate pulsed substrate biasing scheme to obtain a high sp^3C content and maximum density.

To probe the interfacial bonding, the XPS core level spectra of C 1s, Si 2p, N 1s, Ti 2p and Al 2p recorded after 7 min etching were chosen for analysis. This choice was based on the relatively strong signals obtained from the Si 2p and N 1s spectra at this etching time, which were deduced to arise from the SiN_x interlayer region. The deconvoluted spectra at 7 min etching time are shown in Figures 6.19(b)–(f). The analyses revealed the formation of several key interfacial bonds in this region, such as Si–C, (Ti, Al)C, (Al, Ti)N, nitrile (C≡N), C=N, (Ti, Al)N–Oxide and Al–N. These bonds were in addition to Si–N bonding originally present in the SiN_x interlayer and Ti-C bonding originally present in the AlTiC substrate. It can be concluded that these interfacial bonds were formed at the interfaces and within the SiN_x interlayer region due to the FCVA pre-treatment process, resulting in carbon embedment into the SiN_x interlayer to form composite mixed layer, in addition to interaction of the atoms between the layers at the interfaces to form strong interfacial bonding.

6.3.7 Long-term functional testing in a tape drive environment

While the initial characterizations and tests revealed the excellent properties of the developed overcoat on flat substrates, the main highlight of this work is to evaluate the feasibility of the ~ 20 nm SiN_x/ta-C overcoat when applied onto a functional tape head, via long-term functional tape testing in a simulated tape drive environment up to a total length of 50 million meters. Parametric tests were conducted at various intervals during the long-term test to measure the variation in the electrical/recording performance of the head

with time, and optical micrographs on the same element of the head were captured at various intervals to examine any wear of the head overcoat.

6.3.7.1 Parametric test data

The electrical parametric data of BBSNR, 2T output and resolution extracted from the functional test measurements of the SiN_x/ta-C coated tape head were recorded and plotted in a combined graph as shown in Figure 6.20. As usual, the variations in the signals were measured based on the change with respect to the signals obtained before the wear test (0 million meters), i.e. the resolution and 2T output values measured at 0 million meters were normalized to 100% and the BBSNR measured at 0 million meters was normalized to 0 dB.

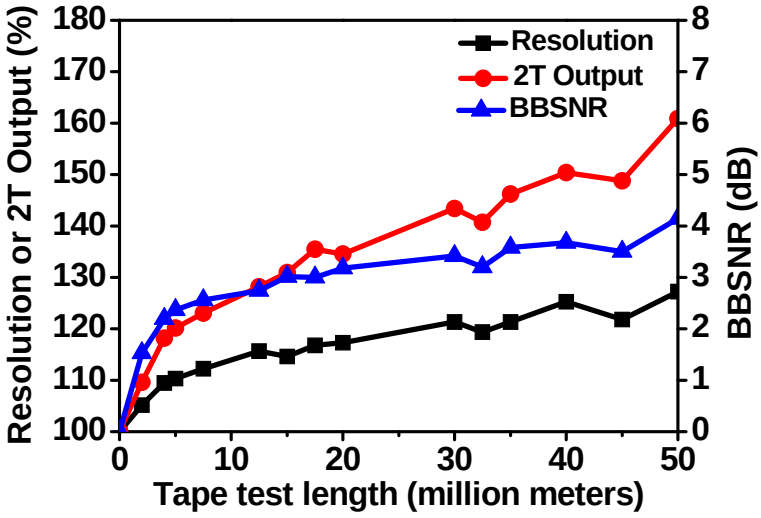

Figure 6.20 Parametric data measurements showing the variation of resolution, 2T output and BBSNR on the SiN_x/ta-C coated functional tape head with respect to tape test length. The variations in the signals are based on the change with respect to the signals obtained before the wear test (0 million meters).

At the initial stage of the parametric data measurement, it is worth noting that the ability to obtain the electrical data from the SiN_x/ta-C coated

functional tape head proved that the RF sputtering process and the FCVA coating process for overcoat fabrication as well as the overcoat structure were able to maintain the electrical functionality of the tape head. As the test progressed, it is evident that there is a continuous increasing trend in the BBSNR, 2T output and resolution (i.e. improvement in the recording performance). As mentioned in Section 6.2.8, the increase in the three readback signal parameters can be explained by a reduction in the magnetic spacing due to the gradual wear of the overcoat leading to a reduction in the overcoat thickness. It can be observed that the steepest increases in the BBSNR (+2.5 dB), resolution (+10 percentage points) and 2T output (+20 percentage points) occurred in the first 5 million meters of the wear test, after which the rates of increase were more gradual for all three curves, reaching a peak of +4.1 dB, +25 percentage points, and +60 percentage points for the BBSNR, resolution and 2T output respectively after 50 million meters. Thus it can be inferred from the parametric data that the rate of overcoat wear experienced during the first 5 million meters of tape testing was the highest, after which a lower and relatively constant wear rate was observed all the way until the end of the test at 50 million meters. The increasing trend of the parametric data throughout the test until 50 million meters additionally indicated an important result – that the recession of the magnetic read/write elements and PTR had not yet occurred even at 50 million meters, since the occurrence of PTR would lead to an increase in the magnetic spacing and hence a decrease in the signals detected from the parametric tests. This result thus showed that the application of the ~ 20 nm SiN_x/ta-C bi-layer overcoat

could delay the onset of PTR to at least above 50 million meters of running with tape.

6.3.7.2 Optical characterization of the tape head surface

The wear progression of the overcoat can also be observed from the optical micrographs captured at various intervals of tape testing, as presented in Figure 6.21. Similar to the observations made in Section 6.2.8, the regions on the tape head with lighter contrast (in particular on the AlTiC substrate and closure regions) represent the presence of the bi-layer SiN_x/ta-C overcoat on the tape head surface, whereas the darker regions indicate the absence of the overcoat. After the first 5 million meters, it was found that the overcoat had already started to wear out at both skiving edges of the module, due to the higher contact pressures of the tape on the head in these areas [67, 198]. Nevertheless, it can be seen that the overcoat was still present over most of the AlTiC substrate regions as well as over the magnetic elements at this stage. With increasing tape test length over 5 million meters, the overcoat was observed to recede away from the module edges, but at a slower rate compared to the first 5 million meters. In general, this indicated a lower rate of overcoat wear after the first 5 million meters of tape testing as compared to the first 5 million meters, which corroborated well with the parametric test results in Figure 6.20. After 50 million meters, the overcoat appeared to have been totally worn off from the tape head surface, which is evident from the darker contrast over the whole AlTiC substrate and closure regions and even over the Al_2O_3 dielectric. Hence, it can be deduced from the optical images that the wear life of the overcoat was between 40–50 million meters.

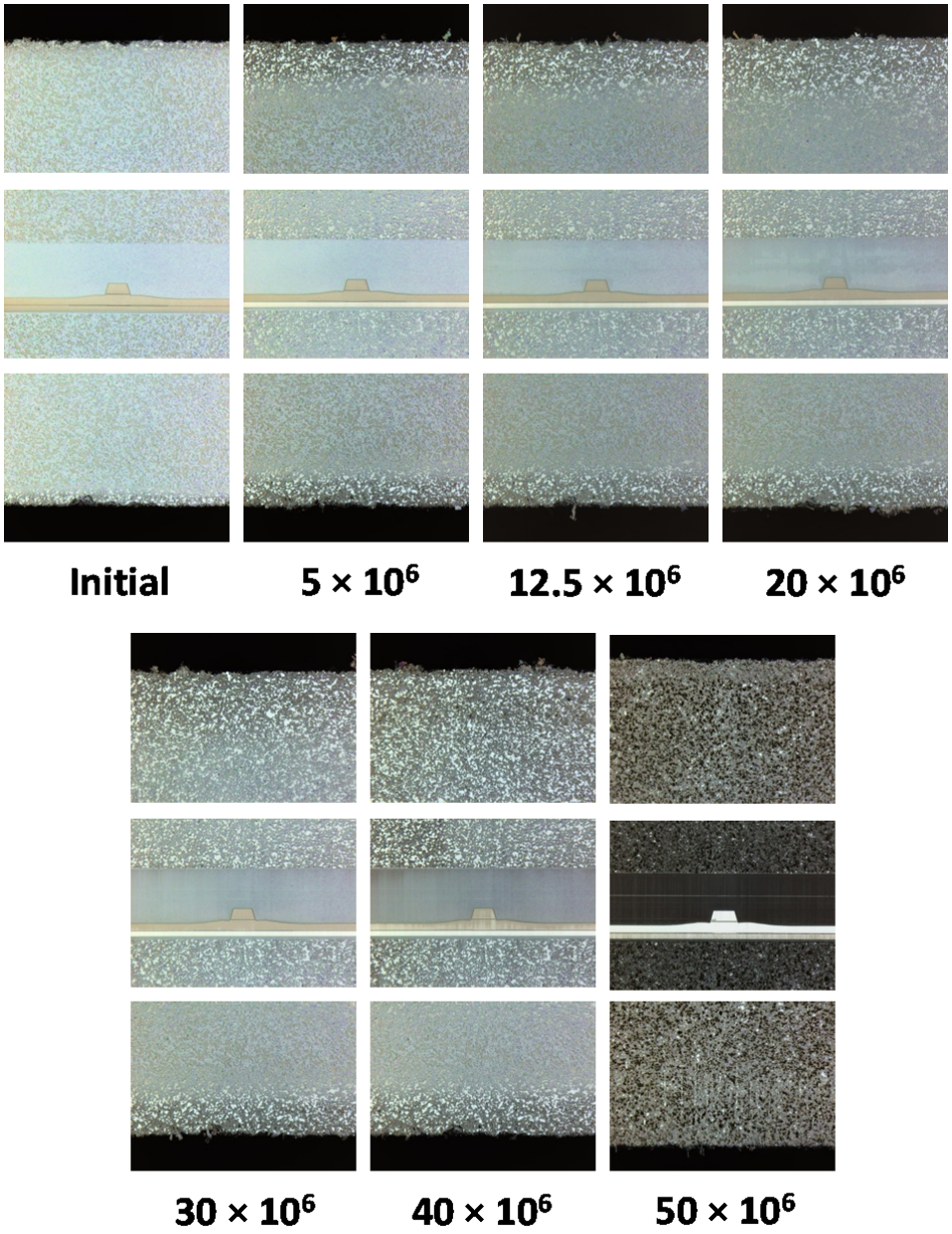

Figure 6.21 Optical micrographs of the same read/write element and its adjacent AlTiC substrate and closure regions of the SiN_x/ta-C coated functional tape head, captured before the tape test and after 5, 12.5, 20, 30, 40 and 50 million meters of tape testing.

The variation of the wear rate of the SiN_x/ta-C overcoat throughout the long-term functional test can be associated with the variation of the ta-C layer microstructure with the thickness and interfacial bonding. This is explained as follows. The top ~ 16–17 nm thick ta-C layer of the bi-layer overcoat can be

considered to comprise three layers: a) a surface layer, b) a bulk layer, and c) an interface layer immediately adjacent to the SiN_x interlayer [200], as described in Section 2.4 of the thesis. The surface layer of ta-C would possess mainly sp^2 bonding with lower density and lower wear resistance, whereas the bulk ta-C layer would possess a high sp^3 bonding fraction with high density due to subplantation by the FCVA growth process, giving higher wear resistance. Although the interface layer would be expected to possess lower sp^3C bonding, extensive interfacial bonding between the SiN_x interlayer with carbon was observed by XPS. Hence, the higher wear rate during the initial 5 million meters can be attributed to a higher rate of removal of the sp^2C bonded surface region of the ta-C layer. However, as the test progressed further, a reduction in the wear rate was observed as the high sp^3C bonded bulk region was approached. As the wear reached the interfacial region of ta-C and SiN_x and the mixed SiN_x interlayer region, the wear rate continued to remain low due to the high amount of strong interfacial bonding present.

6.3.8 Role of sp^2C/sp^3C bonding on friction and wear

The difference in the tribological (friction and wear) properties between sputtered and FCVA-processed overcoats can be explained in terms of their differences in sp^2C/sp^3C bonding and substrate-overcoat adhesion. Generally, high sp^2-bonded carbon films show low friction but also possess low wear resistance. On the other hand, amorphous carbon films with higher sp^3C bonding (such as those fabricated by energetic processes like FCVA) possess higher wear resistance, but can also exhibit low friction, especially in ambient RH conditions (RH ~ 50-60%), which is the range that the films in

this work were tested. High sp^3-bonded carbon films possess dangling bonds which contribute to high adhesion and friction. However in high RH conditions, the dangling bonds are easily saturated by OH and H groups from water vapor in the air. Thus the films can show lower friction due to surface passivation [201]. Furthermore, during the ball-on-disk tribological test, when the counterface slides over the carbon surface, an sp^2-rich tribolayer can be formed on the wear track through $sp^3 \rightarrow sp^2$ rehybridization [202] which can also contribute to lower friction.

Nevertheless, it was observed that although the sputtered carbon overcoats (samples C7 and SiN3C4) in Section 6.2 showed low friction based on the ball-on-disk tribological tests, they exhibited poor wear resistance in the functional tape test due to their low sp^3C bonding. On the other hand, the FCVA-processed overcoat of SiN_x/ta-C not only showed low friction but also significantly higher wear resistance in the functional tape test due to its higher sp^3C bonding, although it had a higher thickness than the sputtered overcoats (the tribological properties of these overcoats with similar thickness will be compared and discussed in a forthcoming paper [203]). Furthermore, the friction and wear of the overcoats were controlled by tuning the substrate-overcoat adhesion. Between the sputtered overcoats, the wear resistance was improved by introducing a 3 nm SiN_x interlayer without affecting its friction. This was due to the SiN_x interlayer providing increased interfacial adhesion. In comparison, the FCVA-processed SiN_x/ta-C overcoat demonstrated both high wear resistance and low friction with increased interfacial adhesion. The trend of high adhesion strength achieving higher wear resistance and lower friction has also been observed previously [204].

6.3.9 Conclusions

In summary, the efficacy of the ~ 20 nm SiN_x/ta-C bi-layer protective overcoat, which has been developed on an electrically functional tape head, was demonstrated in a long-term functional tape test for up to 50 million meters. The overcoat design and fabrication process by RF sputtering and FCVA were shown to be feasible for coating a functional tape head, without damaging its electrical functionality. The excellent wear protection of the overcoat was derived from the enhanced interfacial bonding and high sp^3C fraction in the ta-C layer, as a consequence of the combined effects of the SiN_x adhesion interlayer, FCVA C^+ ion pre-treatment, and optimized FCVA C^+ ion energy used for the deposition of ta-C. The high sp^3 bonding in the ta-C layer (~ 72%) provided strength and rigidity to the overcoat while the increased interfacial bonding simultaneously enhanced the adhesion. The synergistic effect of both led to the remarkable wear resistance of the bi-layer overcoat on the tape head, which protected the head surface even after 40–50 million meters of tape wear. From this study, the crucial role of high sp^3C bonding and increased interfacial bonding can be clearly seen in enhancing the life of the overcoat and hence the long-term functionality of the tape head at relatively lower overcoat thicknesses. This provides a potential and promising direction for designing ultrathin and wear-durable overcoats for future tape heads.

6.4 Characterization of monolithic and bi-layer overcoats fabricated by sputtering and FCVA

6.4.1 Motivation of this work

So far, based on the long-term tape test performances of the ~ 7 nm SiN_x/a-C bi-layer overcoat and the ~ 20 nm SiN_x/ta-C bi-layer overcoat, it has been shown that their wear lives as tested with commercial tape in a simulated tape drive environment were 3 million meters and 40–50 million meters respectively. By a linear extrapolation of the wear life of the sputtered SiN_x/a-C overcoat to a thickness of ~ 20 nm, it would have possessed a wear life of ~ 10 million meters, which is still considerably much less than the SiN_x/ta-C overcoat which contains the FCVA-processed ta-C overlayer. Hence, it can be inferred that while interfacial bonding was formed in both types of overcoats, the higher durability in SiN_x/ta-C may be attributed to the presence of high sp^3C bonding in the ta-C layer, which was absent in SiN_x/a-C. It is well-known that high sp^3C content would give rise to a higher hardness and elastic modulus of the carbon layer, which directly contributes to the wear resistance of the overcoat.

It is therefore appropriate that the bonding and microstructures of sputtered and FCVA-processed carbon overcoats with and without an interlayer of SiN_x should be compared on a similar thickness scale, in order to understand how the carbon microstructure, chemical bonding and the presence of the interlayer affect the wear durability of the overcoat. Thus, the structure-property relationship of the overcoats would be elucidated in this section, by evaluating their mechanical and electrical properties and relating these

properties to the differences in chemical and interfacial bonding and microstructure. Five types of overcoats were prepared in the thickness range of ~ 17–20 nm for comparison, namely: 1) monolithic sputtered a-C overcoat, 2) bi-layer sputtered SiN_x/C overcoat, 3) monolithic FCVA-processed ta-C overcoat, 4) bi-layer SiN_x/ta-C overcoat with the SiN_x interlayer processed by sputtering and ta-C layer processed by FCVA, and 5) monolithic sputtered SiN_x overcoat. The overcoats were evaluated in terms of their surface topography, mechanical properties, electrical properties, carbon layer microstructures and chemical bonding environment. The analyses of these results aim to provide a deeper understanding on the wear and electrical behavior of the overcoats for functional tape heads.

6.4.2 Experimental methodology

All the overcoats in this work were fabricated on flat AlTiC and Si substrates in a newly acquired custom-built PVD75 system (Kurt J Lesker Company, USA), whereby the magnetron sputtering and FCVA processes can be performed *in situ* within the same chamber. This eliminates the need for sample transfer between chambers which exposes the sample to oxidation and contamination in the ambient. The base pressure of the system was maintained at ~ 8.0×10^{-8} Torr for all depositions. Prior to deposition, all substrates were subjected to Ar plasma cleaning of surface impurities by applying an RF bias to the substrate for a short time of 1–2 min. All SiN_x layers were deposited by an RF magnetron sputtering process using a Si_3N_4 target. All a-C layers were deposited by pulsed DC magnetron sputtering using a pulsed DC power supply (Advanced Energy Industries Inc., USA) at a pulse frequency of 150

kHz and duty cycle of 40%. All ta-C layers were grown using the FCVA bi-level energy process, where highly energetic C^+ ions at ~ 350 eV were used for the pre-treatment step and moderate energy C^+ ions at ~ 90 eV were used for the ta-C deposition step. The energies were tuned by applying a pulsed substrate bias scheme with pulse frequency of 100 kHz and duty cycle of 70%. A substrate bias of -335 V was used to achieve the high C^+ ion energy of ~ 350 eV whereas a substrate bias of -75 V was used to achieve the medium C^+ ion energy of ~ 90 eV.

Table 6.2 summarizes the structures of the five overcoats, their respective nomenclatures used in this work and their actual overcoat thicknesses which were determined by HRTEM cross-sectional imaging. Subsequently, the surface roughnesses of the five samples deposited on flat AlTiC substrates were measured by tapping mode AFM over an area of 10 × 10 μm^2 on at least three locations of each sample to obtain relatively consistent readings. The mechanical properties of the overcoats deposited on flat AlTiC substrates were evaluated by nano-indentation, by probing only the top 5 nm of the overcoats to reduce the influence of the measurement by the substrate. The rate of indentation used was 10 nm/s. A total of at least 10 indentations were performed for each sample, randomly selected within an area of 300 × 300 μm^2 at the center of the sample. From the nano-indentation process, a curve of hardness versus nano-indentation depth was directly retrieved from each measurement. Electrical measurements using the four-probe configuration as described in Section 3.2.5 were performed on the overcoats deposited on Si substrates. I-V measurements were performed on at least two different locations for each sample to obtain consistent results. The

electrodes in this case were defined by an optical lithography method to pattern the areas for electrode deposition using photoresist. Electrode deposition was conducted by depositing a Ta/Ag/Ta tri-layer electrode of ~ 100 nm thickness via sputtering, after which a liftoff process was performed to remove the photoresist layer, leaving only the patterned electrodes on the overcoat surfaces. The electrode configuration and dimensions are shown in Figure 6.22.

Table 6.2 Structures, nomenclature and overcoat thickness of the five overcoats used in this work.

Sample Nomenclature	Sample Structure	Carbon Deposition Process	Overcoat Thickness Measured by HRTEM
20CP	Substrate/a-C (20 nm)	Pulsed DC sputtering	20.0 ± 0.5 nm
3SiN17CP	Substrate/SiN_x (3 nm)/ a-C (17 nm)	Pulsed DC sputtering	20.0 ± 0.5 nm
17CF	Substrate/ta-C (17 nm)	FCVA	17.0 ± 0.5 nm
3SiN14CF	Substrate/SiN_x (3 nm)/ ta-C (14 nm)	FCVA	17.0 ± 0.5 nm
18SiN	Substrate/SiN_x (18 nm)	RF sputtering	18.0 ± 0.5 nm

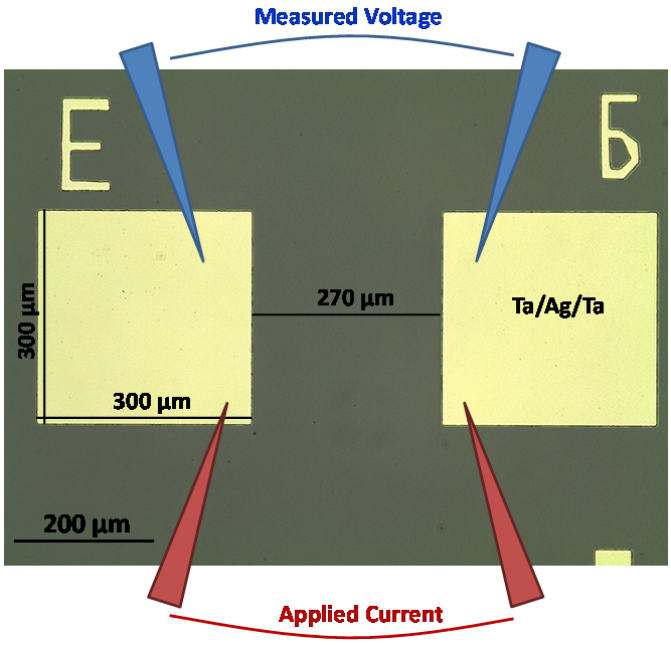

Figure 6.22 Electrode configuration and dimensions used for the four-probe electrical measurements in this work.

Finally, for the overcoats deposited on the flat AlTiC substrates, the microstructures of the carbon layers were probed using UV and visible Raman spectroscopy and the bonding environments within the overcoats were probed using XPS depth profiling.

6.4.3 Overcoat thickness and surface roughness

The thicknesses of all films measured from cross-sectional HRTEM imaging as shown in Figures 6.23(a)–(e) were found to be in the range ~ 17–20 nm with an error bar of about ± 0.5 nm for each measurement. For the bi-layer overcoats, the thickness of SiN_x interlayer was kept to ~ 3 nm based on the sputter deposition rate calibration. However, due to the similar contrast of the SiN_x interlayer and the carbon layer, the layers could not be clearly distinguished. Nevertheless, upon closer inspection, a barely distinguishable layer corresponding to the SiN_x interlayer can be seen near the bottom Ta

capping layer of each bi-layer overcoat. The presence of the SiN_x interlayer in each bi-layer overcoat was subsequently confirmed by XPS depth profile analyses.

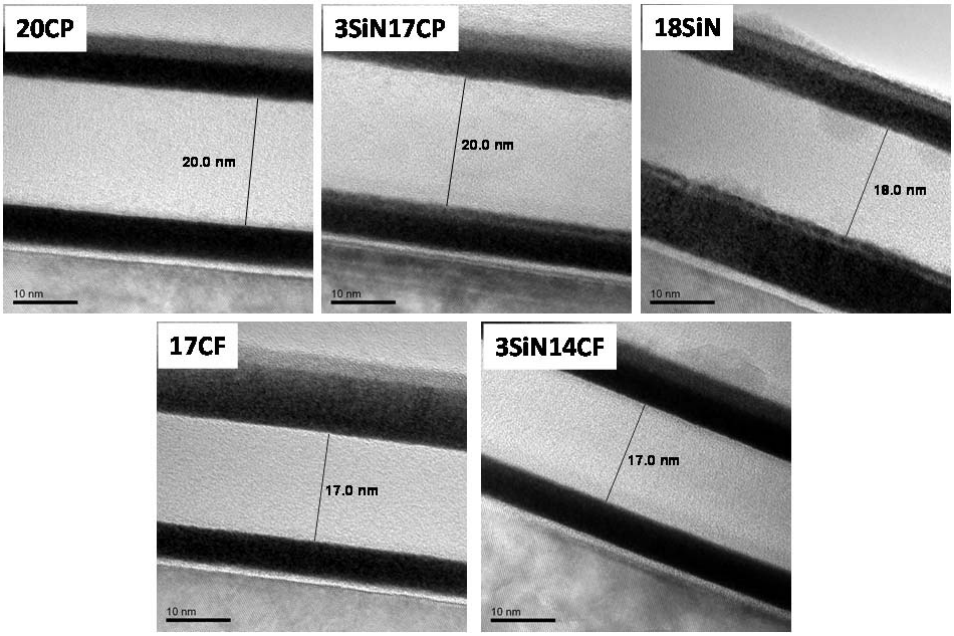

Figure 6.23 Cross-sectional HRTEM images of the five overcoats used in this work, with their thicknesses measured and indicated.

Figure 6.24(a) and Table 6.3 shows the R_q values of the overcoats deposited on AlTiC substrate, as well as for the bare AlTiC substrate itself, taken over an area of 10 × 10 μm^2 at different locations on the substrate. The R_q of AlTiC was found to be ~ 5.5 nm, and the R_q values of the monolithic carbon overcoats and bi-layer overcoats were found to be similar, within the range error bars of each other. However, in comparison, the average R_q was found to be slightly higher in the bi-layer overcoats than the monolithic carbon overcoats. On the other hand, the monolithic SiN_x overcoat (sample 18SiN) was found to have a comparably higher R_q of ~ 7.5 nm.

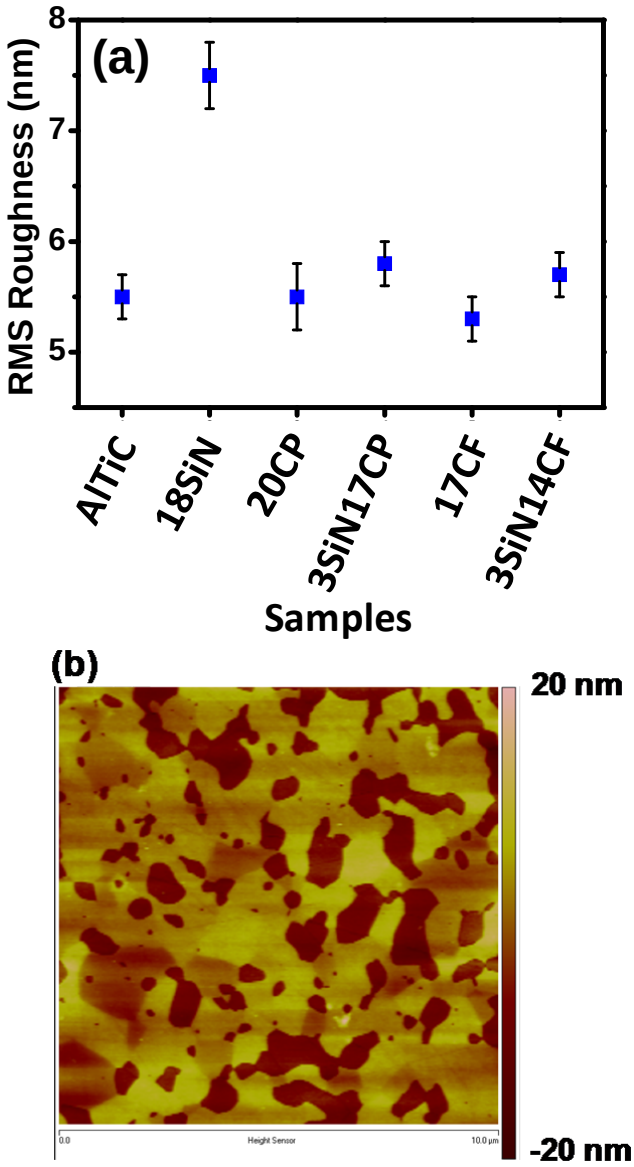

Figure 6.24 (a) RMS roughness (R_q) values of the various overcoats deposited on AlTiC substrates. The R_q value of a bare AlTiC substrate was also plotted comparison. (b) 2D AFM image showing the surface topography of a bare AlTiC surface over an area of 10 × 10 µm^2.

Table 6.3 Tabulated average values of R_q, H at 3 nm and 4.5 nm penetration depths for all five overcoats deposited on AlTiC substrates as well as bare AlTiC substrate itself.

Samples	R_q (nm)	H (GPa) @ 3 nm	H (GPa) @4.5 nm
Bare AlTiC	5.5 ± 0.2	27.0 ± 3.0	31.0 ± 3.0
18SiN	7.5 ± 0.3	34.0 ± 3.5	34.5 ± 3.5
20CP	5.5 ± 0.3	27.0 ± 3.0	29.0 ± 3.0
3SiN17CP	5.8 ± 0.2	32.0 ± 3.0	36.0 ± 3.0
17CF	5.2 ± 0.2	64.0 ± 3.0	69.0 ± 3.0
3SiN14CF	5.7 ± 0.2	61.0 ± 3.0	65.5 ± 3.0

The observation of such a high R_q in a-C films, especially FCVA-processed ta-C films, is strange as ta-C films usually exhibit ultra-low roughness with R_q values < 0.2 nm being observed, as reported by Casiraghi et al. [19]. Moreover, ultra-low R_q values of < 0.2 nm had also been observed in FCVA- and sputter-processed carbon-based overcoats with < 2 nm thickness. The reason for the high roughness of the overcoats on AlTiC, as compared to hard disk media, is due to the inherent structure of the AlTiC substrate material. A 2D AFM image showing the topography of a bare AlTiC substrate is shown in Figure 6.24(b). Owing to this composite structure, the R_q of AlTiC is comparably high. The observed high R_q in these carbon-based overcoats therefore can be attributed to the dominant effect of the AlTiC substrate roughness over the carbon-based overcoats, hence the roughnesses of the carbon-containing monolithic and bi-layer overcoats were found to be similar to the roughness of AlTiC substrate. Casiraghi et al. have also encountered a similar behavior when they deposited carbon films on slightly rougher silicon surfaces [19]. Thus, the roughness of the carbon films, especially at ultrathin

levels, depends largely on the smoothness of the underlying substrate which it is grown on.

6.4.4 Mechanical properties

Nano-indentation measurements were performed to measure the mechanical properties of the overcoats on AlTiC substrate. Out of the 10 data points taken for each sample, those giving the most consistent and reasonable hardness (H) readings, i.e. falling within a range of approximately ± 3 GPa, were considered. At least five data points had to be obtained within this range in order for the measurement to be considered consistent and reliable. A representative H versus penetration depth curves for each sample (having its H values closest to the average H values calculated for that sample) was chosen and all the curves are plotted in a combined graph in Figure 6.25(a). From the representative curves, the H values at penetration depths of 3 nm (~ $1/6^{th}$ of the overcoat thickness) and 4.5 nm (~ $1/4^{th}$ of the overcoat thickness) were extracted, as shown by the dashed vertical line in Figure 6.25(a). The values were plotted in a graph as shown in Figure 6.25(b) and also summarized in Table 6.3.

It should be noted, however, that the nano-indentation technique has a limitation in measuring the hardness of ultrathin films, due to the contribution of the substrate effect in the measurement. In general, the substrate effect becomes significant when the tip penetrates more than ~ 10% of the film thickness. Here, while the total thickness of the films was 20 nm, the maximum indentation depth into the films was 5 nm, which was up to 25% of the film thickness; hence there will be a substrate effect in these measurements

which will affect the final hardness value. Nevertheless, the main objective of these measurements is to compare the values of hardness between the samples deposited on the same substrate (AlTiC). Moreover, the hardness of the bare AlTiC substrate was also recorded as a reference.

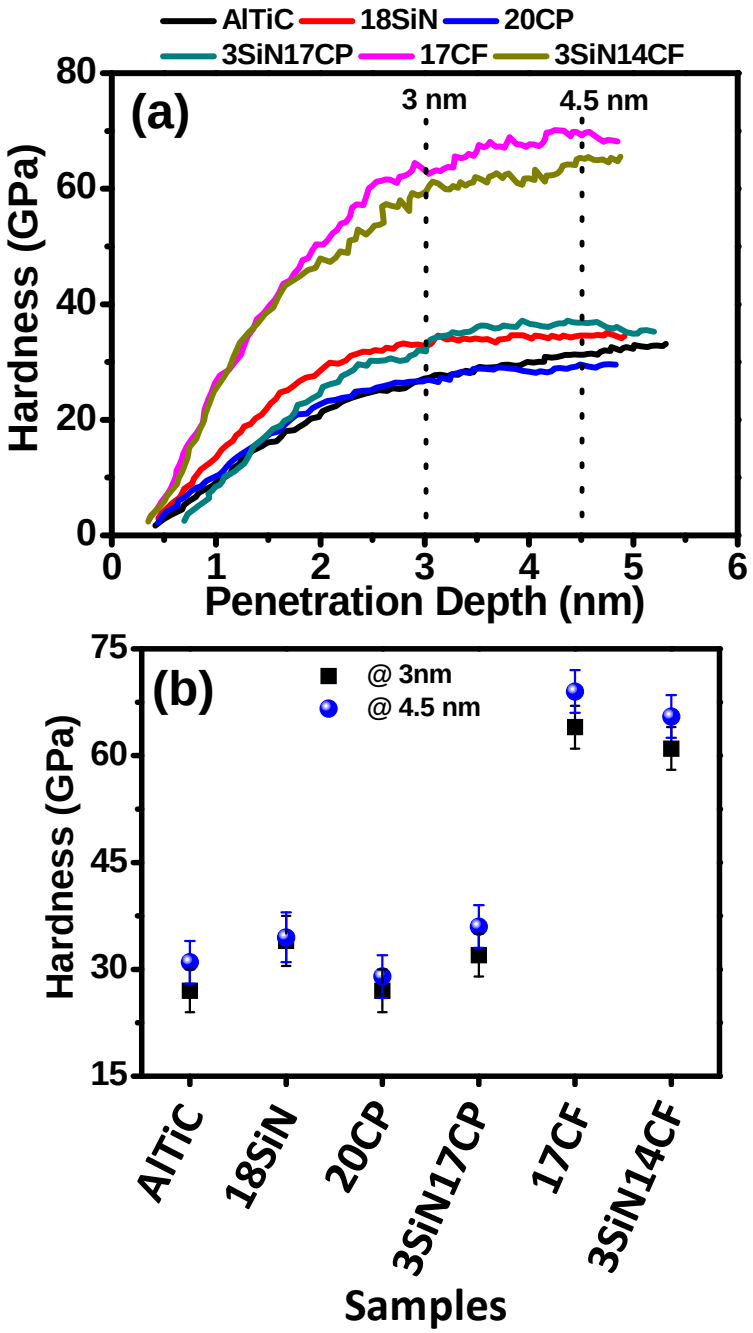

Figure 6.25 (a) Representative hardness (H) versus penetration depth curves obtained for the five overcoated samples and one for bare AlTiC substrate. H values at the penetration depths of 3 nm and 4.5 nm into the surface were extracted from the curves and plotted in (b).

The hardness values for all samples were found to be slightly higher at 4.5 nm due to the reduction of the surface effect [205]. For samples 18SiN, 20CP and 3SiN17CP, the hardness values at 4.5 nm depth were found to be close to the hardness of the AlTiC substrate (~ 31 GPa at 4.5 nm). Nevertheless, sample 3SiN17CP exhibited slightly higher hardness than sample 20CP. The reason for this observation was attributed to the slight SiN_x interlayer-induced increase in the sp^3C bonding within the a-C layer, formation of strong Si-C interfacial bonding, and the effect of the SiN_x interlayer itself contributing to the higher hardness (monolithic SiN_x in sample 18SiN was found to possess a higher hardness than monolithic sputtered a-C in sample 20CP). On the other hand, the monolithic and bi-layer overcoats in samples 17CF and 3SiN14CF containing FCVA-processed ta-C layers showed much higher hardness than samples 20CP and 3SiN17CP containing sputtered a-C. This is a consequence of significantly higher sp^3C bonding present in the FCVA-processed ta-C layer, resulting in a higher intrinsic hardness. Between samples 17CF and 3SiN14CF, the hardness values can be regarded as similar.

6.4.5 Electrical properties

The average electrical resistance values were calculated by taking the gradients of the I-V curves obtained from the electrical measurements. The average electrical resistance values for the five overcoats are presented in Figure 6.26 and in Table 6.4. The highest resistance was observed in 18SiN, which indicated that the monolithic SiN_x overcoat was the most electrically insulating. Conversely, the pulsed DC sputtered monolithic 20 nm a-C in sample 20CP showed the lowest electrical resistance, which was expected due

to its high sp^2C content. With the introduction of a ~ 3 nm thick SiN_x layer to obtain a bi-layer overcoat in sample 3SiN17CP, the electrical resistance was slightly increased over sample 20CP. This increase can be attributed to three possible factors: 1) the increase in sp^3C-induced bonding due to the introduction of the SiN_x interlayer, 2) the contribution of the electrically insulating SiN_x interlayer to the higher overall resistance, and 3) the reduction in overall a-C thickness in 3SiN17CP as compared to 20CP.

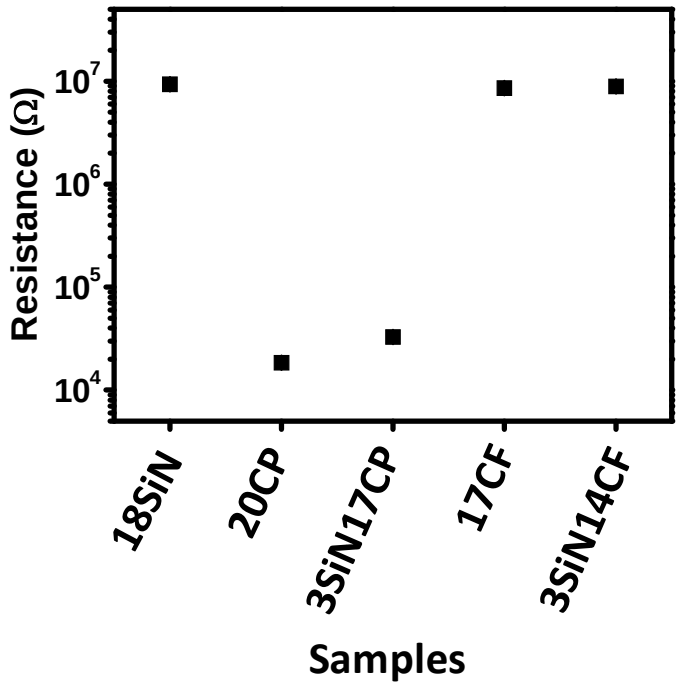

Figure 6.26 Average electrical resistance values calculated from the measured I-V curves of the five overcoats deposited on Si substrates.

Table 6.4 Average electrical resistance values for the five overcoats measured on Si substrates.

Samples	Resistance (Ω)
18SiN	$(9.34 \pm 0.05) \times 10^6$
20CP	$(1.84 \pm 0.03) \times 10^4$
3SiN17CP	$(3.28 \pm 0.04) \times 10^4$
17CF	$(8.60 \pm 0.12) \times 10^6$
3SiN14CF	$(8.91 \pm 0.01) \times 10^6$

On the other hand, the FCVA-processed 17 nm thick monolithic ta-C in sample 17CF showed significantly higher electrical resistance than overcoats containing pulsed DC sputtered carbon, with an increase of about two orders of magnitude. The electrical resistance of the SiN_x/ta-C bi-layer overcoat in sample 3SiN14CF showed a further increase over sample 17CF, with the introduction of the 3 nm thick SiN_x interlayer. Since the sp^3C content is already high in FCVA-processed ta-C, the increase in the electrical resistance upon introduction of the SiN_x interlayer could be attributed to the contribution of the electrically insulating SiN_x interlayer to the higher overall resistance, as well as the reduction in overall ta-C thickness in 3SiN14CF as compared to 17CF.

In general, the higher electrical resistance in the ta-C containing overcoats processed by FCVA was attributed to formation of higher sp^3C bonding in the ta-C layer. Among the sputtered and FCVA-processed overcoats, sufficient electrical resistance is one of the essential requirements to avoid the issue of electrical shorting at the tape head surface when they are deposited onto the functional tape heads. Since the electrical readback signals could be obtained on functional tape heads coated with the bi-layer overcoat

designs using both sputtering and FCVA processes, this indicated that the overcoats possessed sufficient electrical resistance to avoid this problem.

6.4.6 Microstructure and interfacial bonding

Visible (514 nm) and UV (325 nm) Raman spectroscopic measurements were performed to examine the microstructure of the carbon layers deposited by the two different techniques. XPS measurements were performed on as-deposited and after depth profile sputter etching from surface-to-interface-to-substrate regions, in order to completely understand the chemical structure and interfacial bonding of the overcoats. Due to the length limitation of this thesis, the detailed analyses for the Raman and XPS spectra are presented in Appendix C, and only the key results and conclusions are presented here.

Based on the analyses of the fitted UV and visible Raman spectra, it was found that the FCVA-processed ta-C films in samples 17CF and 3SiN14CF possessed much higher sp^3C bonding than the sputtered a-C films in samples 20CP and 3SiN17CP. However, when comparing between the FCVA-processed samples 17CF and 3SiN14CF, the sp^3C bonding fractions were almost similar with marginal variation. This was also the case when comparing between the sputtered samples 20CP and 3SiN17CP. From the XPS analyses of the deconvoluted C 1s core level spectra of the monolithic and bi-layer overcoats, sp^3C bonding fractions in samples 20CP, 3SiN17CP, 17CF and 3SiN14CF were found to be 18.0%, 22.0%, 76.5% and 71.3%, respectively, with an error bar of ± 5% each. Thus, it is clear that the FCVA-processed ta-C films in samples 17CF and 3SiN14CF showed much higher

sp^3C bonding than the sputtered a-C films in samples 20CP and 3SiN17CP, which corroborated with the Raman results. Subsequently, from XPS analyses of the deconvoluted C 1s, Si 2p, N 1s, Al 2p and Ti 2p core level spectra of the bi-layer overcoats at the carbon-SiN_x and SiN_x-AlTiC interfaces after depth profiling, various types of interfacial bonding were found similar to what has been discussed previously in Sections 6.3 and 6.4.

Therefore, overall, it was found that when comparing between the monolithic and bi-layer overcoats fabricated by each technique, there was only a marginal difference in the sp^2C/sp^3C content and their related hardness and electrical resistance values. The reason for this can be attributed to larger thicknesses of the carbon layers (in this case the carbon layer thickness was at least 14 nm compared to only 3 nm of SiN_x), the influence of the SiN_x interlayer on the microstructure of the carbon layer is not as much as compared to a thinner carbon layer such as in the case of hard disk overcoats.

6.4.7 Conclusions

In this work, the fundamental properties of monolithic and bi-layer overcoats with thicknesses in the range of ~ 17–20 nm were compared, and the findings were related to the observed wear and functional behavior of the overcoats on electrically functional tape heads. It was first seen that the topography of the overcoats conform well to the AlTiC substrate at such low thicknesses, which causes the roughness of the overcoats to generally follow the roughness of the AlTiC substrate itself. The electrical properties of the overcoats showed that the FCVA-processed overcoats were more electrically insulating, based on the fact that the FCVA ta-C layer had higher sp^3C

bonding while sputtered a-C had higher sp^2C bonding. This was also confirmed by Raman and XPS analyses on the carbon layers. The difference in the sp^2C/sp^3C bonding fractions also contributed to a significant difference in the hardness between the sputtered and FCVA-processed overcoats, where the FCVA-processed overcoats with higher sp^3C bonding fractions showed higher hardness values as compared with the sputtered overcoats with lower sp^3C fractions.

Most importantly, the combined role of both interfacial bonding and carbon microstructure in influencing the wear life of the overcoats is elucidated. Firstly, it has been shown in Sections 6.2 and 6.3 that even with a SiN_x interlayer in both samples of SiN_x/a-C and SiN_x/ta-C, the carbon microstructure (higher sp^3C content in SiN_x/ta-C) is essential in providing higher wear durability. Secondly, the importance of enhanced interfacial bonding was emphasized in Section 6.2. By introducing a SiN_x layer between the AlTiC substrate and carbon overlayer, the creation of enhanced carbon-SiN_x and SiN_x-AlTiC interfaces improved the wear durability of the bi-layer SiN_x/a-C overcoat over the monolithic a-C overcoat. As such, it can be concluded that the highest wear durability can be achieved only with both high sp^3C and enhanced interfacial bonding working together synergistically.

Chapter 7: Graphene as a protective overcoat for hard disk media

7.1 Introduction

Graphene is a sp^2-bonded two-dimensional monolayer of carbon arranged in a hexagonal lattice. It can be regarded as the basic building block for a variety of sp^2-bonded carbon allotropes, ranging from three-dimensional graphite crystals to one-dimensional carbon nanotubes and zero-dimensional fullerenes, as shown in Figure 7.1 [206]. Graphene has seen a rapid rise in its popularity in recent years, owing to its unique and fascinating optical, electrical and thermal properties which arise from the exceptional behavior of electrons and phonons within the graphene monolayer [206, 207]. For a one-atom thick material (~ 3.5 Å based on the interplanar spacing of crystalline graphite), it has been found to exhibit high optical absorbance [208], high in-plane thermal conductivity and charge carrier mobility [209], and high electrical conductivity [206, 210].

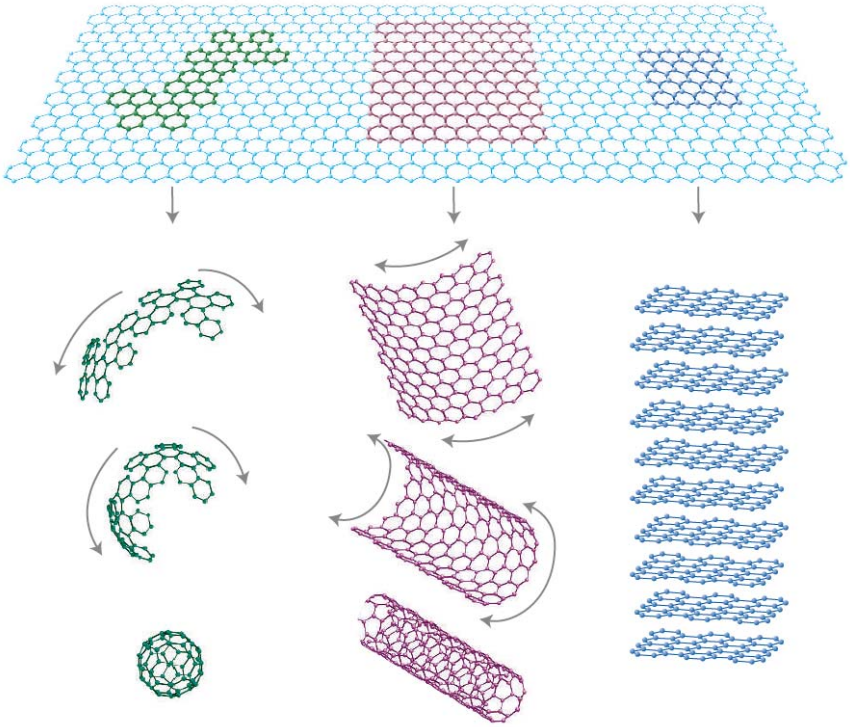

Figure 7.1 How two-dimensional graphene is a building block for other sp^2-bonded carbon allotropes such as zero-dimensional fullerenes, one-dimensional carbon nanotubes and three-dimensional crystalline graphite. [206].

Besides the above properties, the mechanical, tribological and chemical properties of graphene have also brought about an exciting area of research. Recent experiments have shown that graphene possesses extremely high intrinsic strength of up to 130 GPa, Young's modulus of up to 1 TPa, as well as ultra-low friction [211–214]. In terms of chemical properties, graphene is considered to be chemically inert and hydrophobic in nature, because of its non-polar covalent bonding which prevents hydrogen bonding with water [215]. Furthermore, it has been reported that a single-layer graphene membrane can exhibit impermeability to common gas molecules including helium [216]. These chemical characteristics of graphene are found to be

beneficial in making it an effective corrosion barrier layer for copper substrates [217].

Hence, just based on its remarkable mechanical, tribological and chemical properties, graphene is positioned as a material with great potential for countless applications in the future – especially for high strength, anti-wear and corrosion protection applications at the nanoscale. With this in mind, one of the possible applications for graphene could be as an ultrathin protective overcoat for commercial hard disk media. Clearly, the advantage of using an atomically-thin overcoat of graphene is that it would lead to a drastic reduction in the HMS and dramatically increase the areal density of HDDs [218]. Although this idea has been around for several years [218–220], no empirical results have been reported on the role of graphene as a protective overcoat layer for hard disk media. Thus, this chapter explores the use of single-layer graphene as a possible hard disk media overcoat. This was done by applying a graphene layer directly onto a bare commercial media disk surface and experimentally characterizing its tribological and corrosion protectiveness on commercial media.

7.2 Experimental methodology

The fabrication of single-layer graphene was performed with the help of an international collaborator. The graphene monolayer was first fabricated on copper substrates via a conventional CVD growth process using gaseous hydrocarbon precursors such as methane, which is one of the many processes used in producing commercial graphene on a large scale [221]. A specially

prepared bare commercial media disk without a protective commercial COC layer and without a PFPE lubricant layer was used as the starting substrate in this work, with a media structure similar to that of sample BM used in Sections 4.2 and 4.3, but from a newer batch. To differentiate this new bare media sample from the previous batch, it is named sample BM1 in this work. Using a typical wet etching and transfer process such as the one reported by Li et al. [222], the graphene layer was transferred onto the BM1 substrate. Each graphene film had an area of ~ 2 × 2 cm^2 in size. Due to the limitation whereby graphene transfer had to be performed in an ambient environment, no treatment was performed on the BM1 surface before graphene transfer, although efforts were made to maintain its cleanliness throughout the process. Hence it should be noted that a top native oxide layer would exist on the media surface before the graphene was applied.

Immediately after graphene transfer, visible Raman spectroscopy (514.5 nm) was performed on the coated media substrates to verify the presence of the graphene layer. Subsequently, ball-on-disk tribological tests were performed to evaluate its frictional properties and wear resistance. The wear resistance of the graphene layer was additionally evaluated by AES surface elemental mapping by observing the carbon intensity around the wear track region. Finally, to evaluate the corrosion protection properties, the graphene-coated media substrate was tested using the electrochemical potentiodynamic polarization technique.

7.3 Raman spectroscopy of the graphene overcoat

To determine the presence of the graphene overcoat on the media substrates, five visible Raman spectra were taken at five different locations within the ~ 2 × 2 cm^2 area of each sample, to ascertain that the whole area had been covered with graphene. Concurrently, a visible Raman spectrum of sample BM1 was also taken as a background spectrum. It was found that all five locations gave similar Raman spectra which showed two distinct characteristic peaks of graphene, namely the G and 2D peaks. Figure 7.2 shows a representative Raman spectrum taken at one of the locations on one of the graphene-coated media samples after background subtraction, with the G and 2D peaks labeled. Due to the absence of a significant number of defects in graphene, the D peak was almost absent in the Raman spectrum of graphene [223]. The spectrum and the location of the G and 2D peaks (at wavenumbers of 1580 cm^{-1} and 2680 cm^{-1} respectively) were consistent with that reported in literature [223, 224], showing that high quality graphene was indeed successfully deposited onto the commercial media substrates.

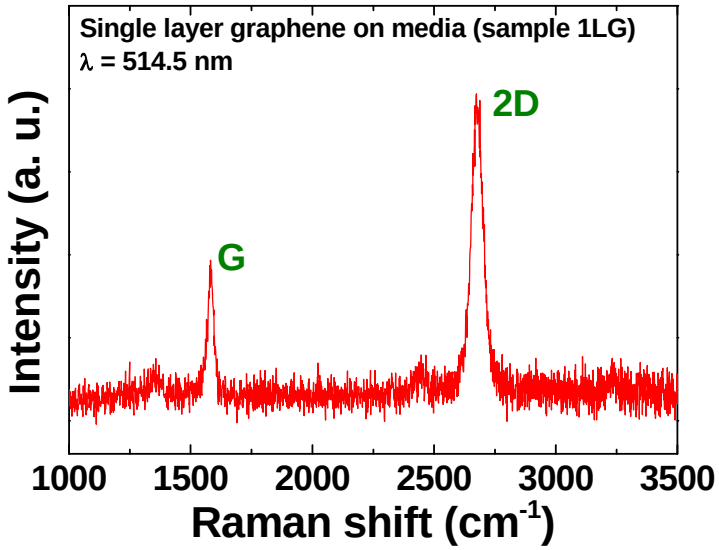

Figure 7.2 Visible Raman (514.5 nm) spectrum of single-layer graphene-coated commercial media sample 1LG, with its characteristic G and 2D peaks labeled.

7.4 Tribological performance

The tribological performance of the single-layer graphene-coated media sample (hereon referred to as sample 1LG) was compared with that of sample BM1 as well as a specially prepared commercial media disk sample with a ~ 2.7 nm commercial COC but without lubricant. Since this commercial disk sample was also from a different batch from sample CM used in Sections 4.2 and 4.3, it is named CM1 in this work. Figure 7.3(a) presents the combined plots of the COF versus number of cycles of the tribological test, whereas Figure 7.3(b) presents the optical micrographs of the wear track region and counterface ball for each sample after the tribological test.

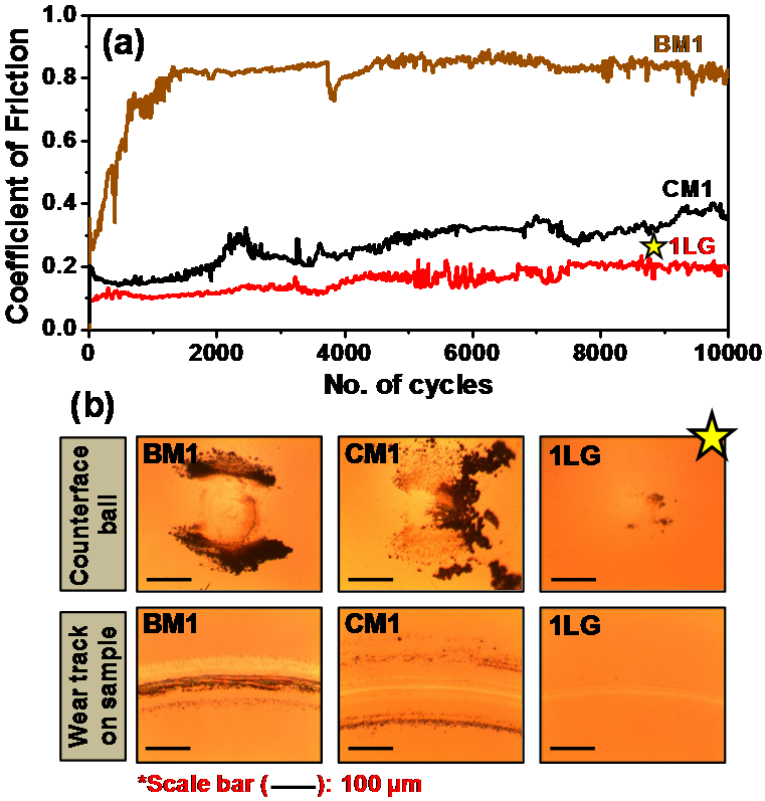

Figure 7.3 (a) Combined plot of COF versus number of cycles and (b) optical micrographs of the counterface ball and wear track region on samples BM1, CM1 and 1LG after the ball-on-disk tribological tests.

Surprisingly, it was revealed in Figure 7.3(a) that with respect to samples BM1 and CM1, sample 1LG exhibited distinctly lower friction, starting with an average COF of ~ 0.10 and ending at ~ 0.15 after 10,000 cycles. In comparison, samples BM1 and CM1 showed COF values of ~ 0.80 and ~ 0.35 at the end of the test. This result demonstrated the impressive role of a one-atom thick layer graphene in creating a low friction surface over bare commercial media, reducing the friction to less than 25% of what was observed for the bare media surface. Its frictional performance also exceeded that of commercial COC with much higher thickness of ~ 2.7 nm, thereby accentuating the excellent tribological characteristics of monolayer graphene. The wear resistance of the three samples after the tribological tests can also be compared by observing the optical micrographs of the counterface ball and

wear track region in Figure 7.3(b). At a glance, it can be seen that the tribological tests resulted in severe wear tracks and large amounts of debris transfer for samples BM1 and CM1, but in contrast, very little debris transfer and a small wear track was observed for sample 1LG. This result suggested that the introduction of the graphene layer significantly improved the wear resistance of commercial media, and enabled it to perform even better than commercial COC.

To further evaluate the wear resistance of the single-layer graphene, AES surface elemental imaging was performed at the wear track region of sample 1LG to image the surface intensities of C, O, Co and Cr inside and outside the wear track. Figures 7.4(a)–(d) present the surface elemental color maps of C, O, Co and Cr respectively, and Figure 7.4(e) presents a SEM image of the analyzed region as a reference. In the AES color maps, the hotter colors (such as red) represent a high intensity of the element in that region, whereas the cooler colors (such as black and blue) represent a low intensity of the element in that region, according to the color scale on the right.

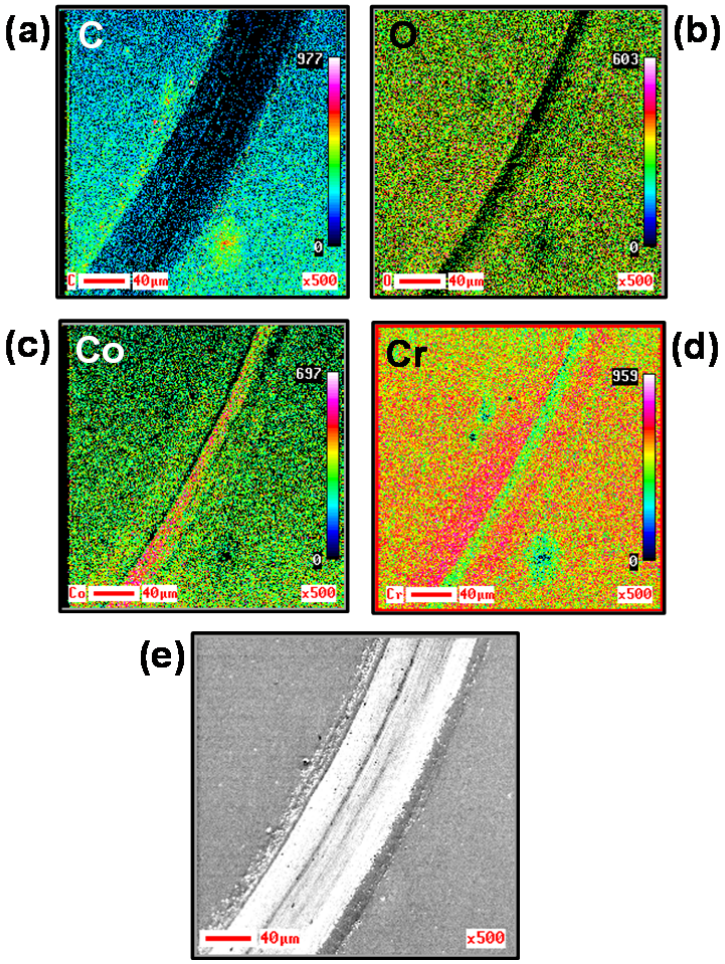

Figure 7.4 AES surface elemental color maps of (a)–(d) C, O, Co and Cr, respectively, at the wear track region of sample 1LG after the ball-on-disk tribological test. (e) SEM image of the analyzed area for AES elemental mapping.

As can be seen from the maps, sample 1LG had a low intensity of C inside the wear track as compared to the regions outside the wear track. Correspondingly, higher amounts of Co and Cr were observed in the region inside the wear track as compared to outside the wear track. This clearly indicated that the graphene inside the wear track region had been removed by wear after the tribological test, simultaneously exposing the underlying media (which contains Co and Cr). Additionally, it was observed that the intensity of O was particularly low in the middle of the wear track. This can be explained

by the presence of high amounts of Co and Cr in the middle of the wear track, which could have been much higher in relation to O, thus lowering the relative intensity of O. Finally, a comment should be made about the relatively high intensities of O, Co and Cr outside the wear track as well. This observation can be attributed to the thinness of the monolayer graphene overcoat (~ 3.5 Å), which is thin enough to allow the Auger electrons from O, Co and Cr in the underlying media to escape out of the surface and be detected. The question may arise as to why the COF observed in the tribological test was still low (~ 0.15) even at the end of the wear test. A possible reason could be that the worn-out graphene flakes or debris are trapped as third-body particles between the counterface ball and the media which could act as a lubricating agent at the interface.

7.5 Corrosion performance

Representative Tafel plots of the potentiodynamic polarization curves for samples BM1, CM1 and 1LG are plotted in a combined plot in Figure 7.5, in order to compare the differences in the corrosion behavior for the three samples. The j_{corr} values of the samples were extrapolated from these plots and are tabulated in Table 7.1. It was expected that sample BM1 which did not contain any protective overcoat gave the highest j_{corr} of ~ 23 nA/cm^2, showing that the corrosion rate was the highest when no protective overcoat was applied on the media. In contrast, sample CM1 with a ~ 2.7 nm thick COC gave the lowest j_{corr} of ~ 4.5 nA/cm^2, thus exhibiting the lowest corrosion rate and highest corrosion resistance out of all three samples. In comparison, the

j_{corr} of 1LG was found to be ~ 8.1 nA/cm^2, which was considerably lower than that of sample BM1, but still higher than that of sample CM1.

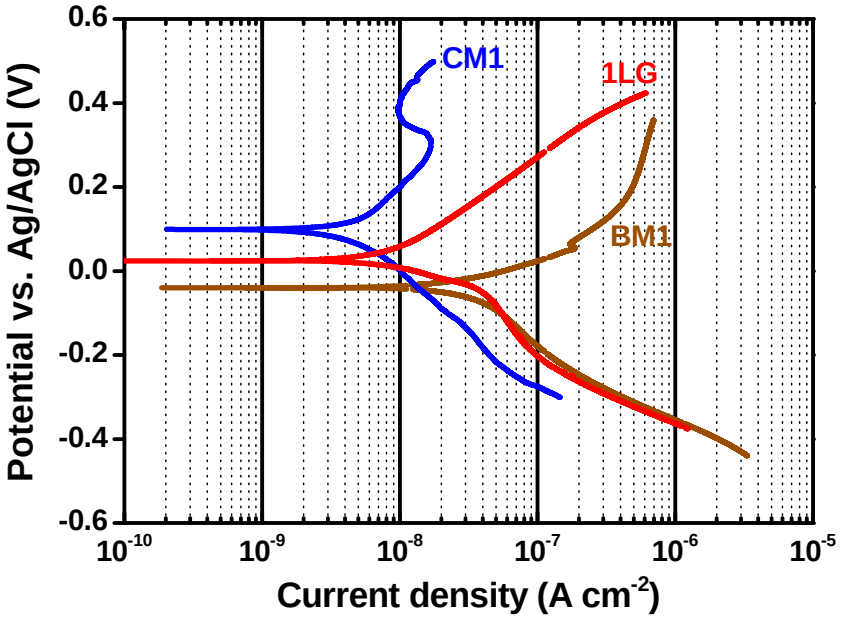

Figure 7.5 Tafel plots showing the potentiodynamic polarization curves of the three samples CM1, BM1 and 1LG, from which the j_{corr} values are extracted.

Table 7.1 Values of j_{corr} and calculated PEs based on the Tafel plots in Figure 7.5.

Sample Nomenclature	j_{corr} extrapolated from the Tafel plot in Figure 7.5 (nA/cm^2)	PE (%)
BM1	23	--
CM1	4.5	80.4
1LG	8.1	64.8

The protectiveness of the commercial COC and the graphene overcoat can be compared by calculating their protective efficiencies (PE) using the equation introduced previously in Section 4.2.2. The PEs of samples CM1 and 1LG were calculated using the j_{corr} value of the bare media sample BM1 as j^0_{corr} (which is 23 nA/cm^2), and are tabulated in Table 7.1. Despite the commercial disks coming from a new batch, it can be seen that the PE of the

commercial COC in sample CM1 of 80.4% was quite similar to that of sample CM in the previous batch which showed a PE of 82.9% when compared with BM. In comparison, the PE of 1LG was 64.8%, which is markedly lower than that of CM1. It is amazing, however, that just a monolayer of graphene was still able to reduce the corrosion rate of the bare commercial media surface by more than 50%. This highlights the efficiency of a monolayer of graphene in acting as a barrier layer to provide a certain amount of corrosion protection for the underlying media.

7.6 Conclusions and future work

Experimental results of single-layer graphene on commercial hard disk media have shown that a one-atom thick graphene layer of only ~ 3.5 Å had the capability to significantly improve the tribological properties and corrosion resistance of a bare media surface. However, in terms of wear resistance based on surface elemental analysis, it was found that the graphene layer was not able to withstand the rigorous ball-on-disk tribological testing of up to 10,000 cycles, in contrast to the ultrathin FCVA-processed overcoats used in Chapters 4 and 5. Furthermore, the corrosion protection of single-layer graphene was not sufficient to meet the protectiveness of commercial media COC. Therefore, despite the mono-atomic thinness of single-layer graphene which is desirable for drastically reducing the HMS, the results indicate that it is still not quite protective enough for wear and corrosion protection in HDDs.

Nevertheless, it is worthy to mention here that based on the current technology of graphene growth, there were many limitations in this

experiment which may have affected the performance of graphene and even the results of this experiment, such as the oxidation of the media surface before graphene transfer and the wet transfer process of graphene itself onto the media surface. Hence, much more work is needed to develop a clean and carefully controlled process for graphene on media for the experiment to be more reliable. In addition, further experiments could be performed on multi-layer graphene overcoats to evaluate the dependence of the corrosion and wear performance on the number of graphene layers used. It is expected that with higher overall thickness, although the HMS would be increased, the corrosion protection would be reduced. In terms of tribological protection, it is possible that multi-layer graphene could have a different mechanism for lowering friction as compared to single-layer graphene, due to low friction sliding between the graphene layers.

Chapter 8: Conclusions and future work

As the areal densities of magnetic storage systems continue to increase in the future, the necessary reduction of the magnetic spacing requires the protective overcoats at the head-media interface to be thinned down further while maintaining their reliability. Ultrathin carbon-based overcoats have shown their efficacy in such aggressive environments. Besides being chemically inert, amorphous carbon films with sufficiently high sp^3C content can possess high mechanical strength for high wear resistance, high density and coverage for good corrosion/oxidation resistance, and high thermal stability. In this thesis, several carbon-based overcoat designs were introduced to tailor the microstructure (i.e. maintain or improve the sp^3C content) at ultrathin levels and improve the interfacial bonding. These overcoats were found to exhibit improved wear resistance (in terms of low debris generation in ball-on-disk tribological tests), higher wear durability (from long-term tape tests), high corrosion/oxidation resistance and low friction. In the following sections, the highlights of all the works described in this thesis to create ultrathin protective carbon-based overcoats (monolithic, bi-layer and overcoats possessing a composite interlayer and/or interfacial layer) for magnetic hard disk media and magnetic tape heads are reviewed. Finally, some future works in this research area are proposed.

8.1 Ultrathin carbon-based overcoats for future magnetic hard disk media

For HDDs, current media COCs that are fabricated via conventional techniques are not able to effectively protect the media at thicknesses of ≤ 2 nm, and are not thermally stable for future HAMR technology which is required to achieve areal densities of > 1 Tb/in^2. By tuning the carbon ion energy during the deposition process, higher sp^3C content and better carbon-substrate mixing can be achieved at lower thicknesses as compared to conventional PECVD and sputtering processes. As such, the FCVA technique was used to develop the media overcoats. A bi-level energy process using C^+ ion bombardment at 350 eV followed by overcoat deposition at 90 eV was employed on commercial CoCrPt:Oxide media, which promoted the formation of a dense, nano-layered COC. This ~ 1.8 nm COC was found to have enhanced tribological properties and wear resistance, as well as similar corrosion resistance as compared to commercial PECVD-processed COC with ~ 2.7 nm thickness. Moreover, the FCVA bi-level energy processed COC was capable of withstanding HAMR-like conditions, demonstrating outstanding thermal stability due to its higher sp^3C content. Upon laser irradiation, no carbon degradation was found on the FCVA-processed overcoat after microstructural and topographical analyses were performed at the irradiated spot.

Nevertheless, the high energy 350 eV pre-treatment step was found to be detrimental to the macromagnetic properties of the recording layer, resulting in the increase of its overall coercivity due to the displacement of the

media atoms in the top recording layer. Through additional optimization of the FCVA process, a bi-level energy process of 90 eV followed by 50 eV was subsequently developed. The resultant ~ 1.8 nm overcoat demonstrated excellent tribological properties and corrosion resistance properties without any degradation in the magnetic performance.

The application of an atomically-thin (~ 4 Å) SiN_x interlayer between the media substrate and a ~ 12 Å carbon overlayer fabricated by FCVA was a new design considered in this thesis. This 16 Å bi-layer overcoat of SiN_x/C was found to be effective not only in providing good corrosion resistance but also showed a much higher wear resistance and better tribological performance than commercial media COC. The enhanced performance of the overcoat was due to the beneficial effect of the SiN_x interlayer, which is known to be a good corrosion-inhibiting barrier as well as a good adhesion layer for metals and carbon due to its tendency to form strong bonds with these elements. Not only did it contribute to the higher corrosion resistance, but through the formation of strong interfacial bonds between the atomically-thin SiN_x and both the media substrate and carbon overlayer, the wear resistance was improved. In addition, the SiN_x interlayer was found to act as an ultrathin barrier layer between carbon and the media atoms containing transition elements such as Co and Pt which can act as catalysts in the transformation of $sp^3C \rightarrow sp^2C$ in the carbon layer. Hence, the presence of the SiN_x barrier layer also helped in maintaining or improving the sp^3C content within the carbon overlayer.

Finally, some initial experiments were conducted using monolayer graphene as an overcoat. While it showed better tribological properties and better corrosion performance as compared to bare commercial media, monolayer graphene did not perform as well as the FCVA-processed carbon-based overcoats in terms of wear and corrosion resistance, albeit being just ~ 3.5 Å thin.

8.2 Ultrathin carbon-based overcoats for future magnetic tape heads

In magnetic tape drives, a magnetic spacing of 22 nm is desired by 2018 to achieve an areal density of ~ 20 Gb/in^2. Degradation of the magnetic spacing occurs through excessive wear both on the tape head as well as on the tape, leading to accumulation of debris, PTR and undesirable tribo-chemical reactions between the tape media and head. With the application of an ultrathin wear-durable tape head overcoat to prevent direct contact between the tape and the head surface, such issues can be eliminated or delayed. Carbon-based overcoats of ≤ 20 nm (based on approximately half of the magnetic spacing budget of ~ 36 nm in 2012 when the project was started) were developed for magnetic tape heads in this thesis, with the objective of improving the lifetime of the tape head by reducing the amount of wear at the head-tape interface.

The SiN_x/C bi-layer overcoat design was proposed for this work, considering the excellent qualities of SiN_x as an adhesion interlayer which could contribute to high wear durability of the overcoat. On top of that, the

SiN_x interlayer is electrically insulating which would prevent shorting of the read elements at the tape head surface. Two different SiN_x/C overcoats for the tape head were studied, using two different processes to fabricate the carbon layer – one by conventional magnetron sputtering (giving an overall SiN_x/a-C overcoat thickness of ~ 7 nm) and one by the FCVA bi-level energy process of 350 eV followed by 90 eV (giving an overall SiN_x/ta-C overcoat thickness of ~ 20 nm). Additionally, both overcoats were applied onto electrically functional tape heads for the first time to evaluate their performance with commercial tape media in a simulated tape drive environment.

When compared with its monolithic ~ 7 nm a-C counterpart, the SiN_x/a-C overcoat developed by sputtering exhibited better wear performance in 1 million meter tape tests as a result of strong interfacial bonding at the two enhanced interfaces of carbon-SiN_x and SiN_x-AlTiC. When applied on the functional tape head, it survived up to 3 million meters of tape testing. However, in comparison, the ~ 20 nm SiN_x/ta-C bi-layer overcoat developed using the FCVA bi-level energy process demonstrated a remarkable wear life of up to 40–50 million meters of tape testing. This great improvement in the wear life as seen in the SiN_x/ta-C bi-layer overcoat over the SiN_x/a-C overcoat could be attributed to three factors: 1) greater amount of intermixing between the carbon overlayer and SiN_x interlayer due to the 350 eV pre-treatment step in SiN_x/ta-C, 2) higher amount of sp^3C content in the ta-C layer of SiN_x/ta-C, and 3) higher thickness of the SiN_x/ta-C overcoat.

To address the third factor, a separate experiment was conducted on monolithic carbon and bi-layer SiN_x/C overcoats fabricated by either the

sputtering or the FCVA process with similar thicknesses of ~ 17–20 nm, in order to compare the carbon microstructure as well as the intrinsic mechanical and electrical properties of the different overcoats. It was revealed that the FCVA-processed overcoats indeed exhibited much higher sp^3C bonding as compared to the sputtered overcoats. This was also the main contributor to the higher overall hardness and higher electrical resistivity obtained for the FCVA-processed overcoats than the sputtered overcoats. Additionally, by introducing a 3 nm SiN_x interlayer in the bi-layer sputter-processed and FCVA-processed SiN_x/C overcoats, this resulted in the creation of two enhanced carbon-SiN_x and SiN_x-AlTiC substrate interfaces possessing extensive interfacial bonding, which contributed to the overcoats' higher wear durability as compared to their monolithic counterparts. As such, it can be concluded that both high sp^3C bonding and enhanced interfacial bonding are very crucial factors in creating overcoats for tape heads with high wear durability for the tape drive environment.

8.3 Novelty of the thesis

Based on this work, several novel ultrathin protective carbon-based overcoats for HDD media and magnetic tape drive heads were developed and investigated in terms of their functional performance, chemical bonding environment, interfacial chemistry and carbon microstructure, with the goal of making such overcoats feasible for implementation in actual HDDs and tape drives.

HDD media overcoat thicknesses of 1.6–1.8 nm were fabricated to achieve an areal density of 4 Tb/in^2, which is projected to be achieved only by 2020–21 based on the current roadmap [13]. Hence, the media overcoats developed in this work may enable HMS requirement to be achieved well ahead of the roadmap's timeline. By tailoring the energetics of the carbon species during deposition, such as via the FCVA process which was used in this work, a COC with high sp^3C bonding can be obtained. As a result, the FCVA-processed carbon-based media overcoats developed in this work showed comparable corrosion and better wear/friction performance than thicker commercial COCs (~ 2.7 nm) as well as high thermal stability in HAMR conditions.

In magnetic tape drives, the improvement in the wear durability of 7 to 20 nm tape head overcoats was addressed by enhancing the adhesion and interfacial bonding at the head substrate-overcoat interface, which is counterintuitive to conventional approaches of overcoat fabrication. The ~ 20 nm FCVA-processed SiN_x/C bi-layer tape head overcoat developed in this work, which was deposited on an electrically functional tape head, demonstrated an exceptional wear life of up to 40–50 million meters after being subjected to long-term testing in a simulated tape drive environment without damaging its electrical functionality. This is the best performance reported in literature to date.

In the final part of this work, an atomically-thin (~ 3.5 Å) monolayer graphene overcoat was explored to investigate its protectiveness on commercial HDD media. Such a low thickness would contribute to a

substantial reduction in the magnetic spacing at the HDI. Based on preliminary results, monolayer graphene was shown to improve the tribological properties and corrosion resistance of uncoated commercial media despite its thinness.

8.4 Future work

The ever-increasing demand for digital data storage positions magnetic storage systems such as HDDs and tape drives favorably for the near future, due to their low cost and competitive storage performance. However, to further increase the areal densities in these systems above what has been discussed in this thesis, major efforts to advance the current HDD and tape drive technology are still required.

Firstly, the improvement of the tribological and wear properties of the overcoats developed in this thesis have been related to the enhanced interfacial bonding, as observed through characterization methods such as XPS, TOF-SIMS and AES. However, to obtain a fundamental understanding of how the role of enhanced interfaces contributes to the improved friction, it would be useful to perform atomic-level simulations to probe the friction mechanisms occurring at the interface. Not only can the FCVA-processed and bi-layer overcoats on commercial HDD media and AlTiC substrates be studied, but the application of the monolayer graphene overcoat on commercial HDD media substrate (which was observed to reduce the friction of the bare media surface) can be studied as well.

Secondly, the use of the PFPE lubricant has not been thoroughly explored in this work for hard disk media overcoats. More extensive testing on

these developed overcoats coated with a monolayer of PFPE lubricant can be performed to study its role in reducing the surface energy and friction, for example, in terms of lubricant-overcoat interaction on the FCVA-processed media overcoats. In addition, other types of lubricants such as PFPE ionic liquids, which have been reported to show improved frictional properties as compared to conventional PFPE lubricants [225], can be further explored. Furthermore, in subsequent stages towards drive-level implementation, functional testing of the PFPE- and carbon-coated disks could be performed, such as disk flyability tests and lubricant pickup analyses.

Thirdly, for the tape head overcoats, environmental testing could be carried out to understand the role of environmental factors in affecting the wear durability of the developed overcoats. For example, functional testing could be conducted at various relative humidities (RH) and temperatures to analyze the effect of the environment on the wear of the overcoat. For example, previous experiments on overcoats deposited on tape heads have shown that the RH can significantly affect the overcoat's wear performance [107].

Fourthly, other carbon-based materials or structures for media and tape head overcoats can be explored to obtain higher wear durability. One of the potential materials is nitrogenated carbon (a-C:N or ta-C:N), which was found to possess enhanced wear durability of 3 to 4 times over a-C films at a thickness of 5 nm on hard disk media [226]. These films can be fabricated by sputtering or by FCVA using carbon targets in a nitrogenated environment. Alternatively, the HiPIMS technique can be considered to deposit nitrogenated

carbon films in an Ar/N_2 atmosphere using C^+ ions, while the C^+ ion energy can be tuned by varying the substrate bias similar to FCVA. Furthermore, multilayered structures containing two different carbon-based materials in an alternating fashion could also be explored (e.g. ta-C:N/ta-C/ta-C:N). The benefit of such multilayers is the generation of boundaries between the layers which may inhibit the propagation of cracks through the whole overcoat, thereby increasing the overcoat toughness [155]. In addition, graphene may also be explored as an overcoat for tape heads.

Finally, the reduction of friction and stiction at the head-tape interface is important for reducing the amount of wear. One of the ways that this can be achieved is by incorporating a texture on the overcoat surface which effectively reduces the contact area between the tape and the head. This may be done by depositing the tape head overcoat via a patterning process or by patterning the tape head overcoat after deposition. A significant amount of theoretical simulations, optimization and calibration work will be required in order to analyze the best surface texture which will give the lowest friction or stiction.

List of Publications, Conferences, Workshops and Awards

Selected Publications

1. **R. J. Yeo**, N. Dwivedi, S. Tripathy, and C. S. Bhatia, "Excellent wear life of silicon nitride/tetrahedral amorphous carbon bilayer overcoat on functional tape heads", *Applied Physics Letters* **106**, 091604 (2015).

2. **R. J. Yeo**, N. Dwivedi, L. Zhang, Z. Zhang, C. Y. H. Lim, S. Tripathy, and C. S. Bhatia, "Durable ultrathin silicon nitride/carbon bilayer overcoats for magnetic heads: the role of enhanced interfacial bonding", *Journal of Applied Physics* **117**, 045310 (2015).

3. **R. J. Yeo**, N. Dwivedi, E. Rismani, N. Satyanarayana, S. Kundu, P. S. Goohpattader, H. R. Tan, N. Srinivasan, B. Druz, S. Tripathy, and C. S. Bhatia, "Enhanced tribological, corrosion, and microstructural properties of an ultrathin (< 2 nm) silicon nitride/carbon bilayer overcoat for high density magnetic storage", *ACS Applied Materials & Interfaces* **6**, 9376 (2014).

4. **R. J. Yeo**, E. Rismani, N. Dwivedi, D. J. Blackwood, H. R. Tan, Z. Zhang, S. Tripathy, and C. S. Bhatia, "Bi-level surface modification of hard disk media by carbon using filtered cathodic vacuum arc: reduced overcoat thickness without reduced corrosion performance", *Diamond and Related Materials* **44**, 100 (2014).

5. N. Dwivedi*, **R. J. Yeo***, Z. Zhang, C. Dhand, S. Tripathy, and C. S. Bhatia, "Interface engineering and controlling the friction and wear of ultrathin carbon films: high sp^3 versus high sp^2 carbons", accepted for publication in *Advanced Functional Materials* (2016). (*authors with equal contributions)

6. N. Dwivedi, **R. J. Yeo**, N. Satyanarayana, S. Kundu, S. Tripathy, and C. S. Bhatia, "Understanding the role of nitrogen in plasma-assisted surface modification of magnetic recording media with and without ultrathin carbon overcoats", *Scientific Reports* **5**, 7772 (2015).

7. N. Dwivedi, **R. J. Yeo**, P. S. Goohpattader, N. Satyanarayana, S. Tripathy, and C. S. Bhatia, "Enhanced characteristics of pulsed DC sputtered ultrathin (<2 nm) amorphous carbon overcoats on hard disk magnetic media", *Diamond and Related Materials* **51**, 14 (2015).

8. E. Rismani, **R. Yeo**, H. Mirabolghasemi, W. M. Kwek, H. Yang, and C. S. Bhatia, "An ultrathin multilayer TiN/SiN wear resistant coating for advanced magnetic tape drive heads", *Thin Solid Films* **556**, 354 (2014).

9. E. Rismani, **R. Yeo**, S. K. Sinha, H. Yang, and C. S. Bhatia, "Developing an $(Al,Ti)N_xC_y$ interlayer to improve the durability of the ta-C coating on magnetic recording heads", *Tribology Letters* **50**, 233 (2013).

10. N. Dwivedi, N. Satyanarayana, **R. J. Yeo**, H. Xu, K. P. Loh, S. Tripathy, and C. S. Bhatia, "Ultrathin carbon with interspersed graphene/fullerene-like nanostructures: a durable protective overcoat for high density magnetic storage", *Scientific Reports* **5**, 11607 (2015).

11. N. Dwivedi, E. Rismani-Yazdi, **R. J. Yeo**, P. S. Goohpattader, N. Satyanarayana, N. Srinivasan, B. Druz, S. Tripathy, and C. S. Bhatia, "Probing the role of an atomically thin SiN_x interlayer on the structure of ultrathin carbon films", *Scientific Reports* **4**, 5021 (2014).

Conferences

1. **R. J. Yeo**, N. Dwivedi, S. Tripathy, and C. S. Bhatia, "Silicon nitride/tetrahedral amorphous carbon bilayer overcoat for exceptional wear life of functional tape heads", IEEE International Magnetics Asia Conference 2015 (INTERMAG 2015), May 11–15, Beijing, China, 2015. (Poster Presentation).

2. **R. J. Yeo**, N. Dwivedi, C. Y. H. Lim, and C. S. Bhatia, "A facile approach of fabricating ultra-thin wear resistant $Si/SiN_x/C$ overcoats for magnetic tape recording heads", ASME 2014 Conference on Information Storage and Processing Systems (ISPS 2014), June 23–24, Santa Clara University, Santa Clara, CA, USA, 2014. (Oral Presentation).

3. **R. J. Yeo**, "Ultra-thin wear resistant overcoats for future generation of magnetic data storage systems", International Forum on Front-line of Tribology in Asian Region, Japanese Society of Tribologists (JAST) Tribology Conference 2014, May 19–21, Tokyo, Japan, 2014. **(Invited Talk)**.

4. **R. J. Yeo**, E. Rismani, N. Satyanarayana, D. J. Blackwood, and C. S. Bhatia, "Effect of developing a graded carbon embedded layer on the corrosion performance of commercial hard disk magnetic media", Yamada Conference LXVII – The 8^{th} International Symposium on Metallic Multilayers 2013 (MML 2013), May 19–24, Tokyo, Japan, 2013. (Poster Presentation).

5. **R. J. Yeo**, S. K. Sinha, and C. S. Bhatia, "Effect of filtered cathodic vacuum arc C^+ ion embedment on the corrosion resistance of hard disk magnetic media", MRS International Conference of Young Researchers on Advanced Materials 2012 (ICYRAM 2012), July 1–6, Singapore, 2012. (Poster Presentation).

6. E. Rismani, **R. J. Yeo**, N. Satyanarayana, M. A. Samad, S. K. Sinha, H. Yang, and C. S. Bhatia, "Ultra-thin overcoats for future hard disks", The Asia-Pacific Magnetic Recording Conference 2012 (APMRC 2012), October 31–November 2, Singapore, 2012. (Poster Presentation).

Patents

1. C. S. Bhatia, E. Rismani, N. Satyanarayana and **R. J. Yeo**, "A bilayer ultrathin coating to protect the hard disk media surface against wear and corrosion and improve the thermal stability of the media overcoat in HAMR condition", ILO Ref: ID14154N, USA Provisional Application No: 61/940,537, (2014).

Workshops

1. C. S. Bhatia and **R. J. Yeo**, Information Storage Industry Consortium (INSIC) TAPE Program Quarterly Technical Reviews Q49, Q51 and Q53–56.

    - Quarterly Technical Review Q49 (May 15, 2012)
    - Quarterly Technical Review Q51 (November 14, 2012)
    - Quarterly Technical Review Q53 (May 14, 2013)
    - Quarterly Technical Review Q54 (August 13, 2013)
    - Quarterly Technical Review Q55 (November 13, 2013)
    - Quarterly Technical Review Q56 (February 20, 2014)

2. **R. J. Yeo**, "Tribological and corrosion performance of surface modified commercial hard disk media", NUS ECE Graduate Students Symposium 2013 (GSS 2013), February 27, 2013. (Oral Presentation).

Awards

1. IEEE Magnetics Society Student Travel Grant for INTERMAG 2015, May 11–15, Beijing, China, 2015.

2. ASME ISPS 2014 Conference Scholarship Award for ISPS 2014, June 23–24, Santa Clara, CA, USA, 2014.

3. JAST Tribology Conference 2014, May 19–21, Tokyo, Japan, 2014. **(Invited Talk)**. "Travel expense support" award.

References

[1] E. D. Daniel, C. D. Mee, and M. H. Clark, *Magnetic Recording: The First 100 Years*, 1st ed. New York, USA: Wiley-IEEE Press, 1998.

[2] IBM Archives. *IBM 350 disk storage unit* [Online]. Available: https://www-03.ibm.com/ibm/history/exhibits/storage/storage_350.html. (Accessed August 11, 2015).

[3] EMC Digital Universe Infobrief, "The Digital Universe of Opportunities", International Data Corporation, Apr. 2014.

[4] G. Binasch, P. Grünberg, F. Saurenbach, and W. Zinn, "Enhanced magnetoresistance in layered magnetic structures with antiferromagnetic interlayer exchange", *Physical Review B* **39**, 4828 (1989).

[5] M. N. Baibich, J. M. Broto, A. Fert, F. N. Van Dau, F. Petroff, P. Etienne, G. Creuzet, A. Friederich, and J. Chazelas, "Giant Magnetoresistance of (001)Fe/(001)Cr Magnetic Superlattices", *Physical Review Letters* **61**, 2472 (1988).

[6] S. Yuasa, T. Nagahama, A. Fukushima, Y. Suzuki, and K. Ando, "Giant room-temperature magnetoresistance in single-crystal Fe/MgO/Fe magnetic tunnel junctions", *Nature Materials* **3**, 868 (2004).

[7] S. S. P. Parkin, C. Kaiser, A. Panchula, P. M. Rice, B. Hughes, M. Samant, and S.-H. Yang, "Giant tunnelling magnetoresistance at room temperature with MgO (100) tunnel barriers", *Nature Materials* **3**, 862 (2004).

[8] C. Reig, C.-B. Maria-Dolores, and D. R. Munoz, "Magnetic field sensors based on giant magnetoresistance (GMR) technology: Applications in electrical current sensing", *Sensors* **9**, 7919 (2009).

[9] W. J. Gallagher and S. S. P. Parkin, "Development of the magnetic tunnel junction MRAM at IBM: From first junctions to a 16-Mb MRAM demonstrator chip", *IBM Journal of Research and Development* **50**, 5 (2006).

[10] Q. H. Zeng and D. B. Bogy, "Stiffness and Damping Evaluation of Air Bearing Sliders and New Designs With High Damping", *Journal of Tribology* **121**, 341 (1999).

[11] H. Kohira, V. Prabhakaran, and F. E. Talke, "Effect of air bearing design on wear of diamond-like carbon coated proximity recording sliders", *Tribology International* **33**, 315 (2000).

[12] Z. Damjanovic. (2011). *HDD head assembly* [Online]. Available: http://www.hddsurgery.com/blog/show/article/hdd-head-assembly. (Accessed July 7, 2015).

[13] B. Marchon, T. Pitchford, Y.-T. Hsia, and S. Gangopadhyay, "The Head-Disk Interface Roadmap to an Areal Density of 4 Tbit/in^2", *Advances in Tribology* **2013**, 521086 (2013).

[14] G.-G. Wang, X.-P. Kuang, H.-Y. Zhang, C. Zhu, J.-C. Han, H.-B. Zuo, and H.-T. Ma, "Silicon nitride gradient film as the underlayer of ultra-thin tetrahedral amorphous carbon overcoat for magnetic recording slider", *Materials Chemistry and Physics* **131**, 127 (2011).

[15] N. Yasui, H. Inaba, and N. Ohtake, "Influence of Substrates on Initial Growth of Diamond-Like Carbon Films", *Applied Physics Express* **1**, 035002 (2008).

[16] C. S. Bhatia, S. Anders, K. Bobb, R. Hsiao, I. G. Brown, and D. B. Bogy, "Ultra-Thin Overcoats for the Head/Disk Interface Tribology", *Journal of Tribology: Transactions of the ASME* **120**, 795 (1998).

[17] H. Han, F. Ryan, and M. McClure, "Ultra-thin tetrahedral amorphous carbon film as slider overcoat for high areal density magnetic recording", *Surface and Coatings Technology* **120–121**, 579 (1999).

[18] H. Inaba, K. Furusawa, S. Hirano, S. Sasaki, S. Todoroki, M. Yamasaka, and M. Endou, "Tetrahedral Amorphous Carbon Films By Filtered Cathodic Vacuum-Arc Deposition For Air-Bearing-Surface Overcoat", *Japanese Journal of Applied Physics* **42**, 2824 (2003).

[19] C. Casiraghi, A. C. Ferrari, R. Ohr, D. Chu, and J. Robertson, "Surface properties of ultra-thin tetrahedral amorphous carbon films for magnetic storage technology", *Diamond and Related Materials* **13**, 1416 (2004).

[20] C. S. Bhatia, C.-Y. Chen, W. Fong, and D. B. Bogy, "Tribochemistry of ZDOL Decomposition on Carbon Overcoats in Ultra-High Vacuum (UHV)", *MRS Online Proceedings Library* **594**, (1999).

[21] C. S. Bhatia, W. Fong, C. Chao-Yuan, W. Jianjun, D. B. Bogy, S. Anders, T. Stammler, and J. Stohr, "Tribo-chemistry at the head/disk interface", *IEEE Transactions on Magnetics* **35**, 910 (1999).

[22] P. H. Kasai, W. T. Tang, and P. Wheeler, "Degradation of perfluoropolyethers catalyzed by aluminum oxide", *Applied Surface Science* **51**, 201 (1991).

[23] J. Robertson, "Ultrathin carbon coatings for magnetic storage technology", *Thin Solid Films* **383**, 81 (2001).

[24] B. D. Strom, D. B. Bogy, R. G. Walmsley, J. Brandt, and C. S. Bhatia, "Gaseous wear products from perfluoropolyether lubricant films", *Wear* **168**, 31 (1993).

[25] T. C. Arnoldussen and E.-M. Rossi, "Materials for Magnetic Recording", *Annual Review of Materials Science* **15**, 379 (1985).

[26] T. Toyaguchi and T. Yamamoto, "Material and tribological properties of a-C:H film by plasma CVD for a disk overcoat", *IEEE Transactions on Magnetics* **34**, 1741 (1998).

[27] T. Yamamoto and H. Hyodo, "Amorphous carbon overcoat for thin-film disk", *Tribology International* **36**, 483 (2003).

[28] S. S. Perry, C. M. Mate, R. L. White, and G. A. Somorjai, "Bonding and tribological properties of perfluorinated lubricants and hydrogenated amorphous carbon films", *IEEE Transactions on Magnetics* **32**, 115 (1996).

[29] A. C. Ferrari, "Diamond-like carbon for magnetic storage disks", *Surface and Coatings Technology* **180-181**, 190 (2004).

[30] D. J. Li, M. U. Guruz, C. S. Bhatia, and Y.-W. Chung, "Ultrathin CN_x overcoats for 1 Tb/in^2 hard disk drive systems", *Applied Physics Letters* **81**, 1113 (2002).

[31] J. Robertson, "Requirements of ultrathin carbon coatings for magnetic storage technology", *Tribology International* **36**, 405 (2003).

[32] A. G. Merzlikine, L. Li, P. Jones, and Y.-T. Hsia, "Lubricant layer formation during the dip-coating process: influence of adsorption and viscous flow mechanisms", *Tribology Letters* **18**, 279 (2005).

[33] G. E. Totten, *Handbook of Lubrication and Tribology: Volume 1 Application and Maintenance*, 2nd ed. vol. 1. Boca Raton, FL, USA: CRC Press, Taylor & Francis Group, 2006.

[34] P. Kasai, "Z-dol and carbon overcoat: the bonding mechanism", *Tribology Letters* **26**, 93 (2007).

[35] R. P. Ambekar, D. B. Bogy, and C. S. Bhatia, "Lubricant Depletion and Disk-to-Head Lubricant Transfer at the Head-Disk Interface in Hard Disk Drives", *Journal of Tribology* **131**, 031901 (2009).

[36] X.-C. Guo, B. Knigge, B. Marchon, R. J. Waltman, M. Carter, and J. Burns, "Multidentate functionalized lubricant for ultralow head/disk spacing in a disk drive", *Journal of Applied Physics* **100**, 044306 (2006).

[37] P. H. Kasai and T. Shimizu, "Bonding of Hard Disk Lubricants with OH-Bearing End Groups", *Tribology Letters* **46**, 43 (2012).

[38] Q. Zhao, H. J. Kang, F. E. Talke, D. J. Perettie, and T. A. Morgan, "Tribological study of phosphazene-type additives in perfluoropolyether lubricant for hard disk applications", *Lubrication Engineering* **55**, 16 (1999).

[39] T. Shiramatsu, M. Kurita, K. Miyake, M. Suk, S. Ohki, H. Tanaka, and S. Saegusa, "Drive Integration of Active Flying-Height Control Slider With Micro Thermal Actuator", *IEEE Transactions on Magnetics* **42**, 2513 (2006).

[40] M. Suk, K. Miyake, M. Kurita, H. Tanaka, S. Saegusa, and N. Robertson, "Verification of thermally induced nanometer actuation of magnetic recording transducer to overcome mechanical and magnetic spacing challenges", *IEEE Transactions on Magnetics* **41**, 4350 (2005).

[41] C. M. Mate, Q. Dai, R. N. Payne, B. E. Knigge, and P. Baumgart, "Will the numbers add up for sub-7-nm magnetic spacings? Future metrology issues for disk drive lubricants, overcoats, and topographies", *IEEE Transactions on Magnetics* **41**, 626 (2005).

[42] J. Li, B. Liu, W. Hua, and Y. Ma, "Effects of intermolecular forces on deep sub-10 nm spaced sliders", *IEEE Transactions on Magnetics* **38**, 2141 (2002).

[43] B. H. Thornton and D. B. Bogy, "Head-disk interface dynamic instability due to intermolecular forces", *IEEE Transactions on Magnetics* **39**, 2420 (2003).

[44] Q. Dai, F. Hendriks, and B. Marchon, "Modeling the washboard effect at the head/disk interface", *Journal of Applied Physics* **96**, 696 (2004).

[45] D. Weller and A. Moser, "Thermal effect limits in ultrahigh-density magnetic recording", *IEEE Transactions on Magnetics* **35**, 4423 (1999).

[46] M. H. Kryder, E. C. Gage, T. W. McDaniel, W. A. Challener, R. E. Rottmayer, J. Ganping, Y.-T. Hsia, and M. F. Erden, "Heat Assisted Magnetic Recording", *Proceedings of the IEEE* **96**, 1810 (2008).

[47] R. E. Rottmayer, S. Batra, D. Buechel, W. A. Challener, J. Hohlfeld, Y. Kubota, L. Li, L. Bin, C. Mihalcea, K. Mountfield, K. Pelhos, C. Peng, T. Rausch, M. A. Seigler, D. Weller, and X. Yang, "Heat-Assisted Magnetic Recording", *IEEE Transactions on Magnetics* **42**, 2417 (2006).

[48] H. J. Richter, A. Y. Dobin, O. Heinonen, K. Z. Gao, R. J. M. v. d. Veerdonk, R. T. Lynch, J. Xue, D. Weller, P. Asselin, M. F. Erden, and R. M. Brockie, "Recording on Bit-Patterned Media at Densities of 1 Tb/in^2 and Beyond", *IEEE Transactions on Magnetics* **42**, 2255 (2006).

[49] B. D. Terris, T. Thomson, and G. Hu, "Patterned media for future magnetic data storage", *Microsystem Technologies* **13**, 189 (2007).

[50] J.-G. Zhu, X. Zhu, and Y. Tang, "Microwave Assisted Magnetic Recording", *IEEE Transactions on Magnetics* **44**, 125 (2008).

[51] S. Greaves, Y. Kanai, and H. Muraoka, "Shingled Recording for 2–3 Tbit/in^2", *IEEE Transactions on Magnetics* **45**, 3823 (2009).

[52] R. Wood, M. Willlams, A. Kavcic, and J. Miles, "The Feasibility of Magnetic Recording at 10 Terabits Per Square Inch on Conventional Media", *IEEE Transactions on Magnetics* **45**, 917 (2009).

[53] D. Reinsel and J. Rydning, “Helium taking HDDs to new heights”, International Data Corporation, White Paper, Nov. 2013.

[54] Advanced Storage Industry Consortium (ASTC). (2014). *ASTC Technology Roadmap 2014 v8* [Online]. Available: http://www.idema.org/?page_id=2269. (Accessed Jul. 8, 2015).

[55] T. R. Albrecht, H. Arora, V. Ayanoor-Vitikkate, J. M. Beaujour, D. Bedau, D. Berman, A. L. Bogdanov, Y. A. Chapuis, J. Cushen, E. E. Dobisz, G. Doerk, G. He, M. Grobis, B. Gurney, W. Hanson, O. Hellwig, T. Hirano, P.-O. Jubert, D. Kercher, J. Lille, Z. Liu, C. M. Mate, Y. Obukhov, K. C. Patel, K. Rubin, R. Ruiz, M. Schabes, L. Wan, D. Weller, T.-W. Wu, and E. Yang, "Bit-Patterned Magnetic Recording: Theory, Media Fabrication, and Recording Performance", *IEEE Transactions on Magnetics* **51**, 0800342 (2015).

[56] B. Marchon, K. Saito, B. Wilson, and R. Wood, "The Limits of the Wallace Approximation for PMR Recording at High Areal Density", *IEEE Transactions on Magnetics* **47**, 3422 (2011).

[57] R. L. Wallace, "The reproduction of magnetically recorded signals", *Bell System Technology Journal* **30**, 1145 (1951).

[58] R. Wood, "The feasibility of magnetic recording at 1 Terabit per square inch", *IEEE Transactions on Magnetics* **36**, 36 (2000).

[59] C. M. Mate, B. K. Yen, D. C. Miller, M. F. Toney, M. Scarpulla, and J. E. Frommer, "New methodologies for measuring film thickness, coverage, and topography", *IEEE Transactions on Magnetics* **36**, 110 (2000).

[60] B. K. Yen, R. L. White, R. J. Waltman, Q. Dai, D. C. Miller, A. J. Kellock, B. Marchon, P. H. Kasai, M. F. Toney, B. R. York, H. Deng, Q. F. Xiao, and V. Raman, "Microstructure and properties of ultrathin amorphous silicon nitride protective coating", *Journal of Vacuum Science & Technology A: Vacuum, Surfaces, and Films* **21**, 1895 (2003).

[61] V. Novotny and N. Staud, "Correlation between environmental and electrochemical corrosion of thin-film magnetic recording media", *Journal of the Electrochemical Society* **135**, 2931 (1988).

[62] R. J. Waltman, J. Joseph, and X. C. Guo, "An AFM study of corrosion on rigid magnetic disks", *Corrosion Science* **52**, 1258 (2010).

[63] Information Storage Industry Consortium (INSIC), "Information Storage Industry Consortium International Magnetic Tape Storage Roadmap 2012-2022", May 2012.

[64] M. Peters, “The technical and operational values of barium ferrite tape media”, Enterprise Strategy Group, White Paper, Mar. 2014.

[65] F. E. Talke, "Tribology in magnetic recording technology", *Industrial Lubrication and Tribology* **52**, 157 (2000).

[66] J. Wang, "Dual module RWW tape head assembly", U.S. Patent US 6 690 542 B1, Fenruary 10, 2004.

[67] P. Poorman, "The effect of tape overwrap angle and head radius on head/tape spacing and contact pressure in linear tape recording", *Tribology International* **31**, 449 (1998).

[68] J. B. C. Engelen, S. Furrer, H. E. Rothuizen, and M. A. Lantz, "Flat-Profile Tape–Head Friction and Magnetic Spacing", *IEEE Transactions on Magnetics* **50**, 34 (2014).

[69] J. C. Engelen and M. Lantz, "Asymmetrically Wrapped Flat-Profile Tape–Head Friction and Spacing", *Tribology Letters* **59**, 16 (2015).

[70] S. H. Muftu and H. F. Hinteregger, "Contact sheet recording with a self-acting negative air bearing", U.S. Patent 6 118 626, September 12, 2000.

[71] M. D. Bijker, J. J. J. Bastiaens, E. A. Draaisma, L. A. M. de Jong, E. Sourty, S. O. Saied, and J. L. Sullivan, "The development of a thin Cr_2O_3 wear protective coating for the advanced digital recording system", *Tribology International* **36**, 227 (2003).

[72] W. W. Scott, B. Bhushan, and A. V. Lakshmikumaran, "Ultrathin diamond-like carbon coatings used for reduction of pole tip recession in magnetic tape heads", *Journal of Applied Physics* **87**, 6182 (2000).

[73] G. S. A. M. Theunissen, "Wear coatings for magnetic thin film magnetic recording heads", *Tribology International* **31**, 519 (1998).

[74] B. Shi, J. L. Sullivan, M. A. Wild, and S. O. Saied, "Study of Generation Mechanism of Three-Body Particles in Linear Tape Recording", *Journal of Tribology* **127**, 155 (2005).

[75] J. L. Sullivan, M. A. Wild, and M. S. Hempstock, "The tribology of linear tape/head interfaces and its impact on signal performance", *Tribology International* **36**, 261 (2003).

[76] R. G. Biskeborn, W. S. Czarnecki, G. M. Decad, R. E. Fontana, I. E. Iben, J. Liang, C. Lo, L. Randall, P. Rice, A. Ting, and T. Topuria, "(Invited) Linear Magnetic Tape Heads and Contact Recording", *ECS Transactions* **50**, 19 (2013).

[77] J. A. Wickert, "Analysis Of Self-excited Longitudinal Vibration Of A Moving Tape", *Journal of Sound and Vibration* **160**, 455 (1993).

[78] G. Cherubini, R. D. Cideciyan, L. Dellmann, E. Eleftheriou, W. Haeberle, J. Jelitto, V. Kartik, M. A. Lantz, S. Olcer, A. Pantazi, H. E. Rothuizen, D. Berman, W. Imaino, P.-O. Jubert, G. McClelland, P. V. Koeppe, K. Tsuruta, T. Harasawa, Y. Murata, A. Musha, H. Noguchi, H. Ohtsu, O. Shimizu, and R. Suzuki, "29.5-Gb/\in^2 Recording Areal Density on Barium Ferrite Tape", *IEEE Transactions on Magnetics* **47**, 137 (2011).

[79] G. M. McClelland, D. Berman, P.-O. Jubert, W. Imaino, H. Noguchi, M. Asai, and H. Takano, "Effect of Tape Longitudinal Dynamics on Timing Recovery and Channel Performance", *IEEE Transactions on Magnetics* **45**, 3587 (2009).

[80] F. Spada, "Contribution of electrochemical processes to increased head-media spacing in tape drives", Univeristy of California, San Diego, Information Storage Industry Consortium TAPE Program Technical Review Report, Aug. 2013.

[81] J. Robertson, "Diamond-like amorphous carbon", *Materials Science & Engineering R-Reports* **37**, 129 (2002).

[82] M. Scarselli, P. Castrucci, and M. D. Crescenzi, "Electronic and optoelectronic nano-devices based on carbon nanotubes", *Journal of Physics: Condensed Matter* **24**, 313202 (2012).

[83] J. Robertson, "Amorphous carbon", *Advances in Physics* **35**, 317 (1986).

[84] D. G. McCulloch, D. R. McKenzie, and C. M. Goringe, "Ab initio simulations of the structure of amorphous carbon", *Physical Review B* **61**, 2349 (2000).

[85] J. Robertson, "Electronic and atomic structure of diamond-like carbon", *Semiconductor Science and Technology* **18**, S12 (2003).

[86] A. C. Ferrari and J. Robertson, "Raman spectroscopy of amorphous, nanostructured, diamond-like carbon, and nanodiamond", *Philosophical Transactions of the Royal Society of London, Series A* **362**, 2477 (2004).

[87] Y. Lifshitz, "Diamond-like carbon — present status", *Diamond and Related Materials* **8**, 1659 (1999).

[88] D. R. McKenzie, "Tetrahedral bonding in amorphous carbon", *Reports on Progress in Physics* **59**, 1611 (1996).

[89] L. Holland and S. M. Ojha, "Deposition of hard and insulating carbonaceous films on an r.f. target in a butane plasma", *Thin Solid Films* **38**, L17 (1976).

[90] B. Marchon, P. N. Vo, M. R. Khan, and J. W. Ager, "Structure and mechanical properties of hydrogenated carbon films prepared by magnetron

sputtering [for magnetic discs]", *IEEE Transactions on Magnetics* **27**, 5160 (1991).

[91] M. Weiler, S. Sattel, T. Giessen, K. Jung, H. Ehrhardt, V. S. Veerasamy, and J. Robertson, "Preparation and properties of highly tetrahedral hydrogenated amorphous carbon", *Physical Review B* **53**, 1594 (1996).

[92] C. Casiraghi, J. Robertson, and A. C. Ferrari, "Diamond-like carbon for data and beer storage", *Materials Today* **10**, 44 (2007).

[93] R. Kalish, Y. Lifshitz, K. Nugent, and S. Prawer, "Thermal stability and relaxation in diamond-like-carbon. A Raman study of films with different sp3 fractions (ta-C to a-C)", *Applied Physics Letters* **74**, 2936 (1999).

[94] C. Donnet and A. Erdemir, *Tribology of Diamond-like Carbon Films*, 1st ed. New York, NY, USA: Springer, 2008.

[95] Y. Lifshitz, S. Kasi, J. Rabalais, and W. Eckstein, "Subplantation model for film growth from hyperthermal species", *Physical Review B: Condensed Matter* **41**, 10468 (1990).

[96] J. Robertson, "Deposition mechanisms for promoting sp3 bonding in diamond-like carbon", *Diamond and Related Materials* **2**, 984 (1993).

[97] S. Aisenberg and R. Chabot, "Ion-Beam Deposition of Thin Films of Diamondlike Carbon", *Journal of Applied Physics* **42**, 2953 (1971).

[98] A. Libassi, A. C. Ferrari, V. Stolojan, B. K. Tanner, J. Robertson, and L. M. Brown, "Density and sp^3 Content in Diamond-Like Carbon Films by X-ray Reflectivity and Electron Energy Loss Spectroscopy", *MRS Online Proceedings Library* **593**, (1999).

[99] M. Chhowalla, J. Robertson, C. W. Chen, S. R. P. Silva, C. A. Davis, G. A. J. Amaratunga, and W. I. Milne, "Influence of ion energy and substrate temperature on the optical and electronic properties of tetrahedral amorphous carbon (ta-C) films", *Journal of Applied Physics* **81**, 139 (1997).

[100] P. J. Fallon, V. S. Veerasamy, C. A. Davis, J. Robertson, G. A. J. Amaratunga, W. I. Milne, and J. Koskinen, "Properties of filtered-ion-beam-deposited diamondlike carbon as a function of ion energy", *Physical Review B* **48**, 4777 (1993).

[101] J. Zhu, J. Han, X. Han, H. I. Schlaberg, and J. Wang, "sp^3-rich deposition conditions and growth mechanism of tetrahedral amorphous carbon films deposited using filtered arc", *Journal of Applied Physics* **104**, 013512 (2008).

[102] F.-X. Liu and Z.-L. Wang, "Thickness dependence of the structure of diamond-like carbon films by Raman spectroscopy", *Surface and Coatings Technology* **203**, 1829 (2009).

[103] M. G. Beghi, A. C. Ferrari, K. B. K. Teo, J. Robertson, C. E. Bottani, A. Libassi, and B. K. Tanner, "Bonding and mechanical properties of ultrathin diamond-like carbon films", *Applied Physics Letters* **81**, 3804 (2002).

[104] C. A. Davis, G. A. J. Amaratunga, and K. M. Knowles, "Growth Mechanism and Cross-Sectional Structure of Tetrahedral Amorphous Carbon Thin Films", *Physical Review Letters* **80**, 3280 (1998).

[105] A. C. Ferrari, A. Libassi, B. K. Tanner, V. Stolojan, J. Yuan, L. M. Brown, S. E. Rodil, B. Kleinsorge, and J. Robertson, "Density, sp^3 fraction, and cross-sectional structure of amorphous carbon films determined by x-ray reflectivity and electron energy-loss spectroscopy", *Physical Review B* **62**, 11089 (2000).

[106] S. Kundu, "Study of bit-patterned FePt media for high density magnetic recording", Ph.D. dissertation, Dept. Elect. and Comp. Eng., National Univ. of Singapore, Singapore, 2014.

[107] E. Rismani-Yazdi, "Tribological studies of ultra-thin films at head/media interface for magnetic data storage systems", Ph.D. dissertation, Dept. Mech. Eng., National Univ. of Singapore, Singapore, 2012.

[108] J. W. Bradley, H. Bäcker, P. J. Kelly, and R. D. Arnell, "Time-resolved Langmuir probe measurements at the substrate position in a pulsed mid-frequency DC magnetron plasma", *Surface and Coatings Technology* **135**, 221 (2001).

[109] N. Dwivedi, R. J. Yeo, P. S. Goohpattader, N. Satyanarayana, S. Tripathy, and C. S. Bhatia, "Enhanced characteristics of pulsed DC sputtered ultrathin (<2nm) amorphous carbon overcoats on hard disk magnetic media", *Diamond and Related Materials* **51**, 14 (2015).

[110] P. J. Kelly, C. F. Beevers, P. S. Henderson, R. D. Arnell, J. W. Bradley, and H. Bäcker, "A comparison of the properties of titanium-based films produced by pulsed and continuous DC magnetron sputtering", *Surface and Coatings Technology* **174–175**, 795 (2003).

[111] A. Tomala, A. Pauschitz, and M. Roy, "Nanotribology of pulsed direct current magnetron sputtered diamond like carbon films", *Surface Science* **616**, 60 (2013).

[112] H. Inaba, K. Furusawa, and S. Sasaki, "Filtered Cathodic Vacuum Arc Process Conditions and Properties of Thin Tetrahedral Amorphous Carbon Films", *Japanese Journal of Applied Physics* **43**, 2681 (2004).

[113] A. Anders, W. Fong, A. V. Kulkarni, F. W. Ryan, and C. S. Bhatia, "Ultrathin diamond-like carbon films deposited by filtered carbon vacuum arcs", *IEEE Transactions on Plasma Science* **29**, 768 (2001).

[114] S. Schmidt, Z. Czigány, G. Greczynski, J. Jensen, and L. Hultman, "Ion mass spectrometry investigations of the discharge during reactive high power pulsed and direct current magnetron sputtering of carbon in Ar and Ar/N_2", *Journal of Applied Physics* **112**, 013305 (2012).

[115] M. Weiler, S. Sattel, K. Jung, H. Ehrhardt, V. S. Veerasamy, and J. Robertson, "Highly tetrahedral, diamond-like amorphous hydrogenated carbon prepared from a plasma beam source", *Applied Physics Letters* **64**, 2797 (1994).

[116] M. Weiler, K. Lang, E. Li, and J. Robertson, "Deposition of tetrahedral hydrogenated amorphous carbon using a novel electron cyclotron wave resonance reactor", *Applied Physics Letters* **72**, 1314 (1998).

[117] D. J. O'Connor, B. A. Sexton, and R. St. C. Smart, *Surface Analysis Methods in Materials Science*, 2nd ed. vol. 23. New York, NY, USA: Springer-Verlag, 2003.

[118] M. Sardela, *Practical Materials Characterization*, 1st ed. New York, NY, USA: Springer, 2014.

[119] M. A. Samad, E. Rismani, H. Yang, S. K. Sinha, and C. S. Bhatia, "Overcoat Free Magnetic Media for Lower Magnetic Spacing and Improved Tribological Properties for Higher Areal Densities", *Tribology Letters* **43**, 247 (2011).

[120] E. Rismani, S. K. Sinha, S. Tripathy, H. Yang, and C. S. Bhatia, "Effect of pre-treatment of the substrate surface by energetic C^+ ion bombardment on structure and nano-tribological characteristics of ultra-thin tetrahedral amorphous carbon (ta-C) protective coatings", *Journal of Physics D: Applied Physics* **44**, 115502 (2011).

[121] B. Balakrisnan, B. Tomcik, and D. J. Blackwood, "Influence of Carbon Sputtering Conditions on Corrosion Protection of Magnetic Layer by an Electrochemical Technique", *Journal of the Electrochemical Society* **149**, B84 (2002).

[122] D. G. Enos and L. L. Scribner, "The Potentiodynamic Polarization Scan", Solartron Analytical, Hampshire, UK, Technical Report 33, Jan. 1997.

[123] T. P. Hoar, "On the relation between corrosion rate and polarization resistance", *Corrosion Science* **7**, 455 (1967).

[124] M. Hakovirta, J. Salo, R. Lappalainen, and A. Anttila, "Correlation of carbon ion energy with sp^2/sp^3 ratio in amorphous diamond films produced with a mass-separated ion beam", *Physics Letters A* **205**, 287 (1995).

[125] W. C. Oliver and G. M. Pharr, "Measurement of hardness and elastic modulus by instrumented indentation: Advances in understanding and refinements to methodology", *Journal of Materials Research* **19**, 3 (2004).

[126] B. Raeymaekers and F. E. Talke, "Measurement and Sources of Lateral Tape Motion: A Review", *Journal of Tribology* **131**, 011903 (2008).

[127] A. C. Ferrari and J. Robertson, "Interpretation of Raman spectra of disordered and amorphous carbon", *Physical Review B: Condensed Matter* **61**, 14095 (2000).

[128] M. A. Samad, S. M. Xiong, L. Pan, H. Yang, S. K. Sinha, D. B. Bogy, and C. S. Bhatia, "A Novel Approach of Carbon Embedding in Magnetic Media for Future Head/Disk Interface", *IEEE Transactions on Magnetics* **48**, 1807 (2012).

[129] M. Abdul Samad, E. Rismani, W. M. Kwek, and C. S. Bhatia, "Energy gradient carbon embedding in the magnetic media for improved tribological performance", *Surface and Coatings Technology* **242**, 152 (2014).

[130] S. N. Piramanayagam and C. T. Chong, *Developments in data storage: Materials perspective*, 1st ed. New Jersey, NJ, USA: John Wiley & Sons, Inc., 2012.

[131] G. M. Pharr, D. L. Callahan, S. D. McAdams, T. Y. Tsui, S. Anders, A. Anders, J. W. Ager, I. G. Brown, C. S. Bhatia, S. R. P. Silva, and J. Robertson, "Hardness, elastic modulus, and structure of very hard carbon films produced by cathodic-arc deposition with substrate pulse biasing", *Applied Physics Letters* **68**, 779 (1996).

[132] Y. Wang, H. Li, L. Ji, F. Zhao, X. Liu, Q. Kong, Y. Wang, W. Quan, H. Zhou, and J. Chen, "The effect of duty cycle on the microstructure and properties of graphite-like amorphous carbon films prepared by unbalanced magnetron sputtering", *Journal of Physics D: Applied Physics* **43**, 505401 (2010).

[133] S. Anders, A. Anders, I. G. Brown, B. Wei, K. Komvopoulos, J. W. Ager Iii, and K. M. Yu, "Effect of vacuum arc deposition parameters on the properties of amorphous carbon thin films", *Surface and Coatings Technology* **68–69**, 388 (1994).

[134] N. Dwivedi, N. Satyanarayana, R. J. Yeo, H. Xu, K. P. Loh, S. Tripathy, and C. S. Bhatia, "Ultrathin Carbon with Interspersed Graphene/Fullerene-like Nanostructures: A Durable Protective Overcoat for High Density Magnetic Storage", *Scientific Reports* **5**, 11607 (2015).

[135] N. W. Khun, E. Liu, and M. D. Krishna, "Structure, Adhesive Strength and Electrochemical Performance of Nitrogen Doped Diamond-Like Carbon Thin Films Deposited via DC Magnetron Sputtering", *Journal of Nanoscience and Nanotechnology* **10**, 4752 (2010).

[136] C. Gao, Y. C. Lee, J. Chao, and M. Russak, "Dip-coating of ultra-thin liquid lubricant and its control for thin-film magnetic hard disks", *IEEE Transactions on Magnetics* **31**, 2982 (1995).

[137] N. W. Khun and E. Liu, "Investigation of corrosion behavior of nitrogen doped and platinum/ruthenium doped diamond-like carbon thin films in Hank's solution", *Materials Science and Engineering C* **31**, 1539 (2011).

[138] H. S. Zhang and K. Komvopoulos, "Surface modification of magnetic recording media by filtered cathodic vacuum arc", *Journal of Applied Physics* **106**, 093504 (2009).

[139] H.-S. Zhang and K. Komvopoulos, "Synthesis of ultrathin carbon films by direct current filtered cathodic vacuum arc", *Journal of Applied Physics* **105**, 083305 (2009).

[140] T. L. Barr, "An ESCA study of the termination of the passivation of elemental metals", *The Journal of Physical Chemistry* **82**, 1801 (1978).

[141] M. C. Biesinger, B. P. Payne, A. P. Grosvenor, L. W. M. Lau, A. R. Gerson, and R. S. C. Smart, "Resolving surface chemical states in XPS analysis of first row transition metals, oxides and hydroxides: Cr, Mn, Fe, Co and Ni", *Applied Surface Science* **257**, 2717 (2011).

[142] D. Briggs and M. P. Seah, *Practical Surface Analysis by Auger and X-ray Photoelectron Spectroscopy*, 1st ed. Chichester, United Kingdom: John Wiley & Sons, 1983.

[143] N. S. McIntyre and M. G. Cook, "X-ray photoelectron studies on some oxides and hydroxides of cobalt, nickel, and copper", *Analytical Chemistry* **47**, 2208 (1975).

[144] V. I. Nefedov, D. Gati, B. F. Dzhurinskii, N. P. Sergushin, and Y. V. Salyn, "X-ray electron study of oxides of elements", *Zhurnal Neorganicheskoi Khimii* **20**, 2307 (1973).

[145] C. D. Wagner, W. M. Riggs, L. E. Davis, and J. F. Moulder, *Handbook of X-ray Photoelectron Spectroscopy*, 1st ed. Minnesota: Perkin-Elmer Corp. (Physical Electronics), 1979.

[146] P. Marcus and J. M. Grimal, "The anodic dissolution and passivation of NiCrFe alloys studied by ESCA", *Corrosion Science* **33**, 805 (1992).

[147] B. Stypula and J. Stoch, "The characterization of passive films on chromium electrodes by XPS", *Corrosion Science* **36**, 2159 (1994).

[148] P. M. Jones, J. Ahner, C. L. Platt, H. Tang, and J. Hohlfeld, "Understanding Disk Carbon Loss Kinetics for Heat Assisted Magnetic Recording", *IEEE Transactions on Magnetics* **50**, 144 (2014).

[149] N. Wang, K. Komvopoulos, F. Rose, and B. Marchon, "Structural stability of hydrogenated amorphous carbon overcoats used in heat-assisted magnetic recording investigated by rapid thermal annealing", *Journal of Applied Physics* **113**, 083517 (2013).

[150] B. K. Pathem, X. C. Guo, F. Rose, N. Wang, K. Komvopoulos, E. Schreck, and B. Marchon, "Carbon Overcoat Oxidation in Heat-Assisted Magnetic Recording", *IEEE Transactions on Magnetics* **49**, 3721 (2013).

[151] S. Kundu, N. Dwivedi, N. Satyanarayana, R. J. Yeo, J. Ahner, P. M. Jones, and C. S. Bhatia, "Probing the Role of Carbon Microstructure on the Thermal Stability and Performance of Ultrathin (<2 nm) Overcoats on L10 FePt Media for Heat-Assisted Magnetic Recording", *ACS Applied Materials & Interfaces* **7**, 158 (2014).

[152] P. S. Goohpattader, N. Dwivedi, E. Rismani-Yazdi, N. Satyanarayana, R. J. Yeo, S. Kundu, and C. S. Bhatia, "Probing the role of C^+ ion energy, thickness and graded structure on the functional and microstructural characteristics of ultrathin carbon films (< 2 nm)", *Tribology International* **81**, 73 (2015).

[153] Z. Kovac and V. J. Novotny, "Silicon nitride overcoats for thin film magnetic recording media", *IEEE Transactions on Magnetics* **27**, 5070 (1991).

[154] B. K. Yen, R. L. White, R. J. Waltman, C. M. Mate, Y. Sonobe, and B. Marchon, "Coverage and properties of a-SiN_x hard disk overcoat", *Journal of Applied Physics* **93**, 8704 (2003).

[155] E. Rismani, R. Yeo, H. Mirabolghasemi, W. M. Kwek, H. Yang, and C. S. Bhatia, "An ultrathin multilayer TiN/SiN wear resistant coating for advanced magnetic tape drive heads", *Thin Solid Films* **556**, 354 (2014).

[156] F. Rose, B. Marchon, V. Rawat, D. Pocker, Q.-F. Xiao, and T. Iwasaki, "Ultrathin TiSiN overcoat protection layer for magnetic media", *Journal of Vacuum Science and Technology A* **29**, 051502 (2011).

[157] F. Rose, D. Pocker, Q.-F. Xiao, V. Rawat, E. Brinkman, and B. Marchon, "Low surface energy and corrosion resistant ultrathin TiSiC disk overcoat", *Journal of Applied Physics* **113**, 213513 (2013).

[158] M. Azzi, P. Amirault, M. Paquette, J. E. Klemberg-Sapieha, and L. Martinu, "Corrosion performance and mechanical stability of 316L/DLC coating system: Role of interlayers", *Surface and Coatings Technology* **204**, 3986 (2010).

[159] N. Dwivedi, E. Rismani-Yazdi, R. J. Yeo, P. S. Goohpattader, N. Satyanarayana, N. Srinivasan, B. Druz, S. Tripathy and C. S. Bhatia, "Probing the Role of an Atomically Thin SiN_x Interlayer on the Structure of Ultrathin Carbon Films", *Scientific Reports* **4**, 5021 (2014).

[160] R. J. Yeo, N. Dwivedi, E. Rismani, N. Satyanarayana, S. Kundu, P. S. Goohpattader, H. R. Tan, N. Srinivasan, B. Druz, S. Tripathy, and C. S. Bhatia, "Enhanced Tribological, Corrosion, and Microstructural Properties of an Ultrathin (<2 nm) Silicon Nitride/Carbon Bilayer Overcoat for High

Density Magnetic Storage", *ACS Applied Materials & Interfaces* **6**, 9376 (2014).

[161] A. Ferrari and J. Robertson, "Resonant Raman spectroscopy of disordered, amorphous, and diamondlike carbon", *Physical Review B: Condensed Matter* **64**, 075414 (2001).

[162] D. S. Bethune, C. H. Klang, M. S. de Vries, G. Gorman, R. Savoy, J. Vazquez, and R. Beyers, "Cobalt-catalysed growth of carbon nanotubes with single-atomic-layer walls", *Nature* **363**, 605 (1993).

[163] N. Dwivedi, S. Kumar, J. D. Carey, R. K. Tripathi, H. K. Malik, and M. K. Dalai, "Influence of Silver Incorporation on the Structural and Electrical Properties of Diamond-Like Carbon Thin Films", *ACS Applied Materials & Interfaces* **5**, 2725 (2013).

[164] N. W. Khun, E. Liu, G. C. Yang, W. G. Ma, and S. P. Jiang, "Structure and corrosion behavior of platinum/ruthenium/nitrogen doped diamondlike carbon thin films", *Journal of Applied Physics* **106**, 013506 (2009).

[165] C. S. Lee, T.-Y. Kim, K. R. Lee, and K. H. Yoon, "Nanoscale manipulation of tetrahedral amorphous carbon films", *Thin Solid Films* **447–448**, 169 (2004).

[166] G. A. Tritsaris, C. Mathioudakis, P. C. Kelires, and E. Kaxiras, "Optical and elastic properties of diamond-like carbon with metallic inclusions: A theoretical study", *Journal of Applied Physics* **112**, 103503 (2012).

[167] F. E. Spada, D. F. Paul, and J. S. Hammond, "Application Of Surface Analytical Techniques For Understanding Deposit Formation On Magnetic Tape Recording Head Surfaces", *Microscopy and Microanalysis* **18**, 874 (2012).

[168] B. Bhushan, B. K. Gupta, R. Sundaram, S. Dey, S. Anders, A. Anders, I. G. Brown, and P. D. Reader, "Development of hard carbon coatings for thin-film tape heads", *IEEE Transactions on Magnetics* **31**, 2976 (1995).

[169] B. Shi, J. L. Sullivan, and S. O. Saied, "A Study of Thin Coating Wear in High Data Density Tape Heads", *Journal of ASTM International* **5**, JAI101192 (2008).

[170] E. Sourty, J. L. Sullivan, and M. D. Bijker, "Chromium oxide coatings applied to magnetic tape heads for improved wear resistance", *Tribology International* **36**, 389 (2003).

[171] E. Rismani, R. Yeo, S. K. Sinha, H. Yang, and C. S. Bhatia, "Developing an (Al,Ti)N (x) C (y) Interlayer to Improve the Durability of the ta-C Coating on Magnetic Recording Heads", *Tribology Letters* **50**, 233 (2013).

[172] E. Rismani, S. K. Sinha, H. Yang, and C. S. Bhatia, "Effect of pretreatment of Si interlayer by energetic C^+ ions on the improved nanotribological properties of magnetic head overcoat", *Journal of Applied Physics* **111**, 084902 (2012).

[173] G. W. Brock, D. Conolly and W. S. Czarnecki, "Contact Recording on Bidirectional Thin-Film Tape Head Structures", in *Advances in Information Storage Systems*, vol. 6, B. Bhushan, Ed., 1st ed. Singapore: World Scientific Publishing, 1995, pp. 373-384.

[174] S. I. Raider, R. Flitsch, J. A. Aboaf, and W. A. Pliskin, "Surface Oxidation of Silicon Nitride Films", *Journal of the Electrochemical Society* **123**, 560 (1976).

[175] E. Sourty, M. Wild, and J. L. Sullivan, "Pole tip recession and staining at the head to tape interface of linear tape recording systems", *Wear* **252**, 276 (2002).

[176] Y. Wu and F. E. Talke, "Design of a head-tape interface for ultra low flying", *IEEE Transactions on Magnetics* **32**, 160 (1996).

[177] N. Dwivedi, S. Kumar, R. K. Tripathi, J. D. Carey, H. K. Malik, and M. K. Dalai, "Structural and Electronic Characterization of Nanocrystalline Diamondlike Carbon Thin Films", *ACS Applied Materials & Interfaces* **4**, 5309 (2012).

[178] N. Dwivedi, S. Kumar, J. D. Carey, H. K. Malik, and Govind, "Photoconductivity and characterization of nitrogen incorporated hydrogenated amorphous carbon thin films", *Journal of Applied Physics* **112**, 113706 (2012).

[179] R. J. Yeo, E. Rismani, N. Dwivedi, D. J. Blackwood, H. R. Tan, Z. Zhang, S. Tripathy, and C. S. Bhatia, "Bi-level surface modification of hard disk media by carbon using filtered cathodic vacuum arc: Reduced overcoat thickness without reduced corrosion performance", *Diamond and Related Materials* **44**, 100 (2014).

[180] E. Rismani, M. A. Samad, S. K. Sinha, R. Yeo, H. Yang, and C. S. Bhatia, "Ultrathin Si/C graded layer to improve tribological properties of Co magnetic films", *Applied Physics Letters* **101**, 191601 (2012).

[181] K. H. Ernst, J. Patscheider, R. Hauert, and M. Tobler, "XPS study of the a-C:H/Al_2O_3 interface", *Surface and Interface Analysis* **21**, 32 (1994).

[182] T. Peng, Z. Kou, H. Wu, and S. Mu, "Graphene from Amorphous Titanium Carbide by Chlorination under 200[deg]C and Atmospheric Pressures", *Scientific Reports* **4**, 5494 (2014).

[183] S. Zhang, X. L. Bui, J. Jiang, and X. Li, "Microstructure and tribological properties of magnetron sputtered nc-TiC/a-C nanocomposite", *Surface and Coatings Technology* **198**, 206 (2005).

[184] P. Bunnak, Y. Gong, S. Limsuwan, A. Pokaipisit, and P. Limsuwan, "Chemical Bonding in Composite SiN_x/Diamond-Like Carbon Films Prepared by Filter Cathodic Arc Deposition of Graphite Incorporated with Radio Frequency Sputtering of Silicon Nitride", *Japanese Journal of Applied Physics* **52**, 095501 (2013).

[185] M. Matsuoka, S. Isotani, W. Sucasaire, L. S. Zambom, and K. Ogata, "Chemical bonding and composition of silicon nitride films prepared by inductively coupled plasma chemical vapor deposition", *Surface and Coatings Technology* **204**, 2923 (2010).

[186] Y. Fu, H. Du, S. Zhang, and S. E. Ong, "Effects of silicon nitride interlayer on phase transformation and adhesion of TiNi films", *Thin Solid Films* **476**, 352 (2005).

[187] N. Hellgren, J. Guo, Y. Luo, C. Såthe, A. Agui, S. Kashtanov, J. Nordgren, H. Ågren, and J.-E. Sundgren, "Electronic structure of carbon nitride thin films studied by X-ray spectroscopy techniques", *Thin Solid Films* **471**, 19 (2005).

[188] R. McCann, S. S. Roy, P. Papakonstantinou, M. F. Bain, H. S. Gamble, and J. A. McLaughlin, "Chemical bonding modifications of tetrahedral amorphous carbon and nitrogenated tetrahedral amorphous carbon films induced by rapid thermal annealing", *Thin Solid Films* **482**, 34 (2005).

[189] R. Bertoncello, A. Casagrande, M. Casarin, A. Glisenti, E. Lanzoni, L. Mirenghi, and E. Tondello, "TiN, TiC and Ti(C, N) film characterization and its relationship to tribological behaviour", *Surface and Interface Analysis* **18**, 525 (1992).

[190] H. Yan, W. R. Cannon, and D. J. Shanefield, "Evolution of Carbon during Burnout and Sintering of Tape-Cast Aluminum Nitride", *Journal of the American Ceramic Society* **76**, 166 (1993).

[191] X. B. Yan, T. Xu, G. Chen, S. R. Yang, H. W. Liu, and Q. J. Xue, "Preparation and characterization of electrochemically deposited carbon nitride films on silicon substrate", *Journal of Physics D: Applied Physics* **37**, 907 (2004).

[192] L. Ramqvist, K. Hamrin, G. Johansson, A. Fahlman, and C. Nordling, "Charge transfer in transition metal carbides and related compounds studied by ESCA", *Journal of Physics and Chemistry of Solids* **30**, 1835 (1969).

[193] A. Schüler and P. Oelhafen, "In situ core-level and valence-band photoelectron spectroscopy of reactively sputtered titanium aluminum nitride films", *Physical Review B* **63**, 115413 (2001).

[194] I. l. Strydom and S. Hofmann, "The contribution of characteristic energy losses in the core-level X-ray photoelectron spectroscopy peaks of TiN and (Ti, Al)N studied by electron energy loss spectroscopy and X-ray photoelectron spectroscopy", *Journal of Electron Spectroscopy and Related Phenomena* **56**, 85 (1991).

[195] Y. Liu, T. P. Chen, P. Zhao, S. Zhang, S. Fung, and Y. Q. Fu, "Memory effect of Al-rich AlN films synthesized with rf magnetron sputtering", *Applied Physics Letters* **87**, 033112 (2005).

[196] P. J. Matsuo, T. E. F. M. Standaert, S. D. Allen, G. S. Oehrlein, and T. J. Dalton, "Characterization of Al, Cu, and TiN surface cleaning following a low-K dielectric etch", *Journal of Vacuum Science & Technology B* **17**, 1435 (1999).

[197] *Data Interchange on 12.7 nm 384-Track Magnetic Tape Cartridges - Ultrium-1 Format*, ECMA Standard 319, 2001.

[198] S. Tan and F. E. Talke, "Numerical and Experimental Investigations of the Head/Tape Interface in a Digital Linear Tape Drive", *Journal of Tribology* **123**, 343 (2000).

[199] E. Rismani, S. K. Sinha, H. Yang, S. Tripathy, and C. S. Bhatia, "Development of a ta-C Wear Resistant Coating with Composite Interlayer for Recording Heads of Magnetic Tape Drives", *Tribology Letters* **46**, 221 (2012).

[200] N. Wang and K. Komvopoulos, "The multilayered structure of ultrathin amorphous carbon films synthesized by filtered cathodic vacuum arc deposition", *Journal of Materials Research* **28**, 2124 (2013).

[201] A. R. Konicek, D. S. Grierson, A. V. Sumant, T. A. Friedmann, J. P. Sullivan, P. U. P. A. Gilbert, W. G. Sawyer, and R. W. Carpick, "Influence of surface passivation on the friction and wear behavior of ultrananocrystalline diamond and tetrahedral amorphous carbon thin films", *Physical Review B* **85**, 155448 (2012).

[202] A. A. Voevodin, A. W. Phelps, J. S. Zabinski, and M. S. Donley, "Friction induced phase transformation of pulsed laser deposited diamond-like carbon", *Diamond and Related Materials* **5**, 1264 (1998).

[203] N. Dwivedi, R. J. Yeo, Z. Zhang, C. Dhand, S. Tripathy, and C. S. Bhatia, "Interface engineering and controlling the friction and wear of ultrathin carbon films: high sp^3 versus high sp^2 carbons", accepted for publication in *Advanced Functional Materials* (2016).

[204] N. W. Khun and E. Liu, "Influence of carbon sputtering power on structure, corrosion resistance, adhesion strength and wear resistance of platinum/ruthenium/nitrogen doped diamond-like carbon thin films", *Surface and Coatings Technology* **205**, 853 (2010).

[205] P. Lemoine, J. F. Zhao, J. P. Quinn, A. A. Ogwu, J. A. McLaughlin, P. Maguire, F. McGinnity and X. Shi, "Naniondentation and scratch resistance testing on magnetic tape heads coated with ultra-thin amorphous carbon layers", *Wear* **244**, 79 (2000).

[206] A. K. Geim and K. S. Novoselov, "The rise of graphene", *Nature Materials* **6**, 183 (2007).

[207] C. N. R. Rao, A. K. Sood, K. S. Subrahmanyam, and A. Govindaraj, "Graphene: The New Two-Dimensional Nanomaterial", *Angewandte Chemie International Edition* **48**, 7752 (2009).

[208] R. R. Nair, P. Blake, A. N. Grigorenko, K. S. Novoselov, T. J. Booth, T. Stauber, N. M. R. Peres, and A. K. Geim, "Fine Structure Constant Defines Visual Transparency of Graphene", *Science* **320**, 1308 (2008).

[209] E. Pop, V. Varshney, and A. K. Roy, "Thermal properties of graphene: Fundamentals and applications", *MRS Bulletin* **37**, 1273 (2012).

[210] N. O. Weiss, H. Zhou, L. Liao, Y. Liu, S. Jiang, Y. Huang, and X. Duan, "Graphene: An Emerging Electronic Material", *Advanced Materials* **24**, 5782 (2012).

[211] C. Lee, X. Wei, J. W. Kysar, and J. Hone, "Measurement of the Elastic Properties and Intrinsic Strength of Monolayer Graphene", *Science* **321**, 385 (2008).

[212] D. Berman, S. A. Deshmukh, S. K. R. S. Sankaranarayanan, A. Erdemir, and A. V. Sumant, "Macroscale superlubricity enabled by graphene nanoscroll formation", *Science* **348**, 1118 (2015).

[213] P. Egberts, G. H. Han, X. Z. Liu, A. T. C. Johnson, and R. W. Carpick, "Frictional Behavior of Atomically Thin Sheets: Hexagonal-Shaped Graphene Islands Grown on Copper by Chemical Vapor Deposition", *ACS Nano* **8**, 5010 (2014).

[214] Y. J. Shin, R. Stromberg, R. Nay, H. Huang, A. T. S. Wee, H. Yang, and C. S. Bhatia, "Frictional characteristics of exfoliated and epitaxial graphene", *Carbon* **49**, 4070 (2011).

[215] O. Leenaerts, B. Partoens, and F. M. Peeters, "Water on graphene: Hydrophobicity and dipole moment using density functional theory", *Physical Review B* **79**, 235440 (2009).

[216] J. S. Bunch, S. S. Verbridge, J. S. Alden, A. M. van der Zande, J. M. Parpia, H. G. Craighead, and P. L. McEuen, "Impermeable Atomic Membranes from Graphene Sheets", *Nano Letters* **8**, 2458 (2008).

[217] R. K. Singh Raman, P. Chakraborty Banerjee, D. E. Lobo, H. Gullapalli, M. Sumandasa, A. Kumar, L. Choudhary, R. Tkacz, P. M. Ajayan,

and M. Majumder, "Protecting copper from electrochemical degradation by graphene coating", *Carbon* **50**, 4040 (2012).

[218] S. H. Vemuri, P. S. Chung, R. L. Smith, N.-E. Lee, L. T. Biegler, and M. S. Jhon, "Head-disk interface design in magnetic data storage", *Journal of Applied Physics* **111**, 07B721 (2012).

[219] NUS Graphene Centre. (2013). *Joint graphene research to boost data storage* [Online]. Available: http://news.nus.edu.sg/highlights/6946-joint-graphene-research-to-boost-data-storage. (Accessed August 11, 2015).

[220] B. A. Gurney, E. E. Marinero, and S. Pisana, "Magnetic devices and magnetic media with graphene overcoat", U.S. Patent Application Publication No. US 2011/0151278 A1, June 23, 2011.

[221] F. Bonaccorso, A. Lombardo, T. Hasan, Z. Sun, L. Colombo, and A. C. Ferrari, "Production and processing of graphene and 2d crystals", *Materials Today* **15**, 564 (2012).

[222] X. Li, Y. Zhu, W. Cai, M. Borysiak, B. Han, D. Chen, R. D. Piner, L. Colombo, and R. S. Ruoff, "Transfer of Large-Area Graphene Films for High-Performance Transparent Conductive Electrodes", *Nano Letters* **9**, 4359 (2009).

[223] A. C. Ferrari, J. C. Meyer, V. Scardaci, C. Casiraghi, M. Lazzeri, F. Mauri, S. Piscanec, D. Jiang, K. S. Novoselov, S. Roth, and A. K. Geim, "Raman Spectrum of Graphene and Graphene Layers", *Physical Review Letters* **97**, 187401 (2006).

[224] A. C. Ferrari, "Raman spectroscopy of graphene and graphite: Disorder, electron–phonon coupling, doping and nonadiabatic effects", *Solid State Communications* **143**, 47 (2007).

[225] H. Kondo, "Tribochemistry of Ionic Liquid Lubricant on Magnetic Media", *Advances in Tribology* **2012**, 526726 (2012).

[226] E. C. Cutiongco, D. Li, Y.-W. Chung, and C. S. Bhatia, "Tribological Behavior of Amorphous Carbon Nitride Overcoats for Magnetic Thin-Film Rigid Disks", *Journal of Tribology* **118**, 543 (1996).

Appendix A: Details of characterization methods used in this thesis

A.1 The working principle of HRTEM

A schematic diagram of a HRTEM system is presented in Figure A.1.

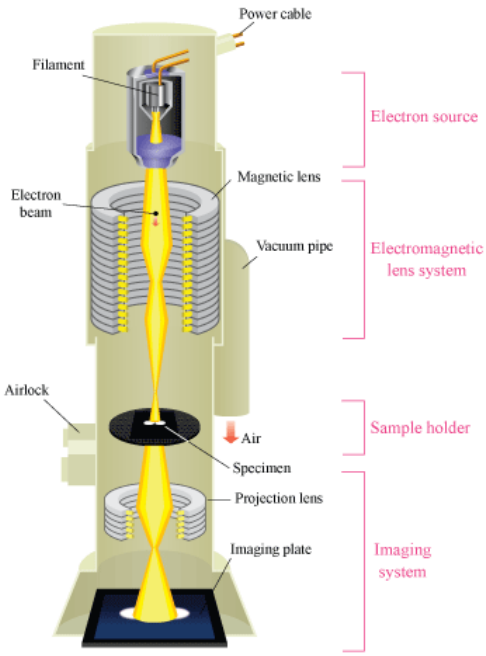

Figure A.1 Schematic diagram of a HRTEM system column. [1].

In HRTEM, imaging is performed via the interaction and transmission of electrons through an electron-transparent sample. Electrons, which are mainly generated by a field emission source, are accelerated from the source towards the sample at a high accelerating voltage (typically a few hundred kilovolts). Down the column, the electron beam passes through electromagnetic condenser and objective lenses which focus and direct the beam onto the location on the sample for imaging. After interaction with the sample, the beam passes through a final set of projector lenses which project

the beam onto a charge coupled device (CCD) camera to capture the resulting image.

The interaction of electrons with the sample can be used to extract various types of information about the sample, such as relative atomic composition, crystallographic orientation, lattice defects, etc. However, in this work, the HRTEM system is primarily used in the bright field mode for cross-sectional thickness measurement of the carbon-based overcoats. Electrons which encounter areas of the sample with higher atomic masses are scattered more from the normal incident axis of the electron beam and fewer of these scattered electrons pass through the aperture. As a result, these areas appear as a darker contrast in the image. Hence, to distinguish the overcoat from other layers, a capping layer of tantallum (Ta) or titanium nitride (TiN) which has a higher atomic mass than carbon, is usually deposited to provide image contrast.

A.2 The working principle of tapping mode AFM

AFM is used to map the topography of the sample surface, when it possesses features on the scale of a few hundred nanometers or less. A schematic of the AFM system is shown in Figure A.2. The topographical information is obtained by scanning the surface using a probe, which comprises a cantilever and a probe tip typically made of silicon. A laser beam is shone onto the top of the cantilever, which is reflected into a photodiode detector. The detector is calibrated to detect any shift in the laser spot, which occurs when there is a deflection in the cantilever.

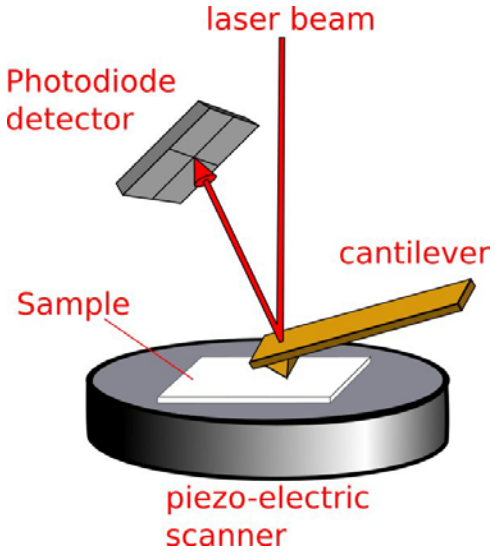

Figure A.2 Schematic showing the important parts of the AFM which are responsible for topographical mapping of the surface. [2].

In general, AFM can be conducted in one of three modes, namely contact mode, non-contact mode and intermittent contact (tapping) mode. One of the advantages of the non-contact and tapping modes of AFM over the contact mode is that the tip-sample forces can be reduced while maintaining good surface topography sensitivity, thereby reducing the damage between the tip and the sample surface. At distances of less than 100 nm, short-range forces such as van der Waals, electrostatic, chemical and capillary forces give rise to attractive forces as represented by the negative portion of the force-distance curve in Figure A.3. However, when the tip comes almost in contact with the surface, it experiences a net repulsive force arising from Coulombic and Pauli repulsion. This is represented by the large positive portion of the force-distance curve.

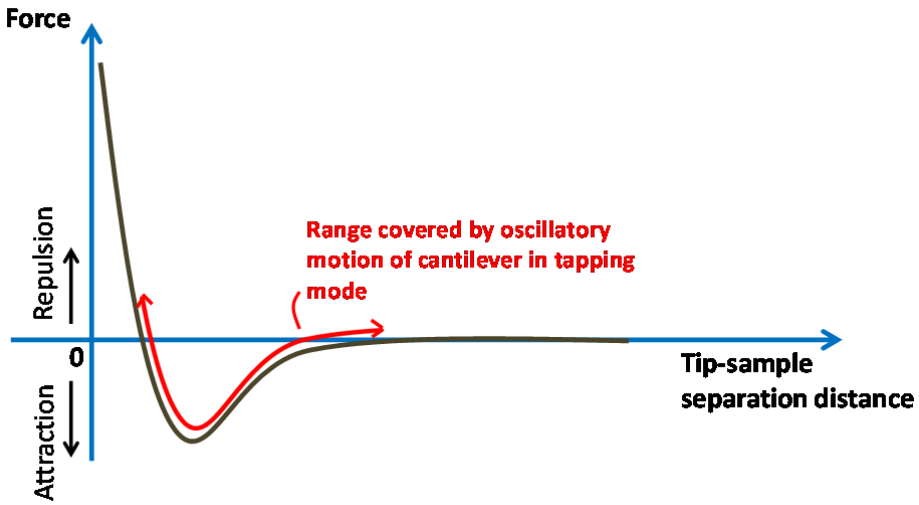

Figure A.3 Typical force-distance curve experienced by the tip when it is in close proximity to the surface. The range of the cantilever's oscillatory motion in tapping mode AFM is shown in red.

Tapping mode AFM employs the oscillatory motion of the cantilever in the z-axis with a large amplitude at the tip's resonance frequency within close proximity of the surface. This oscillatory motion crosses between the attractive and repulsive region (hence resulting in intermittent contact with the surface), as indicated in Figure A.3. Using a feedback loop mechanism, the AFM system maintains a constant oscillation amplitude for topography measurement. As the tip scans the surface, whenever the tip approaches a higher step on the surface, this causes a decrease in the oscillation amplitude, as shown in Figure A.4. The feedback loop compensates this amplitude decrease by increasing the tip-sample distance such that the amplitude is maintained. The increase in the tip-sample distance thus results in a cantilever deflection, which is registered as an increase in the z-height in the AFM topographical image. Similarly, when the tip senses a lower step on the surface, the oscillation amplitude increases and the tip-sample distance is decreased to maintain a constant oscillation amplitude. This is registered as a decrease in the z-height in the AFM topographical image. By this method, the

topographical features such as step heights and surface roughness can be evaluated.

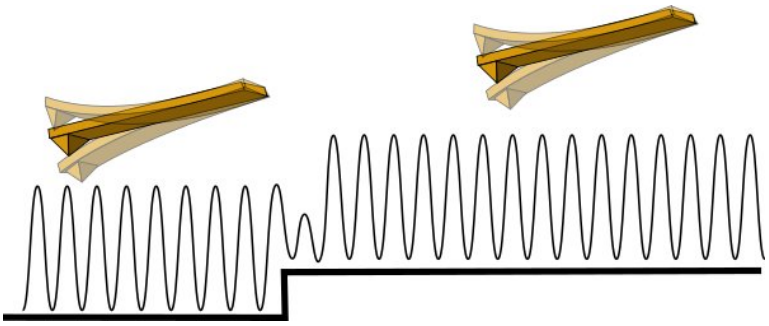

Figure A.4 Variation of oscillation amplitude when the tip encounters a higher step. A feedback mechanism increases the tip-sample distance by deflecting the cantilever upwards, in order to maintain a constant oscillation amplitude on the higher step. [2].

The resolution of the AFM topographical image is dependent on several factors, such as the scan rate, scanning step size, detector sensitivity and tip radius. A sharper tip, usually with a tip radius of < 10 nm, is able to obtain higher resolution due to its ability to probe smaller features.

A.3 Brief description of the nano-indentation technique

As the name suggests, nano-indentation uses a sharp tip (most often, a diamond Berkovich geometry tip is used) to penetrate the topmost surface of the film at nanoscale depth resolution. During the nano-indentation process, the tip is indented up to a certain depth and then withdrawn at low speeds of ~ 10 nm/s. Typically, a load versus displacement curve is plotted, whereby the load is the load applied by the tip and the displacement is the depth of penetration into the surface. The load-displacement curve consists of the loading cycle (during surface penetration) and the unloading cycle (during tip withdrawal). From this curve, important information such as the hardness,

elastic modulus and plastic deformation can be extracted based on the method by Oliver and Pharr [3].

A.4 Working principle of TOF-SIMS

TOF-SIMS is a surface sensitive chemical composition analysis technique which possesses high depth resolution and excellent detection limits. In the TOF-SIMS technique, a pulsed primary ion beam is used to bombard and sputter out positive or negative secondary ions from the surface which are then accelerated towards a mass spectrometer via an electric field to be analyzed. TOF-SIMS analysis is performed based on the time taken for the secondary ions to "fly" towards the mass spectrometer detector. The time of flight of the ion is proportional to its mass/charge ratio, i.e. the heavier the ion or the less charge it has, the longer it takes for it to reach the detector. Hence, with proper calibration, the identities of the ions can be deduced. Due to the variation in the secondary ion yields depending on the sputtered ion and primary ion beam used, TOF-SIMS is useful mostly as a relative comparison technique. As a result of the sputtering process, it is not uncommon to also detect molecular ions coming from the substrate, if the film is a multi-elemental compound film or contains contaminants. Moreover, secondary ions can also interact with trace gaseous atoms in the vacuum chamber such as H and O, which result in molecular ions being detected.

The TOF-SIMS technique can be used to perform a 2D chemical composition mapping of the surface (based on relative ion counts at each location within the map), as well as depth profiling to probe just beneath the

surface. Depth profiling is carried out in a repeated two-step sequence of firstly ion beam sputtering of the surface for a certain amount of time to form a crater, followed by performing a TOF-SIMS analysis on a small area at the bottom of the freshly formed crater (to avoid detection of secondary ions from the crater walls). Each TOF-SIMS analysis after each sputtering step would correspond to the chemical composition at a certain depth beneath the original surface. Hence, plotting the various ion counts with respect to sputter time would give a depth profile.

A.5 Working principle of AES

Most AES systems utilize an electron beam to excite the atoms at the surface. The electron beam interacts with the surface in a way which can be modeled by an interaction volume, as illustrated in Figure A.5. In AES, Auger electrons are the species of interest to be detected, which arise from the top ~ 1–2 nm of the surface due to their typically lower energies and hence shorter mean free path through the solid.

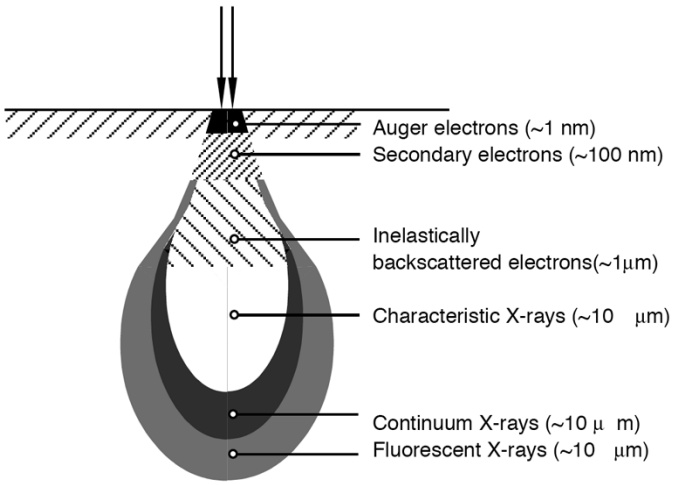

Figure A.5 Characteristic electron beam interaction volume with the sample surface, showing the various types of electrons and X-rays that are emitted at different depth ranges. [4].

Figure A.6 illustrates the Auger process when an incident electron collides with and knocks out an inner K-shell electron of a surface atom. To maintain a minimum energy in the atom, an electron from the higher energy L_1-shell fills the vacancy via a relaxation process, thus releasing energy in the process in the form of photons (X-ray fluorescence) or electron emission from a higher energy level, such as from the $L_{2,3}$-shell (Auger electron emission).

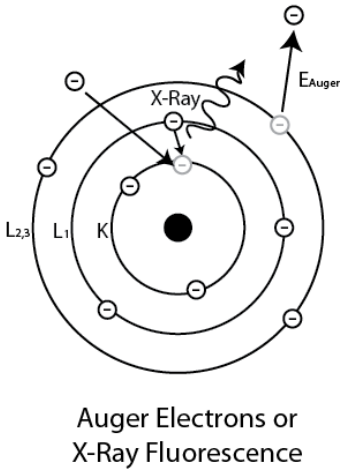

Figure A.6 Auger process occurring in an atom resulting in emission of X-ray fluorescence or Auger electrons. [4].

In AES, the Auger electrons are carried towards the Auger analyzer and detected according to the number of electron counts N(E) as a function of their kinetic energy (KE). For an Auger electron, the KE is the resultant energy that the electron possesses after the Auger process. In the example above, this can be represented by:

$$KE = BE_K - BE_{L_1} - BE_{L_{2,3}}$$

where BE_K is the binding energy of the K-shell electron, BE_{L1} is the binding energy of the L_1-shell electron, and $BE_{L2,3}$ is the binding energy of the $L_{2,3}$-shell electron. This particular transition is termed as the $KL_1L_{2,3}$ transition. Consequently, other Auger transitions with different KEs are possible

involving various combinations of electron shells. As the electron shell binding energies for each element are fixed and well documented, the various Auger peaks appearing in the Auger spectra at different KEs can be used to determine the element detected in the sample surface. Due to the low intensities of the Auger peaks and high background noise level in a N(E) versus KE plot, most Auger spectra are presented in a first derivative plot of dN(E) versus KE.

A.6 Working principle of XPS

The working principle of XPS is based on the photoelectric effect. When an incident X-ray photon with energy *hv* is absorbed by an atom, a photoelectron is emitted with a certain KE, which is measured by an energy analyzer and detector positioned at an angle to the surface, known as the take-off angle. The KE is dependent on the following relation:

$$KE = hv - BE - \Phi$$

where BE is the binding energy of the electron, and Φ is the spectrometer work function which is usually calibrated and known beforehand [5]. Since the BE reveals information about the material and its chemical state, XPS spectra are usually plotted as a function of BE, which can be calculated from the above equation.

Atoms in a solid are bonded to neighboring atoms in a lattice, and this leads to characteristic BEs for different types of bonds. This is because bonding involves electron sharing between the valence electrons, to various degrees depending on the adjacent atom and type of bond. For example, the

BE of a photoelectron emitted from the carbon 1s (C 1s) orbital of a C–H bond would be slightly different from the BE of a photoelectron that is emitted from the C 1s orbital of a C=O bond, on the order of a few eV. As such, for a solid containing significant amounts of both C–H and C=O bonds, a broad peak would appear across these two BE values in the C 1s core level XPS spectrum. This is, in fact, a convoluted peak comprising the sum of the respective two peaks corresponding to C–H and C=O bonding. By using mathematical fitting methods, deconvolution of the various XPS core level spectra obtained for different elements in the sample can be performed to get a good estimate of the various types of chemical bonding present for the element. Quantitative analysis of the bonding ratios of an element can also be performed based on the ratios of the deconvoluted peak areas.

A.7 Working principle of Raman spectroscopy

Raman spectroscopy employs the Raman effect as a tool for understanding the structure of materials. The Raman effect is derived from the inelastic scattering of light when light interacts with a material, where the energy of the incident absorbed photon is different from the energy of the photon released during scattering. Figure A.7 shows two possible scenarios when inelastic scattering of light occurs. In the first scenario, the incident photon energy is greater than the scattered photon energy, due to the absorption of energy by the material to bring the atoms to an excited vibrational state. This is known as Stokes Raman scattering. In the second scenario, the incident photon energy is less than the scattered photon energy due to a net release of energy by the atoms when they transition from the

excited state to the ground state. This is known as anti-Stokes Raman scattering. From Figure A.7, it is clear that anti-Stokes Raman scattering requires the atom to be at an initial excited state before photon interaction. This scenario is much less likely to occur as compared to an atom initially being at the ground state. Hence, most of the Raman scattering observed originates from the Stokes Raman scattering process. Raman spectroscopy exploits this effect and the characteristic resonant vibration modes and frequencies of a particular material to determine the microstructure.

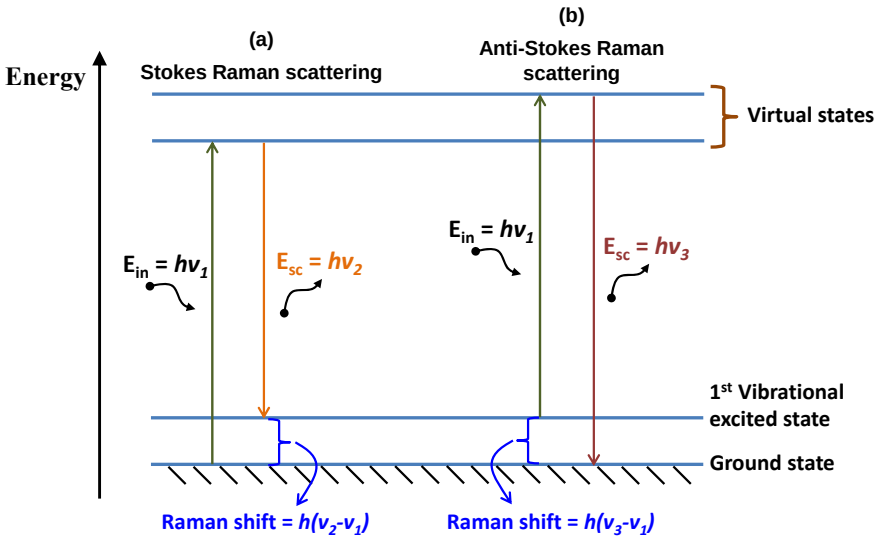

Figure A.7 Energy diagram illustrating (a) the Stokes Raman scattering and (b) the anti-Stokes Raman scattering processes. The Raman shift which is picked up by the spectrometer is recorded in the Raman spectrum.

With respect to amorphous carbon, the excitation energies of sp^1, sp^2 and sp^3 bonding fall between a range of 0–5.5 eV, which corresponds to the energy range of photons in the IR to visible to UV range. Today, lasers with wavelengths in this range are used for surface excitation. After surface interaction, some of the scattered photons are extracted through a lens towards a spectrometer, and the Raman spectrum of intensity versus the Raman shift (in terms of wavenumber, cm^{-1}) is recorded using a CCD camera. By careful

interpretation of the Raman spectra, the microstructure of the carbon film can be deduced.

References for Appendix A

[1] Department of Physics, City Univeristy of Hong Kong. Department of Physics. *Atomic World: Basic principle of transmission electron microscope* [Online]. Available: http://www.hk-phy.org/atomic_world/tem/tem02_e.html. (Accessed August 11, 2015).

[2] C. Ronduit. (2010). *AFM Figures* [Online]. Creative Commons Attribution. Available: www.freesbi.ch. (Accessed August 11, 2015).

[3] W. C. Oliver and G. M. Pharr, "An improved technique for determining hardness and elastic modulus using load and displacement sensing indentation experiments", *Journal of Materials Research* **7**, 1564 (1992).

[4] M. Dewar, "Characterization and Evaluation of Aged 20Cr32Ni1Nb Stainless Steels", M.S. thesis, Dept. Chem. and Mater. Eng., Univ. of Alberta, Edmonton, AB, Canada, 2012.

[5] M. Sardela, *Practical Materials Characterization*, 1st ed. New York, NY, USA: Springer, 2014.

Appendix B: Details of the parametric data measurements for the long-term tape test of functional tape heads

B.1 Measurement of BBSNR

The BBSNR is the ratio of the average read signal power to the average integrated broad band root-mean-square noise power expressed in decibels (dB). To measure the BBSNR, the tape head is installed in a modified tape drive connected to a pre-amplifier. A spectrum analyzer is connected at the output of the pre-amplifier. A tape cartridge pre-recorded with magnetic bits having a repetitive bit pattern of 10101010…. is used to measure the BBSNR across the head (linear density of 15142 bits per millimeter and fundamental recording frequency of f_1). At this stage, the peak detect function on the spectrum analyzer is switched on to measure the spectrum for signal detection. This peak signal is denoted as S_{signal}. Next, the spectrum analyzer's peak detect function is switched off to measure the noise level. The noise is measured at a minimum of 8 points across the bandwidth of 0–20 MHz. The total base noise (TBN) is calculated by integrating the noise values obtained over the range of 0 MHz to $2f_1$ and square rooting the result. Finally, the BBSNR in dB is calculated as 20 log (S_{signal}/TBN).

B.2 Measurement of 2T Output

The 2T output is the average peak-to-peak value of the output signal that is obtained when a tape cartridge pre-recorded with magnetic bits having a repetitive bit pattern of 10101010…. runs across the head. The output signal is measured using an oscilloscope connected to the read sensor output from the head.

B.3 Measurement of Resolution

The resolution is simply the ratio of the 2T output to the 8T output. Similar to the 2T output, the 8T output is the average peak-to-peak value of the output signal that is obtained when a tape cartridge pre-recorded with magnetic bits having a repetitive bit pattern of 10000000…. runs across the head (4 times lower fundamental frequency compared to 2T output). The output signal is measured using an oscilloscope connected to the read sensor output from the head.

Appendix C: Details of the Raman and XPS spectra analyses for the 17–20 nm monolithic and bi-layer overcoats

C.1 UV and visible Raman spectra analyses

Figure C.1 presents the visible (514.5 nm) and UV (325 nm) Raman spectra of the five monolithic and bi-layer overcoats deposited on flat AlTiC substrates.

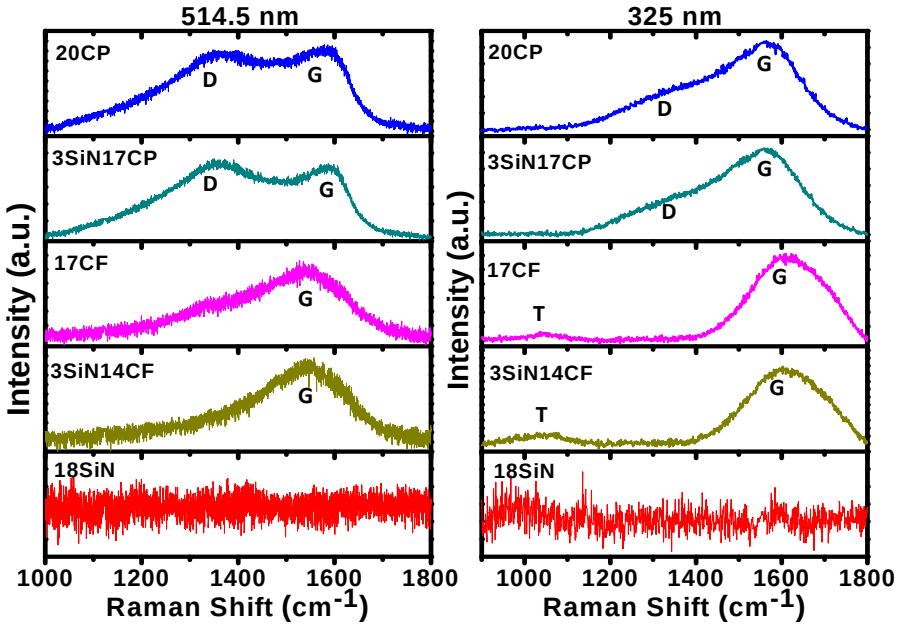

Figure C.1 Visible (514 nm) and UV (325 nm) Raman spectra of the various monolithic and bi-layer overcoats deposited on flat AlTiC substrates.

From the visible Raman spectra, the D peak was found to be very faint (almost negligible) in the FCVA-processed ta-C layers in samples 17CF and 3SiN14CF while the G peak was significantly intense. To analyze the microstructure in detail, appropriate fitting functions were used to fit the D and G peaks in the visible Raman spectra. The fitting results revealed the

location of the G peak at wavenumbers of 1591 cm^{-1} and 1596 cm^{-1} in samples 20CP and 3SiN17CP, respectively, whereas the G peak locations were located at wavenumbers of 1557 cm^{-1} and 1555 cm^{-1} in samples 17CF and 3SiN14CF, respectively. The I_D/I_G ratios were also calculated and found to be ~ 1.0 and ~ 1.1 in samples 20CP and 3SiN17CP, respectively. The same fitting functions were used to fit the UV Raman spectra of the carbon films. The fitted UV Raman spectra revealed the observation of the G peak at wavenumbers of 1571 cm^{-1} and 1569 cm^{-1} in samples 20CP and 3SiN17CP, respectively, whereas the locations of the G peaks were observed at wavenumbers of 1621 cm^{-1} and 1615 cm^{-1} in samples 17CF and 3SiN14CF, respectively. The I_D/I_G ratios were estimated to be ~ 0.4 in both samples 20CP and 3SiN17CP. It should be noted that in the UV Raman spectra of the FCVA-processed carbon layers in samples 17CF and 3SiN14CF, even a very faint D peak was not observed in the spectra. Interestingly however, the UV Raman spectra showed the presence of a weak T peak in the FCVA-processed samples, which is due to the presence of significant amount of sp^3C bonding within the carbon layer [1]. On the other hand, the T peak was absent in the UV Raman spectra of the sputtered a-C films, thereby showing that there is a low amount of sp^3C bonding within the sputtered a-C.

The G-peak dispersion values for these samples based on the shift of the G peak positions in the UV and visible Raman spectra were also calculated. The G-peak dispersion, which is defined as the rate of change of the change in G peak position as a function of excitation wavelength, is calculated based on the following equation [2]:

$$G\ peak\ dispersion = \frac{G\ peak\ pos.(325\ nm) - G\ peak\ pos.(514.5\ nm)}{(514.5 - 325)\ nm}$$

For sputter deposited carbon, the G-peak dispersion values were found to be 0.11 cm^{-1}/nm and 0.14 cm^{-1}/nm in samples 20CP and 3SiN17CP, respectively. On the other hand, FCVA-processed carbon showed G-peak dispersion values of 0.34 cm^{-1}/nm and 0.32 cm^{-1}/nm in samples 17CF and 3SiN14CF, respectively. The results showed that the G-peak dispersion was significantly higher in FCVA-processed carbon films than sputtered carbon films. However, between samples 17CF and 3SiN14CF, no significant difference in G-peak dispersion values was observed. Similarly, among sputter deposited carbon films, sample 3SiN17CP showed only marginally higher G-peak dispersion than sample 20CP. Although the D and G peaks are associated to sp^2 bonding, however, based on G-peak dispersion, the G peak position in the UV Raman spectra, the I_D/I_G ratio, the shape of the spectra and the appearance of the T peak in the UV Raman spectra, it can be concluded that FCVA-processed carbon has a much higher sp^3 carbon bonding than sputter deposited carbon films. However, sp^3 carbon bonding seems to be almost similar in samples 17CF when compared to sample 3SiN14CF, and in sample 20CP when compared to sample 3SiN17CP, with marginal variation. In other words, the sp^3C bonding may be slightly higher in sample 17CF than 3SiN14CF, and also slightly higher in sample 3SiN17CP than 20CP, but they are not very different.

C.2 XPS spectra analyses

XPS measurements were performed on as-deposited and after depth profile sputter etching from the surface to the interface to the substrate, in order to completely understand the chemical structure and interfacial bonding of the overcoats. For the calculation of sp^3 and sp^2 carbon bonding and bonding of carbon with oxygen, the C 1s spectra recorded on as-deposited samples were considered. However, for examination of interfacial bonding, the C 1s, Si 2p, N 1s, Al 2p and Ti 2p core level spectra recorded after etching so as to reach the different interfaces were considered and only the necessary spectra for interfacial analyses given here. Because of the different thicknesses and etch rates, the etching times required to reach the interfacial regions were different between samples.

Figures C.2(a)–(d) shows the deconvoluted C 1s core level spectra for the four carbon-containing overcoats at 0 min etching time. The deconvolution was performed using different Gaussian-Lorentzian components with background subtraction in Shirley mode. The C 1s core level spectra of these samples revealed four constituent peaks corresponding to sp^2C bonding, sp^3C bonding, C–O bonding, and C=O bonding. By estimating the ratio of the areas under the peaks, the sp^2C and sp^3C bonding fractions of these samples were calculated. The sp^3C bonding in samples 20CP, 3SiN17CP, 17CF and 3SiN14CF was found to be 18.0%, 22.0%, 76.5% and 71.3%, respectively, with an error bar of ± 5%. Thus, it is clear that FCVA-processed carbon films in samples 17CF and 3SiN14CF showed much higher sp^3C bonding than the sputter deposited carbon films in samples 20CP and 3SiN17CP. This

difference is due to the energetics involved in the deposition of these two different types of the overcoats, which has already been discussed in previous two sections. Between the sputtered carbon overcoats in samples 20CP and 3SiN17CP however, the sp^2C/sp^3C contents can be said to be similar (within the error range), with marginal variation. The sp^2C/sp^3C contents in the FCVA-processed overcoats in samples 17CF and 3SiN14CF were also similar (within the error range). Therefore, based on the Raman and XPS C 1s spectra, it was concluded that the microstructures of the carbon layers in the carbon-based monolithic and bi-layer overcoats were similar.

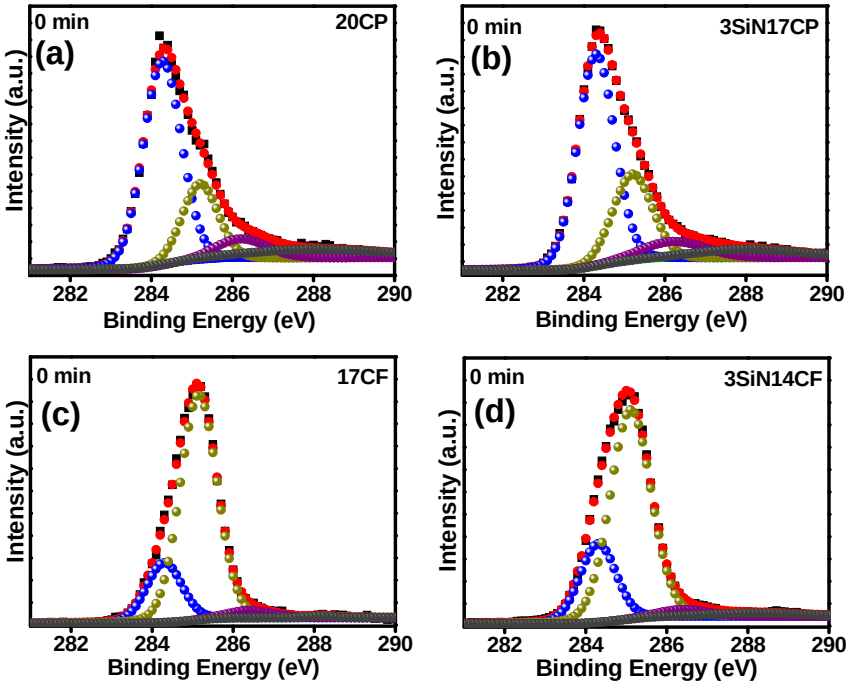

Figure C.2 Deconvoluted XPS C 1s core level spectra of carbon-containing overcoats (a) 20CP, (b) 3SiN17CP, (c) 17CF, and (d) 3SiN14CF deposited on flat AlTiC substrates. Constituent peaks are represented by the following colors: sp^2C (blue), sp^3C (dark yellow), C–O (purple), C=O (gray).

Further, in order to understand the behavior at the interfaces and interfacial bonding, the spectra corresponding to the depths at which the interfaces were detected were analyzed. Based on our analyses the C 1s, Si 2p

and N 1s spectra recorded after etching for 7 min, 8.5 min and 10min for sample 3SiN17CP, and 7 min and 8.5 min for sample 3SiN14CF were considered for analyses and are presented in Figures C.3 (for sample 3SiN17CP) and C.4 (for sample 3SiN14CF) respectively.

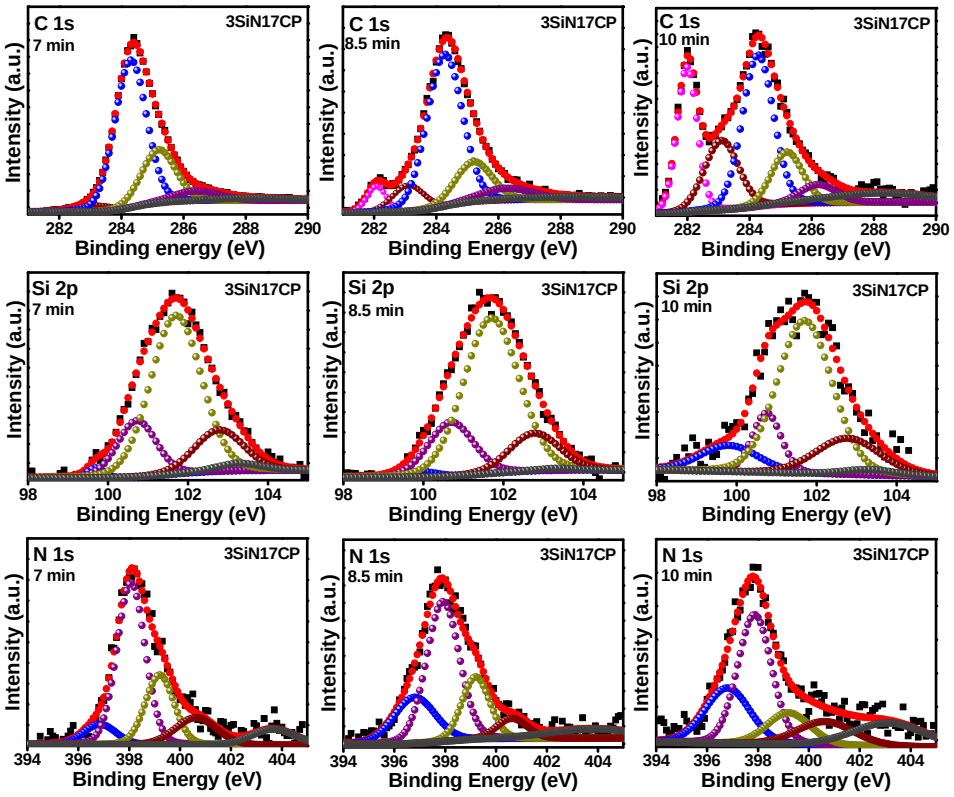

Figure C.3 Deconvoluted XPS C 1s, Si 2p and N 1s core level spectra of sample 3SiN17CP on flat AlTiC substrate, at etching times of 7, 8.5 and 10 mins to probe the interfacial bonding at the carbon-SiN_x and SiN_x-AlTiC interfaces. Constituent peaks of C 1s spectra are represented by the following colors: sp^2C (blue), sp^3C (dark yellow), C–O (purple), C=O (gray), Si–C (maroon), Ti–C (pink). Constituent peaks of Si 2p spectra are represented by the following colors: Si–N (dark yellow), Si–C (purple), Si–O/Si–N (maroon), Si=O (gray), Si–Si (blue). Constituent peaks of N 1s spectra are represented by the following colors: Si–N (purple), Nitrile (dark yellow), C=N (maroon), (Al,Ti)N (blue), N–O (gray).

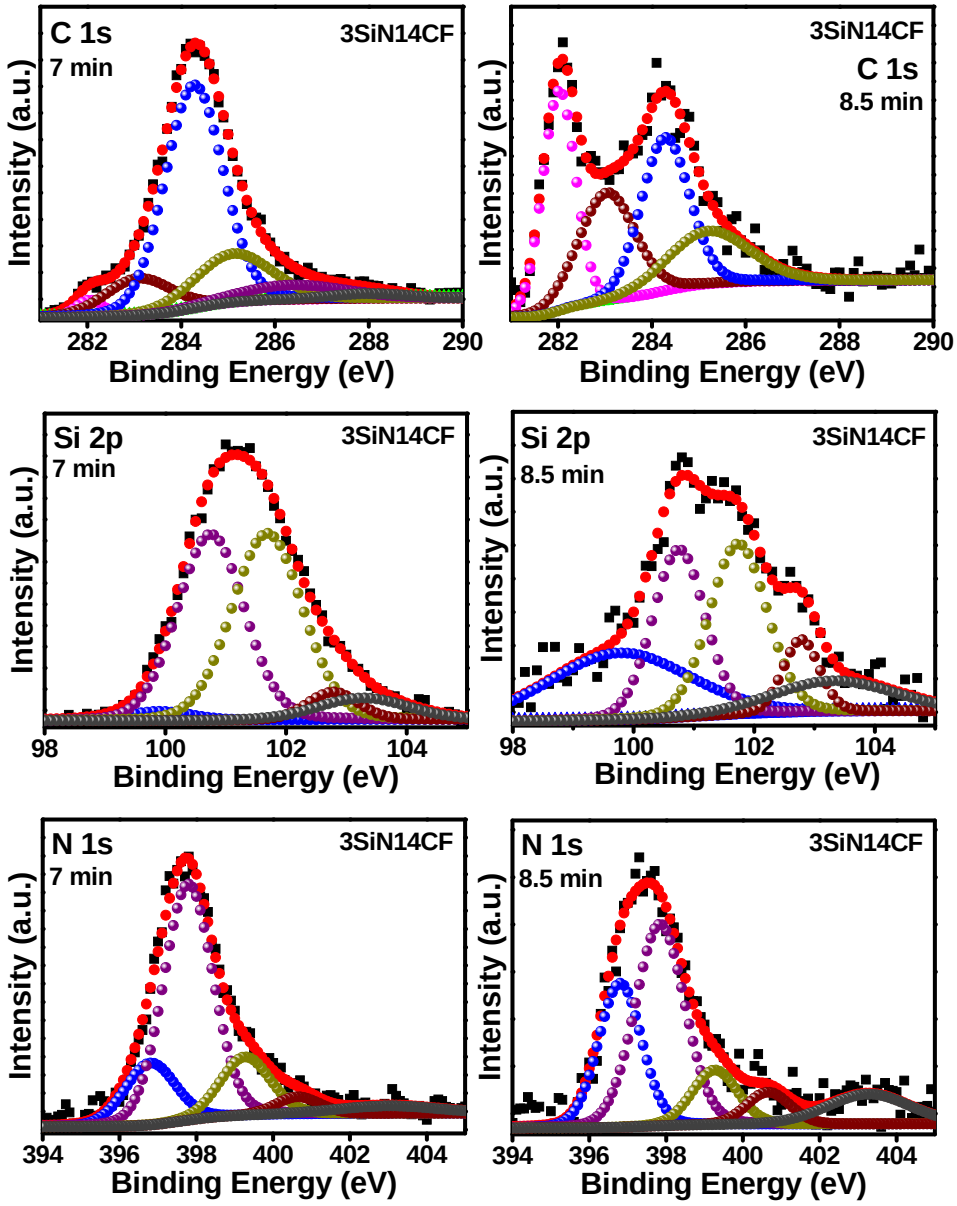

Figure C.4 Deconvoluted XPS C 1s, Si 2p and N 1s core level spectra of sample 3SiN14CF on flat AlTiC substrate, at etching times of 7 and 8.5 mins to probe the interfacial bonding at the carbon-SiN_x and SiN_x-AlTiC interfaces. Constituent peaks of C 1s spectra are represented by the following colors: sp^2C (blue), sp^3C (dark yellow), C–O (purple), C=O (gray), Si–C (maroon), Ti–C (pink). Constituent peaks of Si 2p spectra are represented by the following colors: Si–N (dark yellow), Si–C (purple), Si–O/Si–N (maroon), Si=O (gray), Si–Si (blue). Constituent peaks of N 1s spectra are represented by the following colors: Si–N (purple), Nitrile (dark yellow), C=N (maroon), (Al,Ti)N (blue), N–O (gray).

Similarly, the Al 2p and Ti 2p spectra recorded after etching for 10 min each for sample 3SiN17CP and 8.5 min each for sample 3SiN14CF were

considered for analysis and presented in Figure C.5. From all the C 1s, Si 2p, N 1s, Al 2p and Ti 2p spectra of both bi-layer overcoats, the formation of the different types of interfacial bonding such as Si-C, nitrile, C-N, (Al, Ti)N, (Al, Ti)N-oxide, and Al-N bonding were observed (which had also been discussed in Sections 6.2 and 6.3 of the thesis). These bonds were observed in addition to the existing Si-N bonding present in SiN_x and TiC and Al-O present in AlTiC. The formation of such interfacial bonds is very important due to its vital role in enhancing the wear resistance of the overcoats.

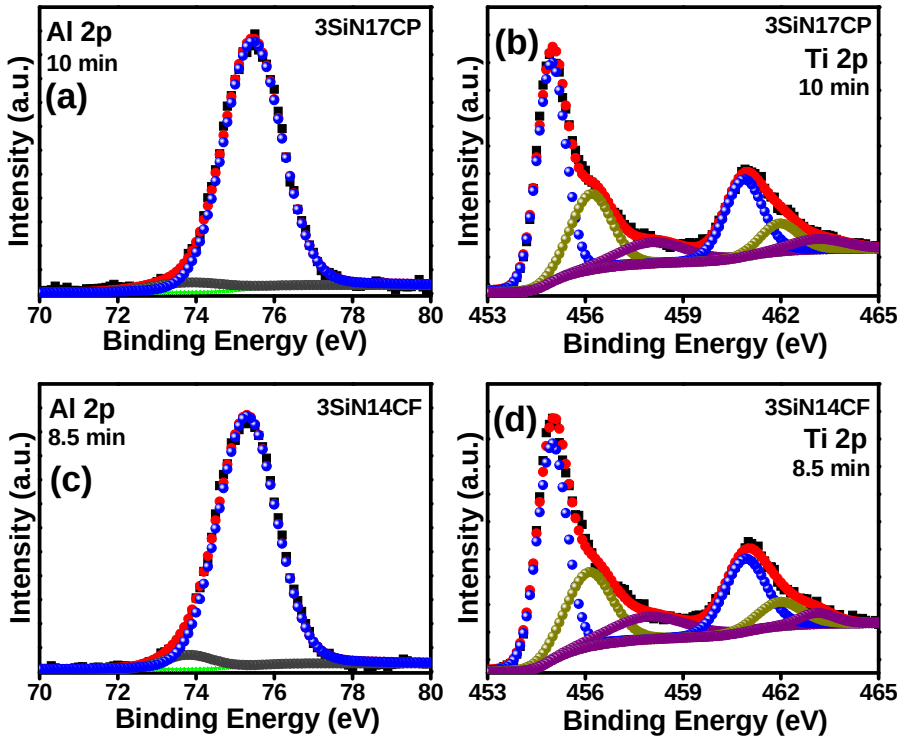

Figure C.5 Deconvoluted XPS Al 2p and Ti 2p core level spectra of (a)–(b) sample 3SiN17CP on flat AlTiC substrate taken at etching time of 10 min, and (c)–(d) sample 3SiN14CF on flat AlTiC substrate at etching time of 8.5 min to probe the interfacial bonding at the carbon-SiN_x and SiN_x-AlTiC interfaces. Constituent peaks of Al 2p spectra are represented by the following colors: Al–O (blue), Al–N (gray). Constituent peaks of Ti 2p spectra are represented by the following colors: Ti–C (blue), (Ti,Al)N (dark yellow), (Ti,Al)N–O (purple).

References for Appendix C

[1] A. Ferrari and J. Robertson, "Resonant Raman spectroscopy of disordered, amorphous, and diamondlike carbon", *Physical Review B: Condensed Matter* **64**, 075414 (2001).

[2] A. C. Ferrari and J. Robertson, "Raman spectroscopy of amorphous, nanostructured, diamond-like carbon, and nanodiamond", *Philosophical Transactions of the Royal Society of London, Series A* **362**, 2477 (2004).